THE DYNAMICS AND KINEMATICS

OF THE COASTAL BOUNDARY LAYER OFF LONG ISLAND

by

NEAL ROBERT PETTIGREW

A.B., Dartmouth College (1972)

M.S., Louisiana State University (1975)

SUBMITTED IN PARTIAL FULFILLMENT OF THE

REQUIREMENTS FOR THE DEGREE OF

DOCTOR OF PHILOSOPHY

at the

MASSACHUSETTS INSTITUTE OF TECHNOLOGY

and the

WOODS HOLE OCEANOGRAPHIC INSTITUTION

December, 1980

Signature of Author..
    Joint Program in Oceanography, Massachusetts Institute of Technology
    – Woods Hole Oceanographic Institution, and Department of Earth and
    Planetary Sciences, and Department of Meteorology, Massachusetts
    Institute of Technology, December, 1980.

Certified by..
                                              Thesis Supervisor

Accepted by...
    Chairman, Joint Oceanography Committee in Earth Sciences,
    Massachusetts Intsitute of Technology – Woods Hole Oceanographic
    Institution.

THE DYNAMICS AND KINEMATICS

OF THE COASTAL BOUNDARY LAYER OFF LONG ISLAND

by

NEAL ROBERT PETTIGREW

Submitted to the Massachusetts Institute of Technology — Woods
Hole Oceanographic Institution Joint Program in Oceanography on
December 30, 1980, in partial fulfillment of the requirements for
the degree of Doctor of Philosophy

ABSTRACT

Data from the COBOLT experiment, which investigated the first 12 km
off Long Island's south shore, are analyzed and discussed. Moored cur-
rent meter records indicate that the nearshore flow field is strongly
polarized in the alongshore direction and its fluctuations are well cor-
related with local meteorological forcing. Complex empirical orthogonal
function analysis suggests that subtidal velocity fluctuations are baro-
tropic in nature and are strongly influenced by bottom friction.

Wind-related inertial currents were observed within the coastal boun-
dary layer (CBL) under favorable meteorolgical and hydrographical condi-
tions. The magnitude of these oscillations increases with distance from
shore, and they display a very clear $180°$ phase difference between sur-
face and bottom layers. Nearshore inertial oscillations of both velocity
and salinity records appear to lead those further seaward, suggesting
local generation and subsequent radiation away from the coast.

The response of the coastal zone to impulsive wind forcing is dis-
cussed using simple slab and two-layer models, and the behavior of the
nearshore current field examined. The major features of the observed
inertial motions are in good qualitative agreement with model predic-
tions. It is found that, in a homogeneous domain, the coastal boundary
condition effectively prohibits inertial currents over the entire coastal
zone. In the presence of stratification the offshore extent of this pro-
hibition is greatly reduced and significant inertial currents may occur
within one or two internal deformation radii of the coast. The "coastal
effect", in the form of surface and interfacial waves which propagate

away from the coast, modifies the "pure" inertial response as it would exist far from shore. The kinematics of this process is such that a 180° phase difference between currents in the two layers is characteristic of the entire coastal zone even before the internal wave has had time to traverse the CBL. It is also suggested that, for positions seaward of several internal deformation radii, interference between the surface and internal components of the coastal response will cause maximum inertial amplitudes to occur for $t > x/c_2$, where c_2 is the phase speed of the internal disturbance.

The hydrographic structure of the CBL is observed to undergo frequent homogenization. These events are related to both advective and mixing processes. Horizontal and vertical exchange coefficients are estimated from the data, and subsequently used in a diffusive model which accurately reproduces the observed mean density distribution in the nearshore zone.

Dynamic balance calculations are performed which indicate that the subtidal cross-shore momentum balance is very nearly geostrophic. The calculations also suggest that the longshore balance may be reasonably represented by a steady, linear equation of motion which includes surface and bottom stresses.

Evidence is presented which shows that variations in the longshore wind-stress component are primarily responsible for the energetic fluctuations in the sea surface slope along Long Island. Depth-averaged velocities characteristically show net offshore transport in the study area, and often display dramatic longshore current reversals with distance from shore. These observations are interpreted in terms of a steady circulation model which includes realistic nearshore topography. Model results suggest that longshore current reversals within the CBL may be limited to the eastern end of Long Island, and that this unusual flow pattern is a consequence of flow convergence related to the presence of Long Island Sound.

Thesis Supervisor: Dr. Gabriel T. Csanady

Title: Senior Scientist
       Woods Hole Oceanographic Institution

To

Trish and Morrow

who are both my strength

and my weakness

ACKNOWLEDGEMENTS

I thank Joyce Csanady, Eloise Soderland, and May Reese for their maternal instincts, and "Data Dollies" Terry McKee, Carol Mills, and Nancy Pennington for cheerfully providing programming assistance and strong shoulders to cry on.

I have benefitted from many friendships with the students and staff of the Woods Hole Oceanographic Institution and thank them all for their good humor and camaraderie. In particular, I am grateful to Jerry Needell and Ping-Tung Shaw who frequently served as touchstones for many of my ideas.

Finally I owe a special debt of gratitude to my wife Trish for drafting most of the figures in this thesis, and for her many sacrifices as a student's spouse. Special thanks also to my baby daughter Sarah Morrow for a much needed vote of confidence when, at age 14 months, she came upon a pad of my scribblings and proclaimed it "book".

TABLE OF CONTENTS

CHAPTER I

THE COASTAL BOUNDARY LAYER TRANSECT EXPERIMENT

1.1 Introduction

The shallow coastal regions of the worlds oceans differ from deeper water environments dynamically, geologically, biologically, and in the physical-chemical properties of their associated water masses. In fact, within these shallow regions themselves, subregions may be identified (figure 1.1) such as the continental shelf break, outer shelf, inner shelf, coastal boundary layer, and surf zone, which are in many respects distinct (see Beardsley, Boicourt, and Hansen, 1976) and in some cases almost independent from one another. Yet despite these interesting and important differences, and to some extent because of them, the physical oceanography of these shallow marginal waters has historically remained largely overlooked. Only within the last decade has this trend been reversed with the commencement of a dramatic increase of interest in and understanding of the dynamics and kinematics of the world's coastal seas.

Advances in current meter and mooring technology, together with the recent surge of interest in the physical oceanography of the U.S. continental shelf regions, have resulted in the institution of extensive field programs involving moored instrument arrays often in conjunction
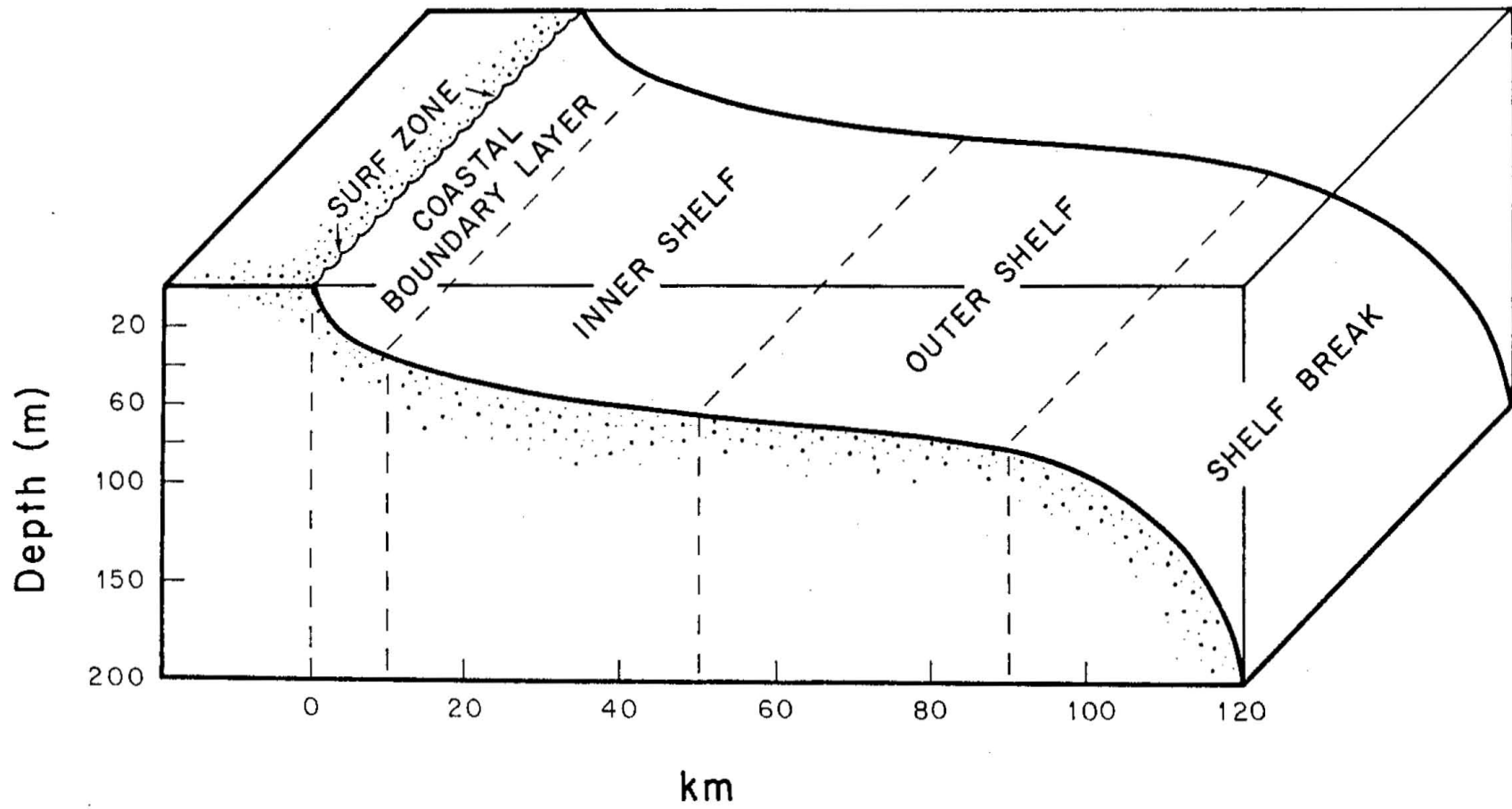
Figure 1.1   Schematic cross-section of Middle Atlantic Bight continental shelf.

with densely spaced hydrographic surveys. Examples of these concerted efforts are the MESA project (Mayer et al., 1979), Coastal Upwelling Experiments 1 and 2 (Kundu and Allen, 1975), the Little Egg Inlet Experiment (EG&G, 1975), and the New England Shelf Dynamics Experiment (Flagg et al., 1976). The excellent returns associated with these initial efforts have allowed characterization of both the mean and fluctuating portions of the scalar and vector fields found in inner shelf and deeper coastal environments. In addition, this rapid increase in basic observational information has sparked new theoretical interest with its attendant advancement in the understanding of the underlying dynamics of the shelf region. For excellent reviews of these observational and theoretical developements see Allen (1980), Csanady (1981), Mysak (1980) and Winant (1980).

In the very shallowest waters of the coastal region, within approximately 100 meters of the runup limit, is the wave-driven surf zone.. This region has historically been the subject of both varied and vigorous study, primarily by civil and coastal engineers, and as such posesses its own elaborate literature. The dynamics and the unique qualitative flow structure within this zone are fairly well known although their relationship to deeper water processes is still an intriguing and unsettled question.

Between the surf zone and the inner shelf is a region often called the coastal boundary layer which has been least studied, is least understood, and which may prove to be of greatest practical importance to an environmentally concerned technological society. This band of water,

extending from the seaward limit of the surf zone to order ten kilo-
meters from the coast, is the subject of this thesis. The author hopes
to illuminate its dynamics and to achieve its local characterization for
a fairly typical eastern seaboard environment off Long Island's south
shore.

1.2 The concept of the coastal boundary layer

The conceptual evolution of the coastal boundary layer (CBL) may be
traced to investigations of the North American Great Lakes dating back
some fifteen years. One of the first clear distinctions between flow
conditions close to the beach and those further offshore was drawn by
Verber (1966). As a result of a large scale experiment in Lake Michigan
it was noted that "straightline" along-isobath flow always occurred
nearshore while mid-lake currents were characterized by horizontally
isotropic near-inertial oscillations. In addition, many investigators
reported that the large thermocline displacements associated with the
upwelling events long observed in the Great Lakes were confined to a
nearshore band some 10 kilometers in width. After the advent of the
International Field Year on the Great Lakes in 1972, detailed coastal
zone observations (Csanady, 1972a,b) left little doubt that the near-
shore band was posessed of a current climatology quite different from
that in deeper water, and that the thermal field and its fluctuations
were also very different from those present at greater distance from the

coastal boundary. These observational facts formed the foundation of the CBL both as a conceptual and a theoretical construct. A more detailed review of the developement Coastal Boundary Layer concept is given by Csanady (1977b).

The Great Lakes experiments have yielded observational and theoretical results of sufficient generality to invite application to different and more complex environments. The most enticing course of action, and perhaps the greatest leap of faith as well, is the wholesale transference of the Coastal Boundary Layer concept with all its lore directly to nearshore oceanic environments. Any such application is bound to be complicated by the additional influences of vigorous tidal fluctuations (May, 1979) as well as interaction with larger scale flow features of the continental shelf and perhaps even the general circulation of the deep ocean. In any event the physical factors which served to differentiate the CBL from interior regions in the Great Lakes will also be operative and apply powerful dynamical constraints on motions in the oceanic boundary layer as well. In something like descending order of importance, these factors are:

1) The coastal boundary constraint which prohibits net cross-shore transport at the coast;

2) The seaward deepening of the water column which results in the generation of powerful vorticity tendencies in association with cross-isobath flow;

3) The general shallowness of the water column which amplifies the importance of frictional effects;

4) The seasonal occurrence of strong stratification which concentrates longshore momentum in the surface waters and leads to dramatic offshore variations in scalar and vector fields over horizontal scales of the baroclinic deformation radius.

It was the purpose of the Coastal Boundary Layer Transect (COBOLT) experiment to discover to what extent and in what manner these constraints continue to operate in the face of additional and complicating influences in the oceanic environment.

1.3 COBOLT deployments and experimental configurations

Although continental shelf experiments have sometimes included occasional moorings within the CBL (eg. CUE 1, CUE2) the COBOLT experiment is the first study specifically designed with sufficient resolution to investigate the temporal and spatial complexities of the oceanic nearshore band. The project, which represents a six year (1974-1979) joint effort between the Woods Hole Oceanographic Institution and the Brookhaven National Laboratory (BNL), was fielded at Tiana Beach on Long Island's south shore. The field site shown in figure 1.2 was chosen largely because it represents a fairly typical long straight section of
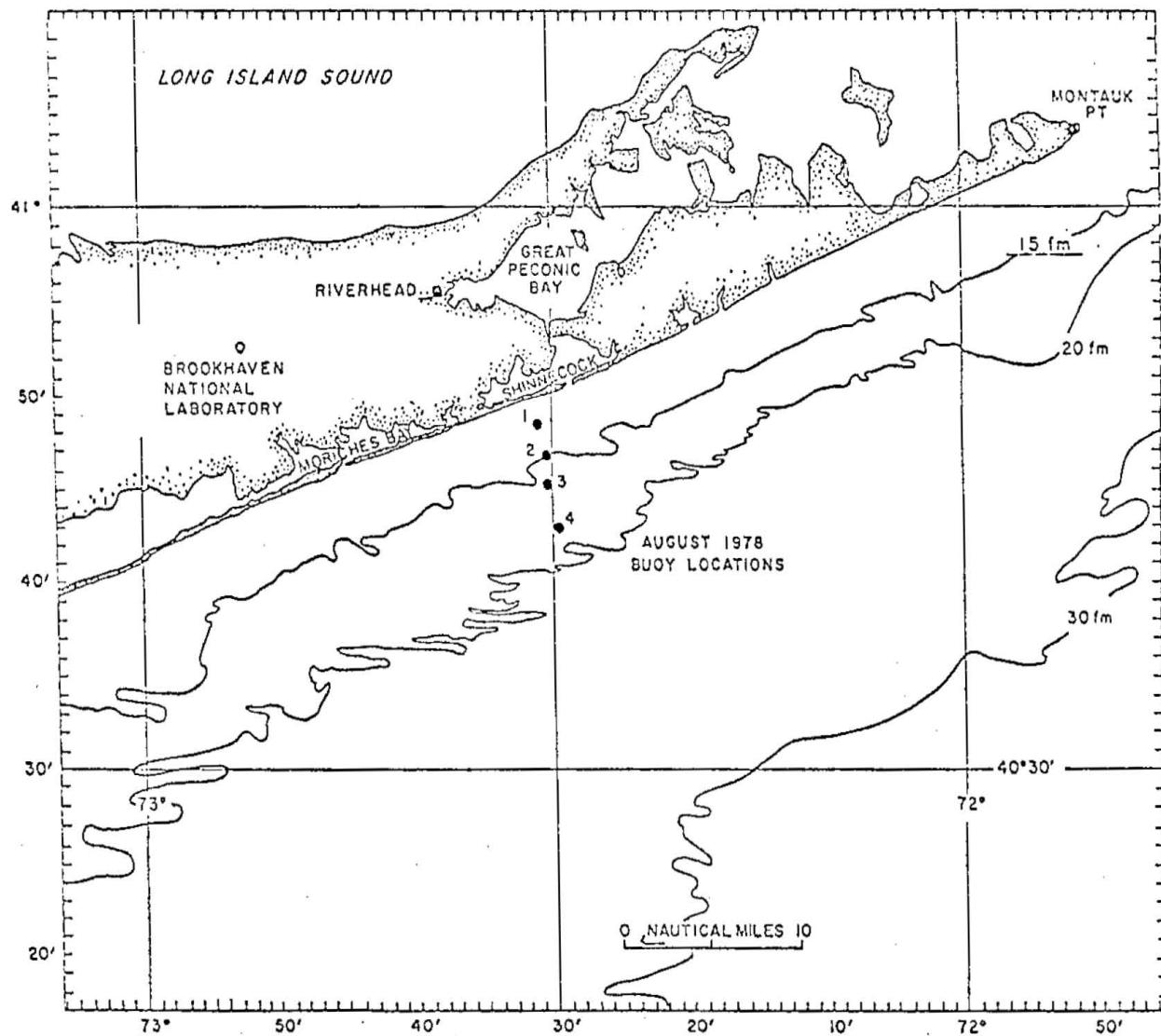
Figure 1.2 Experimental site and mooring locations

coastline without significant topographic irregularities, as well as enjoying convenient access through the nearby (approximately 6 km distant) Shinnecock Inlet. While it was hoped that the simple offshore bottom topography normally associated with barrier beaches would simplify modeling efforts, several potentially complicating local features should be noted. First and foremost is the presence of Long Island Sound which is known to have a major influence upon the tidal currents (Swanson, 1976; May, 1979), the local hydrography (Ketchum and Corwin, 1964), and may perhaps affect wind-driven currents as well. The close proximity of the Shinnecock Inlet may also have some effect upon the study area, although through the analysis of airborne radiation thermometric data, Powell and SethuRaman (1979) have concluded that any influence of the inlet upon scalar variables within the COBOLT region is quite minor.

The COBOLT experiment generally consisted of two main oceanographic components; a moored array collecting time series measurements of temperature, conductivity, and velocity, and a program of daily (weather permitting) "shipboard" surveys. Experimental periods were typically of one month's duration, and under full operation four moorings were deployed at 3, 6, 9 and 12 km from shore employing a combined total of 16 principal instrument packages. Each sensor package recorded conductivity, temperature, and orthogonal velocity components. For the three outer moorings, instrument packages were located at nominal depths of 4, 8, and 16 meters below mean sea level, plus one mounted 2.4 meters above the local bottom. The shallowest mooring (at 3 km) carried its sensors

at 4, 8, 12 meters below the surface, and 2.4 meters above the bottom. In addition, throughout the experiments as many as four additional supplementary temperature sensors per mooring were mounted at positions between the primary sensor locations. For clarity and compactness of notation, when referring to multiple mooring experiments offshore positions will be numbered 1-4 progressing seaward. Vertical positions will also be denoted 1-4 numbered from the shallowest to the deepest instrument position. The convention will be mooring number followed by vertical position number so that, for instance, the number pair (3,2) refers to measurements at level 2 (8 m depth) on mooring 3 approximately 9 km from shore.

In order to provide increased spatial resolution, daily surveys were conducted at permanently maintained anchor stations along a transect coincident with the mooring array. These stations were located at 1 km intervals out to 8 km, and at 2 km intervals thereafter, to a total distance of 12 km from the shoreline. Figure 1.3 illustrates a typical experimental configuration as well as the local bottom topography. Meteorological information was collected at the 22 meter Tiana Beach tower and/or on site at BNL atop a 110 meter tower some 35 km distant from the field experiment.

In its initial operation in 1974, the COBOLT program was limited to daily surveys. In September 1975 however, in addition to the surveys, one pilot mooring which collected time series measurements was success-fully deployed. Preliminary analysis of the current meter data from this experiment was reported by Scott and Csanady (1976). The summer of
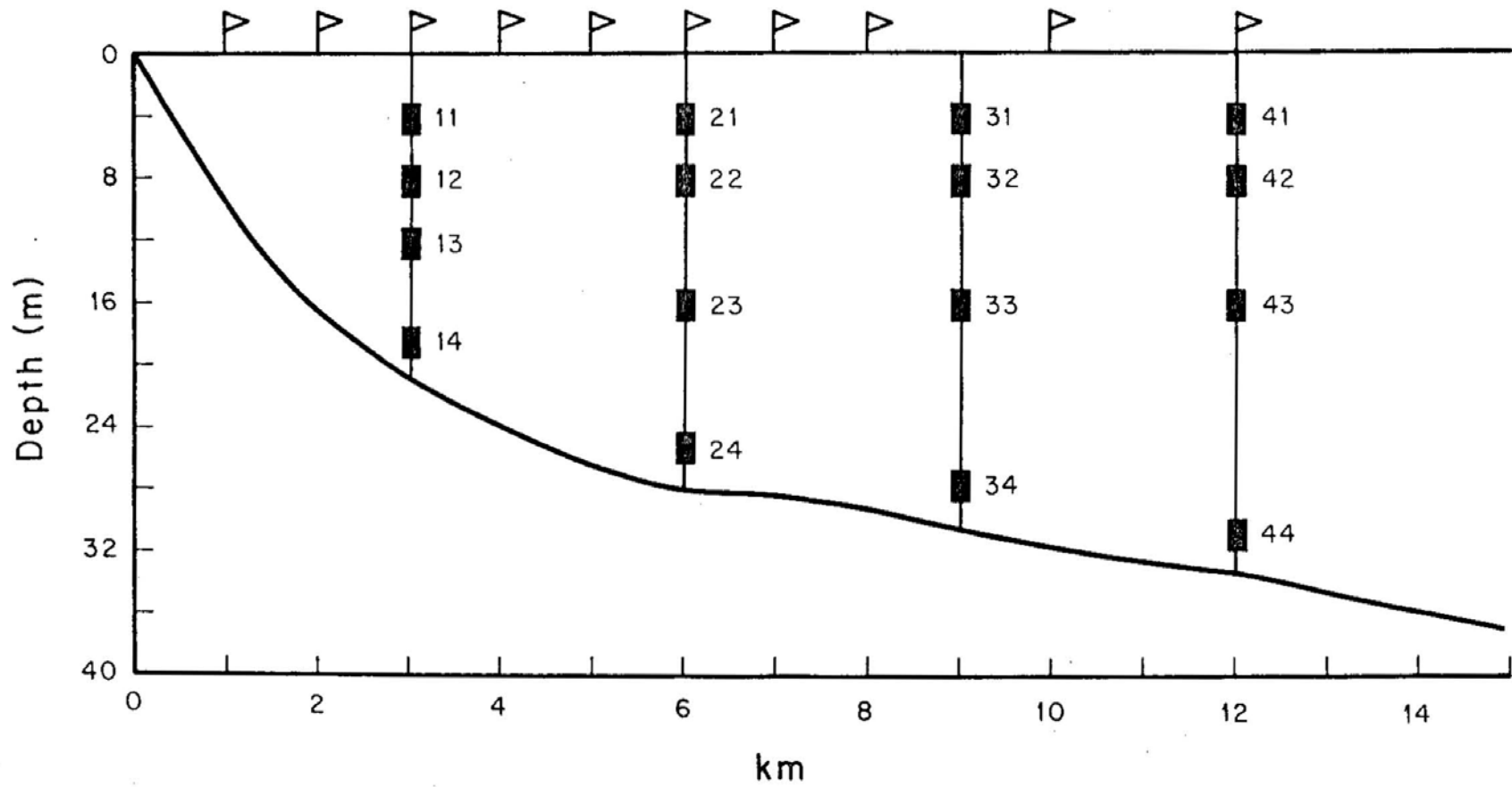
Figure 1.3 Experimental configuration including location of mooring, instrument packages, and anchor stations.

1976 was scheduled to be the first full deployment of the COBOLT mooring array but heavy damage due to hurricane Belle together with technical problems precluded the collection of useful data. In an independent experiment in October-November of that same year however, BNL was able to successfully maintain a single mooring in the same region during a very interesting period of flow. These data, as reported by Scott et. al. (1978), represent an important addition to the COBOLT data set and are therefore included in the discussions which follow.

Full deployments occurred during May 1977, March 1978, and August 1978 representing a successful monitoring of the CBL during respective periods of spring warming, unstratified conditions, and mature stratification. Table 1.1 summarizes the data returns from the mooring program during all experiments, while figure 1.4 indicates the dates of shipboard surveys, the occurrence of significant data gaps, and start and stop (failure) times for individual buoys.

1.4 Instrumentation

The moorings employed in COBOLT are of the Shelton spar buoy type which were specifically designed for use in coastal environments (see Lowe, Inman, and Brush, 1972). It is constructed of sections of 6.5 cm diameter PVC pipe joined together by universal joints which allow free articulation while maintaining torsional rigidity. The spar buoy, which has large positive buoyancy, is anchored by the massive (900 kg) battery

TABLE 1.1

Data Returns from COBOLT Mooring Program

Date	Mooring no.	Position	Depth of useful current meters
Sept., 1975	4	11 km	4, 16, 30 m
Oct., 1976	4	11 km	4, 8, 16, 30 m
May, 1977	2	6 km	4, 8, 16, 25 m
	3	9 km	8, 16, 28 m
	4	12 km	4, 8, 16, 30 m
Mar., 1978	1	3 km	4, 8, 12, 18 m
	3	9 km	4, 8, 16, 28 m
Aug., 1978	1	3 km	4, 8, 12, 18 m
	2	6 km	4, 8, 16, 25 m
	3	9 km	8, 16, 28 m
	4	12 km	4, 8, 16, 30 m

Figure 1.4   Mooring performance, and dates of shipboard surveys for COBOLT "full" deployments.

pack necessary to power sensors, the in-situ data processor, and the telemetry system.

Figure 1.5 shows a typical mooring configuration containing four main instrument packages (which measure temperature, conductivity, and velocity), one pressure sensor, a compass, a pair of orthogonally mounted inclinometers, a data processing unit, and the telemetry receiver-transmitter. In operation, output from all sensors is low pass filtered in real time with a 5 second time constant and the results continuously integrated by the data processor. Upon scheduled interrogation, the buoy transmits the integrated (averaged) data to a computer on site at BNL and restarts the integration. For a more detailed technical decription of the mooring and telemetry system see Dimmler et. al. (1976).

The sensor packages used in all COBOLT deployments consisted of an inductance conductivity cell, a thermistor, and either a Marsh-McBirney 711 or 555 electromagnetic current meter. Both models of current meter feature an orthogonal set of single axis electrodes, the difference being in the geometry of the probes on which the electrodes are mounted. The 555 employs a 2.5 cm spherical probe while the 711 uses a 2.2 cm diameter cylindrical configuration. In both cases the electrodes protrude 3 mm from the probe surface. The principles of operation and some operational properties of these current meters are discussed by Cushing (1976). Figure 1.6 shows the configuration of the instrument package mounted within its stainless steel cage.

ANTENNA

FLOTATION COLLAR

4.0 m — CURRENT METER
TEMPERATURE & CONDUCTIVITY

COMPASS & INCLINOMETER

8.0 m — CURRENT METER
TEMPERATURE & CONDUCTIVITY

DATA PROCESSOR

16.0 m — CURRENT METER
TEMPERATURE & CONDUCTIVITY

P.V.C. PIPE

CURRENT METER
TEMPERATURE & CONDUCTIVITY

2.5 m

RECOVERY LINE

BATTERY CONTAINER
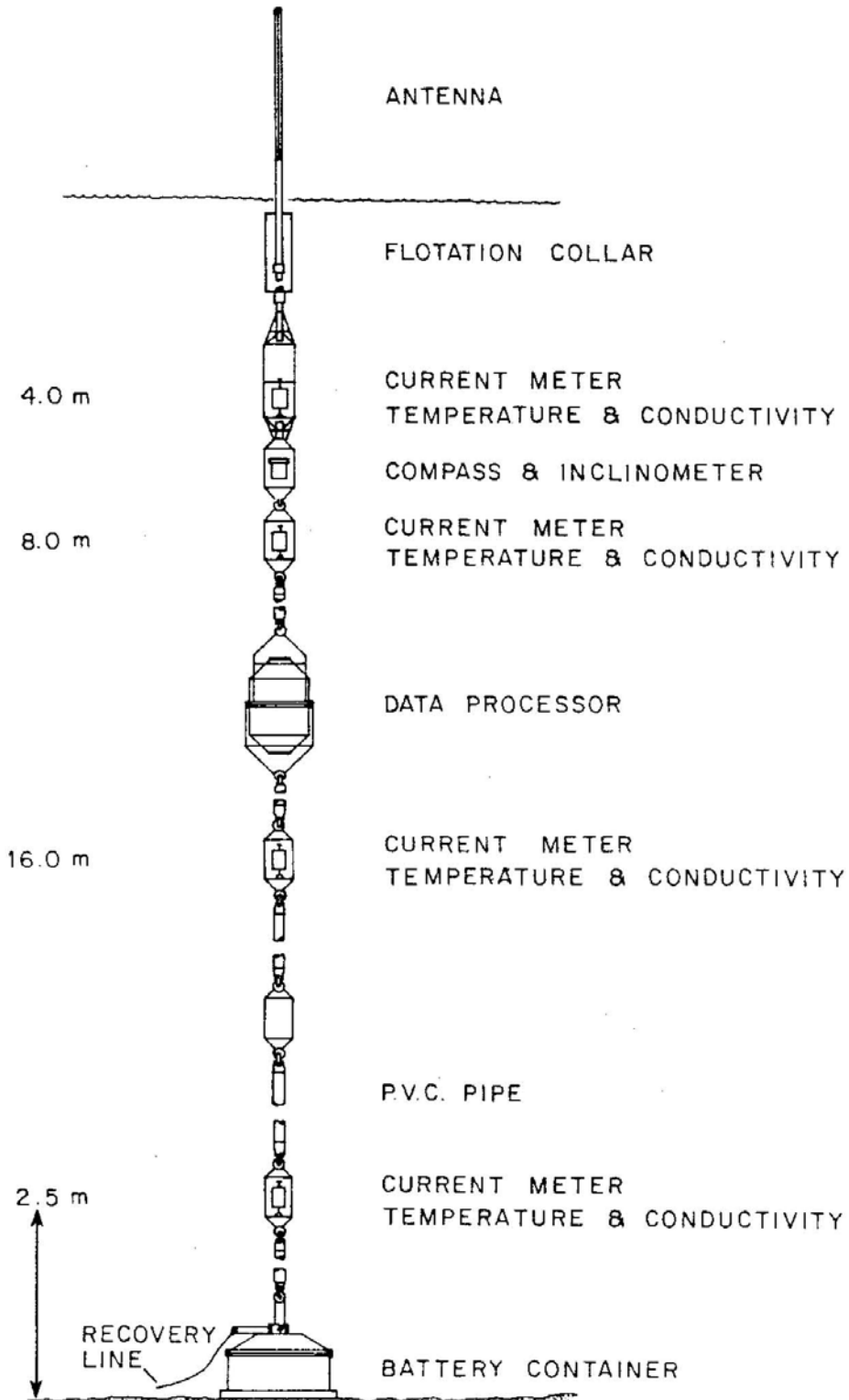
Figure 1.5   COBOLT mooring configuration.
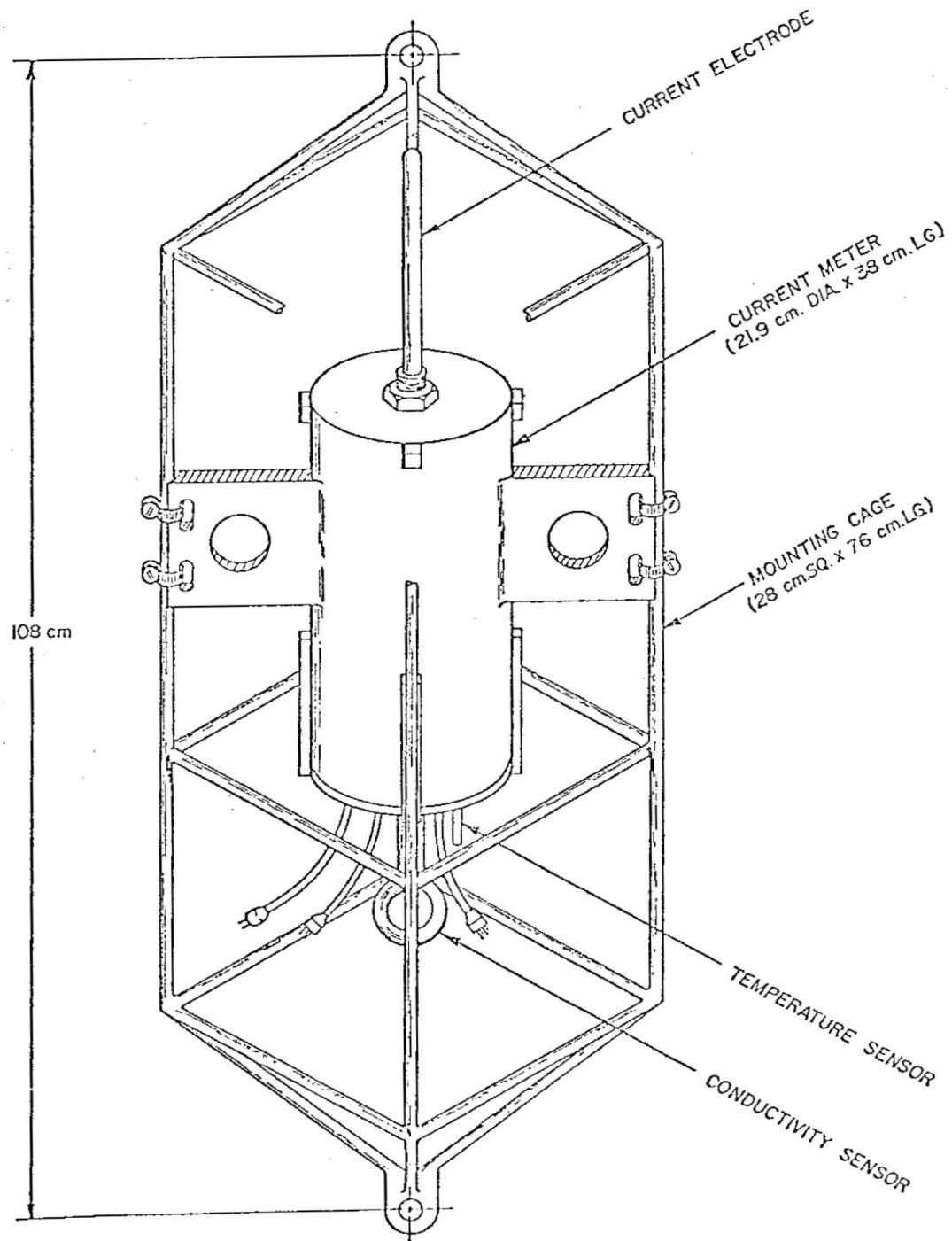
Figure 1.6 Moored instrument package

1.5 Calibration and quality control

In spite of the design sophistication of the COBOLT data acquisition system, and to some extent because of it, there have been and continue to be failures of individual instruments and even whole moorings. In addition, some concerns have arisen about the quality of the initial data returns.

Perhaps the most chronic problem has been with significant zero off-sets associated with conductivity sensors. Despite repeated and consis-tent calibrations these instruments have not always measured salinity consistently from one position to another. Under field conditions, sen-sors which were otherwise performing satisfactorily, have in rare in-stances exhibited offsets as high as 2 $°/_{oo}$ (translated into terms of salinity). Two independent procedures have been applied to correct errant salinity values. The simpler procedure was to introduce constant offsets sufficient to eliminate any calculated density inversions. This procedure is rendered quite effective by the fact that the water column is characteristically observed to homogenize quasi-periodically within the study area. The second procedure involved statistical comparison of salinity data with the STD surveys taken daily along the mooring tran-sect. This method virtually assures a consistent reference between instrument positions and was used whenever statistically reliable cor-rections could be made. The fact that the results of both methods were in close agreement somewhat allays the fear customarily associated with such "tampering". In general salinty measurements are considered to be

good to within $\pm$ 0.2 ppt based upon repeated calibration runs (Hopkins
et al., 1979). In any case it will usually be the time behavior rather
than the absolute value of salinity which is of greatest interest in
this study.

Some concern about the quality of the velocity data arose as a re-
sult of the 1976 Current Meter Inter-Comparison Experiment (CMICE) as
reported by Beardsley et. al. (1977). This experiment was originally
conceived as a test of the performance of existing mooring-current meter
systems against one another. Two COBOLT Shelton spars were compared in
this instance to more conventional taut rope moorings employing a var-
iety of mechanical current meters which sampled speed and direction
independently.

The experiment was conducted in the COBOLT study area approximately
6 km offshore of Tiana Beach, Long Island. An array of six moorings
were deployed in a line parallel to the coast, spanning one kilometer
alongshore. Although no single mooring-current meter combination con-
sistently outperformed the others, several sources of error were iden-
tified for the COBOLT instrumentation. They are:

1) Compass error;

2) Misalignment of sensor packages due to slight differences
   in construction at the moorings articulating joints;

3) Speed and direction errors resulting from zero offsets;

4) Speed and direction errors due to inaccurate gain adjustment;

5) Speed and direction errors due to the non-cosine response of the velocity sensors.

After the CMICE experiment, a concerted effort was made by BNL to upgrade the performance of their system. Problem 2 was easily corrected prior to the May 1977 launch, and model 215 Digi Course Optically Scanned Magnetic Heading Sensors (resolution ± 1.4 degrees) were installed before the March 1978 experiment replacing earlier versions which had proved unreliable. Extensive calibrations at the NOAA tow tank facility in Bay St. Louis, Mississippi, including determinaton of the individual non-cosine response for each current meter, were undertaken in order to address problems 3-5.

No attempt has been made to correct for the vertical non-cosine response associated with the tilting of the mooring under the influence of strong flow conditions. Tilt records from the Humphreys Inc. inclinometers (resolution 0.2 degrees) show extreme values of less than 20 degrees for all moorings, and inclinations even as great as 10 degrees are only occaissionally observed. The deviations from a simple cosine correction based upon the hourly averaged orthogonal tilt records, are clearly negligible for the magnitude of the observed angles.

Despite the corrections applied, an uncertainty in measured velocity remains of 1 cm/sec for each axis, and 5 degrees in orientation (Hopkins

et al., 1979). Based upon four calibration runs on each of 24 thermistors, Hopkins et. al. estimate the uncertainty in temperature as 0.02 degrees Celsius. While no checks were made on the pressure sensors, manufactuers specifcations indicate that they are accurate to better than 1.5 cm of water.

1.6 Data reduction

The first step in the data processing routine was the filling of any existing short data gaps. Record gaps of up to 6 hours were filled by standard cubic spline techniques. In the experiments reported here, any gaps longer than 6 hours turned out to be of several day duration and were considered to either terminate the experiment or break it into separate realizations depending upon the position of occurrence within the time series. Any variations in sampling interval were eliminated and all data were converted to time series of hourly averages.

The schedule by which buoys were interrogated was such that each spar was polled in turn at 15 minute intervals achieveing one polling each per hour. In order to facilitate ordinary time series analysis, each record was therefore linearly interpolated to the nearest whole hour to provide a common time base for all measurements.

The two components of velocity output by the electromagnetic current meters were converted to geographic coordinates in the following manner. As shown in figure 1.5, the compass and inclinometer cage are

rigidly attached to the second current meter package so that compass readings should be directly applicable at this position. However, while the articulated joints used in construction of the moorings allow little torsional motion (less than 1 degree), it is expected that the majority of observed angular displacement occurrs at these sites. Because of the large number of joints and the distance between the compass and the battery-anchor, it is clear that the angular fluctuations are greater at this position than at the current meters closer to the bottom of the mooring. The hourly deviations from the mean compass heading have therefore been linearly interpolated from maximum at current meter 2 down to zero at the top of the battery pack (below the last universal joint). Because the shallowest current meter had only one joint in the 4 m separating it from the compass, no extrapolation was considered necessary at this position. The hourly averaged compass reading appropriate to each level were then used to convert velocity components first into geographic coordinates and finally into local coordinates perpendicular and parallel to the isobaths. The right handed coordinates used throughout this thesis are x positive offshore, and y positve alongshore to the northeast.

Vertical tilt cosine corrections were applied in an analogous manner. That is, maximum tilts were expected and observed (via divers) to occur near the surface, so that tilt corrections were also linearly interpolated with depth.

Chapter II

THE SPECTRAL DESCRIPTION OF THE VELOCITY FIELD

2.1 Introduction

The COBOLT experiment provides a unique opportunity to observe spatial and temporal variations of the spectral properties of nearshore currents. In order to facilitate intercomparisons and to insure resolution between inertial and diurnal frequencies, all spectra in this study were computed with a bandwidth of 0.005 cph. Piece averaging, rather than band averaging, has been employed in an effort to reduce the effects of the nonstationarity which is inherent in oceanographic data in general and in shallow coastal observations in particular (see section 5.3). An $(8/3)^{1/2}$ variance correction for cosine windowing was applied to Fourier coefficients and the corresponding equivalent degrees of freedom were calculated after Nuttall (1971) and Ruddick (1977). Confidence limits were calculated from Koopmans (1974).

In most cases longshore and offshore component energy spectra will be presented in lieu of the somewhat more traditional total kinetic energy spectra. This procedure offers certain advantages in the coastal zone where the influence of the coastal boundary constraint results in a horizontally anisotropic response to forcing. Because the energetic low

frequency motions must be polarized in the alongshore direction, the longshore component spectra will not differ greatly from the total spectra. On the other hand the offshore or cross-shore component spectra, which may well have energy levels too low to make significant contributions to the overall low frequency energy, may show interesting and enlightening spatial variation when calculated separately.

From the 38 pairs of longshore and offshore energy spectra computed from the useable current meter records of the three full COBOLT deployments, certain generalizations can be made. They are:

1) The spectra are "red", that is, the energy generally increases with decreasing frequency.

2) There is a reduction of energy with depth for tidal and lower frequency motions. The most dramatic reduction occurs at the deepest current meter (approximately 2.5 m above the bottom).

3) A substantial asymmetry in amplitude exists between alongshore and offshore energies such that tidal and lower frequency motions (other than inertial) are highly elliptical in nature and have their major axes aligned roughly parallel to the local bathymetry.

4) While cross-shore subtidal energy levels decrease sharply near the coastal boundary, there is a persistent but statistically non-significant rise in alongshore sub-tidal energies as the coast is approached.

5) The semidiurnal (hereafter referred to as SD) signal represents the dominant peak in most cases, and accounts for roughly one-fourth

of the total variance. The peak energy in the diurnal band is often
an order of magnitude smaller than that associated with the SD, and
exhibits more complex spatial and temporal variations. Tidal har-
monics are consistently in evidence.

6) Significant near-inertial motions are possible extremely close
to shore during favorable meteorologic and hydrographic conditions.

It is probably fair to say that each of the above generalizations
with the probable exception of number 6, are not completely unexpected.
It is therefore the degree to which these statements are realized and
the exceptions to them which are of most interest. A brief discussion
follows highlighting the principal points which qualify the foregoing
general observations.

Figure 2.1 is an overlay of alongshore energy spectra at 4, 8, 12,
and 18 m depths, located a distance of 3 km from shore. These results
are typical examples of alongshore component spectra. The dominance of
the SD peak and the general red character are clear. The low frequency
energy varies roughly as ω^{-2}, a value which is quite representative of
results at differing offshore positions during the various experimental
periods. While the energy reduction with depth shown here is quite
substantial (as high as an order of magnitude) it is more often found
that the percentage of energy decrease with depth is not a strong
function of frequency for SD and longer period oscillations. High
frequency motions in this figure and in general are relatively depth
independent, and in fact are statistically isotropic.
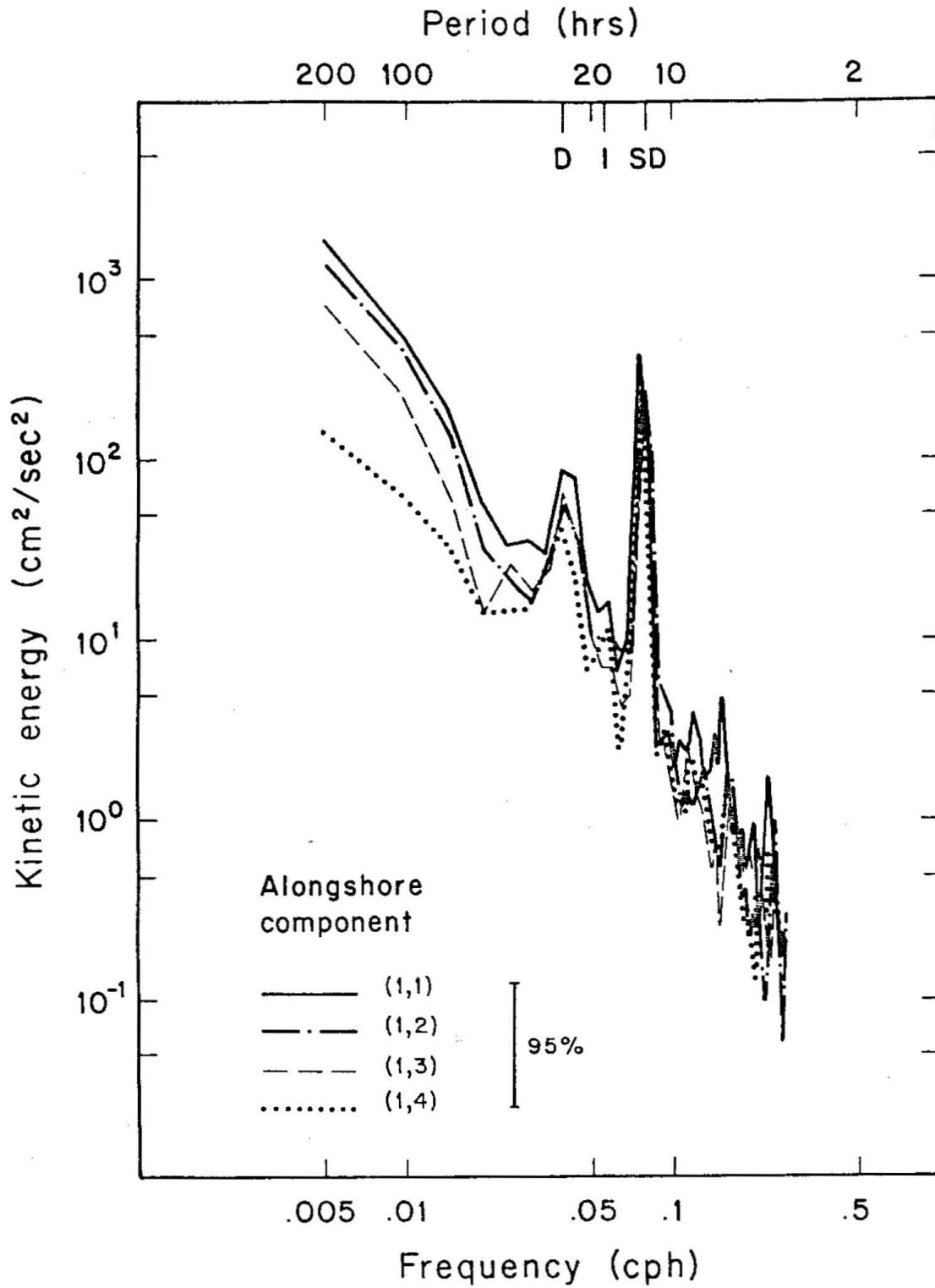
Figure 2.1 Aug '78 alongshore kinetic energy spectra 3km from shore at depths of 4,8,12, and 18 m.

Figure 2.2 shows the corresponding offshore energy levels. The fact that the variation with depth is not as orderly as for the alongshore component is probably at least partly due to the inherent difficulty associated with measuring the cross-shore component of low frequency motions which are highly polarized in the alongshore direction. It is easily appreciated that small angular deviations in current meter orientations could lead to significant contamination of relatively weak cross-isobath signals. In addition to this difficulty, the presence of the coastal boundary may also be expected to contribute to the vertical variability of offshore velocity components because of the general tendency of the nearshore water column to conserve mass through a two dimensional transverse circulation pattern. Despite these additional complications, several observational facts are clear. Energy levels in SD and lower frequencies are significantly reduced relative to alongshore values, and the magnitude of that reduction increases with decreasing frequency. For the lowest frequencies resolved in this study, alongshore to cross-shore energy ratios of order 10 are frequently observed. Energy levels of the higher frequencies (greater than SD) are statistically indistinguishable from their alongshore counterparts.

2.2 Cross-shore variation of energy

In an experiment designed and conceived to investigate the cross-

Period (hrs)
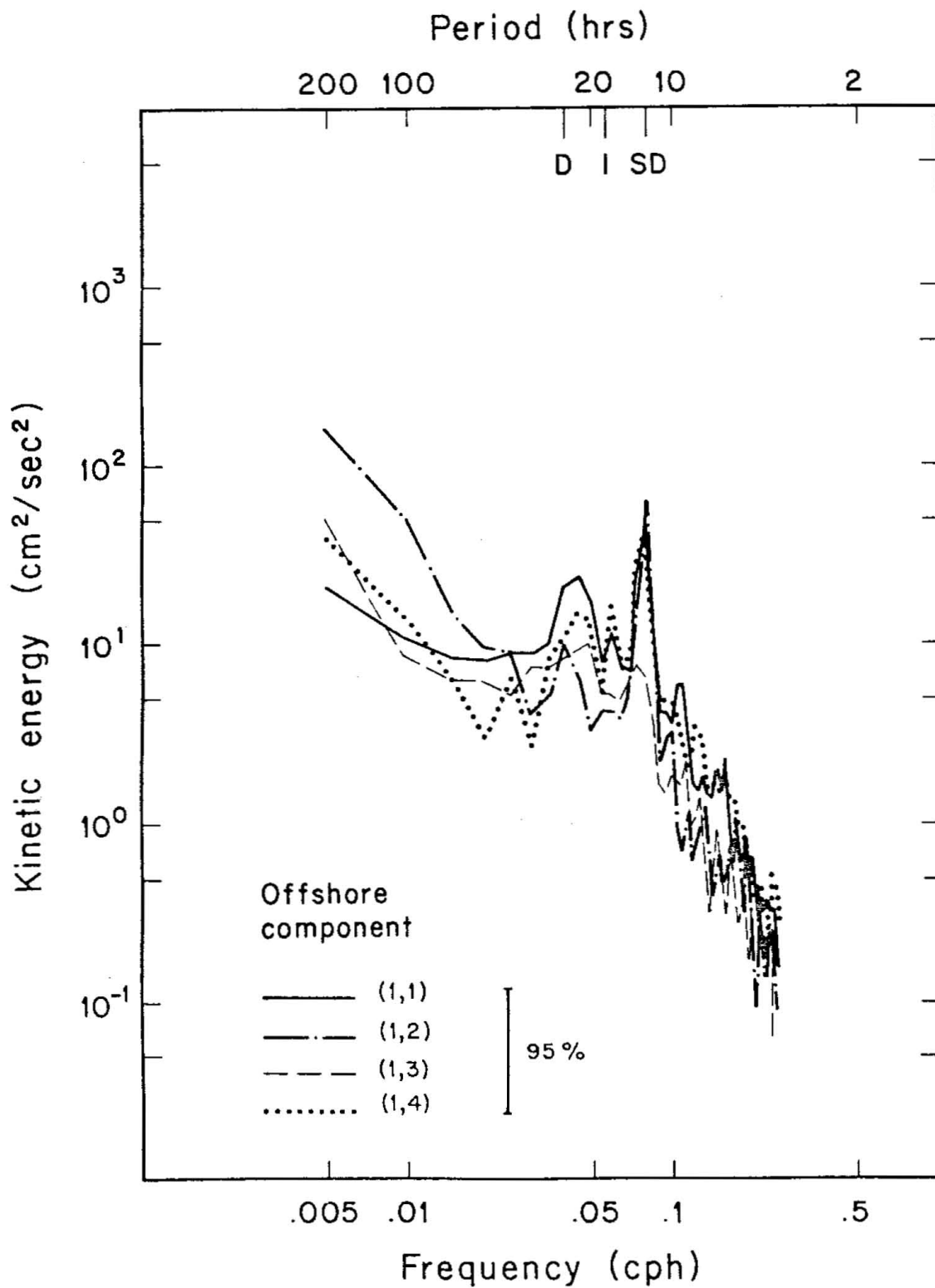
Figure 2.2   Aug '78 offshore kinetic energy spectra 3 km from shore at depths of 4, 8, 12, and 18 m.

shore structure of the CBL it might be expected that energy spectra would be strong functions of the offshore coordinate. In point of fact, however, there is little compelling evidence of this type of behavior except in a few notable cases.

Figure 2.3 illustrates the alongshore energies 4 m below mean sea level at each mooring in the August 1978 experiment. There is some indication here of a monotonic shoreward amplification of the SD tidal velocities at this level. This type of behavior has been previously noted by (among others) Flagg (1977) and Smith et al. (1978) in their respective studies of the New England and Scotian shelves. In the coastal boundary layer, however, this trend is reversed with depth as the effect of friction apparently becomes more important than shoaling. The overall result is that no significant cross-shore variation for SD currents is observed.

Subtidal energy levels show an interesting behavior as the coastline is approached. It may be noted in Figure 2.3 that a statistically insignificant rise in low frequency alongshore energy occurs at mooring 1 located 3 km from shore. The fact that this behavior is noted at all vertical positions and in both the March and August experiments (the only experiments which included a functional mooring at this position) gives some credence to the notion that this may be a characteristic, albeit somewhat subtle, pattern. If the existence of shoreward ampli-fication of low frequency energy levels were accepted it would have several important implications. First, it would indicate that simple linear theories of coastally trapped shelf waves and quasi-steady coastal jets which predict shoreward amplification may be applicable in
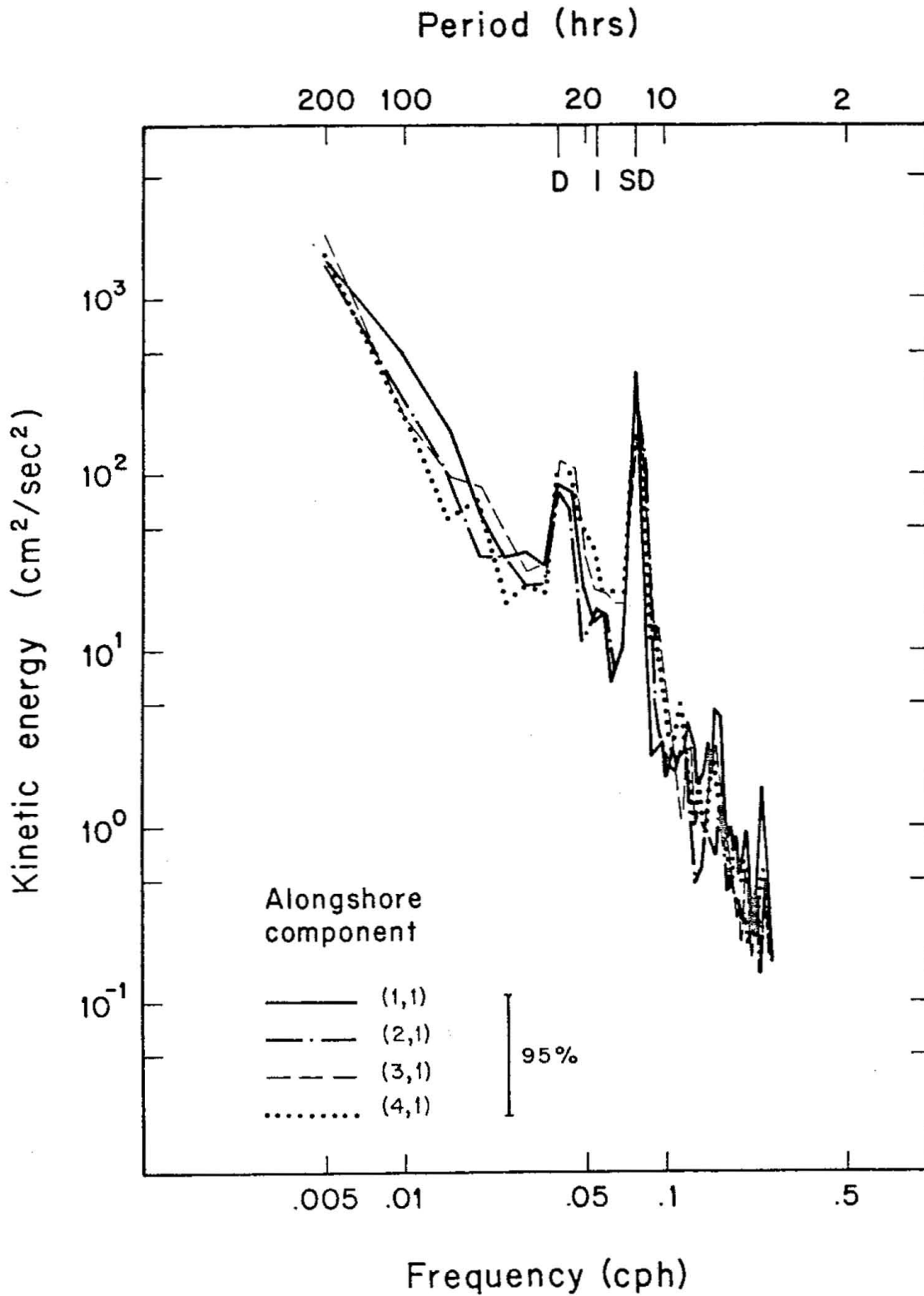
Figure 2.3 Aug '78 alongshore kinetic energy spectra at 4 m depth,
3, 6, 9, and 12 km from shore.

very shallow water only a few km from shore. In addition, since the region of strong topographic variation in the COBOLT study area is shoreward of 5 km i.e., in the same region in which the low frequency amplification seems to occur, it seems likely that consideration of nearshore details of bottom topography would be a key factor influencing cross-shore variability in the CBL.

Not surprisingly, offshore component energy spectra show more clear variations with the cross-shore coordinate. As seen in Figure 2.4 there is a significant decrease in energy between buoys 1 and 4 for subtidal frequencies. This is a "robust" result in that it is evident during all experimental deployments.

Up until this point, spectra shown have been exclusively from the August 1978 experiment because it represents the most complete data set in terms of space-time coverage and instrument performance. Neverthe-less, important complementary information about seasonal and intermit-tent phenomena is available from the other COBOLT deployments. As the reader has doubtless discovered, no significant peaks of inertial fre-quency appear at any location throughout the August experiment. This lack of inertial energy is not surprising given the weak (generally less than 0.5 dyne) wind stress during the period, as well as the shallowness of the water column and the proximity of the shoreline. In contrast, the May 1977 experiment showed strong inertial energy as close as 6 km from the coast in water roughly 25 m deep.

Figure 2.5 is an example of offshore and alongshore kinetic energy spectra which show significant inertial peaks occurring at 16 m depth,

Period (hrs)
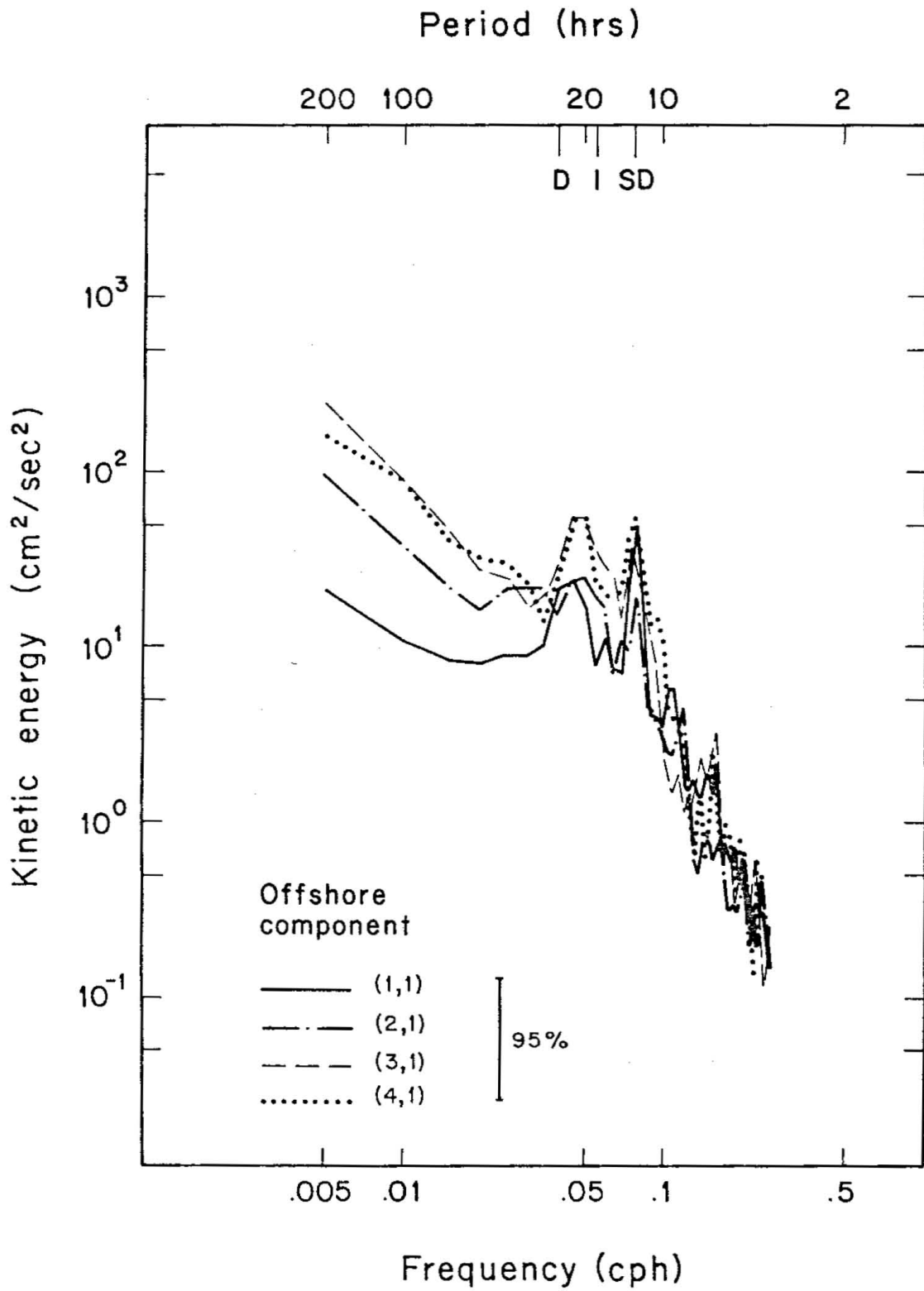
Figure 2.4 Aug '78 offshore kinetic energy spectra at 4 m depth, 3, 6, 9, and 12 km from shore.

Period (hrs)
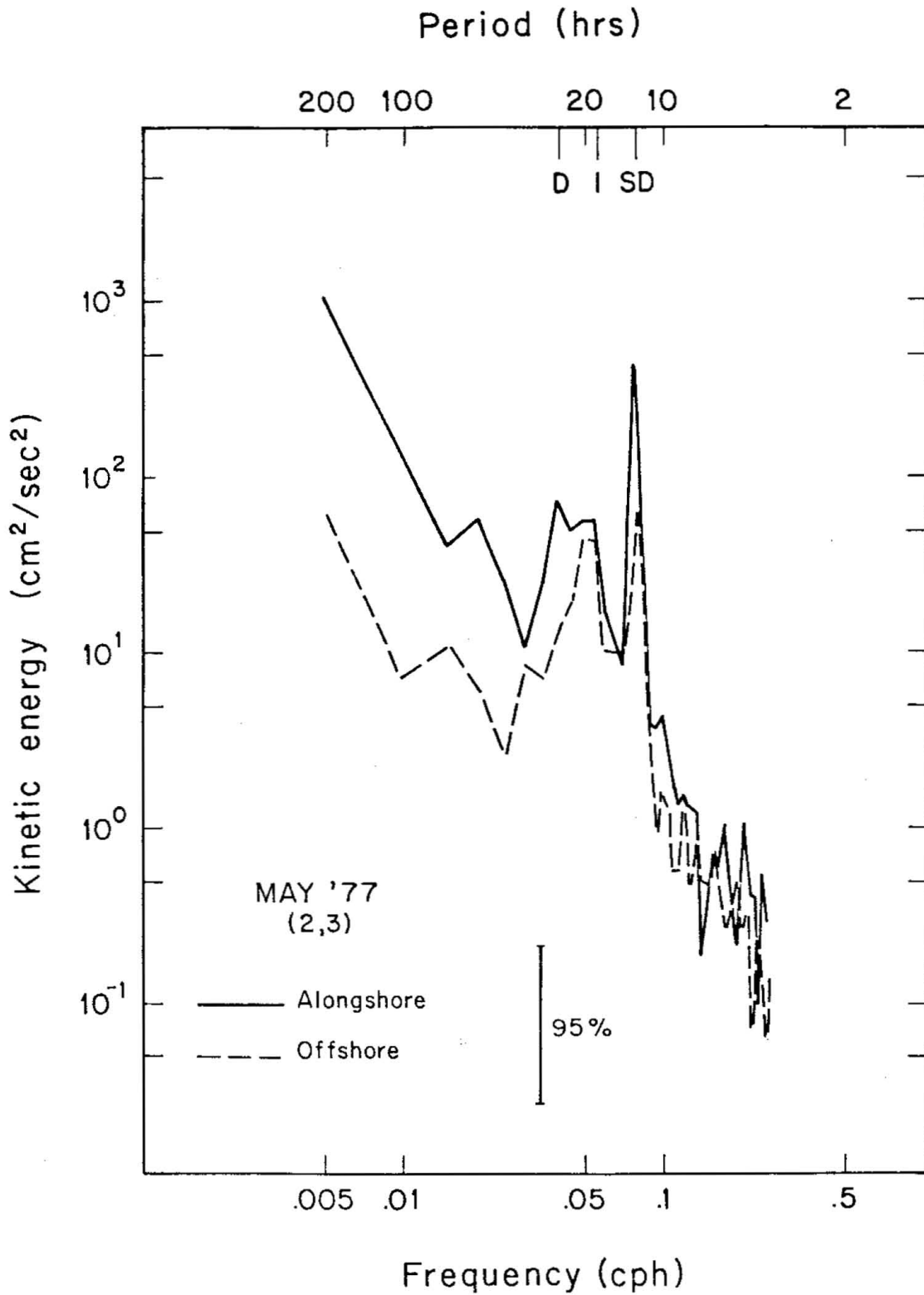
Figure 2.5   May '77 alongshore and offshore spectral energies at
8 m depth, 6 km from shore.

6 km from shore. The inertial energies from the alongshore and offshore signals are seen to be essentially equal (as they must be for an inertial balance) and are comparable to the alongshore diurnal and offshore semidiurnal tidal energy levels. In fact, near-surface inertial energies were observed to dominate the offshore energy spectra. In Figure 2.5 the inertial and diurnal frequencies are contained within one broad lobe and it is important to make a case for contributions from two distinct physical forcing mechanisms rather than, as might be imagined, spectral leakage or frequency shifting of diurnal energy resulting in a broad band of essentially tidal origin. One bit of evidence against the notion that the near-inertial energy observed in May '77 was the result of frequncy shifting of diurnal motions, is the fact that during Aug '78, when conditions were actually more conducive to this process, energy in the inertial band was notably absent. In addition, a clear distinction between inertial oscillations and those of tidal frequency is easily demonstrated through calculation of the so-called rotary spectrum (Gonella, 1972).

2.3 The rotary-spectral description

The rotary component method of data analysis is based upon the fact that any orthogonal pair of velocities u and v which are periodic with frequency ω may be expressed as

$$u + iv = A_a e^{i\omega t} + A_c e^{-i\omega t} \qquad (2.1)$$

where A_a and A_c are complex amplitudes. This formulation in effect represents the combination of two vectors which rotate in an opposite sense so that the velocity signal at a given frequency may be thought of as consisting of both clockwise and anti-clockwise portions. An arbitrary complex time series may be represented by the summation over frequency of equation (2.1). The two sets of complex coefficients resulting from such a Fourier decomposition may be used to compute clockwise and anti-clockwise energy spectra as shown below.

$$S_c(\omega) = 1/2 \sum_\omega A_c(\omega) A_c(\omega)^*$$

$$\qquad (2.2)$$

$$S_a(\omega) = 1/2 \sum_\omega A_a(\omega) A_a(\omega)^*$$

where the * superscript represents complex conjugation. The total spectrum is given by

$$S_T(\omega) = S_c(\omega) + S_a(\omega) \qquad (2.3)$$

The foregoing relations are, of course, invariant under coordinate rotations.

Inertial motions are dynamically constrained (in the northern hemisphere) to be clockwise circular motions and as such should be distinguishable from leakage and other contamination from adjacent

peaks. Figure 2.6 shows the clockwise and anti-clockwise energy spectra corresponding to the previous illustration. There is an unambiguous dicotomy between the structures at diurnal and inertial frequencies. A two order of magnitude discrepancy in clockwise versus anti-clockwise energy exists near inertial frequency which indicates a nearly perfectly circular clockwise motion. In contrast, the diurnal signal while still predominantly clockwise contains relatively high anti-clockwise energy as well, giving rise to a motion which is elliptic in character.

The eccentricity, sense of rotation, and ellipse orientation for these, and all frequencies of interest, are easily quantified within the framework of rotary component analysis (Gonella, 1972). The "rotary coefficient" whose value ranges between ± 1 is defined as

$$R(\omega) = (\ S_c(\omega) - S_a(\omega)\ )/\ S_T(\omega) \qquad (2.4)$$

and tells a great deal about the character of the motion. By inspection it is seen that for predominantly clockwise signals $R > 0$, while $R < 0$ for anti-clockwise motions. In the cases of purely clockwise or anti-clockwise oscillation, the values are 1 and -1 respectively. When the two components are equal, that is for unidirectional (nonrotational) conditions, $R = 0$. In essence, the sign of the rotary coefficient describes the direction of rotation and its magnitude is indicative of the relative ellipticity of the motion. In fact, the rotary coefficient may be related to the more familiar eccentricity of the ellipse by

Period (hrs)
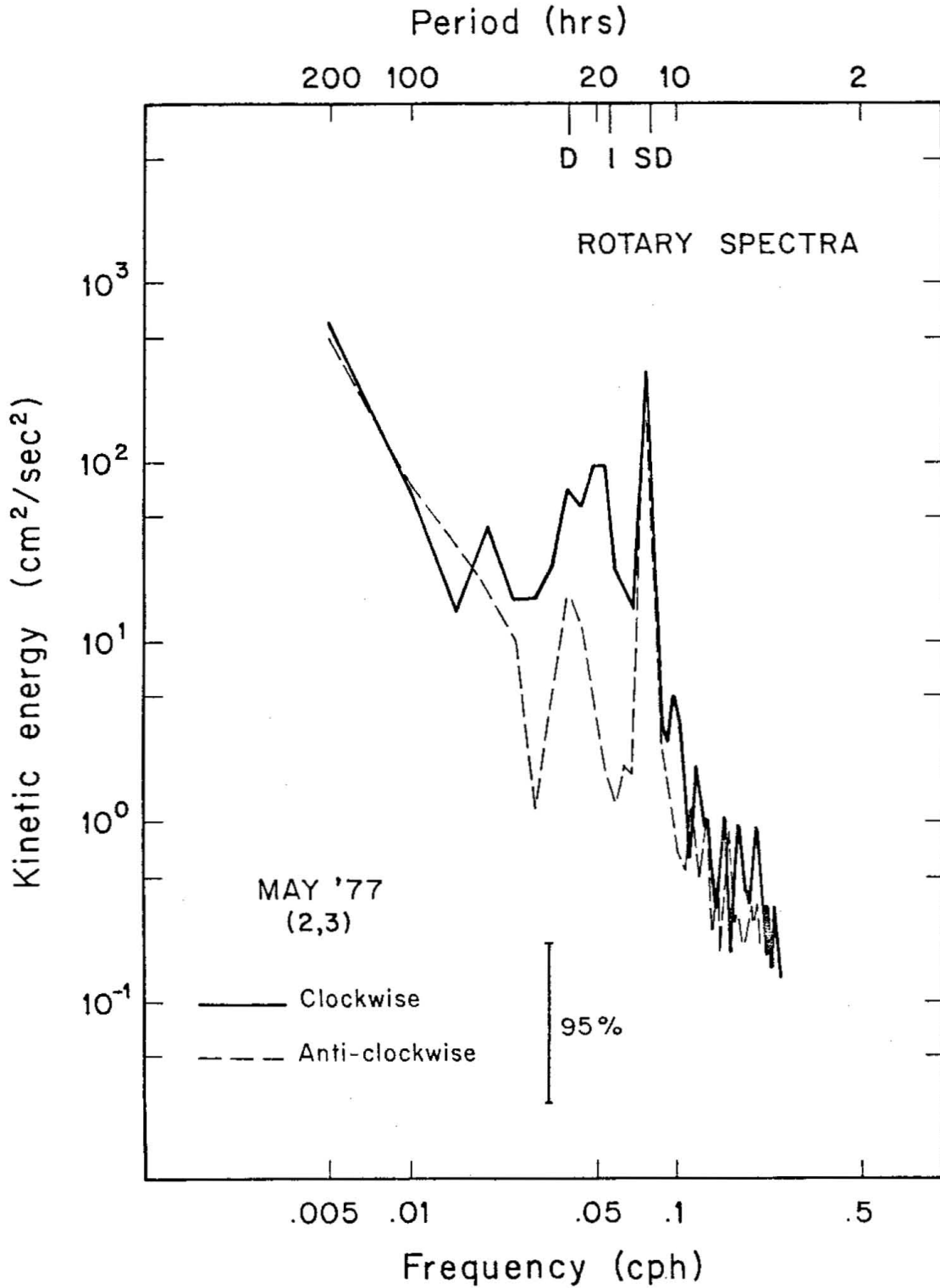
Figure 2.6   May '77 rotary spectral components at 8 m depth, 6 km from shore.

$$\varepsilon = 1 - |R| \qquad\qquad (2.5)$$

For the case corresponding to Figure 2.6, the rotary coefficients for inertial and diurnal frequency are .96 and .56 indicating respectively one circular clockwise motion and a tidal ellipse of eccentricity 0.44.

The rotary coefficient presents a compact representation of the rotational aspects of the flow field. From a compilation of this coefficient for the entire COBOLT program the following general observations can be made:

(1) Low frequency (8 day) motions are essentially rectilinear in nature.

(2) Motions in the 2-4 day band display a general tendency to rotate anti-clockwise near surface and clockwise near bottom.

(3) Diurnal motions are clockwise at all depths.

(4) SD tidal currents rotate clockwise except near bottom where they often reverse their rotational direction.

(5) SD and inertial period motion becomes progressively more eccentric as the bottom is approached. Subinertial eccentricities reveal no clear pattern of vertical variation.

(6) There is no clear pattern to the horizontal variations of eccentricity.

These generalizations are reflected in tables 2.1 and 2.2.

TABLE 2.1

May '77 and Mar. '78 Rotary Coefficients

May '77

Inst. no.	200.0	50.0	25.0	18.2	12.5	(hrs)
(2,1)	.04	-.02	.59	.91	.50	
(2,2)	.15	-.05	.38	.75	.28	
(2,3)	-.08	.36	.56	.96	.29	
(2,4)	.03	-.49	.18	.83	-.26	
(4,1)	.11	-.12	.73	.98	.35	
(4,2)	.15	-.57	.14	.99	.43	
(4,3)	.04	.08	.58	.95	.38	
(4,4)	.25	.62	.73	.83	.24	

Mar. '78

Inst. no.	200.0	50.0	25.0	18.2	12.5	(hrs)
(1,1)	.03	-.22	.28	.66	.35	
(1,2)	-.02	-.12	.11	.90	.41	
(1,3)	-.01	.04	.40	.60	.28	
(1,4)	.00	.15	.57	.08	-.09	
(3,1)	.03	.46	.11	.99	.43	
(3,2)	.01	-.04	.26	.97	.36	
(3,3)	-.09	.38	.62	.62	.36	
(3,4)	-.02	.64	.12	.67	-.01	

TABLE 2.2

Aug.'78 Rotary Coefficients

periods

Inst. no.	200.0	67.7	25.0	12.5	(hrs)
(1,1)	.02	-.06	.43	.53	
(1,2)	.03	.08	.01	.39	
(1,3)	.09	.12	.13	.18	
(1,4)	-.06	.30	.11	-.21	
(2,1)	-.07	-.11	.52	.19	
(2,2)	.01	.07	.23	.25	
(2,3)	-.07	.41	.06	.74	
(2,4)	.06	.56	-.30	-.05	
(3,1)	-.27	-.01	.58	.02	
(3,2)	-.20	-.04	.38	.22	
(3,3)	.00	.08	.26	.53	
(3,4)	.14	.16	.02	.35	
(4,1)	-.35	.15	.71	.14	
(4,2)	-.31	.00	.31	.39	
(4,3)	-.24	.23	.46	.56	
(4,4)	.14	.15	.17	.30	

2.4 The vertical structure of fluctuating currents

The spatial relationships between fluctuating geophysical variables are often key factors in the understanding of regional dynamics. Historically the unraveling of these relationships has proved somewhat tractable through the application of cross-spectral analysis and methods of empirical orthogonal modal analysis. In the general case where more than one type of "wave" structure is present in the same frequency band, there is considerable ambiguity in the interpretation of cross-spectral relationships. In particular, as discussed by Wallace (1971), there is no way to clearly distinguish between independent processes nor to discover their relative contribution to the overall signal. Because of these shortcomings a group of procedures called empirical orthogonal methods (EOMs) have evolved. The basic unifying theme in all such methods is the calculation of a set of eigenvectors, each corresponding to a specified fraction of the total energy, which form a linearly independent basis set in terms of which the observations may be expressed.

The EOM in most common usage involves finding the eigenvectors of the covariance matrix. If one is interested in several frequency bands this procedure becomes cumbersome as it requires making the calculation for various bandpassed versions of the data set. However, as shown by Wallace and Dickinson (1972) one can transform to the frequency domain and calculate the complex eigenvectors of the cross-spectral matrix which, in addition to properties analogous to those of the covariance matrix, contain phase information. Due to the fact that the thrust of

Wallace and Dickinson's work was aimed at the generation of real valued time series corresponding to the independent complex eigenmodes present in observations, the method entails additional complications involving transformation of "augmented" time series; a combination of the original series and their time derivatives. These added complexities are unnecessary, however, if one's principal interest is only the spatial and phase structures of the empirical modes. In this case the complex eigenvectors themselves directly give the amplitude and phase as a function of position, and the associated eigenvalues reveal how much energy is associated with each eigenvector or empirical mode. The advantages of this method are that once the appropriate cross-spectra have been calculated one has merely to perform the numerical diagonalization of the complex hermitian matrix for any frequency of interest in order to obtain the vertical or horizontal modes.

Operationally the calculations performed in the present study went as follows. Cross-spectra were computed for all possible combinations of current meters on a given mooring. Then for any frequecy band of interest over which significant coherence levels were obtained for all current meter pairs, the hermitian cross-spectral matrix was formed as

$$
\begin{pmatrix}
A_{11} & C_{12} + iQ_{12} & C_{13} + iQ_{13} & C_{14} + iQ_{14} \\
C_{12} - iQ_{12} & A_{22} & C_{23} + iQ_{23} & C_{24} + iQ_{24} \\
C_{13} - iQ_{13} & C_{23} - iQ_{23} & A_{33} & C_{34} + iQ_{34} \\
C_{14} - iQ_{14} & C_{24} - iQ_{24} & C_{34} + iQ_{34} & A_{44}
\end{pmatrix}
$$

where A_{ii} are the various autospectra and C_{ij} and Q_{ij} are the cospectra
and quadrature spectra between the ith and jth instruments. This matrix
was then diagonalized by a standard "canned" computer routine yielding
the 4 real eigenvalues and their associated complex eigenvectors. Since
the trace of the matrix is invariant, the sum of the eigenvalues equals
the total energy and is conserved. The amount of the total variance
contained in each eigenmode is determined by the proportion of its
associated eigenvalue relative to the trace. The modes are subsequently
ranked according to energy content and the modal structure determined
from the moduli and phases of the complex elements of the eigenvector.
For presentation the amplitudes were scaled by the maximum value within
each mode and the relative phase of the first element arbitrarily set
equal to zero. Horizontal or crossshore modes may be calculated in an
exactly analogous manner. The preceding methodology was brought to the
author's attention by Dr. N. G. Hogg and was employed in Hogg and
Schmitz (1981).

The question of whether the structures emergent from the empirical
orthogonal function analyses represent bona fide physical processes,
statistical artifices, or manifestations of random noise needs some
consideration. Wallace and Dickinson (1972) suggest that a ratio of at
least 2:1 in successive eigenvalues (variances) is fair assurance of
statisical significance. Hogg and Schmitz point out that this ratio is
approximately the 95 percent confidence level below which successive
eigenvalues and thus eigenfunctions are indistinguishable from white
noise with 20 degrees of freedom. Unfortunately assurance of the

statistical significance of the modes is necessary but insufficient assurance of their physical significance. From a pragmatic point of view, the first several eigenvectors in the expansion are merely the linear combination which most efficiently reconstruct the structure of the cross spectral matrix. In this light it is seen that the empirical mode analysis is most useful when the structures found are consistent with some recognized physical conceptualization of the system being studied.

Representative illustrations of the amplitude and phase structures of vertical empirical eigenmodes of low frequency (.005), tidal frequency, and inertial frequency bands are presented in figures 2.7 and 2.8. Large vertical shears were found to be associated with the dominant alongshore modes calculated for all moorings during all experiments. The fact that the motions are essentially in phase at all depths (except for inertial frequency modes) suggests a barotropic interpretation. The vertical shears observed are likely to have been frictionally induced and underscore the importance of frictional influences in this shallow region. This view is further supported by the slight but consistently observed near bottom phase shifts. The low frequency and SD signals consist almost entirely of these frictional barotropic modes in the March and May experiments, while in August there is evidence of well defined though relatively weak secondary mode as well (present only at 200 hours in figure 2.7). These auxillary modes, which account for approximately 3 percent of the total energy at this frequency, have a phase structure which closely resembles that of the internal response of

AUG '78   LONGSHORE   BUOY #1

MODE 1   MODE 2
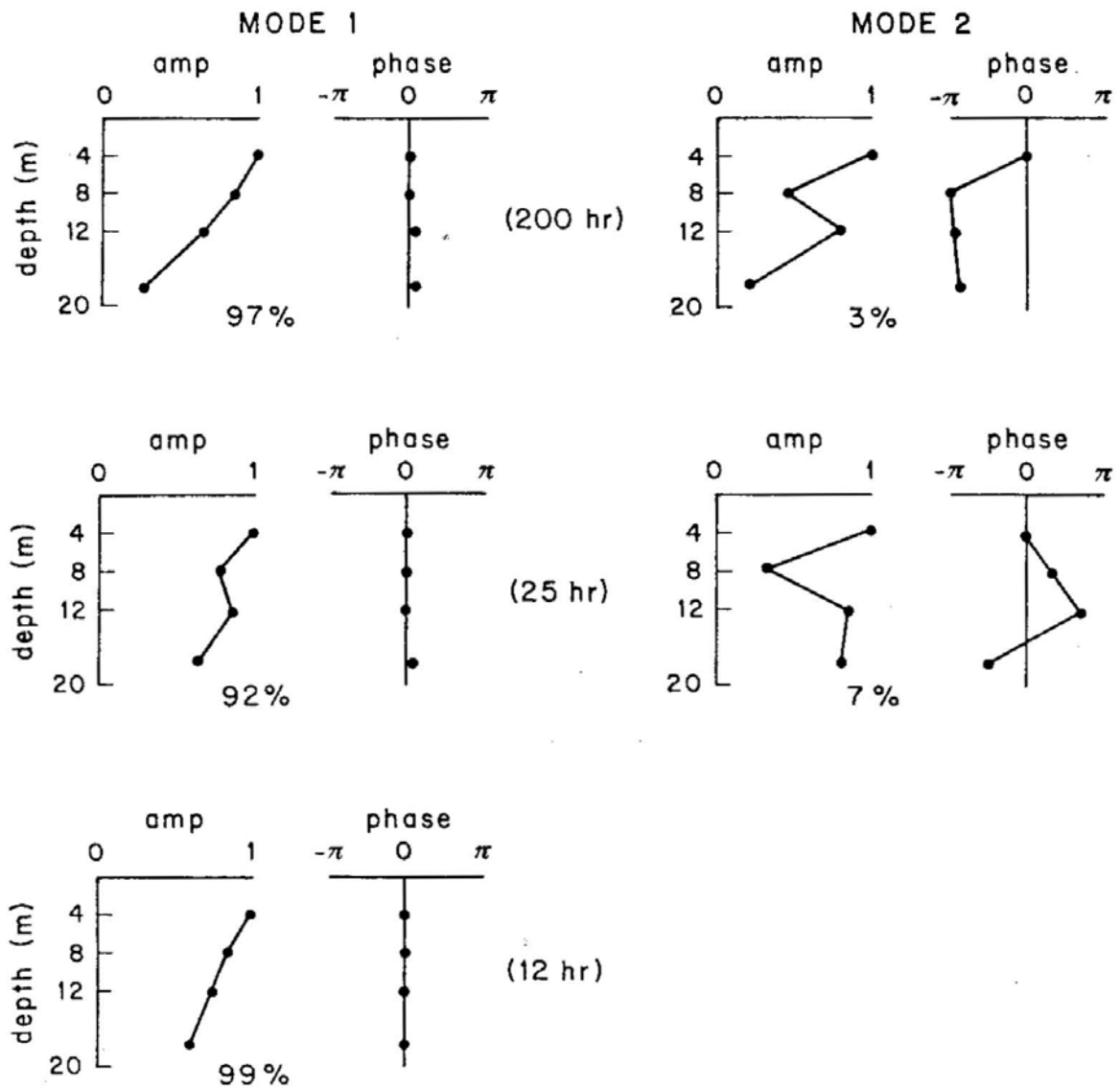
Figure 2.7 Low-frequency, diurnal, and semidiurnal complex eigenmodes.
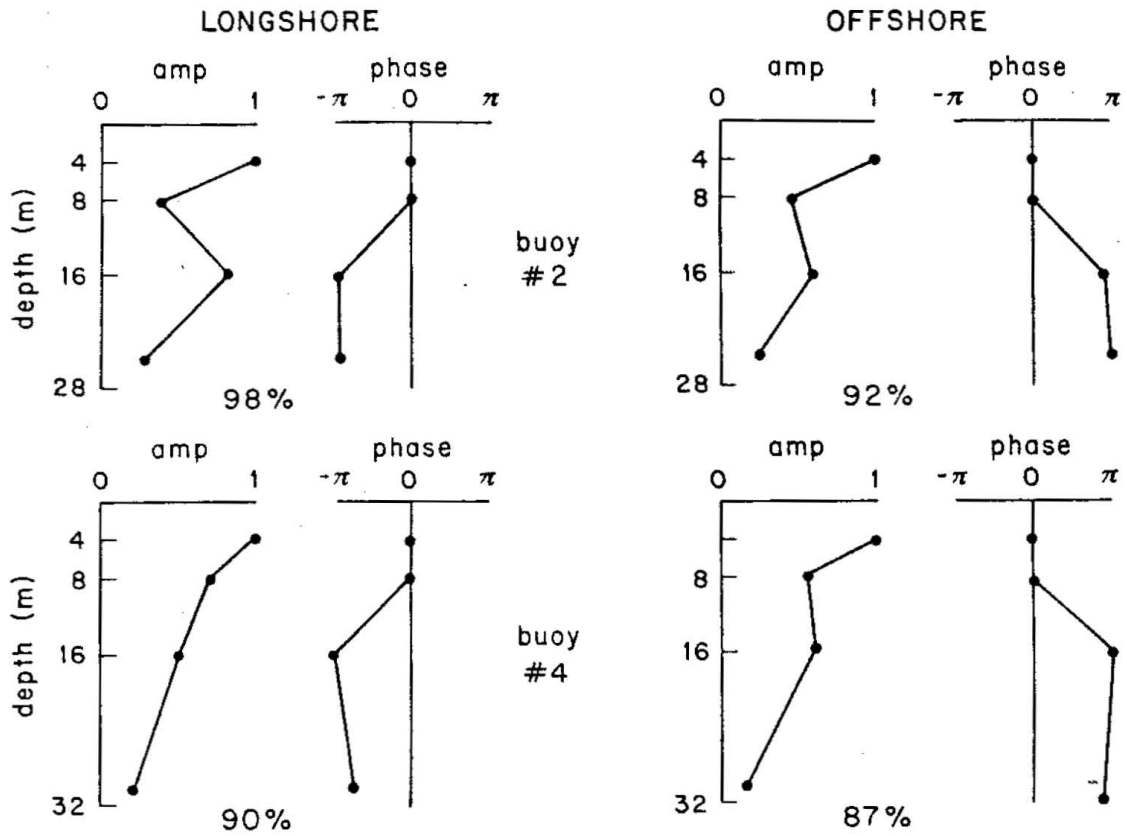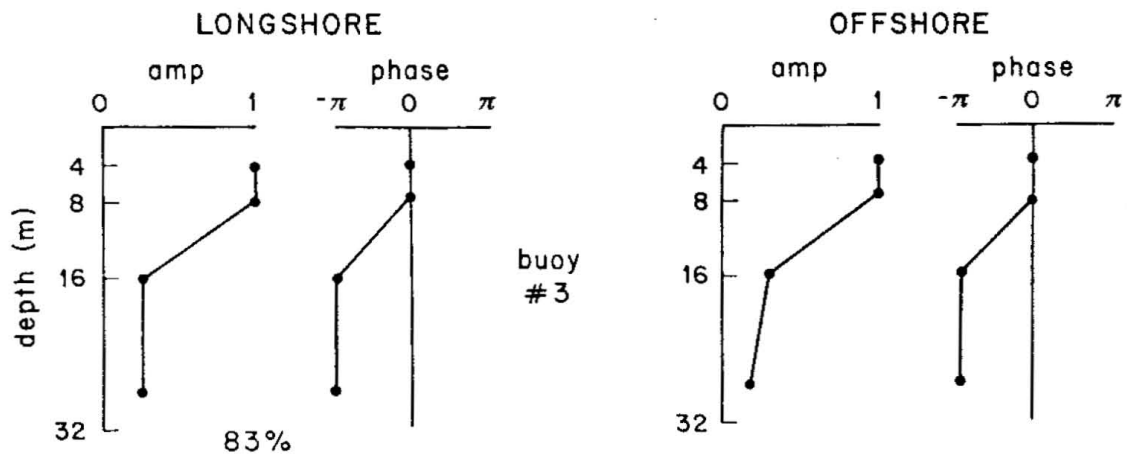
Figure 2.8   Inertial frequency complex eigenmodes.

a two-layer fluid in that it exhibits a 180° phase change with depth. In conjunction with this phase change the amplitude goes through a local minimum in accordance with what one would expect in association with the so-called first mode internal oscillation of a stratified fluid. In this sense the empirical modes may be loosely termed baroclinic. The SD motions are of uniform phase everywhere except at mooring 4 in Aug '78 where an apparent first baroclinic mode contributes approximately 5 percent of observed variance.

Alongshore empirical orthogonal modes of diurnal period character- isically exhibited one or more auxillary modes which at times accounted for as much as 15 percent of the energy at this frequency. The phase and amplitude structures of these modes were generally more complex than those previously discussed, and their relation to dynamical modes of a stratified fluid is not so apparent. Nevertheless, it seems justified to attribute this portion of the diurnal energy to internal tidal oscil- lations.

The most striking result of the empirical orthogonal function decom- position is the observed structure of the inertial period signals shown in figure 2.8. The dominant motions, for both offshore and alongshore components, exhibit a very clear 180 degree phase shift between the upper and lower pairs of current meters. Even at buoy 3 in March '78, where the inertial signal strength and the stratification are weak, this behavior is quite evident, and has the qualitative aspect of an internal or baroclinic response of a two layer fluid. So in effect, while at all other frequencies examined in this study the alongshore component motions

display a uniform phase structure, the inertial frequency response of the coastal boundary layer under conditions of both weak and strong stratification, is characterized by a very clear 180° phase change with depth. Although this phase structure of the inertial motion does owe its existence in part to the presence of stratification, it will be shown in Chapter III that it may not be quite appropriate to label it baroclinic in the usual sense of the terminology.

Vertical modes of the offshore velocity field generally tend to be more complex and to have greater spatial variation than their alongshore counterparts. In fact, only the SD signal consistently shows the constant phase reponse that typifies the (non-inertial) alongshore components. This situation may reflect the expected lower relative accuracy with which cross-shore signals are recorded and/or the also expected increase in vertical structure due to the coastal boundary constraint. However, it may also be, as concluded by May (1979), that the internal motions make a relatively greater contribution to the cross-shore modes since the barotropic motions are strongly polarized in the alongshore direction.

CHAPTER III

INERTIAL CURRENTS IN THE COASTAL ZONE: OBSERVATION AND THEORY

3.1 Introduction

The appearance of significant inertial oscillations in the COBOLT data is believed to represent the first reported observation of inertial frequency motion within a shallow oceanic coastal boundary layer environment. Historically coastal observations of near-inertial oscillations, such as those noted by Flagg (1977), and Mayer et al. (1980), have shown inertial kinetic energy to decay rapidly in the shoreward direction thereby limiting significant levels to middle and outer shelf locations. Off the Oregon coast Hayes and Halpern (1976), and Kundu (1976) have reported substantial near-inertial energy within ~ 15 km of shore in relatively deep (order 100 m) water. The fact that these observations have been exclusively associated with conditions of strong stratification has supported the notion that, in shallow water, frictional dissipation very efficiently damps inertial motions unless they are effectively isolated from such effects by a sufficiently strong pycnocline (Mayer et al., 1979). This interpretation is also suggested by the numerical model of Krauss (1976a,b) which investigated the effects that depth dependent stratification and eddy viscosity had upon the generation of inertial motion. The observation that inertial energy

substantially decreases in the shoreward direction has generally been interpreted as a manifestation of increased frictional influence as the water column shoals (eg. Flagg, 1977).

In some respects, because of the lack of competition from tides, large lakes represent an ideal environment in which to study nearshore inertial oscillations. Malone (1968) and Smith (1972) measured nearshore currents in Lake Michigan and Lake Superior respectively, and noted that near-inertial currents occurred only in the presence of a thermocline. Malone's measurements suggested that these oscillations, which often completely dominated current meter records, were first mode internal waves in that they exhibited a phase difference of 180° across the thermocline. Both investigators noted a dramatic reduction in rotary motion as the shoreline was approached, and attributed this behavior to the increased influence of the coastal boundary condition. Blanton (1974) clearly demonstrated that in Lake Ontario a rapid transition between the predominance of the near-inertial motions of the interior and the lower frequency longshore boundary flow took place within the first 10 km from shore.

The implications of both continental shelf and lake studies are that one might expect both bottom friction and the proximity of the shoreline to inhibit inertial motions within the oceanic CBL. It is also expected that this inhibition will become progressively greater as the coast is approached. Observational evidence also suggests that stratification plays a fundamental role in the realization of inertial motion in shelf regions and enclosed basins.

3.2 Wind stress and inertial currents

During the COBOLT experiment wind speed and direction were recorded
at various nearby towers under the auspices of BNL's Meteorology Group.
In addition, wind profiles were recorded at the field site in a 1974
study relating local mean winds to bulk aerodynamic drag coefficients.
SethuRaman and Raynor (1975) in an analysis of these data concluded that
the drag coefficient was not discernably a function of wind speed. More
recently, however, Amorocho and Devries (1979), using a large collection
of data have presented an empirically determined formula for the drag
coefficient as a function of wind speed. This formula is entirely
consistent with, although not suggested by, the data of SethuRaman and
Raynor which represented a limited range of observed wind speeds. In
the present work the variable coefficient given by Amorocho and Devries
as

$$C_{10} = 0.0015 \left[1 + \exp(\frac{12.5 - U_{10}}{1.56}) \right]^{-1} + 0.00104 \qquad (3.1)$$

is adopted, where C_{10} is the coefficient relevant to mean flow at 10
meters (U_{10}) in MKS units. While one is never overly comfortable
relying on such bulk formulae, it is expected that use of Eq. (3.1)
leads to a reasonable representation of wind stress fluctuations.

The idea that wind stress fluctuations are largely responsible for
the generation of open ocean near-inertial motions is well founded on
both theoretical (Gonella, 1970; Pollard, 1970; Krauss,1976a,b) and

observational grounds (e.g., Pollard and Millard, 1970; Gonella, 1971; Halpern, 1974). The establishment of this relationship has been far from easy. The dilemma facing the observationalist is that inertial oscillations in the ocean are fundamentally transient or intermittent phenomena. The cause of this nonstationarity is not well established and has been variously attributed to dispersion, frictional decay, amplification or destruction by successive wind episodes, and interference phenomena. Whatever the origins, this intermittency results in a dissembling complexity which can confound attempts to establish a causal relation between wind and wave. It is not uncommon to find no oscillations when they might have been expected (Webster, 1968) nor to suddenly observe fluctuations with no apparent cause (Kundu, 1976; Flagg, 1977).

Although it is extremely difficult to precisely observe the transient behavior of inertial motions, the method of complex demodulation (Perkins, 1970) provides one means for attempting to do so. The procedure entails calculation of the first Fourier sine and cosine coefficients, plus the mean and linear (in time) terms, for successive data segments which overlap one another by 50 percent. Lengthening data segments by integral multiples of the inertial period improves frequency resolution while concurrently rendering the determination for the time variation of amplitudes more and more crude. Thus, as noted by Webster (1968), a "relentless uncertainty principle" obtains in observational studies of near-inertial motions. The length of data required to resolve the inertial motion from tides may be longer

than their lifetime. On the other hand, if an effort is made to resolve the nonstationarity of the signal, contamination from tidal motions is inevitable.

These difficulties are aggravated in mid-latitude shallow water environments where shoaling effects assure that the inertial signal will be flanked by highly energetic tidal bands. In the present work a data window of two inertial periods was used eliminating all but roughly 10 percent of the tides. As reference to Figure 2.5 confirms however, even 10 percent of the SD tides can represent significant contamination. The success of the complex demodulation in this situation depends upon the occurrence of an event of intensity sufficient to rise above the high ambient noise level. Fortunately, at least one such event is clearly discernable in the record.

Figure 3.1 shows the offshore and alongshore wind stress time series and the demodulated inertial amplitude for the surface instruments during the May experiment. Although the wind stress records have been smoothed, the duration of wind events has been preserved. The dominant meteorological event durng this time period was a predominantly offshore impulse starting on May 9 and ending May 10. A rise in the inertial amplitude corresponding to the onset of the storm is evident even though the 37 hour data window used tends to broaden the peaks. The sharp decline in inertial amplitude upon relaxation of the wind stress is likely to be in part due to strong frictional decay, but as suggested in section 3.4.1c, it may be more directly related to the disappearance of stratification which occurs at this time (section 4.2). While the
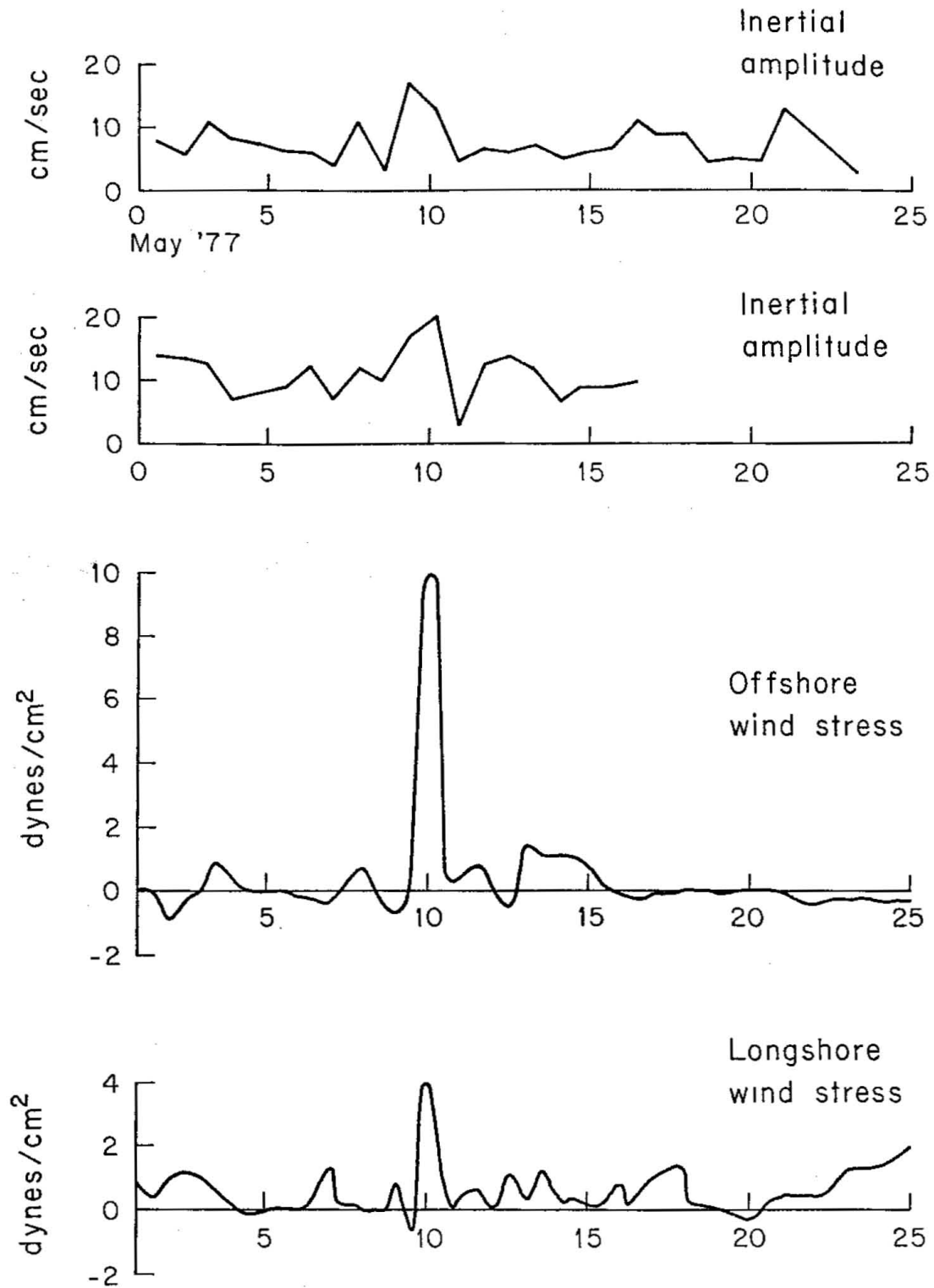
Figure 3.1   May '77 demodulated inertial amplitude at 4 m depth, and wind-stress components

general variations of the demodulated amplitudes do roughly correlate with the wind-stress history, in view of the uncertainties earlier discussed it is probably not profitable to attempt to relate lesser features of the wind with demodulated records. The results shown in Figure 3.1 are taken to be reasonable confirmation of the wind driven origins of the near inertial signal in the COBOLT data set.

3.3 Cross-shore behavior of the inertial signal

Figure 3.2 shows the clockwise component energy spectra for instruments at 8 m depth on moorings 2 and 4 during May'77. The difference in inertial energy over this 6 km separation is statistically significant at the .80 confidence level implying that such an offshore increase in the magnitude of the inertial response is a characteristic feature. There is, of course, no doubt whatever that the inertial level increased with distance from shore for this particular realization. The measured offshore gradients were found to be statistically significant only for the upper water column. In fact, measurements within 2.5 m of the bottom showed no horizontal gradient at all. These results, together with figure 3.1, suggest that (at least in the upper layer) the inertial signal within the CBL gets stronger with increasing distance from shore. The observed weakening of this trend in the lower water column is probably a consequence of bottom friction.

Figure 3.3 shows the corresponding salinity spectra at the same
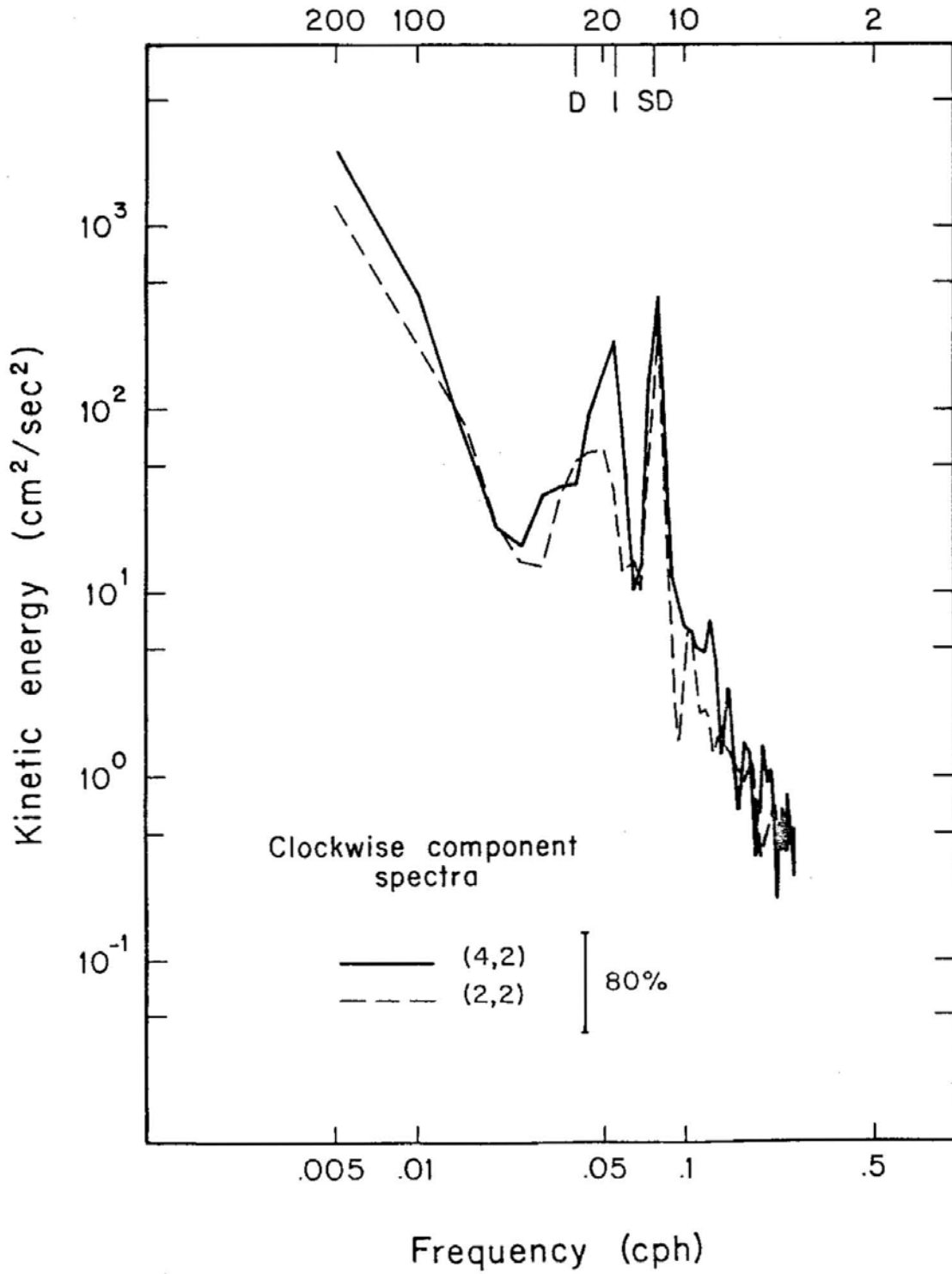
Figure 3.2 Clockwise component energy spectra at 8 m depth, 6 and 12 km from shore.
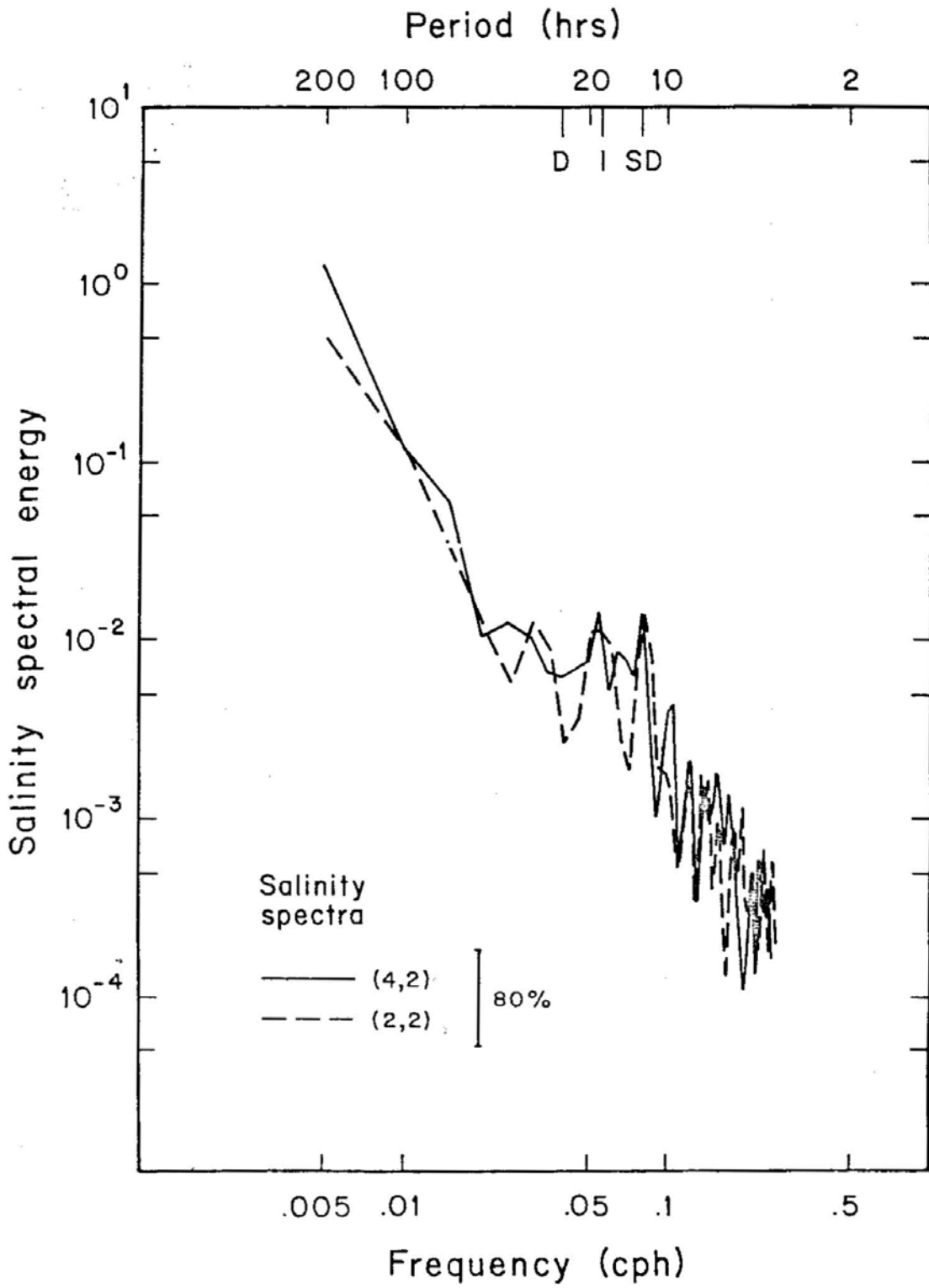
Figure 3.3 Salinity spectra at 8 m depth, 6 and 12 km from shore.

locations. The presence of an inertial peak confirms the notion, sug-
gested by the empirical mode analysis of section 2.4, that a substantial
portion of the inertial energy is baroclinic. The offshore structure
makes an interesting contrast to that of the velocity field in that no
offshore gradient in spectral levels is noted.

Further insight into the nature and method of generation of inertial
waves observed in the CBL comes from consideration of the phase rela-
tionships of oscillations in the inertial band as a function of pos-
ition. Table 3.1 shows the vector coherence and phase of (inertial
frequency) clockwise velocity components, and ordinary phase and coh-
erence of corresponding salinity oscillations, between moorings 2 and
4. The convention used is that positive phase angles reflect a lag at
mooring 4 relative to mooring 2. While the calculated vector coherence
is above the .90 significance level at all depths, the phase lag is
statistically different from zero only at the near surface and bottom
positions. As is perhaps to be expected, the coherence and phase
calculations for salinity are most reliable in the middle water column
where the halocline is present. The results shown in table 3.1 indicate
that nearshore inertial frequency oscillations of both velocity and
salinity consistently lead those further seaward. This fact implies an
offshore propagation of inertial waves. Kundu (1976) also concluded
that inertial oscillations were propagating normal to the Oregon coast,
but his analysis of a single mooring precluded specification of whether
the phase propagation was onshore or offshore. The evidence presented
here, in conjunction with the apparent correlation with local winds,

TABLE 3.1

May'77 Clockwise Inertial Currents

Instruments	Vector Coherence	Phase
(2,1)-(4,1)	.85*	20*
(2,2)-(4,2)	.73*	14
(2,3)-(4,3)	.84*	4
(2,4)-(4,4)	.75*	58*

Inertial Salinity Oscillations

Instruments	Ordinary Coherence	Phase
(21)-(41)	.47	77
(22)-(42)	.57*	35*
(23)-(43)	.64*	21*
(24)-(44)	.09	150

Asterisks indicate phases and coherences different from zero at th .90 significance level.

suggests that the oscillations are generated at the shore and sub-
sequently propagate seaward. These findings suggest that a locally
forced coastal model is appropriate for investigating the nature of
these transient disturbances. The results of the empirical orthogonal
function analysis, which show that more than 90 percent of the inertial
response resembled a first baroclinic mode, make it clear that strat-
ification must be included and that a two layer model may be suffi-
cient. Figure 3.4 shows the mean σ_t profile as deduced from the daily
STD surveys for the May '77 experimental period. Note the strong
pycnocline near mid-depth and the relatively homogeneous surface and
bottom layer (except very near shore). Figure 3.5 shows the vertical
profile of the average buoyancy frequency at moorings 2, 3, and 4.
Obviously a constant N model would not be appropriate in this region.
Therefore it appears that a two-layer model, in addition to being the
most straightforward, may also be the most appropriate of the simple
approaches.

Crepon (1969) studied the interfacial response of a two-layer domain
to spatial discontinuites in wind stress and atmospheric pressure.
Using the method of images he was able to satisfy the no normal flow
boundary conditions appropriate for a coastline. Investigating the ef-
fects of a suddenly imposed constant wind stress, he demonstrated that
the transient response of the interface was characterized by inertial
oscillations which were generated at the coast and subsequently propa-
gated seaward.

Crepon's model is rederived below using a simplified and more direct

MAY 1977 AVERAGE
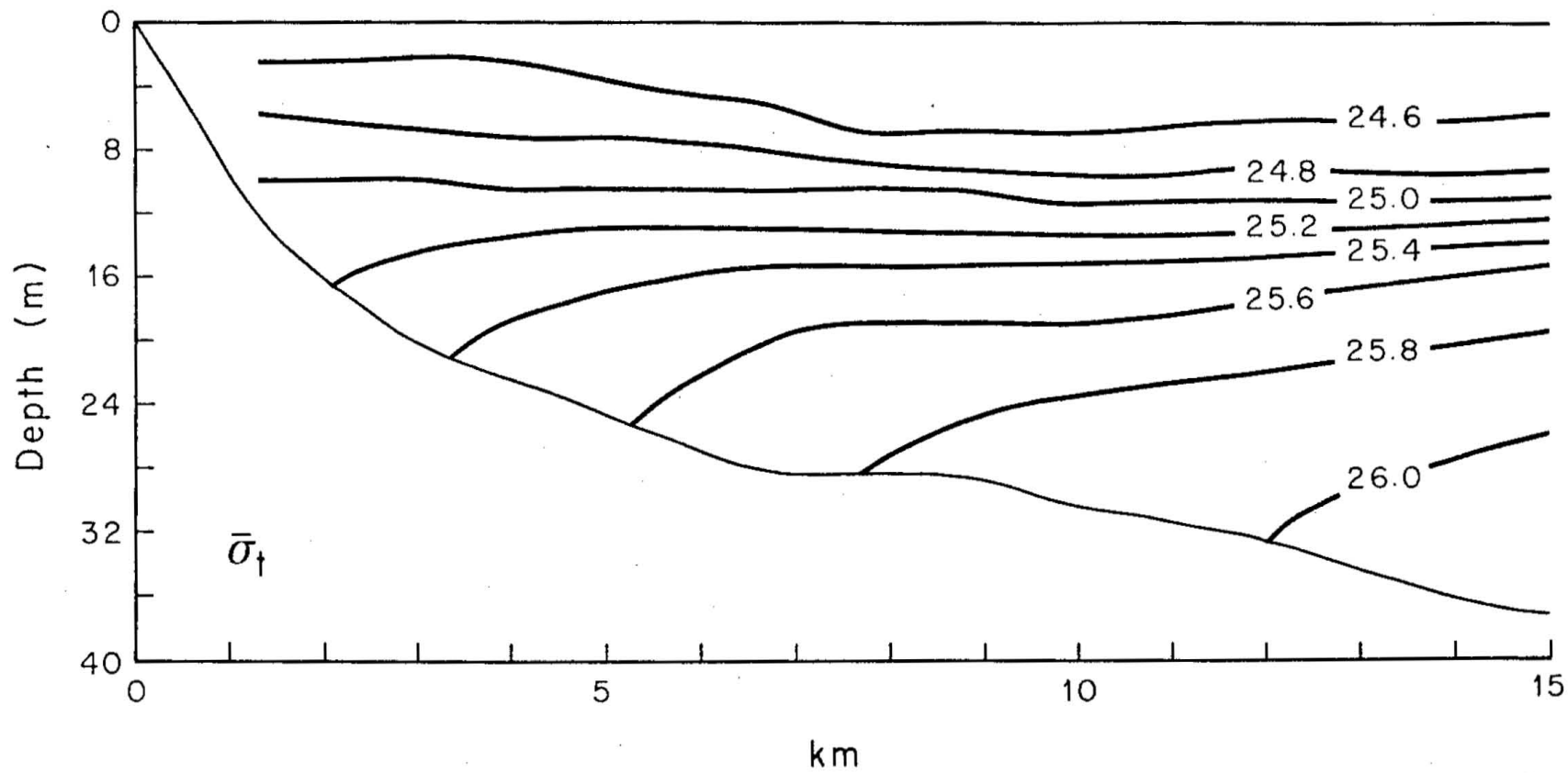
Figure 3.4 Twenty-two day average sigma-t field during May '77.
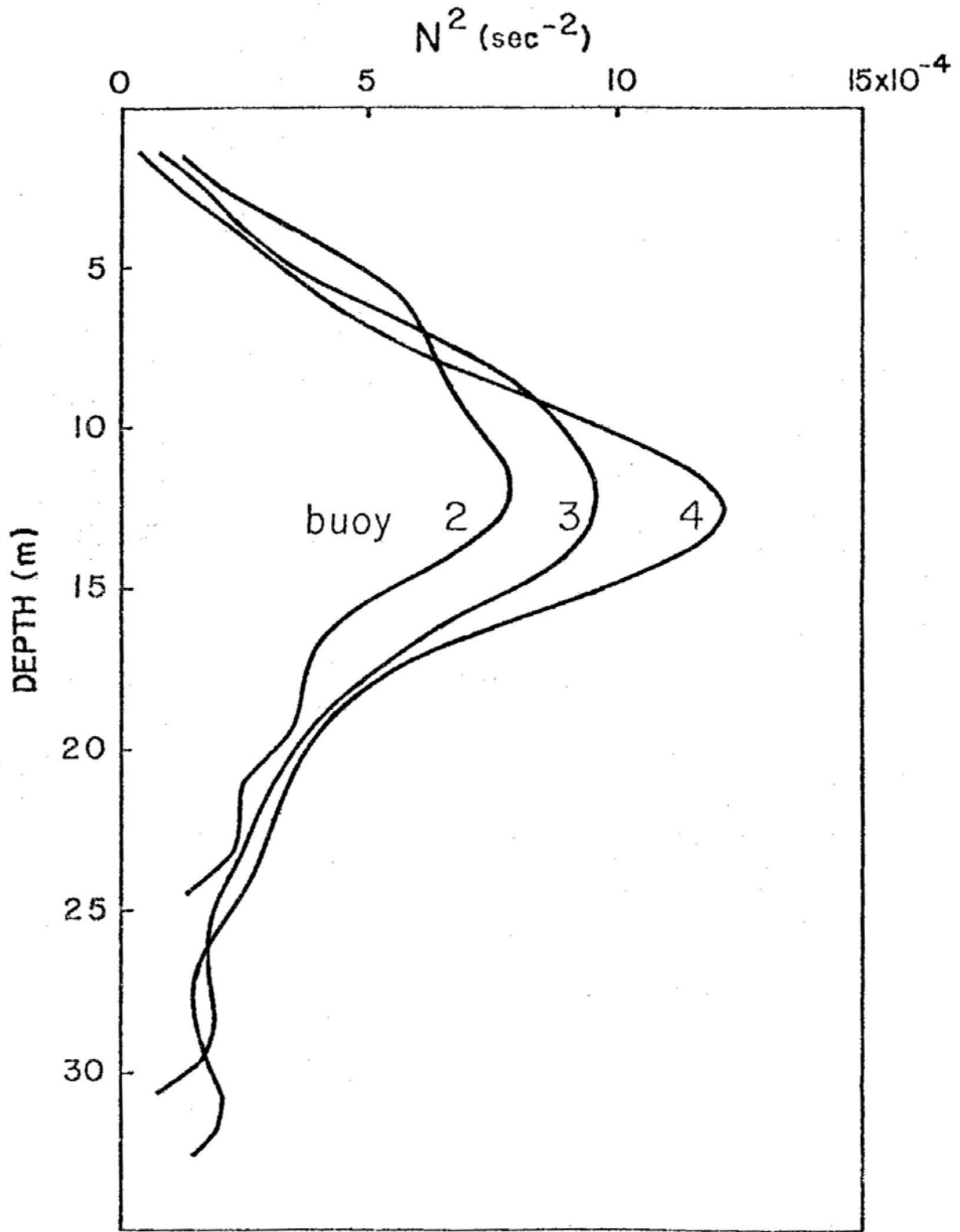
Figure 3.5 Twenty-two day average Brunt-Vaisala frequency profiles at bouys 2, 3 and 4

approach to satisfying boundary conditions, and solutions for the upper and lower layer currents are examined. These results may be directly compared to observations, and the consequences of the coastal boundary constraint, with regard to the realization of nearshore inertial currents, expressly investigated.

3.4 A two-layer model of coastal response to impulsive wind

Figure 3.6 is a definition sketch showing the model topography and coordinate system. The nearshore region is represented as possessing a flat bottom and a vertical coastal boundary. ζ_1 and ζ_2 are the surface and interface deformations respectively, while ρ_i and h_i are the density and water depth appropriate for each layer. The linearized equations of motion vertically averaged over each layer are:

$$\frac{\partial \vec{q}_1}{\partial t} + 2\vec{\Omega} \times \vec{q}_1 = -g\nabla\zeta_1 + \frac{1}{\rho_1 h_1} \int_{-h_1}^{0} \vec{S}_1 \, dz \qquad (3.2)$$

$$\frac{\partial \vec{q}_2}{\partial t} + 2\vec{\Omega} \times \vec{q}_2 = -g(\nabla\zeta_1 + \epsilon\nabla(\zeta_2 - \zeta_1)) \frac{1}{\rho_2 h_2} \int_{-h_2}^{0} \vec{S}_2 \, dz \qquad (3.2)$$

where the subscript everywhere refers to the layer, $\vec{q}$ is the velocity vector, the $\vec{S}_i$ represent surface forces, g is the gravitational
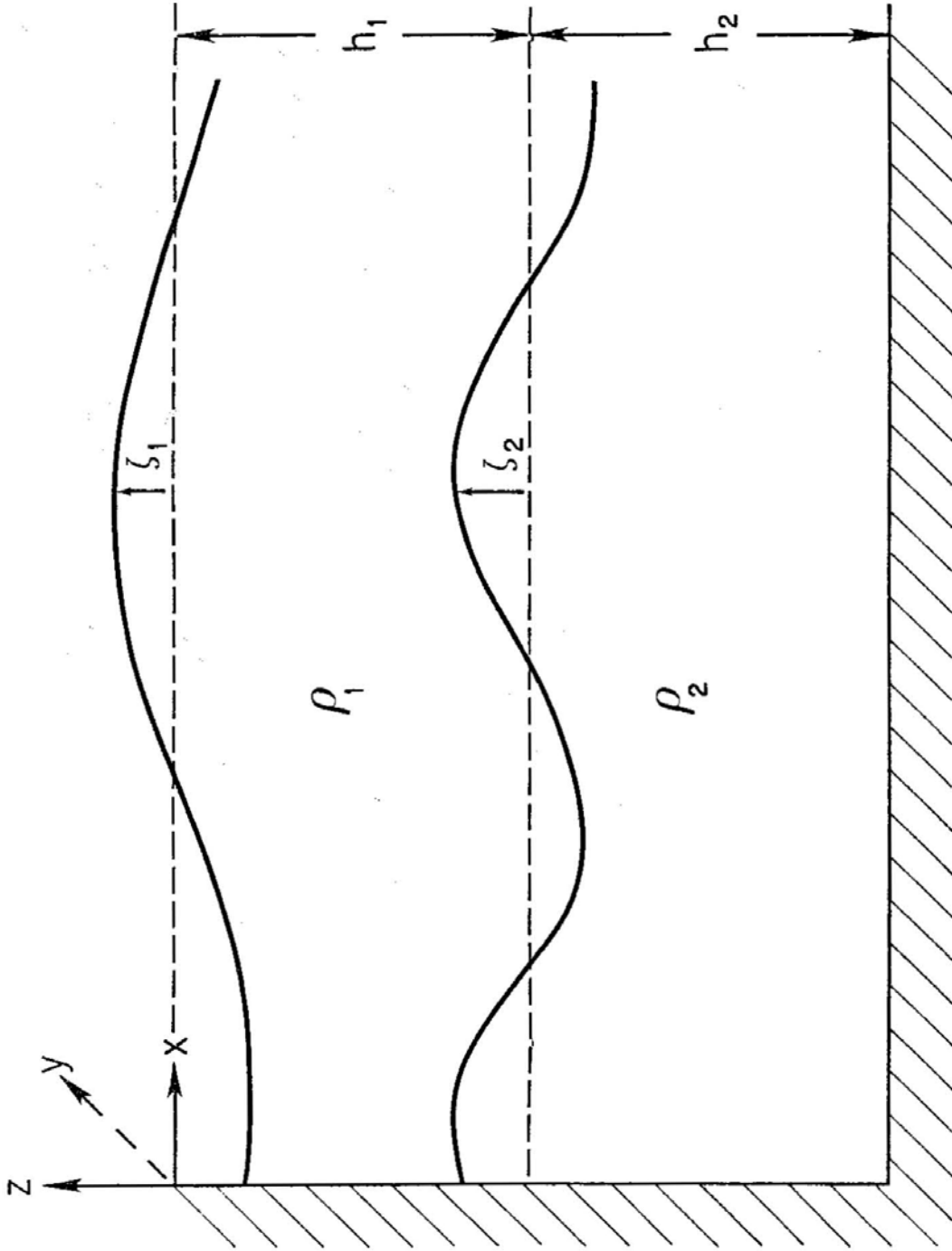
Figure 3.6 Definition sketch of model topography and coordinates

acceleration, ∇ the gradient operator, $2\vec{\Omega}$ the angular velocity of the earth, and ε, given by

$$\varepsilon = \frac{(\rho_2 - \rho_1)}{\rho_2} \quad ,$$

is the proportional density defect. The top and bottom layer equations of continuity are given by

$$\nabla \cdot \vec{q}_1 = \frac{1}{h_1}\left(\frac{\partial \zeta_2}{\partial t} - \frac{\partial \zeta_1}{\partial t}\right)$$

$$\nabla \cdot \vec{q}_2 = - \frac{1}{h_2}\frac{\partial \zeta_2}{\partial t} \tag{3.3}$$

The appropriate boundary and initial conditions are that the surface and interface deformations die away far from shore, the normal component of flow vanishes at the coast, and that a state of rest exists prior to the onset of wind forcing.

Following Crepon one can for convenience let

$$\frac{\partial \phi_1}{\partial t} = - g\zeta_1$$

and

$$\frac{\partial \phi_2}{\partial t} = - g\left[(1-\varepsilon)\zeta_1 + \varepsilon\zeta_2\right] \tag{3.4}$$

so that upon neglect of interfacial and bottom friction, equations (3.2) and (3.3) may be written as

$$\frac{\partial \vec{q}_1}{\partial t} + \vec{f} \times \vec{q}_1 = \nabla \frac{\partial \phi_1}{\partial t} + \frac{\vec{\tau}}{h_1}$$

$$\frac{\partial \vec{q}_2}{\partial t} + \vec{f} \times \vec{q}_2 = \nabla \frac{\partial \phi_2}{\partial t}$$

(3.5a)

$$\nabla \cdot \vec{q}_1 = \frac{1}{g\epsilon h_1} \frac{\partial^2}{\partial t^2} (\phi_1 - \phi_2)$$

(3.5b)

$$\nabla \cdot \vec{q}_2 = \frac{1}{g\epsilon h_2} \left(\frac{\partial^2 \phi_2}{\partial t^2} - (1-\epsilon) \frac{\partial^2 \phi_1}{\partial t^2} \right)$$

where $\vec{\tau}$ represents the wind stress and $\vec{f}$ is the Coriolis parameter. The Laplace transformed versions of these equations are

$$P \vec{Q}_1 + \vec{f} \times \vec{Q}_1 = P \nabla \Phi_1 + \frac{\vec{T}}{h_1}$$

$$P \vec{Q}_2 + \vec{f} \times \vec{Q}_2 = P \nabla \Phi_2$$

(3.6)

$$\nabla \cdot \vec{Q}_1 = \frac{p^2}{g\epsilon h_1} (\Phi_1 - \Phi_2)$$

$$\nabla \cdot \vec{Q}_2 = \frac{p^2}{g\epsilon h_2} (\Phi_2 - (1-\epsilon)\Phi_1)$$

$\vec{Q}_1$ and $\vec{Q}_2$ can be eliminated from equations (3.6) in favor of Φ_1 and Φ_2 resulting in the relations

$$P^2(\Phi_2 - (1-\epsilon)\Phi_1) - \frac{g\epsilon h_2}{k^2} \nabla^2 \Phi_2 = 0$$

$$P^2(\Phi_1 - \Phi_2) - g\epsilon\left[\frac{h_1}{k^2}\nabla^2\Phi_1 + \frac{1}{k^2 P}\left(\nabla \cdot \vec{T} + \frac{f \cdot \nabla \times \vec{T}}{P}\right)\right] = 0$$

(3.7)

where $k^2 = (P^2 + f^2)/P^2$.

Assuming all y derivatives vanish and that the solution decays with distance from shore as

$$\Phi_i \sim e^{-\frac{Pkx}{c_i}}$$

leads to the relation

$$c^4 - c^2 g(h_1 + h_2) + g^2 \epsilon h_1 h_2 = 0$$

for the eigenvalues of the problem. These eigenvalues are approximately given by

$$c_1 \simeq \sqrt{g(h_1 + h_2)}$$

(3.8)

$$c_2 \simeq \sqrt{g \frac{\epsilon h_1 h_2}{h_1 + h_2}}$$

The ratio of $\Phi_1/\Phi_2 = \lambda_i = \dfrac{1}{1 - (g\varepsilon h_1)/c_i^2}$

or

$$\lambda_1 = \frac{1}{1 - \dfrac{\varepsilon h_1}{h_1 + h_2}}$$

and

$$\lambda_2 = \frac{1}{1 - \dfrac{h_1 + h_2}{h_2}}$$

(3.9)

expanding the Φ's in terms of the eigenmodes leads to

$$\Phi_1 = \lambda_1 F_1 \, e^{-\frac{Pkx}{c_1}} + \lambda_2 F_2 \, e^{-\frac{Pkx}{c_2}}$$

$$\Phi_2 = F_1 \, e^{-\frac{Pkx}{c_1}} + F_2 \, e^{-\frac{Pkx}{c_2}}$$

(3.10)

or referring to (3.4)

$$Z_1 = \frac{-P}{g}\left(\lambda_1 F_1 \, e^{-\frac{Pkx}{c_1}} + \lambda_2 F_2 \, e^{-\frac{Pkx}{c_2}} \right)$$

(3.11)

$$Z_2 = \frac{P}{g\varepsilon}\left[((1-\varepsilon)\lambda_1 - 1) \, F_1 \, e^{-\frac{Pkx}{c_1}} + ((1-\varepsilon)\lambda_2 - 1) \, F_2 \, e^{-\frac{Pkx}{c_2}} \right]$$

where F_1 and F_2 are constants to be determined from the shore-line boundary condition, and Z_1 and Z_2 are the Laplace transforms of ζ_1 and ζ_2. From the component form of equations (3.6) it is readily shown that

$$U_1 = \frac{1}{k^2} \frac{\partial \Phi_1}{\partial x} + \frac{1}{Pk^2 h_1} (T_x + \frac{f}{P} T_y)$$

$$U_2 = \frac{1}{k^2} \frac{\partial \Phi_2}{\partial x}$$

(3.12)

having used

$$\vec{Q}_i = \hat{i} \, U_i + \hat{j} \, V_i$$

and

$$\vec{T} = \hat{i} \, T_x + \hat{j} \, T_y$$

where $\hat{i}$ and $\hat{j}$ are the unit vectors in the x and y directions. Setting $U_1 = U_2 = 0$ at $x = 0$ and using equation (3.10) leads directly to

$$F_1 = \frac{c_1}{(\lambda_1 - \lambda_2)} \frac{1}{P^2 k h_1} (T_x + \frac{f}{P} T_y)$$

(3.13)

$$F_2 = \frac{-c_2}{(\lambda_1 - \lambda_2)} \frac{1}{P^2 k h_1} (T_x + \frac{f}{P} T_y)$$

3.4.1 Offshore wind forcing: the delta function

Much of the information concerning the physical mechanism involved in the coastal response to transient wind forcing may be illuminated by the most highly idealized stress; that associated with a spatially uniform delta function wind. It is recognized a priori that such a severe idealization may not lead to any practical predictions relating amplitudes of forcing to amplitudes of response, but the comparative simplicity of the solutions facilitates a physical interpretation of the functional behavior. Solutions for the delta function wind are presented before consideration of slightly more realistic wind stress configurations with the expectation that the qualitative behavior observed will be similar to that induced by wind impulses of short (with respect to an inertial period) duration.

The Laplace transformation of $\vec{\tau} = F_0 \delta(t)$ is simply F_0, so that for an offshore wind stress equations (3.13) yield

$$F_1 = \frac{c_1}{\lambda_1 - \lambda_2} \frac{F_0}{p^2 k h_1}$$

$$F_1 = \frac{-c_2}{\lambda_1 - \lambda_2} \frac{F_0}{p^2 k h_1}$$

(3.14)

Substituting these relations into equations (3.11) leads directly to

$$Z_1 = \frac{-F_0}{g(\lambda_1 - \lambda_2)h_1} \left(\lambda_1 c_1 \frac{e^{-\sqrt{p^2+f^2}\, x/c_1}}{\sqrt{p^2+f^2}} - \lambda_2 c_2 \frac{e^{-\sqrt{p^2+f^2}\, x/c_2}}{\sqrt{p^2+f^2}} \right)$$

(3.15)

$$Z_2 = \frac{F_0}{\varepsilon g(\lambda_1-\lambda_2)h_1}\left[((1-\varepsilon)\lambda_1-1)c_1 \frac{e^{-\sqrt{p^2+f^2}\;x/c_1}}{\sqrt{p^2+f^2}} - ((1-\varepsilon)\lambda_2-1)c_2 \frac{e^{-\sqrt{p^2+f^2}\;x/c_2}}{\sqrt{p^2+f^2}}\right]$$

These functions can be inverse transformed (cf. Abramowitz and Stegun, 1964) to give the solutions

$$\zeta_1 = \frac{-F_0}{gh_1(\lambda_1-\lambda_2)}\left[\lambda_1 c_1 J_0\left(f\sqrt{t^2-x^2/c_1{}^2}\right)\mu(t-x/c_1) - \lambda_2 c_2 J_0\left(f\sqrt{t^2-x^2/c_2{}^2}\right)\mu(t-x/c_2)\right]$$

and   (3.16)

$$\zeta_2 = \frac{F_0}{\varepsilon gh_1(\lambda_1-\lambda_2)}\left[((1-\varepsilon)\lambda_1-1)c_1 J_0\left(f\sqrt{t^2-x^2/c_1{}^2}\right)\mu(t-x/c_1)\right.$$
$$\left. - ((1-\varepsilon)\lambda_2-1)c_2 J_0\left(f\sqrt{t^2-x^2/c_2{}^2}\right)\mu(t-x/c_2)\right]$$

where J_0 is the zero order Bessel function of the first kind, and $\mu(t-x/c_i)$ is the unit step function which takes a value of 0 if its argument is negative and is unity otherwise.

3.4.1a Interfacial response

Consideration of equation (3.9) reveals that for $h_1 = h_2$, λ_1 and λ_2 are approximately equal to plus and minus one respectively. It is then clear that, as expected, the major contribution to $_2$ arises from the baroclinic mode while for $_1$ the reverse is true. The surface and interface deformations originate at the coast (in fact owing their existence to its presence) and propagate offshore. At any particular offshore position the sequence of events is as follows. The initial response to the wind stress impulse arrives at time x/c_1. This contribution corresponds to the rapidly traveling barotropic surface wave. At time x/c_2 the baroclinic contribution arrives having negligible expression in the surface elevation but dramatically amplifying interface oscillations. It is interesting to note that these undulations are ephemeral in nature, even in the absence of friction, and decay as $(t^2 - x^2/c_2)^{-1/4}$. In essence, the disturbance radiates away from the coastal boundary. The frequency of these oscillations asymptotes to f (the lower bound) for $t \gg x/c_i$.

For $h_1 = h_2 = 15$ m and $\varepsilon \sim 10^{-3}$ (corresponding to the strong stratification observed) the barotropic and baroclinic phase speeds are approximately 60 km/hr and 1 km/hr respectively. Clearly, the effects of the barotropic signal would be felt across the entire shelf within a small fraction of an inertial cycle while even after several full cycles the baroclinic effects would still be confined to CBL and inner shelf regions. One might well expect, therefore, a clear dicotomy between the

responses of nearshore and outer shelf regions immediately following a wind stress episode. Far from shore the response as measured by density field fluctuations would be barotropic whereas nearshore the added effects of baroclinicity would be important.

Note that in equations (3.16), and those that follow, the argument of the Bessel function could be written as $[(ft)^2 - x^2/R_i^2]$ where $R_i = c_i/f$ is the familiar radius of deformation. In order to render results somewhat less site specific in their dependence upon local parameters, all solution plots have time expressed in inertial periods and distance in terms of R_2, the baroclinic deformation radius. For the COBOLT experiment $R_2 \sim 3$ km (2.88 km).

Figure 3.7 shows the time histories of analytical interface oscillations for several offshore positions within the CBL. Free surface behavior has not been presented because it is directly analogous to that of the interface, and since it is of a different scale and shows no significant variations over the region of interest. Figure 3.8 shows several time "snapshots" of the interface as function of distance from the coast. Although these solutions are rendered somewhat offensive by the discontinuity of the disturbance's leading edge (an artifice introduced through use of the delta function wind), they clearly exhibit an interesting spatial and temporal variation which will be seen to have some far-reaching consequences in terms of the behavior of the velocity fields. The physical interpretation of these patterns is that the group velocities of the higher frequency components, being faster than those of the lower frequencies, tend to concentrate short period energy near the leading edge of the disturbance.
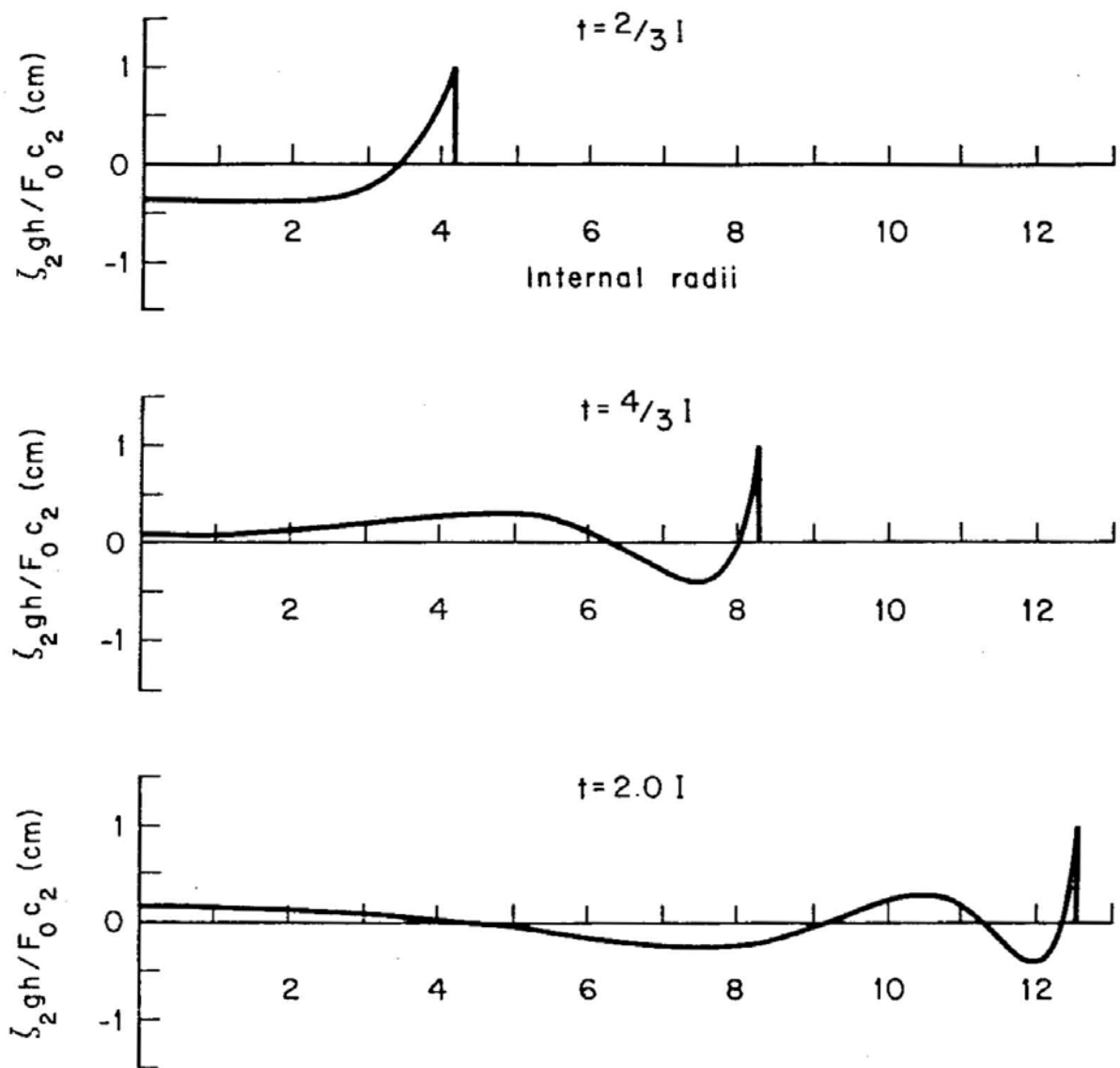
Figure 3.7   Interface deformation across the coastal zone at 2/3, 4/3, and 2 inertial periods.
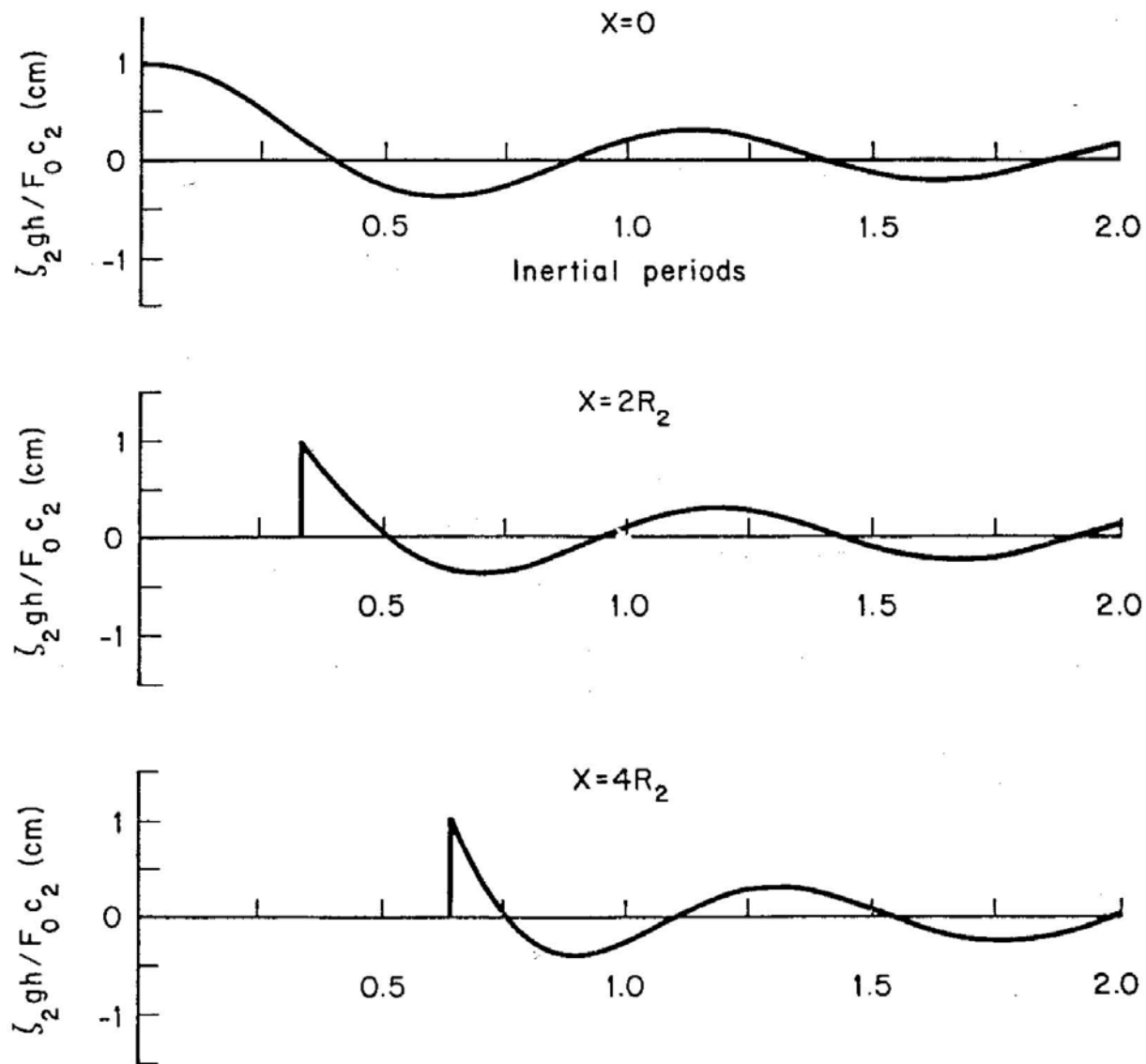
Figure 3.8 Interface deformation as a function of time at the coast, and at 2, and 4 internal radii away.

3.4.1b Current response

The velocity fields associated with the two layer coastal response display some very interesting and realistic properties. For the off-shore wind under consideration, the component equations corresponding to equations (3.6) yield relations

$$V_1 = - f \frac{U_1}{P}$$

$$U_1 = \frac{1}{k^2} \frac{\partial \Phi_1}{\partial x} + \frac{F_0}{Pk^2 h_1}$$

and
(3.17)

$$V_2 = - f \frac{U_2}{P}$$

$$U_2 = \frac{1}{k^2} \frac{\partial \Phi_2}{\partial x}$$

which in light of (3.10) yields

$$U_1 = \frac{-F_0}{(\lambda_1 - \lambda_2) h_1} \left(\frac{\lambda_1 P}{P^2 + f^2} e^{-\sqrt{P^2 + f^2} \, x/c_1} - \frac{\lambda_2 P}{P^2 + f^2} e^{-\sqrt{P^2 + f^2} \, x/c_2} \right) + \frac{P F_0}{h_1 (P^2 + f^2)}$$

$$V_1 = \frac{fF_0}{(\lambda_1-\lambda_2)h_1}\left(\frac{\lambda_1}{p^2+f^2} e^{-\sqrt{p^2+f^2}\ x/c_1} - \frac{\lambda_2}{p^2+f^2} e^{-\sqrt{p^2+f^2}\ x/c_2}\right) - \frac{fF_0}{h_1(p^2+f^2)}$$

$$(3.18)$$

$$U_2 = \frac{-F_0}{(\lambda_1-\lambda_2)h_1}\left(\frac{p}{p^2+f^2} e^{-\sqrt{p^2+f^2}\ x/c_1} - \frac{p}{p^2+f^2} e^{-\sqrt{p^2+f^2}\ x/c_2}\right)$$

$$V_2 = \frac{fF_0}{(\lambda_1-\lambda_2)h_1}\left(\frac{1}{p^2+f^2} e^{-\sqrt{p^2+f^2}\ x/c_1} - \frac{1}{p^2+f^2} e^{-\sqrt{p^2+f^2}\ x/c_2}\right)$$

The inverse Laplace transforms for the velocities may be expressed as

$$v_1 = \frac{fF_0}{(\lambda_1-\lambda_2)h_1}\Bigg(\lambda_1(J_0(ft)*J_0(f\sqrt{t^2-x^2/c_1^2})\quad \mu(t-x/c_1)$$

$$- \lambda_2(J_0(ft)*J_0(f\sqrt{t^2-x^2/c_2^2})\ \mu(t-x/c_2)\Bigg) - \frac{F_0}{h_1}\sin(ft)$$

$$u_1 = -\frac{1}{f}\frac{dv_1}{dt}$$

(3.19)

$$v_2 = \frac{fF_0}{(\lambda_1-\lambda_2)h_1}\left[J_0(ft) * J_0(f\sqrt{t^2-x^2/c_1^2})\quad \mu(t-x/c_1)\right.$$

$$\left. - J_0(ft) * J_0(f\sqrt{t^2-x^2/c_2^2})\quad \mu(t-x/c_2)\right]$$

$$u_2 = -\frac{1}{f}\frac{dv_2}{dt}$$

where the * notation represents convolution.

Much of the nature of these solutions may be deduced from their functional form prior to actually performing the convolution integral. The third term in the surface layer expression corresponds to the pure inertial oscillation as it would exist in an infinite two layer ocean without lateral boundaries: it involves no surface or interface displacement and no spatial variation. The terms involving the convolution thus represent the modifications to the pure inertial response which are due to the presence of the coastal boundary. Since the terms arising

due to the coastal presence are both zero if $t < x/c_1$ it is seen that far from shore, at least initially, classical inertial oscillation exists in the upper layer. At this same position and time there is no motion at all in the lower layer. In effect, the information regarding the presence of the coast has not had time to propagate out from the shore. Upon arrival of the barotropic signal two things happen simultaneously: the upper layer oscillation is reduced, and motion in the lower layer commences. Remembering that λ_1 and λ_2 are given by ± 1 respectively, it is seen that the momentum loss in the upper layer equals the momentum gained by the lower layer.

It is easily established by Laplace transform methods that the con volution $J_0(ft)*J_0(ft)$ is equal to $\sin(ft)/f$. Therefore at $x = 0$, all velocities given in equations (3.19) are identically zero as demanded by the coastal boundary condition. In addition, for $t^2 \gg (x/c1)^2$, the first term in each of equations (3.19) is given approximately by

$$(F_0/2h_1)\sin(ft)$$

The effect, then, of the arrival of the barotropic disturbance is roughly to cancel half the directly wind induced surface layer inertial signal while at the same time initiating an equal and opposite oscillation in the lower layer. Given the rapid phase speed of this disturbance the upper and lower layers on the shelf would be perceived to respond simultaneously with a 180° phase difference between them. At mid-shelf locations all this would occur long before the arrival of the baroclinic

signal. In contrast, some effects of the baroclinic disturbance would
be felt everywhere in the CBL within a fraction of an inertial period.

It is interesting to note that before the interfacial wave arrives
at a particular location, the existing motion already has the appearance
of a baroclinic response. The velocity fluctuation in the two layers
are equal in magnitude and 180 degrees out of phase. This situation
actually arises due to the combination of a barotropic disturbance whose
effects are felt equally throughout the water column, and the directly
wind induced response which is confined to the upper layer. This sur-
prising result suggests that if the baroclinic disturbance never arrived
at a particular location (perhaps due to dissipation) a current meter
string would nevertheless sense a 180° phase shift between upper and
lower waters, and the observer would erroneously infer the presence of
an internal inertial wave. In the presence of a coast, phase relation-
ships are not necessarily a reliable means for locally discriminating
between the effects of surface and internal response components.

The effect of the baroclinic disturbance is to progressively cancel
pre-existing fluctuations in both layers, eventually resulting in a
state of rest. By an argument identical to that presented in the bar-
otropic case, for large enough time, the lower layer velocity fields
forced by the surface and interfacial waves exactly cancel one another
while in the upper waters they combine to balance the motion directly
forced by the wind. The manner in which this effect is achieved,
however, can be far from orderly or monotonic in nature.

From the elementary theoretical considerations already presented it

is clear that no observable transient wavelike inertial velocity signal arises which has a general barotropic (independent of depth) phase structure in a two layer coastal domain. This behavior, while in excellent agreement with observations in this and other field studies, makes an interesting contrast to predicted interfacial behavior. As discussed earlier, the surface and interfacial oscillations in the model owe their existence directly to the presence of of the coastal boundary, and propagate seaward from this origin. The peculiar situation arises that during the time between the arrivals of the surface and internal waves, observations of the density field would theoretically reflect barotropic oscillations while current meter results would exhibit an apparent baroclinic response. Because of the large discrepancy in the magnitude of the hydrographic responses elicited by the barotropic and baroclinic waves, in practice the barotropic signal would be unlikely to be detected and wavelike variations of the scalar variables might be perceived only after the arrival of the baroclinic signal. In this way the near inertial velocity oscillations would appear to lead pycnocline oscillations by x/c_2 . In view of the problems earlier discussed with regard to observing inertial motions in the mid-latitude ocean, it seems likely that only in a nontidal basin such as a large lake, would there be any real chance of definitively observing these effects.

3.4.1c The importance of stratification

The existence of observable near inertial velocities in the coastal

model can be shown to be dependent upon the existence of the stratifi-
cation. The solution for a homogeneous water column is given by

$$\zeta = \frac{-F_0}{\sqrt{gh}} \, J_0(f \sqrt{t^2 - x^2/c^2}) \mu(t - x/c)$$

$$v = \frac{fF_0}{h} \, J_0(ft) * \left(J_0(f \sqrt{t^2 - x^2/c^2}) \, \mu(t - x/c) \right) - \frac{F_0 \sin(ft)}{h} \qquad (3.20)$$

$$u = -\frac{1}{f} \frac{dv}{dt}$$

As discussed earlier, the rapid propagation of the surface wave assures
that the presence of the wall is felt within a few percent of an inertial
period. Even at mid-shelf locations $J_0(ft)*J_0(f\sqrt{t^2-x^2/c_1^2})$ approaches
$\sin(ft)/f$ within a few hours so that the coastal boundary influence
annihilates the inertial oscillation before such motion could complete
even a sizeable fraction of a full cycle.

The common observation that coastal near-inertial oscillations are
found exclusively in conjunction with strong stratification is now seen
in a new light. Rather than merely shielding such motions from the
effect of bottom friction, the presence of stratification is of funda-
mental importance to the occurrence of these oscillations which are not
realizeable near coastal boundaries under homogeneous conditions. These
findings do not in any way indicate that the role of stratification in

limiting frictional dissipation is irrelevant. Once such motions are kinematically allowable, the efficiency with which they may be damped out becomes an important question.

3.4.1d Interference phenomena and offshore amplification

As alluded to earlier, the manner in which the barotropic and baro-clinic fields combine may be complex. The complexity arises from the fact that both signals are reasonably complicated functions of both time and space. From a simplified point of view, for mid-shelf locations, the barotropic signal has achieved its asymptotic form of $\sin(ft)$ by the time the internal signal reaches the area. This baroclinic signal which will ultimately cancel existing motion, arrives with a frequency higher than the motion it is "destined" to destructively combine with. For the sake of demonstration assume (incorrectly) that the baroclinic signal is represented by $\sin(f\sqrt{t^2 - x^2/c_2^2})$. Substitution of $t = t_0 + t_i$ ($t_0 = x/c_2$, or the arrival time) leads to

$$\sin(f\sqrt{1+2x/c_2 t_i})t_i \qquad (3.21)$$

where t_i is time after arrival, and the expression in parenthesis is the time and space dependent "frequency". Clearly for large x/t_i the frequency may be many times the inertial value to which it asymptotes as x/t_i approaches 0. The subtraction of two sinusoids of widely disparate fre-

quency can initially lead to very complex time histories. As time goes on and the frequency difference lessens, a beat phenomenon may commence. This situation could, for a time, as much as double existent ampitudes rather than decrease them. Since the frequency difference is a monotonically decreasing function of time, the envelope of the beat continually lengthens and its amplitude steadily decreases. That is, this beat is not periodic. After the original amplification the signal steadily (although not necessarily rapidly) decays. As equation (3.19) indicates, this interference phenomenon is very dependent upon the ratio x/c_2. Very close to shore the frequency disparities would be slight and the two signals would cancel efficiently. As x/c_2 increases the phenomena would exist for increasing periods of time.

The implications of these ideas are somewhat startling. One cannot necessarily expect the largest inertial oscillation to occur immediately after a transient wind stress event. Depending upon distance from shore it would occur some time after the arrival of the baroclinic wave. This phenomenon may be a partial explanation of the difficulty commonly experienced when attempting to correlate wind events and inertial period velocity observations in coastal environments. The interference pattern may have no clear relationship to wind forcing, and would contribute to the general intermittency of the response.

Figure 3.9 shows the calculated upper and lower layer longshore velocity time series at distances of $2R_2$ (6 km) and $4R_2$ (12 km) from shore. Note that except for a phase difference of 180°, the upper and lower layer signals are virtually identical. It is also shown that the
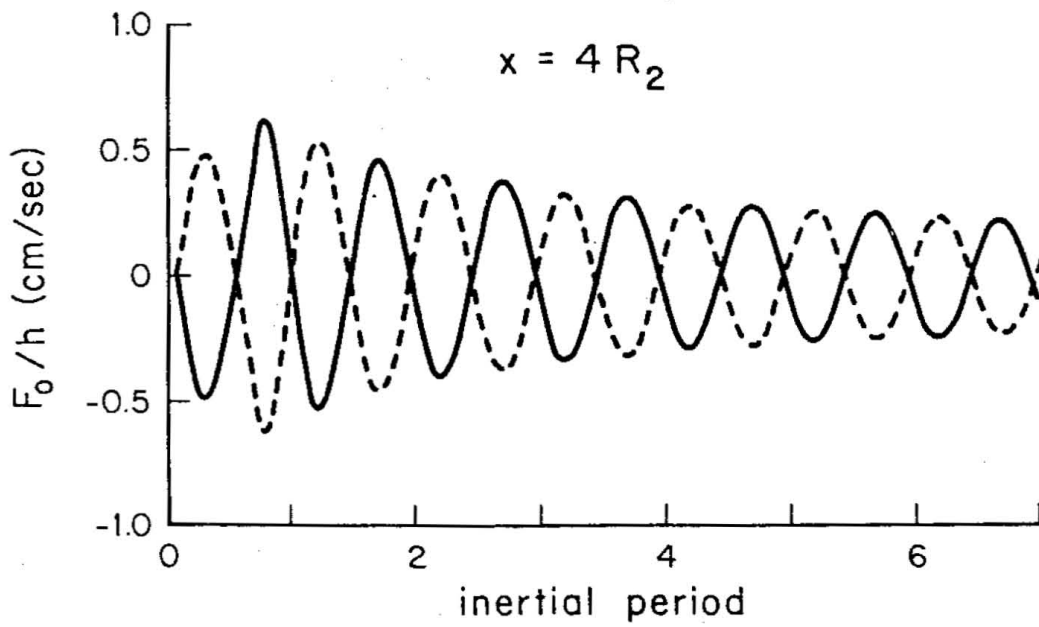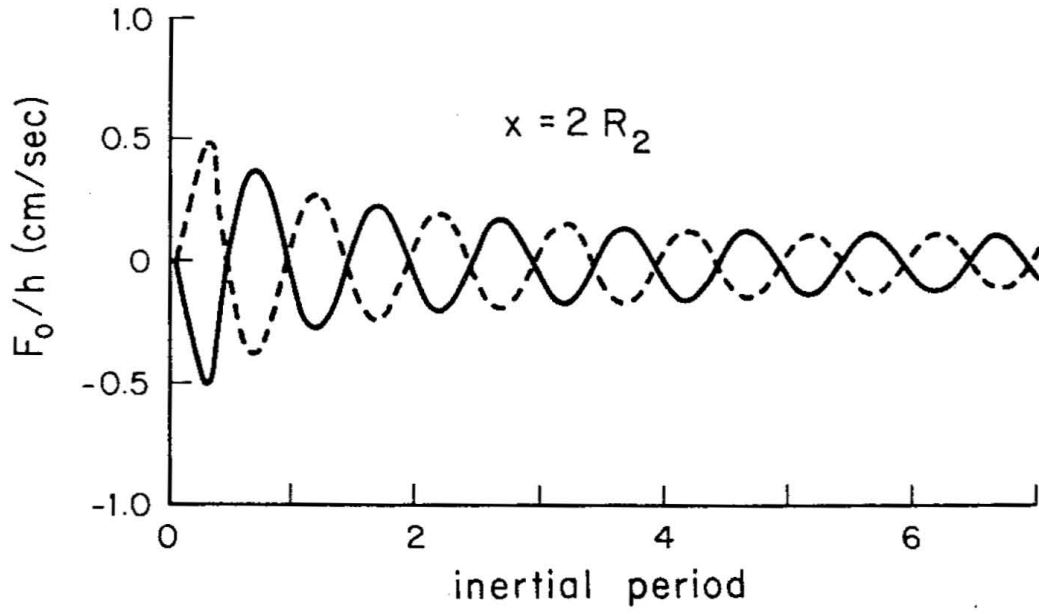
Figure 3.9 Current response to delta-function forcing.
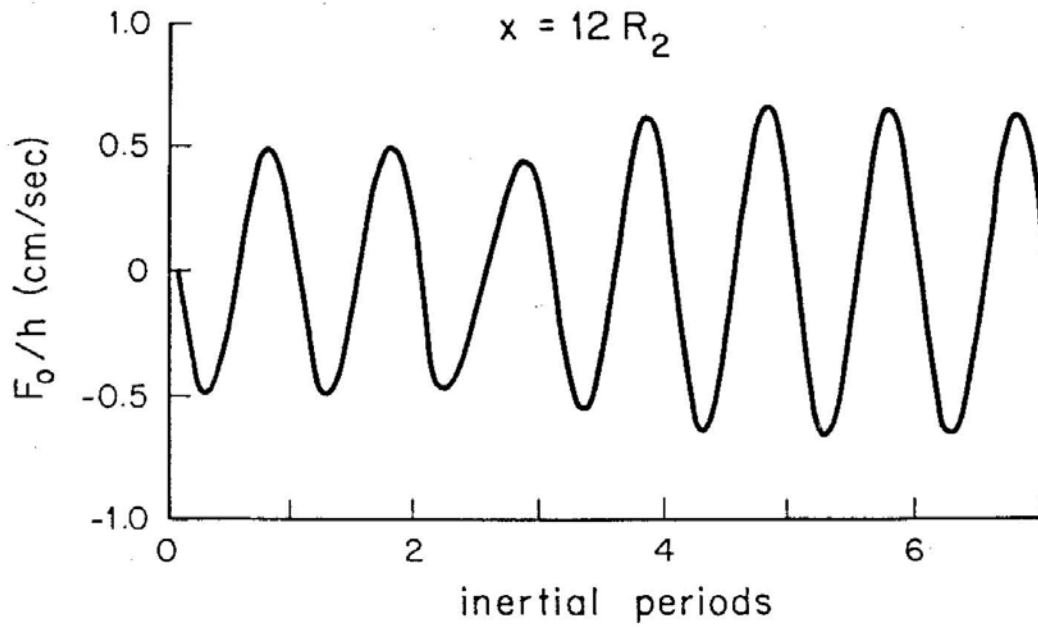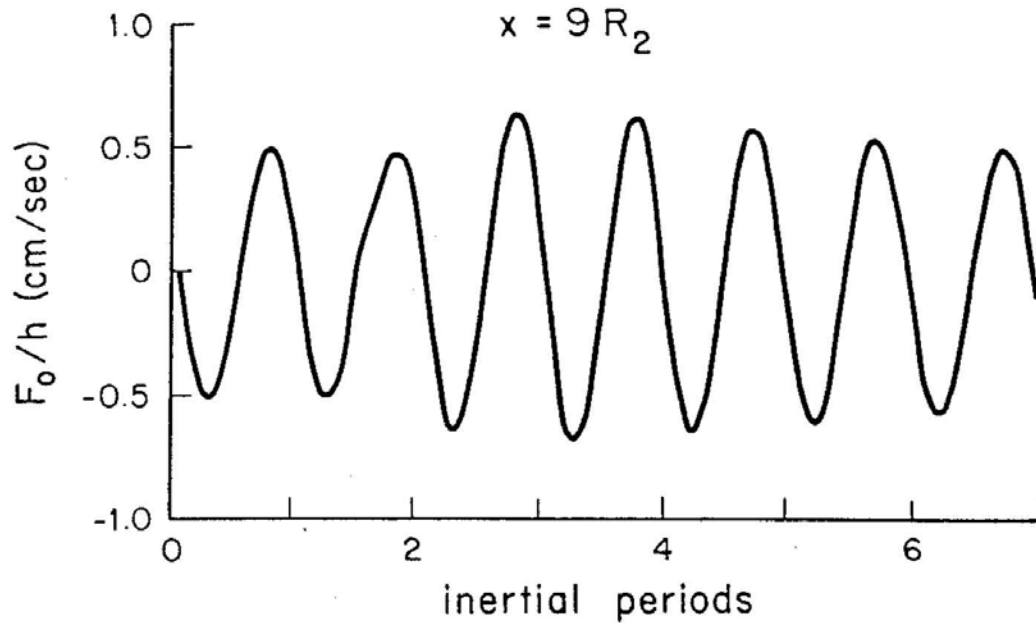
Figure 3.10 Upper layer velocities showing amplification

km
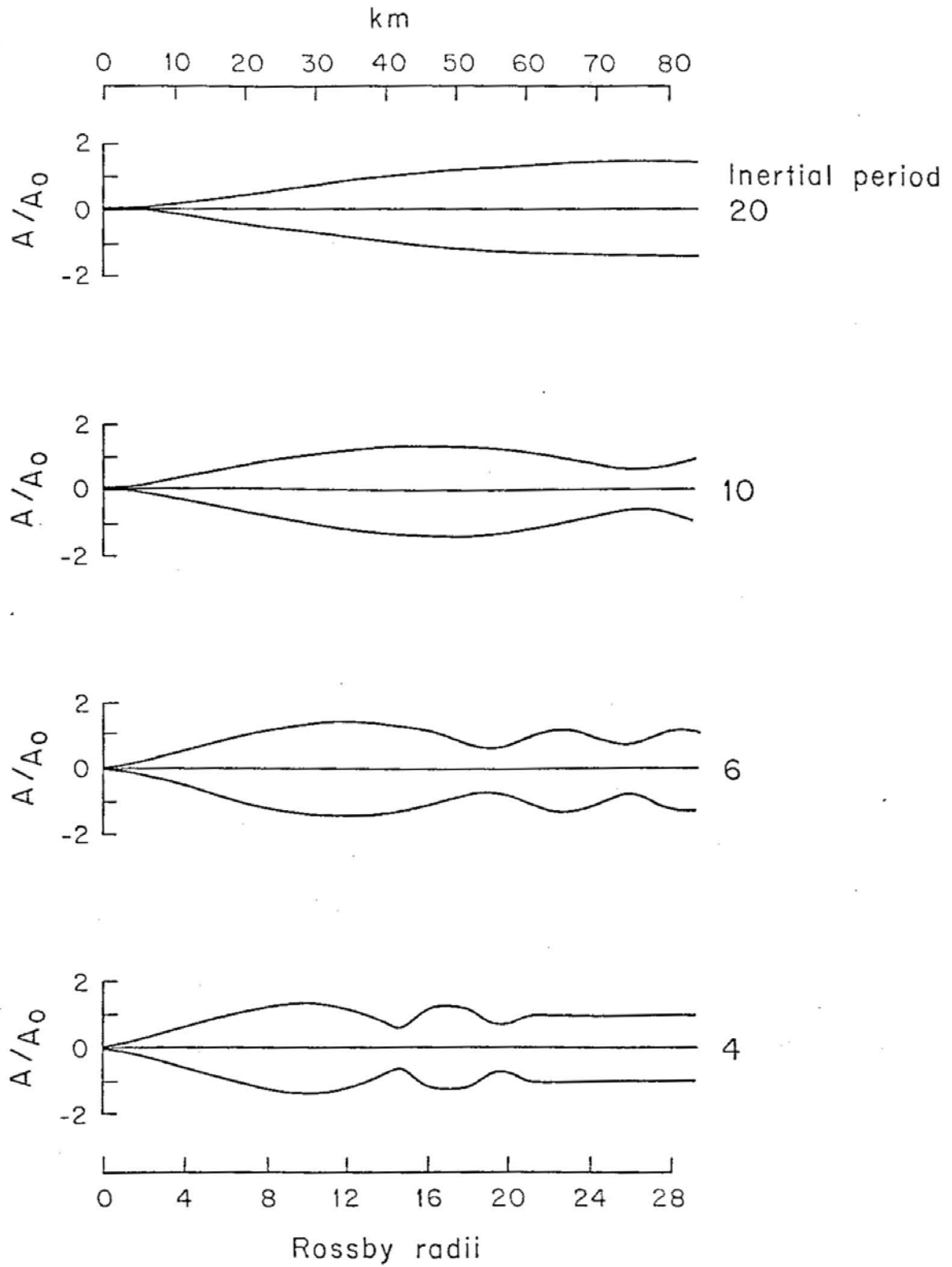
Figure 3.11 "Inertial envelope" as a function of position
and time

signal at 12 km has roughly twice the amplitude of that at 6 km, and decay is slower at the more seaward position. Apparently within the CBL the previously mentioned beat phenomenon is unimportant. Figure 3.10 shows plots of upper layer velocity at distances of $9R_2$ and $12R_2$ from shore. At these positions the amplificaton is already clearly evident.

It is interesting to determine in at least a crude way the extent of the amplification effects as a function of space and time. Figure 3.11 illustrates the maximum and minimum velocities over various inertial cycles as a function of distance from the coast. As an indication of the amplitude envelope, any extremum outside ± 1.0 shows amplification relative to conditions before the arrival of the interfacial disturbance. It may be noted that there are a series of quasi-nodes which propagate seaward. Outside the CBL there is only very gradual decay in the absence of friction and seaward of $12R_1$ amplification is still observed even after 20 inertial cycles. Clearly at these distances the shoreline is no deterrent to inertial motion.

3.4.2 Offshore wind forcing of finite duration

It is of interest to briefly consider wind events of finite duration, the effects of which are somewhat more directly interpretable and com-parable with observations. Consider a "top hat" wind function where the stress commences abruptly at $t = 0$ and remains constant until $t = \alpha$, at which point it ceases. The Laplace transform of a pulse of magnitude

F_0 is given by

$$\frac{F_0(1 - e^{-\alpha P})}{P}$$

where α represents the width or duration of the wind stress impulse. Equation (3.13) may subsequently be used to determine the parameters F_1 and F_2. For the case of an offshore wind and $(\lambda_1 - \lambda_2)$ once again approximately equal to 2, they are

$$F_1 = \frac{F_0 c_1}{2h_1} \frac{1-e^{-\alpha P}}{P^3 k}$$

and

$$F_2 = \frac{-F_0 c_2}{2h_1} \frac{1-e^{-\alpha P}}{P^3 k}$$

Using these relations in equations (3.11) leads directly to

$$\zeta_1 = \frac{-F_0}{2gh_1} \left[c_1 \left(\int_0^t J_0\left(f\sqrt{T^2-x^2/c_1^2}\right) \mu\ (T-x/c_1)\ dT \right. \right.$$

$$\left. - \int_0^t J_0\left(f\sqrt{(T-\alpha)^2-x^2/c_1^2}\right)\ \mu\ (T-\alpha-x/c_1)\ dT \right) \qquad (3.22)$$

$$+ c_2 \left(\int_0^t J_0\left(f\sqrt{T^2-x^2/c_2^2}\right) \mu(T-x/c_2)\ dT \right.$$

$$- \int_0^t J_0\left(f\sqrt{(T-\alpha)^2-x^2/c_2^2}\right)\mu(T-\alpha-x/c_2)\ dT\ \Bigg)\Bigg]$$

<div align="right">(3.23)</div>

$$\zeta_2 = \frac{F_0}{2gh_1}\Bigg[-c_1\left(\int_0^t J_0\left(f\sqrt{T^2-x^2/c_1^2}\right)\mu(T-x/c_1)\ dT\right.$$

$$-\int_0^t J_0\left(f\sqrt{(T-\alpha)^2-x^2/c_1^2}\right)\mu(T-\alpha-x/c_1)\ dT\Bigg)$$

$$+\left(\frac{2}{\varepsilon}-1\right)c_2\left(\int_0^t J_0\left(f\sqrt{T^2-x^2/c_2^2}\right)\mu(T-x/c_2)\ dT\right.$$

$$-\int_0^t J_0\left(f\sqrt{(T-\alpha)^2-x^2/c_2^2}\right)\mu(T-\alpha-x/c_2)\ dT\Bigg)\Bigg]$$

where ζ_1 and ζ_2 once again represent the free surface and interface deformations respectively.

The solutions given above naturally separate into contributions associated with the onset and cessation of the wind stress, each of which has a barotropic and a baroclinic component. As α approaches infinity, which corresponds to an unceasing suddenly imposed wind, the terms involving $(T-\alpha)$ are zero and only those parts of the solution due to the commencement and persistence of the wind remain.

Following a procedure exactly analogous to that employed in the case of the delta function wind forcing, the solution for the upper and lower layer velocities are found to be:

$$u_1 = \frac{-F_0}{2h_1} \left[J_0(ft) * \left(J_0(f\sqrt{t^2-x^2/c_1^2})\, \mu(t-x/c_1) \right) \right.$$

$$- \left(J_0\left(f(t-\alpha)\mu(t-\alpha) \right) * \left(J_0\left(f\sqrt{t^2-x^2/c_1^2} \right) \mu(t-x/c_1) \right) \right.$$

$$+ J_0(ft) * \left(J_0\left(f\sqrt{t^2-x^2/c_2^2} \right) \mu(t-x/c_2) \right) \tag{3.24}$$

$$\left. - \left(J_0\left(f(t-\alpha) \right) \mu(t-\alpha) \right) * \left(J_0\left(f\sqrt{t^2-x^2/c_2^2} \right) \mu(t-x/c_2) \right) \right]$$

$$+ \frac{F_0}{fh_1} \left(\sin(ft) - \sin\left(f(t-\alpha) \right) \quad \mu(t-\alpha) \right)$$

$$v_1 = -f \int_0^t u_1 \, dT$$

$$u_2 = \frac{-F_0}{2h_1} \left[J_0(ft) * \left(J_0\left(f\sqrt{t^2-x^2/c_1^2} \right) \mu(t-x/c_1) \right) \right.$$

$$\left. - \left(J_0\left(f(t-\alpha) \right) \mu(t-\alpha) \right) * \left(J_0\left(f\sqrt{t^2-x^2/c_1^2} \right) \mu(t-x/c_1) \right) \right)$$

$$- J_0(ft) * \left(J_0\left(f\sqrt{t^2 - x^2/c_2{}^2} \right) \mu(t-x/c_2) \right) \tag{3.25}$$

$$+ \left(J_0\left(f(t-\alpha) \mu(t-\alpha) \right) * \left(J_0\left(f\sqrt{t^2 - x^2/c_2{}^2} \right) \mu(t-x/c_2) \right) \right]$$

$$v_2 = - f \int_0^t u_2 \; dT$$

Once again several interesting aspects of the behavior of these solutions may be deduced prior to performing the convolution integrals. Note that the last term in equation (3.24) corresponds to the directly wind induced (non-coastal) "pure" inertial response of the upper layer, while the remaining terms (involving the convolutions) represent the modifications to this response due to the coastal influence. As mentioned previously these sinusoidal wind forced terms would represent the entire solution in an unbounded fluid. Clearly the first sinusoidal term is associated with the onset of wind forcing while the second is due to its relaxation. It is easily appreciated that the duration of the wind stress event (α) is critical in determining the manner in which these two contributions combine. If αf is an integral multiple of 2π, the two contributions cancel so that for $t > \alpha$, the "pure" inertial response vanishes and the only possible surviving motion is that associated with the baroclinic and barotropic coastal responses. In the case where

$$\alpha = (2P + 1)\pi \qquad\qquad P = 0,1,2\ldots$$

the two sinusoidal contributions add constructively and maximize the directly wind induced inertial response. The role of the wind stress duration in determining the phase relationship between these wavelike contributions in an unbounded fluid was noted by Gonella (1971). He reasoned that this relationship could explain the diversity in the levels of inertial activity observed following storms of comparable intensities. Pollard and Millard (1970) noted in their numerical model that wind events of up to one-half inertial period were highly efficient in the generation of transient motion while those acting for nearly a full inertial cycle induced little response. This behavior, which Pollard and Millard rationalized it in terms of energetics, can be interestingly modified by the presence of a coast.

Wind stress duration plays an analogous, but more complex, role in the interactions between the various components of the coastal response detailed in equations (3.24) and (3.25). While it is true that wind onset and relaxation effects will ultimately independently balance regardless of α, the actual sequence of events leading to the equilibrium state can be dramatically affected by the wind stress duration.

It is easily demonstrated that

$$(J_0(f(t-\alpha)\ \mu(t-\alpha)) \star J_0(ft) = \frac{\sin(f(t-\alpha))}{f} \qquad (3.26)$$

making it apparent from equations (3.24) and (3.25), that at the shore-line (x=0) velocities in both layers vanish as demanded by the coastal

constraint. In addition it is seen that for $t > \alpha$ and $t^2 >> x^2/c_2^2$, veloc-ities approach zero everywhere; a consequence of seaward radiation.

The sequence of events during a storm and its aftermath is dependent not only upon storm duration but upon offshore position as well. This fact may be demonstrated by examining the interactions between the various parts of the solution in two distinct parametric domains. The first regime, that of $\alpha >> x/c_2$, represents the situation where the wind duration is much longer than the time it would take a baroclinic signal to arrive from the coast. In this instance the cancellation processes discussed earlier would be well under way or completed before the wind's cessation so that the phasing determined by α would be largely irrele-vant. Near shore the main interplay would be between associated baro-tropic and baroclinic disturbances with little interaction between those motions arising due to the sudden rise and equally sudden demise of the wind. The situation further from shore could be more chaotic. The arrival of a second set of disturbances in a region already subject to vigorous beating would result in an even more complicated "double beat" pattern and add to the intermittency of an already confusing signal

In the $\alpha << x/c_2$ domain, the possible sequences can be somewhat more involved. As reference to the lower layer velocity relation (equation (3.25)) reveals, the barotropic signal associated with the end of a wind stress impulse may well arrive in a given location before the baroclinic signal due to the wind's onset. Depending upon α the two barotropic signals (which very rapidly approach their asymptotic form) may effi-ciently cancel one another resulting in the absence of motion in the

lower layer between $t = \alpha$ and the arrival of the baroclinic waves. When the first of the baroclinic waves arrives it re-establishes lower layer velocities which are subsequently modified and eventually reduced by the baroclinic relaxation signal. A similar though slightly more involved sequence of events occurs in the upper layer. The net result is that a single wind episode may seem to give rise to two separate inertial events within the water column. This type of analytical behavior may be of some relevance in understanding observations of "extra" events such as those reported by Kundu (1976) and Flagg (1977) which have no obvious meteorological origins. In any case, it is clear that in coastal reg-ions one might well encounter locally generated near inertial motions which exhibit strong spatial variability, are highly intermittent, and not simply correlated with meteorological records.

Most nearshore observations would fall somewhere in a transition zone between the two somewhat extreme domains discussed above. Figure 3.12 illustrates the upper layer u and v velocity components, $4R_2$ from shore, in response to a one dyne wind of four hour duration. Since velocities in the two layers are antisymmetric, lower layer solutions are not presented. The magnitude of the wind stress enters the formu-lations linearly so that the oscillations due to an n dyne wind are found by simply amplifying the plotted signal by n. As expected, the response due to forcing of short duration is in qualitative agreement with that produced by the delta function wind.

Figures 3.13–3.15 depict surface layer oscillations in the coastal zone in response to a wind of 36 hour duration. Since in this case αf
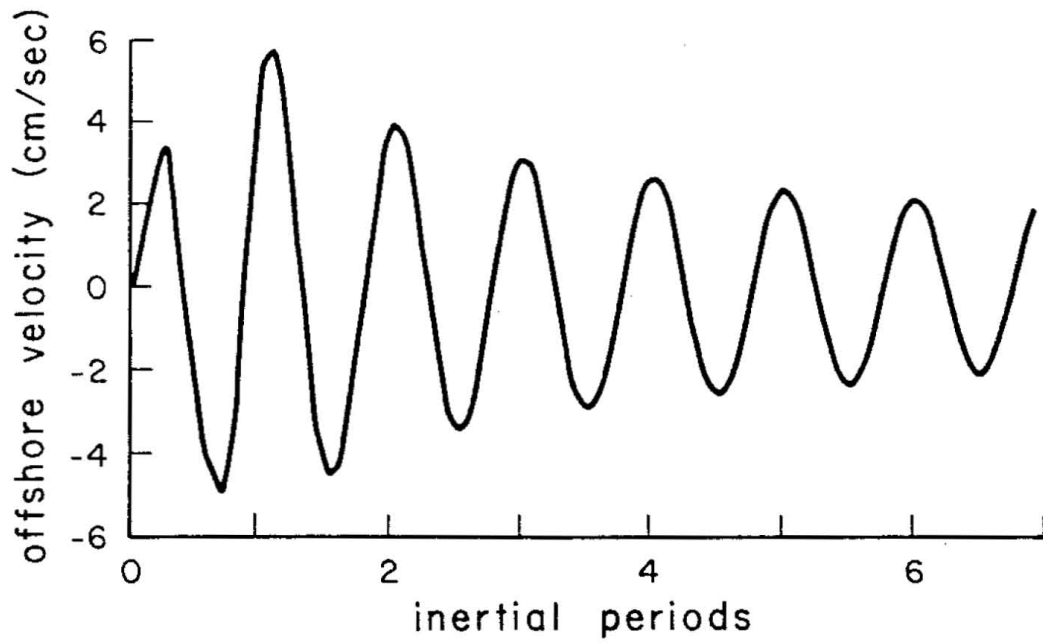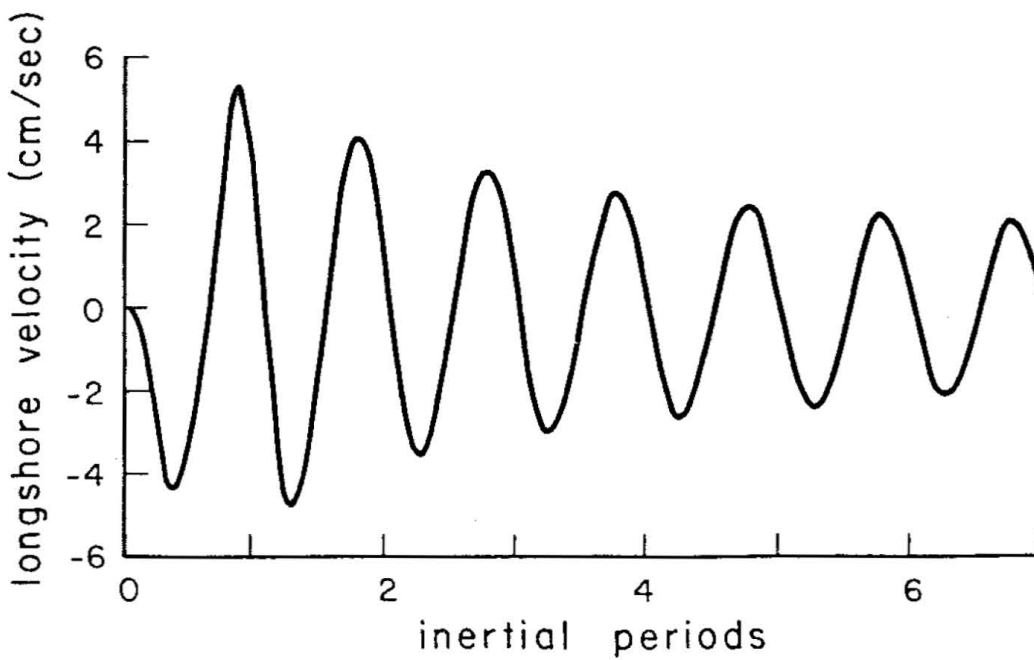
$\alpha = 4\,hrs$

$x = 4\,R_2$

Figure 3.12 Upper layer velocity response to a one dyne wind of
4 hr duration.
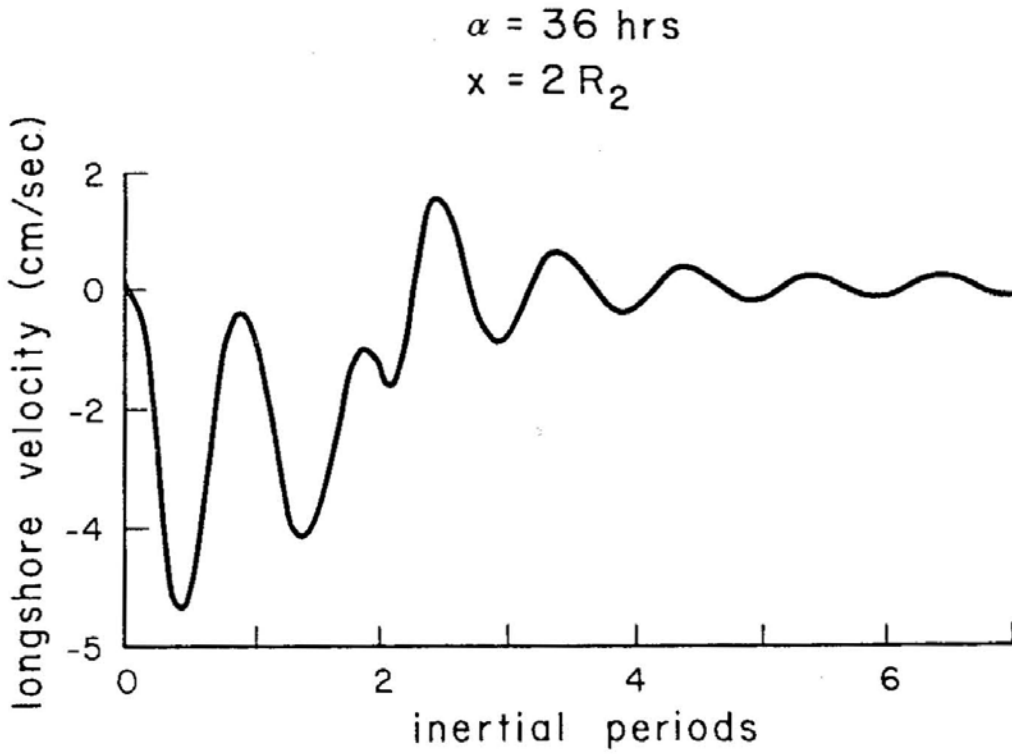
$\alpha = 36$ hrs

$x = 2 R_2$
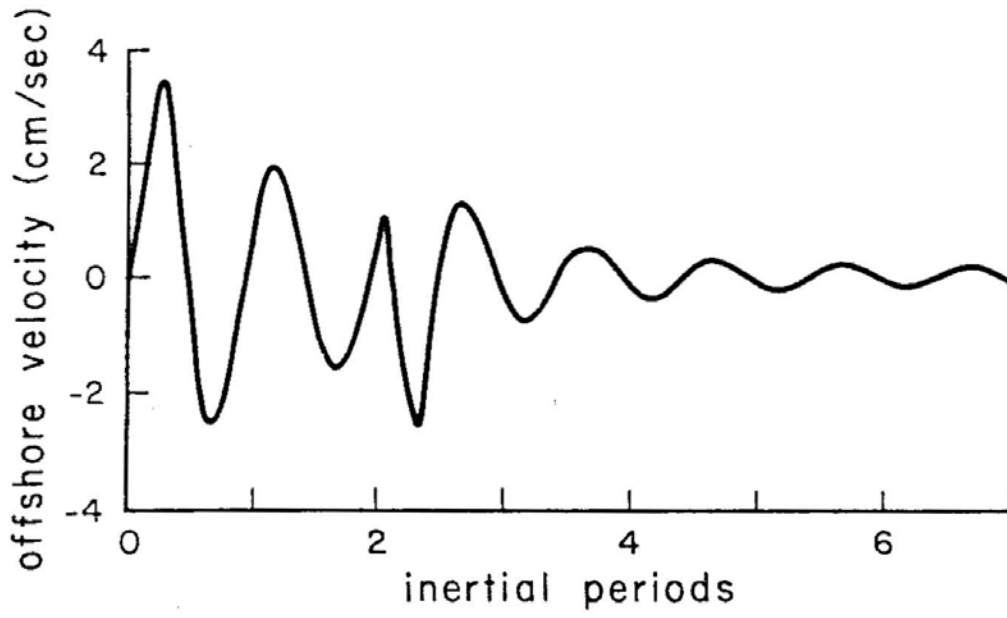
Figure 3.13 Current response to 36 hr wind at 6 km.
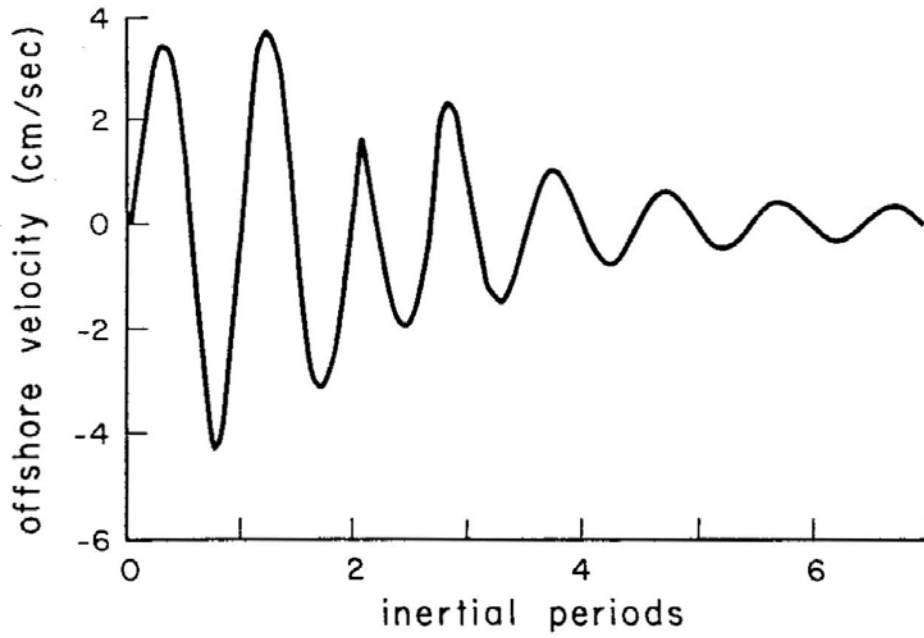
α = 36 hrs

x = 4 R$_2$
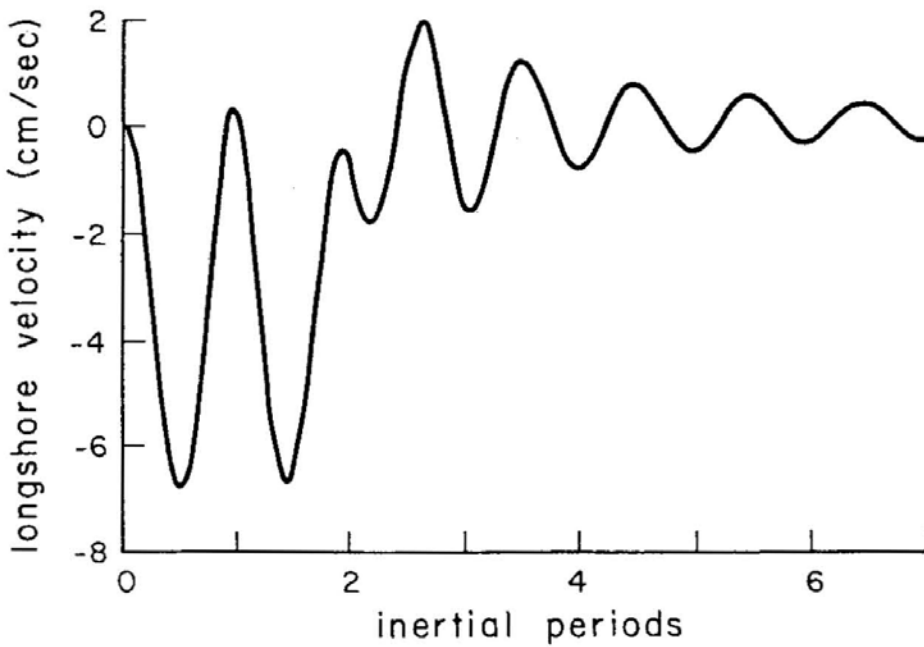
Figure 3.14 Current response to 36 hr wind 12 km from shore.
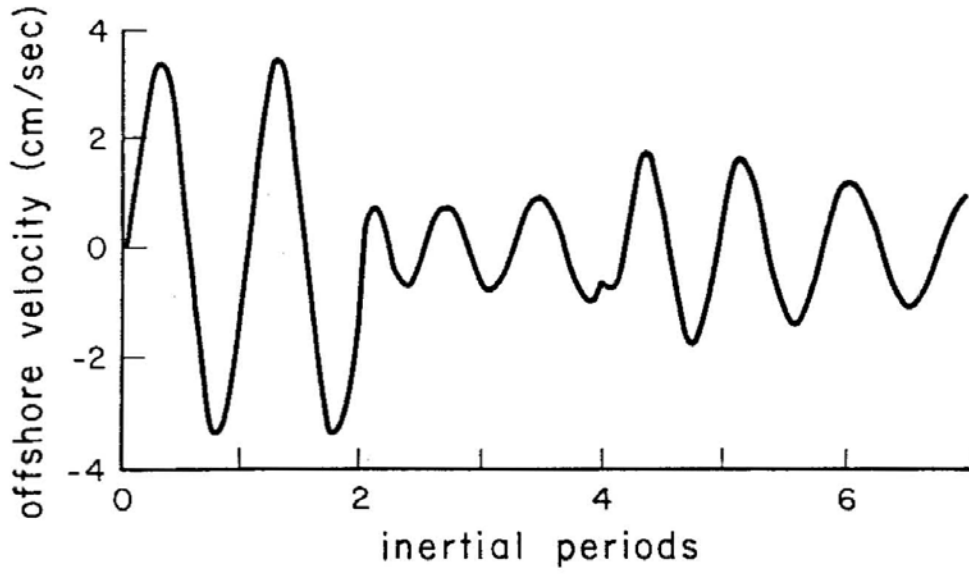
α = 36 hrs

x = 12 R_2
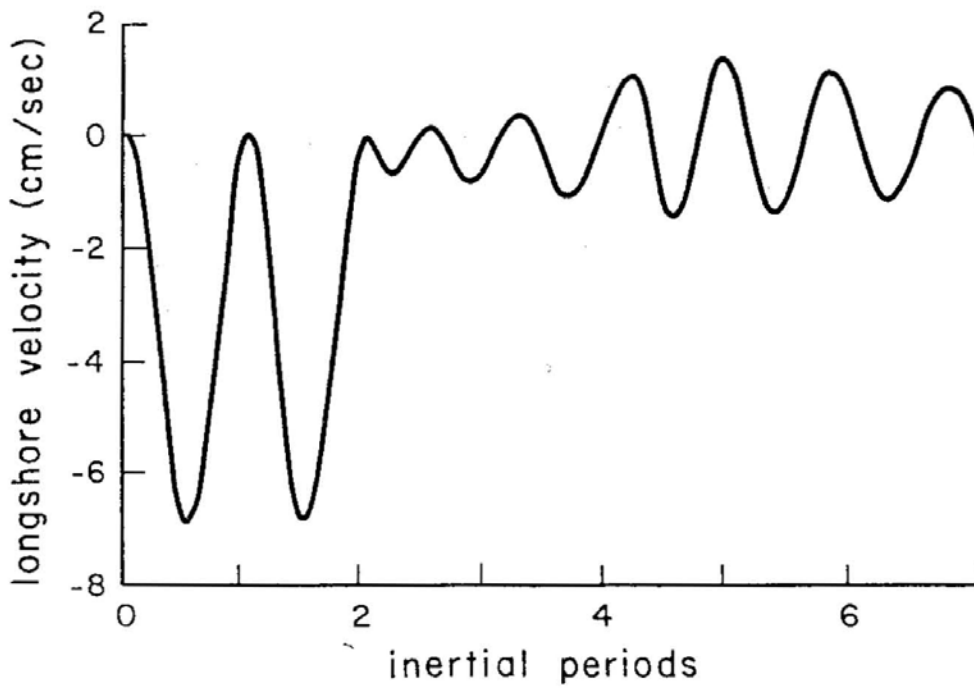
Figure 3.15 Current response to 36 hr wind, 36 km from shore.

is an integral multiple of 2π, as explained above, only the baroclinic coastal response remains for $t > \alpha$. It is of interest to note that the more seaward positions show greater tendency toward a secondary event after the cessation of the wind. This tendency is clearly illustrated by figure 3.15 which displays the analytical velocities $12R_2$ from shore. While in the present context only the wavelike signal is of direct interest, it is notable that during the wind stress episode, the alongshore upper and lower layer velocities have equal and opposite steady components.

Figures 3.16 and 3.17 show model longshore and offshore velocity components of the surface layer in response to a unit wind stress with $\alpha = 27$ hrs. This duration corresponds closely to that observed during the major storm event in the May '77 data. The overall qualitative correspondence between these two diagrams and the demodulated amplitude presented in figure 3.1 is not good. The primary discrepancy stems from the prediction that, since $\alpha f = 3/2 \pi$, a pronounced ringing or persistence of inertial energy is expected after the cessation of the wind. The probable explanation of the very sharp decrease in observed inertial amplitude is that the complete homgenization of the nearshore water column shortly after the storm (see section 4.2) precludes the existence of inertial currents near the coastal boundary as discussed in section 3.4.1c. In other words, the layered model ceases to be appropriate within hours of the cessation of the wind stress due to a combination of mixing and advective effects which render the CBL homogeneous. If one therefore limits attention to the period during the meteorological event
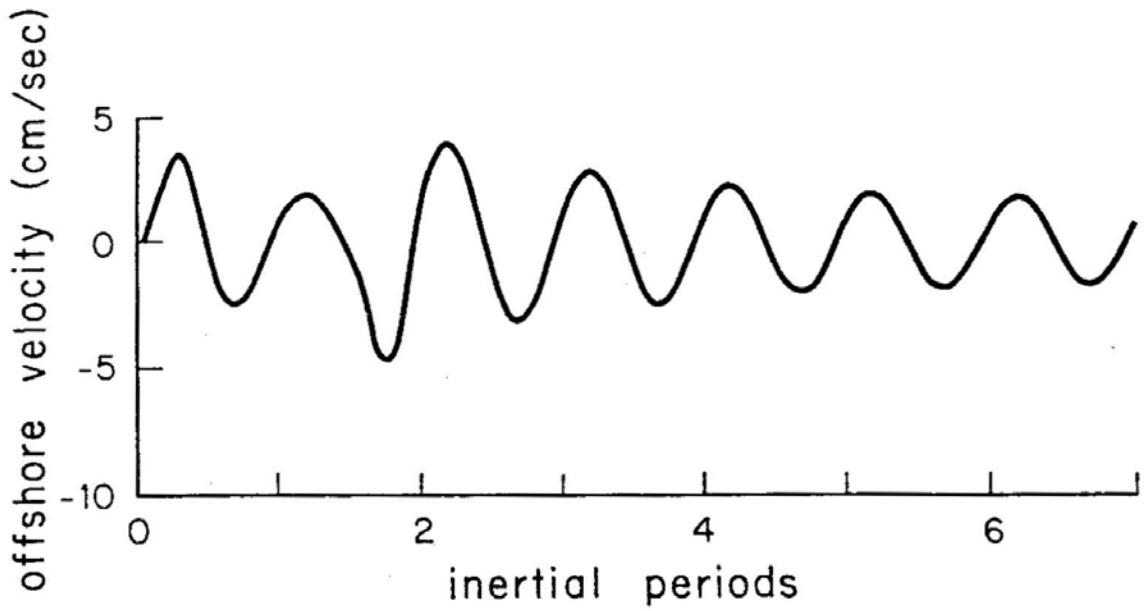
α = 27 hrs

x = 2 R$_2$
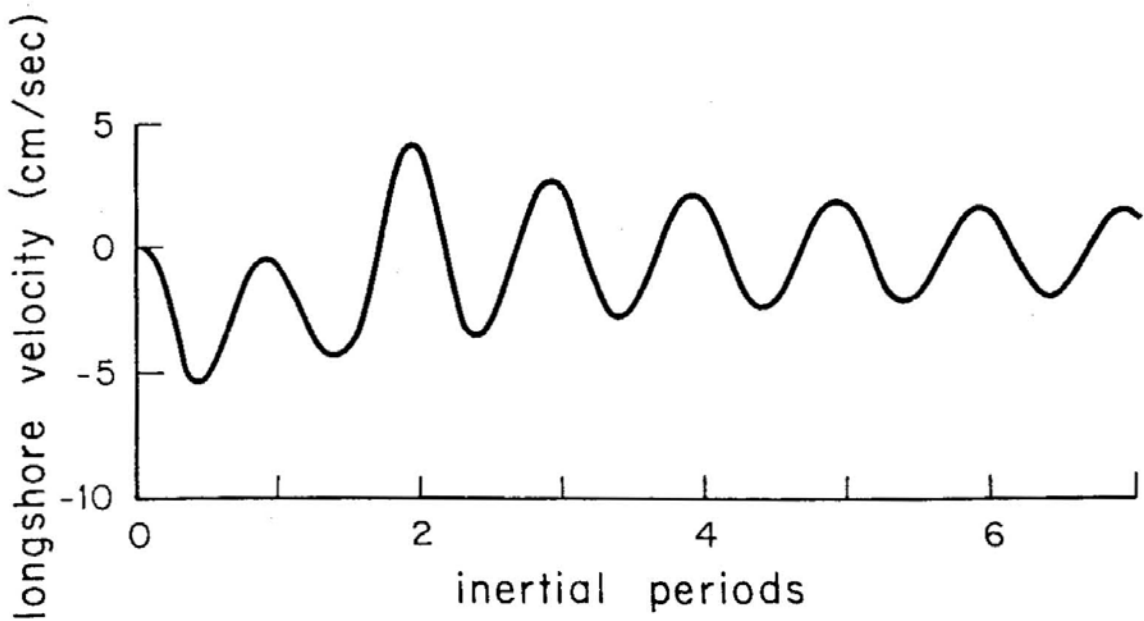
Figure 3.16 Current response to 27 hr wind which corresponds closely to the duration of the May '77 storm. (6 km)
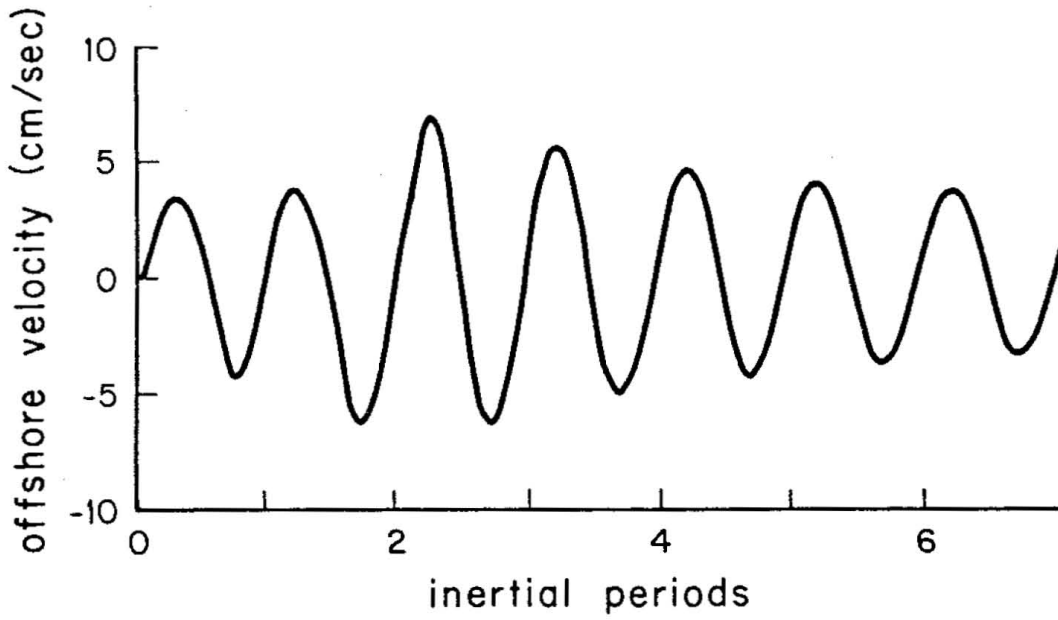
α = 27 hrs

x = 4 R$_2$
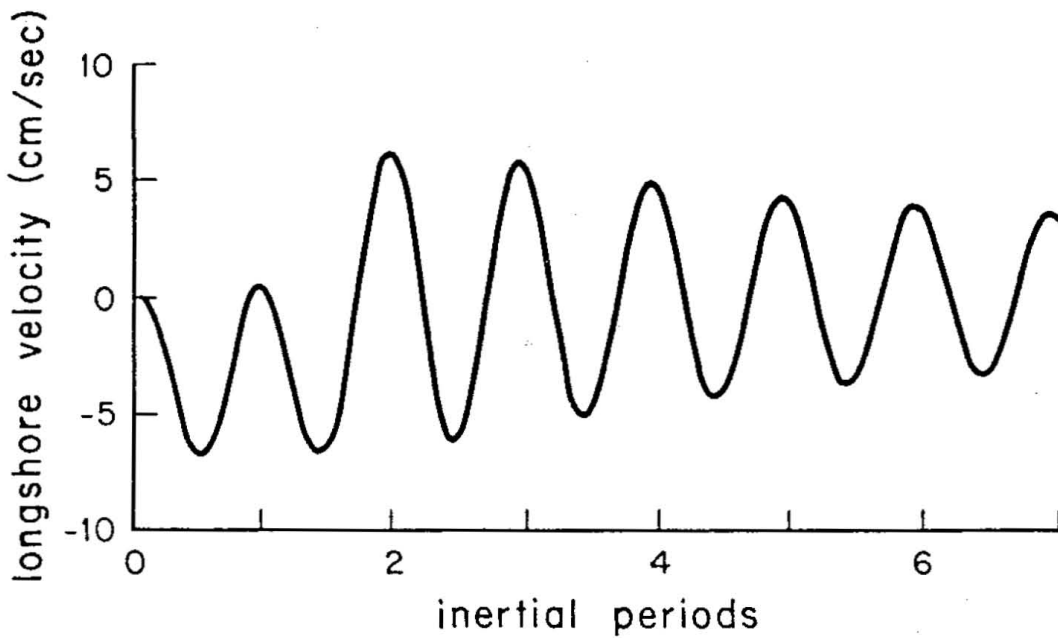
Figure 3.17   Current response to a 27 hr wind at 12 km from shore.

itself, the general agreement between model and observation is satis-
factory. The signal strength increases offshore by roughly a factor of
two and the 180° phase relationship between top and bottom layers is
accurately predicted. In addition, the frictionless model predicts
currents to within approximately 50 percent.

3.4.5 Forcing by longshore winds

Thus far only the effects of offshore winds have been explicitly
considered in the discussion of coastal generation of near-inertial
oscillations. This approach has been followed both because the storm
event responsible for the clearcut inertial episode in the May '77 data
was of this type and because the calculations involved are slightly
simpler (involving one less integration). In addition, as is demon-
strated in an appendix to this chapter, the transient wavelike response
of interest is identical for cross-shore and longshore forcing except
for a $\pi/2$ phase shift. The essential difference between the two types
of forcing is the occurrence of a non-wavelike alongshore flow component
which grows linearly in time during the wind impulse and remains constant
thereafter. This steady component is a shore trapped feature commonly
referred to as a coastal jet (cf. Csanady, 1977a). The important point
is that in terms of the wavelike response of the water column, the
earlier discussions are generally valid regardless of wind stress
direction.

3.5 Summary

Current meter records of the May '77 COBOLT experiment reveal the presence of inertial oscillations within the coastal boundary layer. Complex empirical orthogonal mode analysis shows that more than 90 percent of the inertial energy is characterized by a 180° phase difference between upper and lower current meter pairs. A significant (0.80 level) offshore increase in spectral energy is noted over the 6 km separating the two mooring platforms, while no change was noted for corresponding salinity spectra.

Cross-spectral analysis shows that, for inertial frequency signals of both salinity and clockwise velocity components, the offshore mooring lags the mooring closer to shore. This observation suggests that inertial waves were propagating seaward. The method of complex demodulation was used to examine temporal variations of inertial current amplitude. Comparison with wind-stress records suggests a causal relationship between the inertial signal and meteorological forcing.

The response of a two-layer coastal domain to impulsive wind forcing was investigated and the behavior of the nearshore transient current field examined. The predictions of the model were found to be in substantial agreement with the observational features listed above. It was found that, in a homogeneous domain, the coastal boundary condition effectively prohibits inertial currents over the entire continental shelf region. In the presence of stratification the offshore extent of this prohibition is greatly reduced and significant inertial energy can exist within the coastal boundary layer.

The coastal effect, in the form of surface and internal waves, prop-
agates away from the shore and modifies the "pure" inertial response
which would exist in an unbounded two-layer domain. The kinematics of
this process is such that a 180° phase difference between surface and
bottom layers is characteristic not only of the internal disturbance,
but also of the combination of the surface wave and the directly wind
induced "pure" inertial response. This fact suggests that in coastal
regions one would always measure an apparent baroclinc structure to
inertial frequency currents even before the baroclinic wave has had time
to propagate out from the shoreline.

It is also suggested that outside the CBL one expects an inter-
ference or "beat" phenomenon to occur between the barotropic and
baroclinic portions of the coastal response. This means that the
maximum inertial signal at a given location would not occur until after
the arrival of the baroclinic disturbance. This mechanism may be a
relevent to the observation of bursts of inertial energy which seem
uncorrelated with meteorological forcing in coastal environments.

Chapter IV

HYDROGRAPHIC VARIABILITY IN THE CBL

4.1 Introduction

The hydrographic structure of the coastal boundary waters in the COBOLT study area is often observed to undergo rapid, and sometimes radical, alteration. During the stratified season the region is subject to frequent homogenizing events of varying intensity and spatial extent. In their most dramatic manifestations, these episodes render the nearshore water column virtually vertically homogeneous over the entire coastal boundary layer. Figure 4.1 displays single mooring temperature records at four vertical positions 3 km from shore during the August 1978 experiment. The data are graphic demonstration of the fact that the CBL may be characterized, somewhat paradoxically, as a region of nonseasonal alternation between strongly stratified and nearly homogeneous hydrographic conditions.

Three distinct processes leading to the occurrence of these homogenizing episodes might be envisioned. They are longshore advection of homogeneous "slugs" of water (of undetermined origin) into the study area; shoreward advection of surface mixed layer water via a downwelling mechanism; and mixing due to turbulence associated with energetic meteorological and/or nearshore flow events. Convective overturning can
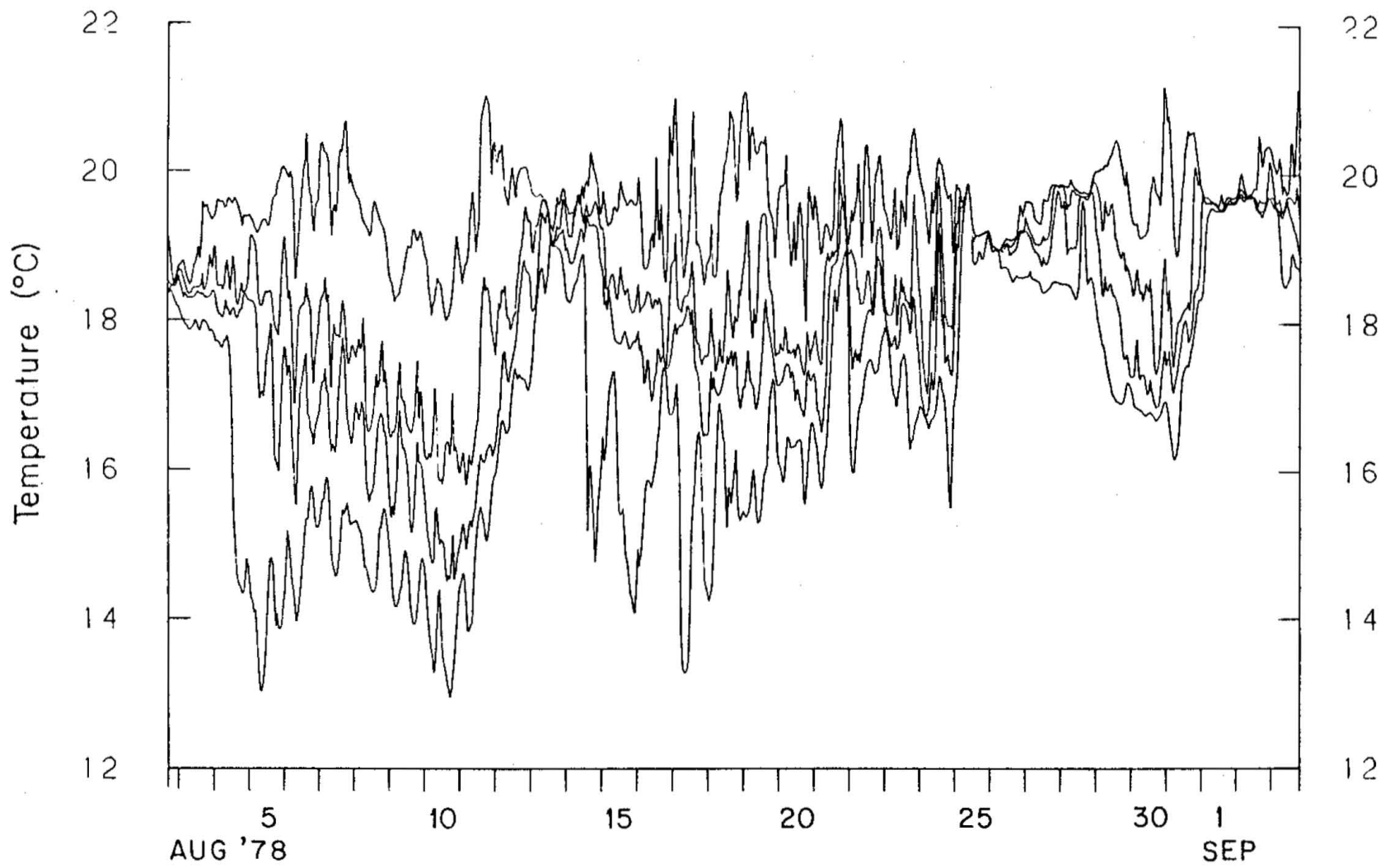
Figure 4.1 Aug '78 temperature records at 4, 8, 12 and 18 m depths, 3 km from shore.

clearly be ruled out during the spring and summer seasons and upwelling generally advects more highly stratified water into the shore zone, rather than more homogeneous water.

Of the three suggested mechanisms only the first need not be well correlated with the local wind. In addition it is not strongly constrained by the local hydrographic structure in that such effects would arise from anomalous conditions upstream of the study area. Therefore longshore advection need be appealed to only when the observed behavior falls outside the domain spanned by the local forcing and hydrographic conditions. Without some reasonable expectation of an upstream source of homogeneous water, it seems logical to assume, that while longshore advective effects may well exert a modifying influence upon the details of the observations, it is unlikely that they are of fundamental importance in understanding the origin of these phenomena.

4.2 Mixing of the nearshore water column

Figure 4.2 shows temperature time series during the May '77 experiment at nominal depths of 4, 8, 16, and 28 m at a position 9 km from shore. The trend of these data clearly reflect the general springtime warming of nearshore waters. The dashed line of slope 0.12°C/day is a linear trend of the net temperature gain of the water column averaged over the three operational moorings.

The dominant event appearing in the record is the collapse of the
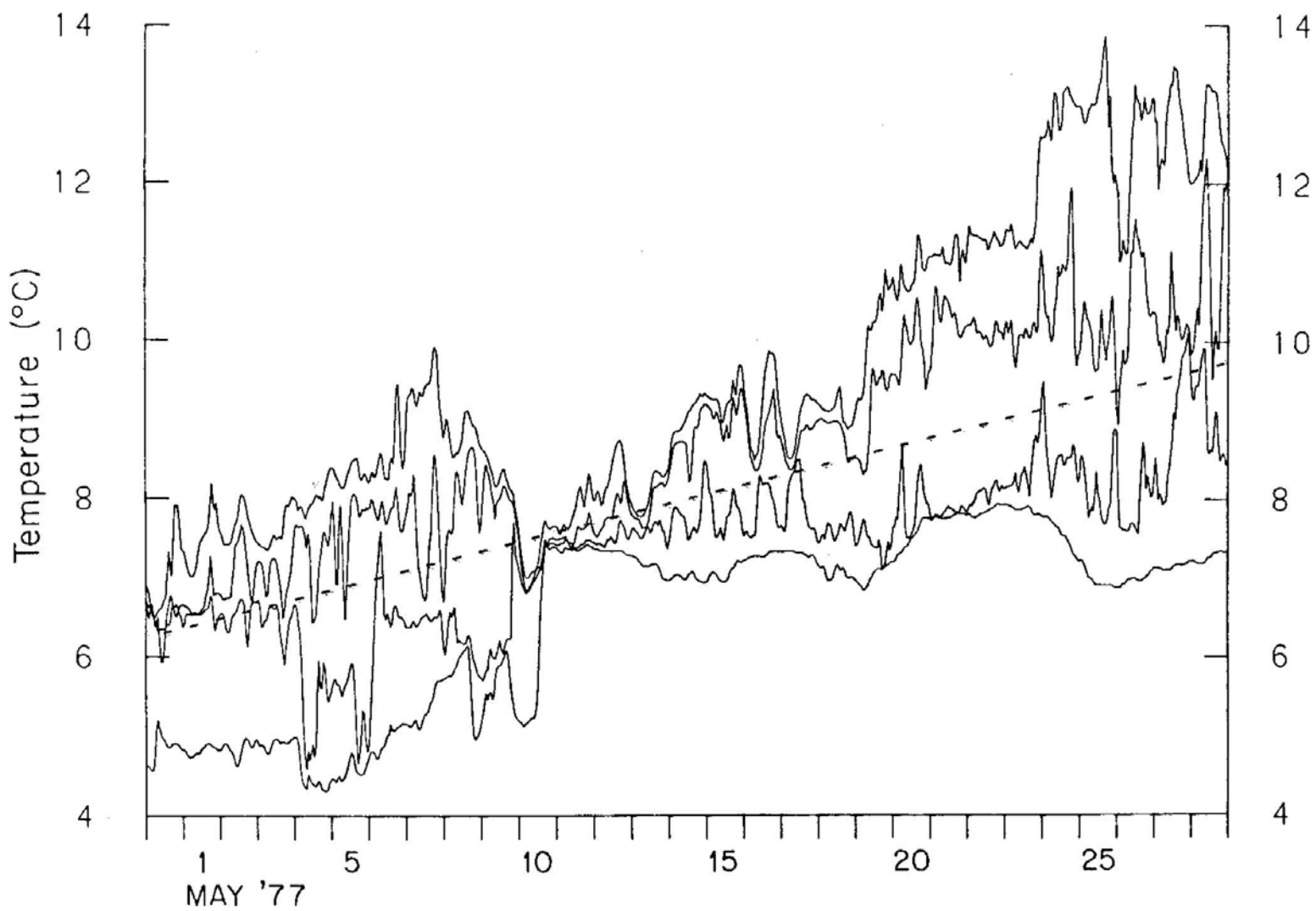
Figure 4.2   May '77 temperature records at 4, 8, 16 and 28 m depths, 9 km from shore.

stratification which occurs during May 9-11. Note that upper and lower layer temperatures converge to a value which corresponds closely to the vertical average of the stratified column. This behavior is consistent with the notion that mixing played a dominant role in this event. A significant change in the mean temperature (a net heat loss or gain) would constitute "prima facie" evidence of the dominant influence of advection; either cross-shore or longshore.

Further support for the idea that the homogenizing event depicted in figure 4.2 is primarily the result of mixing comes from consideration of the corresponding wind-stress records shown in figure 4.3. Gale force winds commenced near mid-day on the 9th of May and persisted through May 10th. Wind-stress values during this storm averaged approximately 8 dynes/cm^2 directed offshore and 1-2 dynes directed alongshore toward the northeast. Both of these wind-stress components were thus of a direction which would tend to induce an upwelling type circulation; thereby eliminating the downwelling mechanism from consideration in this episode.

The nearshore flow field responded dramatically to the arrival of this storm system. Sustained longshore currents as high as 1.5 knots were observed and vertical shears of 1-3 cm/sec/m were common throughout the water column. These conditions provide supporting evidence that the stratification reduction noted in this episode is due to turbulent mixing. Bulk Richardson numbers estimated by

$$Ri = (gh\Delta\rho/\rho) \; / \; (\Delta U)^2$$

Offshore wind stress

Longshore wind stress
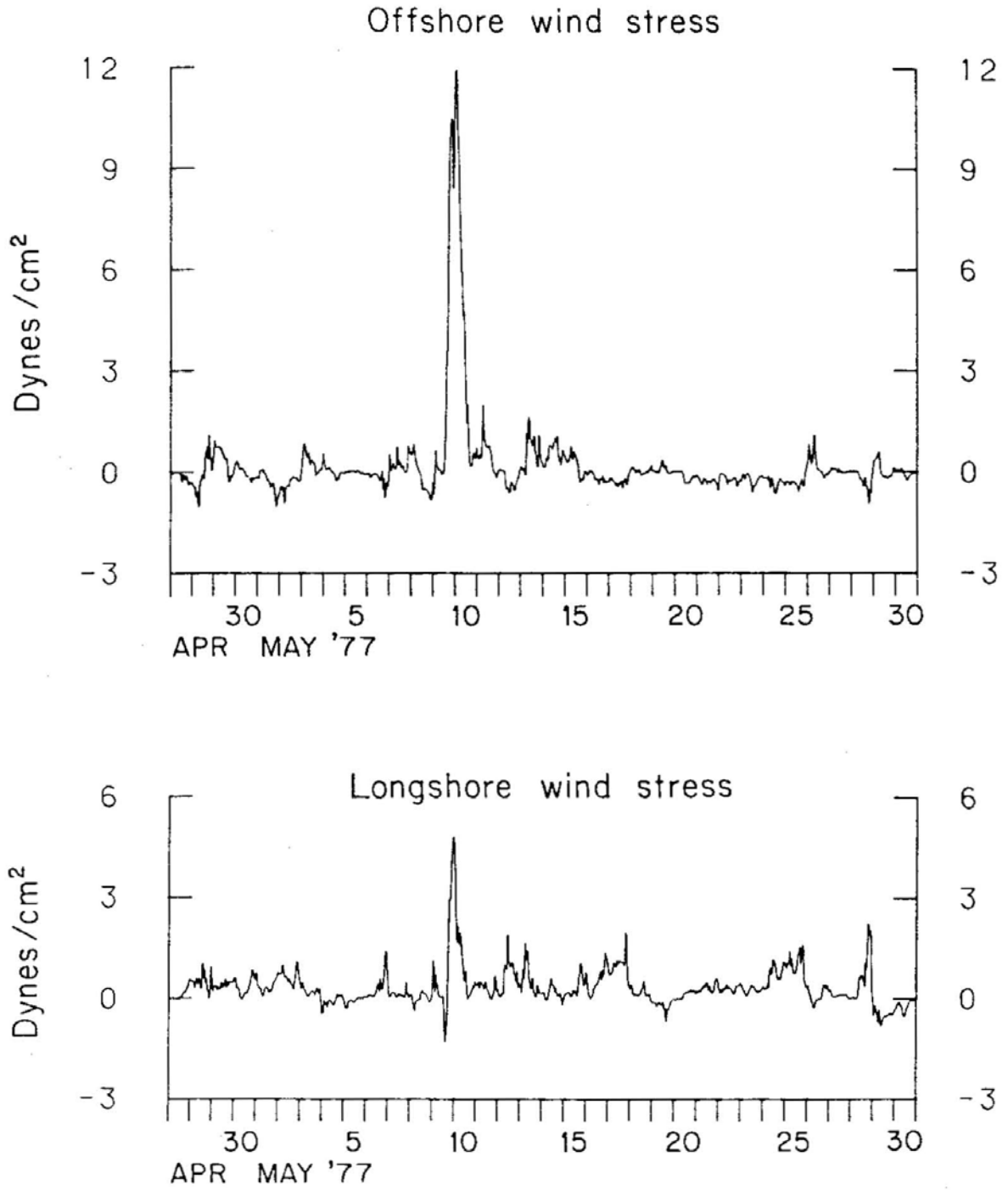
Figure 4.3 May '77 wind-stress components.

are typically ~10 before May 9. After the onset of the wind, however, this ratio drops to $\leq$ 1 throughout the water column. During May 10, typical Richardson numbers are $\leq$ 0.5 everywhere, and < 0.25 at mid-depth. May 11 is a transitional period, and by May 12 the ratio is order 10 and remains large for the duration of the experiment. This behavior is highly suggestive of mixing during the the interval May 9-11.

Further examination of figure 4.2 reveals that the temperature records of sensors at 4, 8, and 16 m depths merge within half a day of the onset of the storm. The observation that the water column homogenized from the top down suggests that wind stirring was more effective than bottom turbulence in eroding the thermocline, although as seen above, both the upper and lower water column would have been suseptible to shear instability.

As pointed out by Pollard, Rhines and Thompson (1973), the depth of a turbulent Ekman layer in a stratified fluid is governed by the non-dimensional variable $U_*/(Nf)^{1/2}$ where U_* is the so-called friction velocity given by $(\tau/\rho)^{1/2}$, N is the local bouyancy frequency, and f is the Coriolis parameter. Their model of the deepening of the wind-mixed layer predicts a deepening depth of

$$h_{max} = 1.7 \ U_*/(fN)^{1/2} \qquad (4.1)$$

which is achieved within half an inertial period of the imposition of a constant stress. Using a value of $N^2 \sim 1.2 \times 10^{-3} \ sec^{-1}$, determined from an STD survey the day before the storm, in conjunction with a U_*

of 3 cm/sec gives a deepening depth of roughly 27 m. This calculation suggests that the entire water column at the Tiana Beach feild site would mix within approximately 9 hours. This prediction is conservative in the sense that it neglects the additional thermocline erosion which would occur from below due to the growth of a bottom mixed layer in association with the large (20-30 cm/sec) near bottom velocities. Using equation 4.1, an estimate of thermocline erosion due to a bottom Ekman layer is ~10 meters. In view of these considerations it is not at all surprising that the ~30 m deep water column at the field site was observed to become virtually homogeneous under the influence of high surface and bottom stresses. What is somewhat surprising, is the time history of the homogenization process and the fact that it took roughly 36 hours, or four times the expected time period.

Closer scrutiny of figure 4.2 reveals that shortly after the successful mixing of the upper 16 m (around midnight May 9), the entire water column underwent a rapid drop in temperature. The magnitude of this temperature change increased with distance from shore and was found to be ~0.5° C at 6 km and ~1.0° C at 12 km from the coast. The temperature decrease was accompanied by a salinity increase which ranged from ~0.3 °/°° at 6 km to ~0.5 °/°° at 12 km from shore. Although this event is clearly advective in nature the details of its physical origin are less than apparent. The changes in water properties involved are entirely consistent with the effects of cross-shore advection which are expected in response to the strong offshore winds. On the other hand, it is unclear why these effects should become suddenly apparent half a

day after the initiation of the wind stress. While a time lag of this sort would not be unexpected if longshore advection were a dominant mechanism, the fact that the deepest density changes lead those in the upper and middle water column by approximately 5 hours seems inconsistent with this hypothesis in view of the much lower mean flow near bottom.

Comparison of figures 4.2 and 4.3 shows that the final homogenization, which effectively removed the vertical gradients of scalar quantities, commenced after the wind stress died down and was associated with a return of the nearshore zone to its previous heat content (and density). It seems likely that this was largely due to a relaxation process as light water returned to the shore zone following a substantial "set-down" of coastal sea level. The tentative interpretation of the episode is as follows. Strong winds and longshore currents induced vigorous mixing in the CBL. The tendency of mixing processes to homogenize the water column was opposed by the transverse circulation which advected denser water shoreward. After the cessation of the offshore wind, the set-down at the shore relaxed and the light, well mixed, surface water returned to the coastal boundary layer. The observational evidence indicates that the collapse of stratification observed was essentially a mixing phenomenon, the details of which have been influenced by the presence of the coastal boundary and its associated cross-shore circulation.

It is illuminating to consider the behavior of the temperature records subsequent to the mixing and relaxation processes. After May 11

restratification began as a progressive warming of the upper layers,
presumably due to direct solar insolation. It is notable that the
temperature in the lower water column remained essentially constant.
That is, after bottom waters had been warmed by mixing with upper waters
they were not replaced by more dense fluid even in the face of the
repeated, though modest, upwelling winds which occurred during this
period. This seems idicative of a substantial volume of the mixed water
and its large offshore extent. In the coastal region such catastrophic
processes have long lasting effects upon the nearshore hydrography.

The relatively high spatial resolution STD sections routinely per-
formed as part of the COBOLT program provide additional insight into the
variations in hydrographic structure. Figure 4.4 illustrates the temp-
erature, salinity and sigma-t cross sections on May 8, 1977 which was
one day before the storm. For comparison, figure 4.5 shows the hydro-
graphy observed one day after the most intense upwelling favorable wind
stress event to occur during the experimental period. The isopycnals
slope sharply downward toward the coast in striking contrast to initial
expectations. In fact, consideration of figure 4.5 without reference to
wind records or time series information would likely lead one to con-
clude that the region was being acted upon by a downwelling favorable
wind stress. This interesting state of affairs is consistent with the
interpretation of events given above. The slope of the isopycnals are
as might be expected due to cross-shore motions in association with a
geostrophic adjustment process after the cessation of the wind stress.
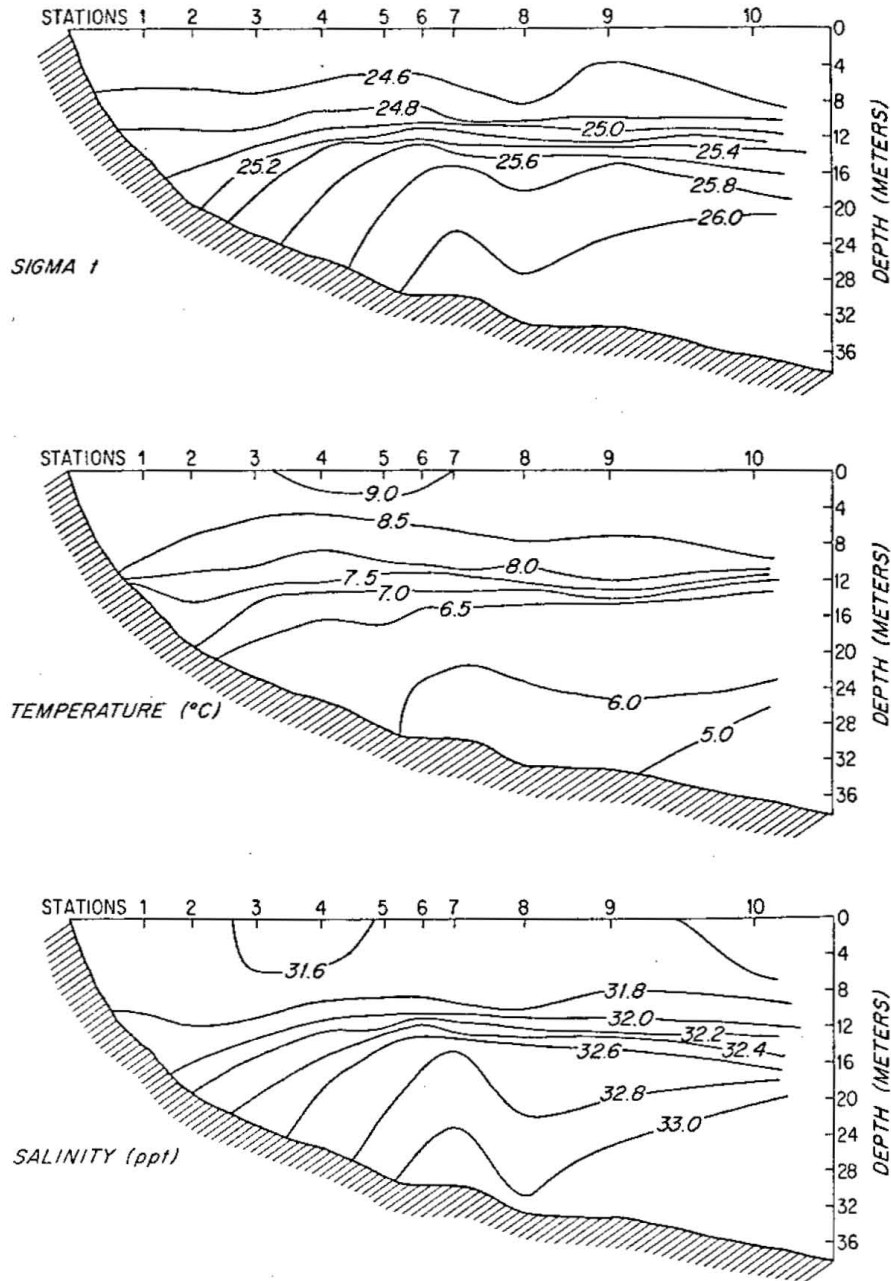
Figure 4.4   May 8, 1977 scalar fields
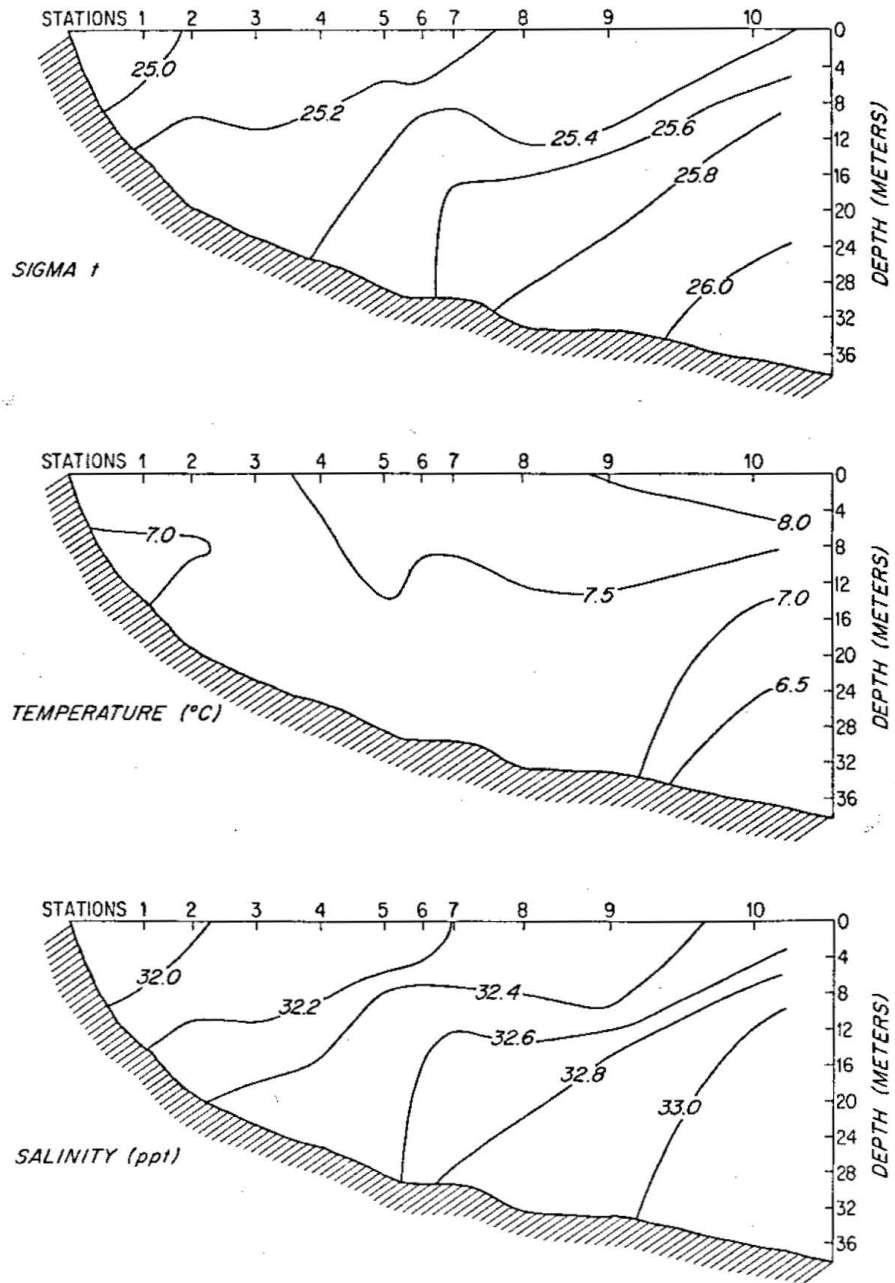
Figure 4.5 May 11, 1977 scalar fields

4.3 Shoreward advection of homogeneous water

Reference to figure 4.1 shows that the temperature time histories of August 1978 have some features which are qualitatively different from those observed in May, 1977. First of all, August is a period of mature stratification in that there is little heating (or cooling) over the experimental period. Second, during the periods of dramatic stratification reduction, the average temperature of the water column is clearly raised. As mentioned earlier this type of behavior is certain indication of significant advective effects. It is also noted that, in sharp contrast to the case previously discussed, restratification of the coastal zone generally commences abruptly and dramatically soon after its homogenization, with the bottom temperature dropping by several degrees within a few hours.

The temperature records from buoy 4 presented in Figure 4.6 give some indication of the seaward extent of each of the four major temperature events occurring in August '78. It is seen that only the third such event achieved impressive lower water column expression as far seaward as 12 km. The calculated local alongshore and offshore wind stress, presented in figure 4.7, shows that this was a period of modest (less than one dyne) winds which were predominantly directed toward the northeast. By comparison with either figure 4.1 or 4.6 it is seen that each case of substantial reduction in stratification was associated with one of the negative alongshore (downwelling favorable) wind-stress episodes. In addition, it is important to note that restratification com-
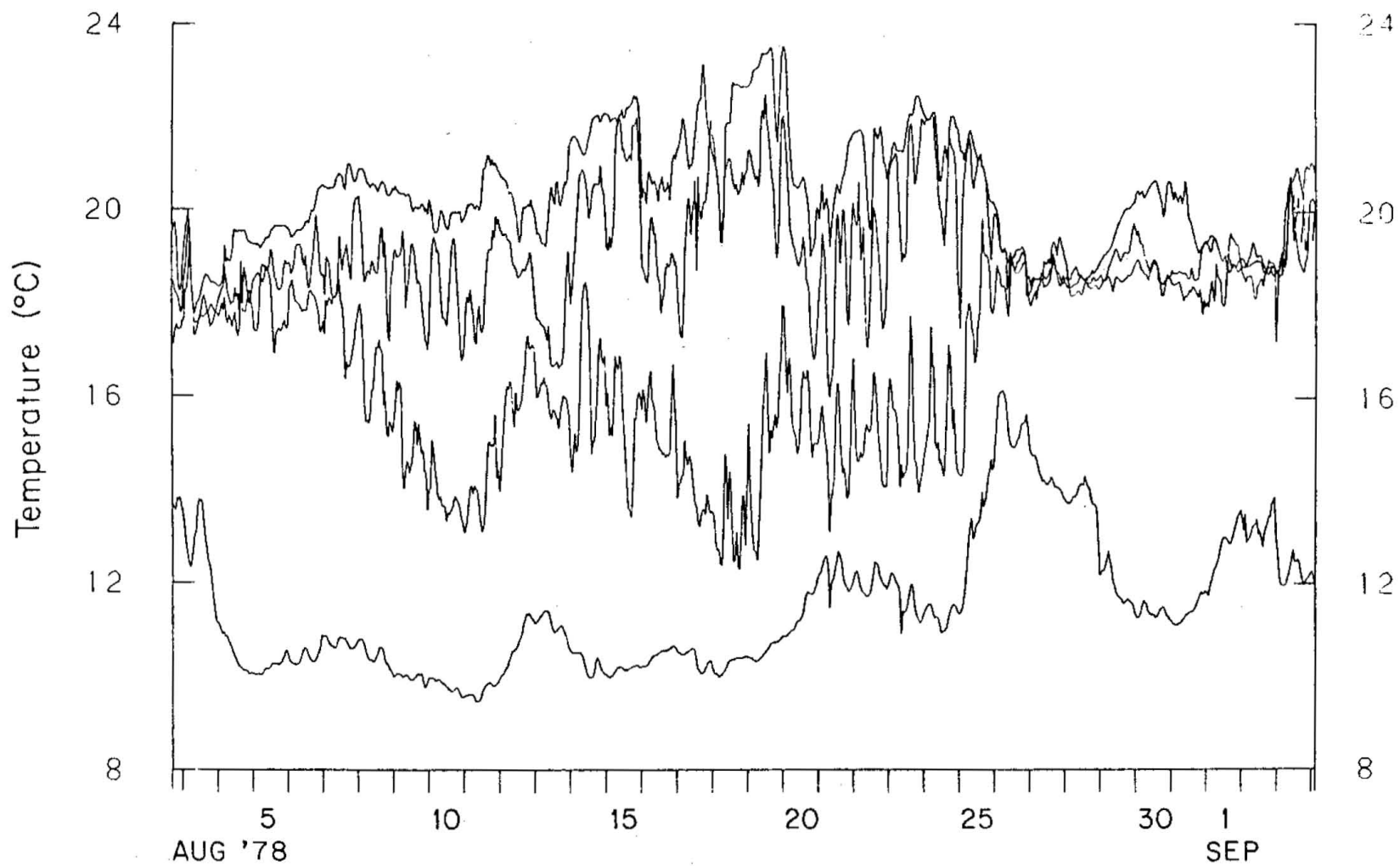
Figure 4.6   Aug '78 temperature records at 4, 8, 16 and 30 m depths, 12 km from shore.
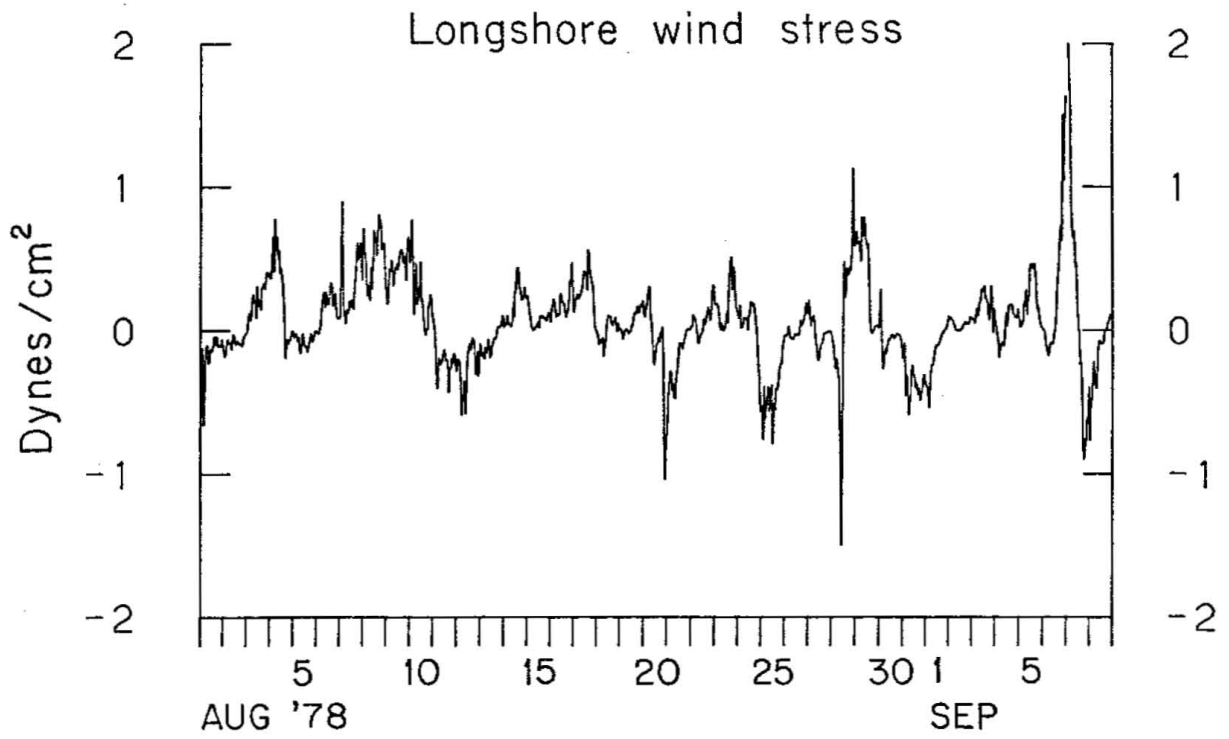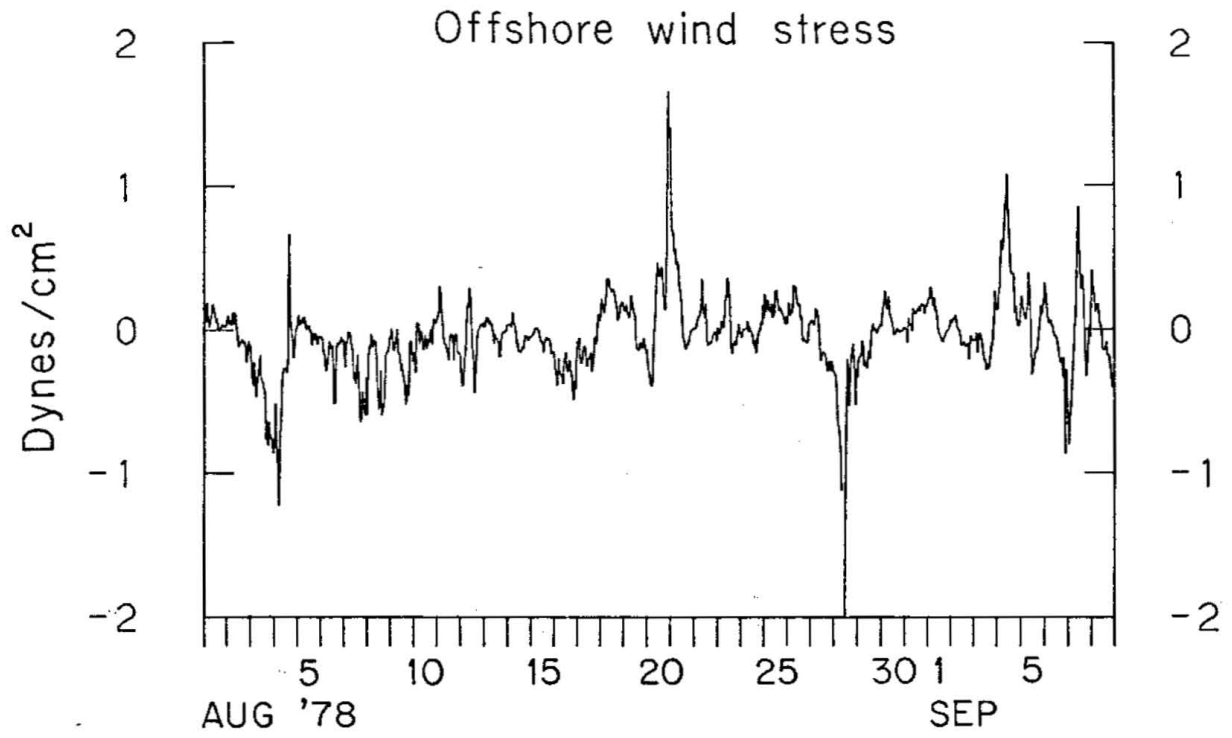
Figure 4.7 Aug '78 wind-stress components

menced upon the onset of positive longshore winds following each event. Comparison of time histories at 3 and 12 km reveals that the restratification begins first at the seaward position with the shoreward location lagging by a day or two. The behavior is as might be expected if the primary restratification mechanism were through cross-shore advection. By the same token it is inconsistent with the notion that the primary means of reinstituting a stratified column was via alongshore advection from upstream.

One generalization which may be drawn from these data is that in the shallow coastal waters off Long Island's south shore, a southwestward longshore wind stress impulse

$$I = \int_0^T \tau_w/\rho \ dt$$

(where T is the stress duration) of roughly 4 m^2/sec results in a homogeneous nearshore zone. This observation is in good agreement with the predictions of a theoretical model by Csanady (1977b) for the finite displacement of a density interface in a flat bottomed domain.

4.4 Advection and mixing

Perhaps the most instructive COBOLT experimental record available with regard to the response of nearshore scalar fields to various types of wind-stress episodes, is that of September 1975. Figures 4.8 and 4.9

show the wind stress and temperature records from a single mooring 11 km from shore. The first clearly significant meteorological event occurred on September 11-12, and displays some similarities to that which produced the marked mixing event in May 1977. In this particular case the longshore wind stress component is positive and would thus tend to induce offshore flow near the surface and onshore flow near bottom. The cross-shore component of the wind is directed onshore and therefore tends to evoke an opposite response. The simple theoretical considerations discussed in Chapter III and in the Appendix show that the longshore stress component should predominate even in the case (as here) when the cross-shore stress is of somewhat larger magnitude. The principal contribution of the large onshore stress in this situation is likely to be increased deepening of the wind mixed layer. Figure 4.9 suggests that any significant mixing effects were limited to the upper layers. In fact, the lower waters demonstrate a decrease in temperature indicating that the upwelling advection is the dominant process, at least in this part of the water column.

On September 17 a 1-2 dyne downwelling wind of two days duration occurred. As expected from previous considerations, a dramatic reduction in thermocline strength also occurred. The net heat gain during this downwelling is clearly evident, and restratification began promptly on the 20th when light upwelling winds advected the thermocline back into the CBL.

The 23rd of September marks the beginning of an intense downwelling type wind of nearly four days duration. Although homogenization of the
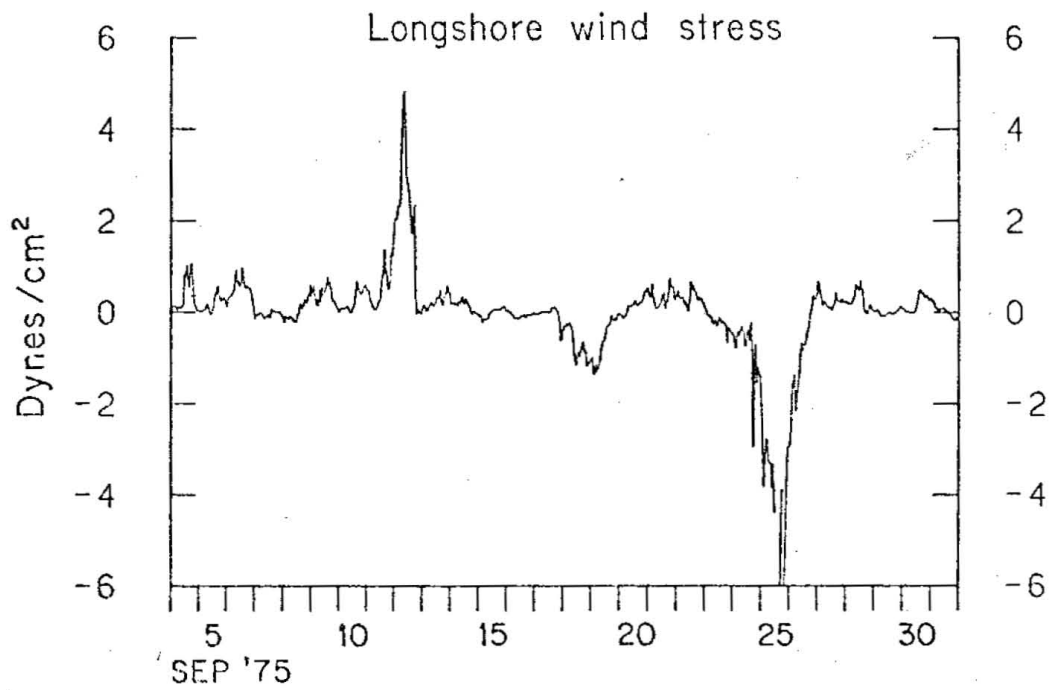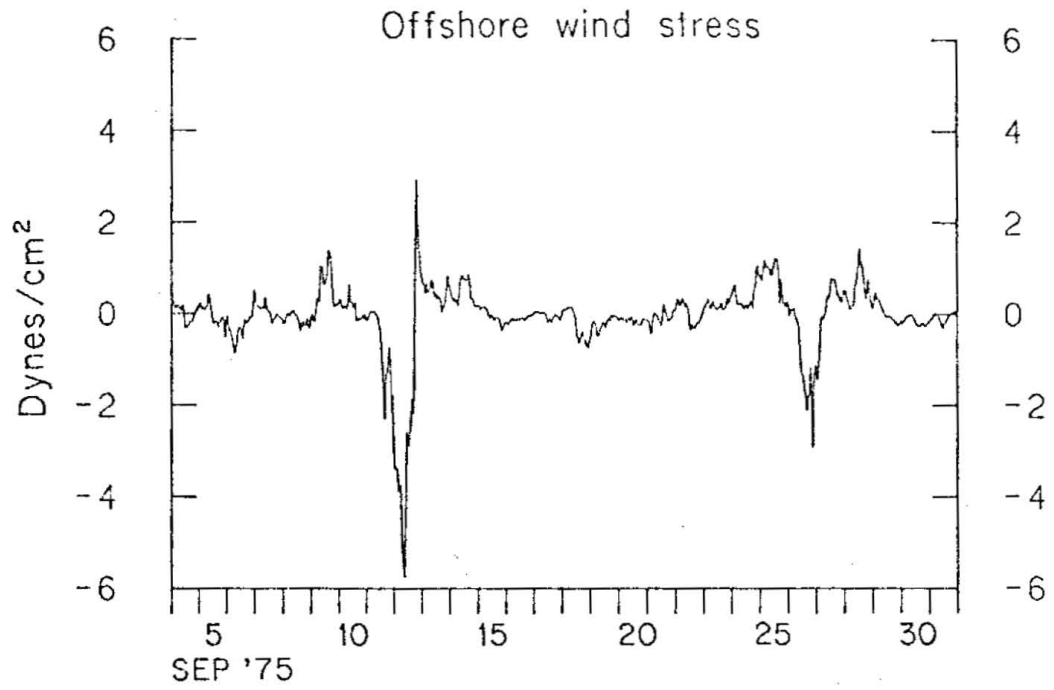
Figure 4.8 Sep '75 wind-stress components
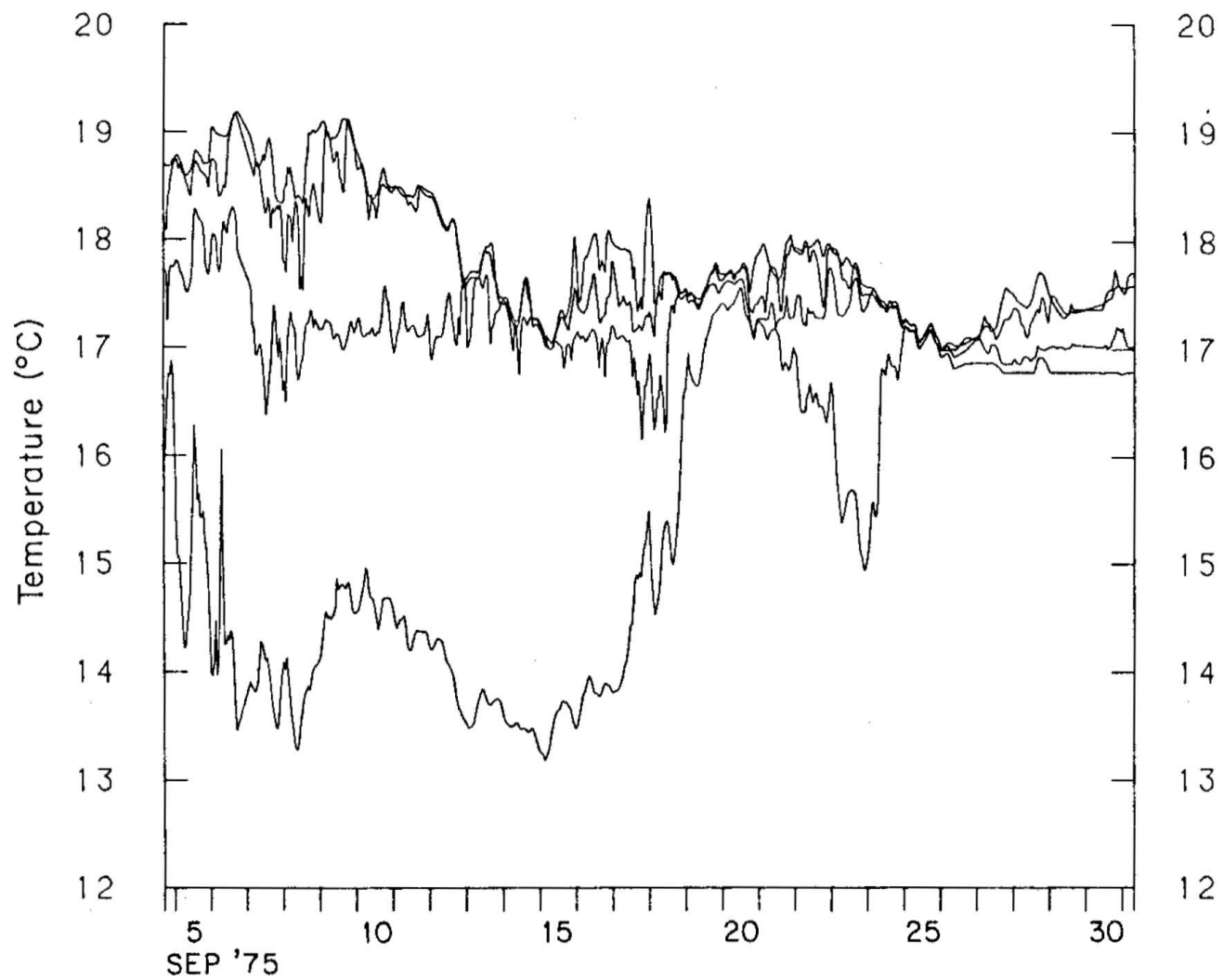
Figure 4.9 Sept '75 temperature records a 4, 8, 16, and 30 m depths, 11 km from shore.

shore zone is inevitable in this situation due to the downwelling alone, there are also indications of the importance of mixing. It is noteworthy that, in contrast to the immediately preceding event, there was a marked near surface decrease in temperature. Although the net heat content of the column was somewhat increased due to the cross-shore advections, the persistence of the changes wrought by the wind event in the face of subsequent upwelling winds (and calculated Richardson numbers < 1), suggest that for sufficiently vigorous meteorological events, mixing processes can be predominant over downwelling effects.

The fortuitous occurrence of three distinct types of meteorological events, each leading to prototypical nearshore hydrographic responses under mean stratified conditions, has produced a particularly illuminating record. The data show that the role of mixing in stratification reduction may be effectively opposed in the lower water column by shoreward advection of thermocline waters during energetic upwelling wind-stress episodes. During strong downwelling winds on the other hand, advective and mixing processes act in concert to affect a lasting stratification reduction in the nearshore region.

4.5 Advective-diffusive exchange coefficients

In addition to exhibiting pronounced temporal variations, the nearshore scalar fields in the COBOLT program reveal interesting spatial patterns. Mean and daily density sections, as observed by STD profiling,

characteristically exhibit a significant shoreward spread of isolines which may be descriptively termed a nearshore fan . Figure 4.10 shows the mean density section observed during September 1974. The density field seems to be qualitatively composed of two regions: an outer region of essentially flat parallel density surfaces, and an inner region (shoreward of 12 km) in which there occurs a distinct shoreward spread of isopycnals. Figure 4.11 shows a typical daily density cross section from the same experiment. The fact that the shoreward reduction of stratification (fan) is evident on a day-to-day basis is reasonable assurance that its appearance in the mean field is due to some physical process (such as mixing) and not merely an artifact of the averaging process. In particular, the downwarped appearance of the near bottom isopycnals in the presence of upwelling winds is certain testimony that some transport phenomenon, in addition to that associated with upwelling advection, is active nearshore.

Data from the COBOLT mooring array provide an opportunity to calculate time averaged values of cross products between the fluctuating components of the cross-shore velocity and temperature or salinity. Estimates of these quantities may provide useful information about the transport of heat and salt by unsteady nearshore flows. Coincident knowledge of mean gradients makes possible the estimation of effective exchange coefficients which often prove useful in predictive models of transport phenomena.

Mean values and the cross-product correlations $\overline{u'T'}$ and $\overline{u'S'}$ were calculated at four vertical positions for each mooring during the August

SEPT. 1974 AVERAGE
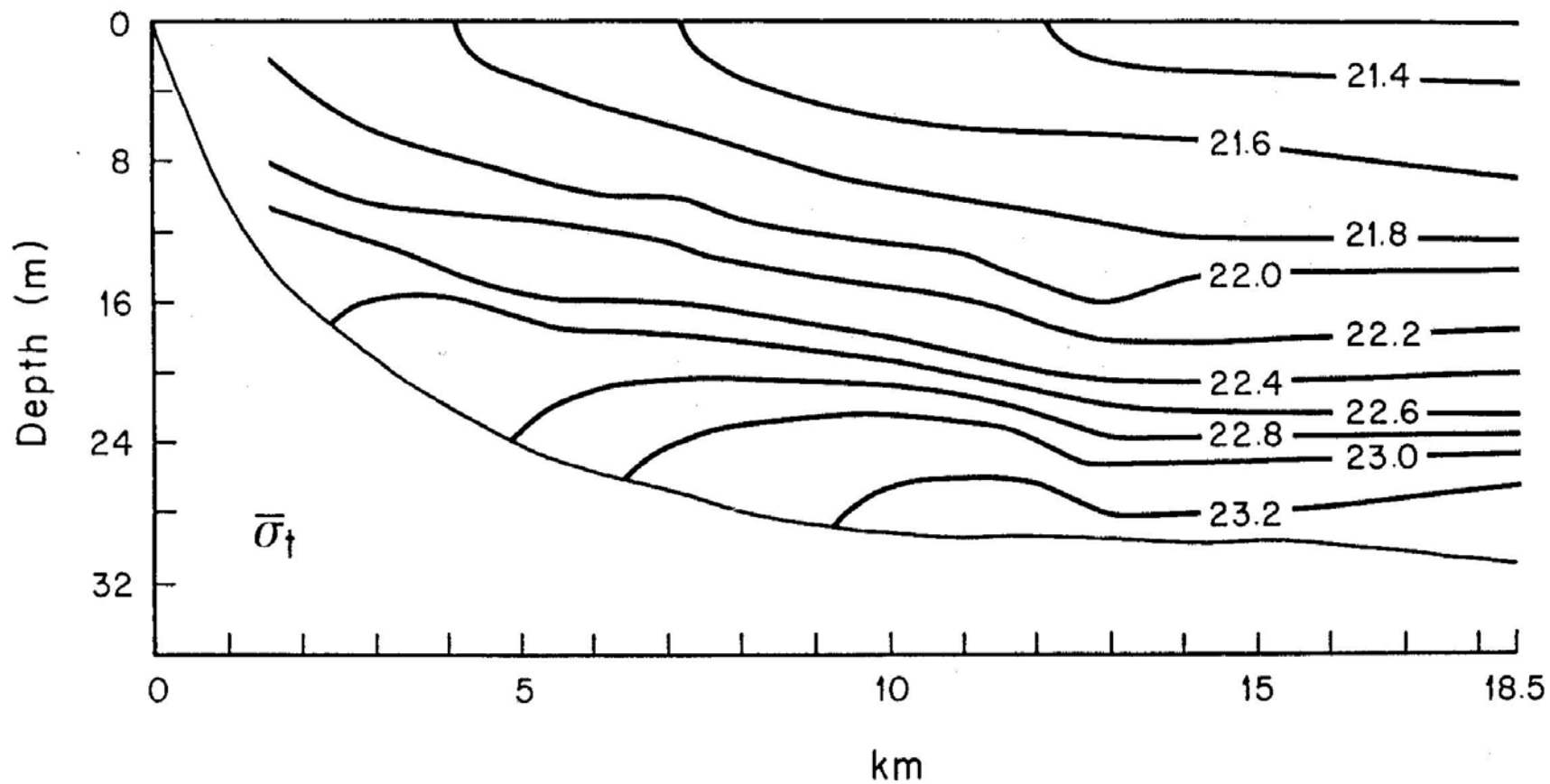
Figure 4.10 Sept '74 mean density section.

SEPT. 16, 1974
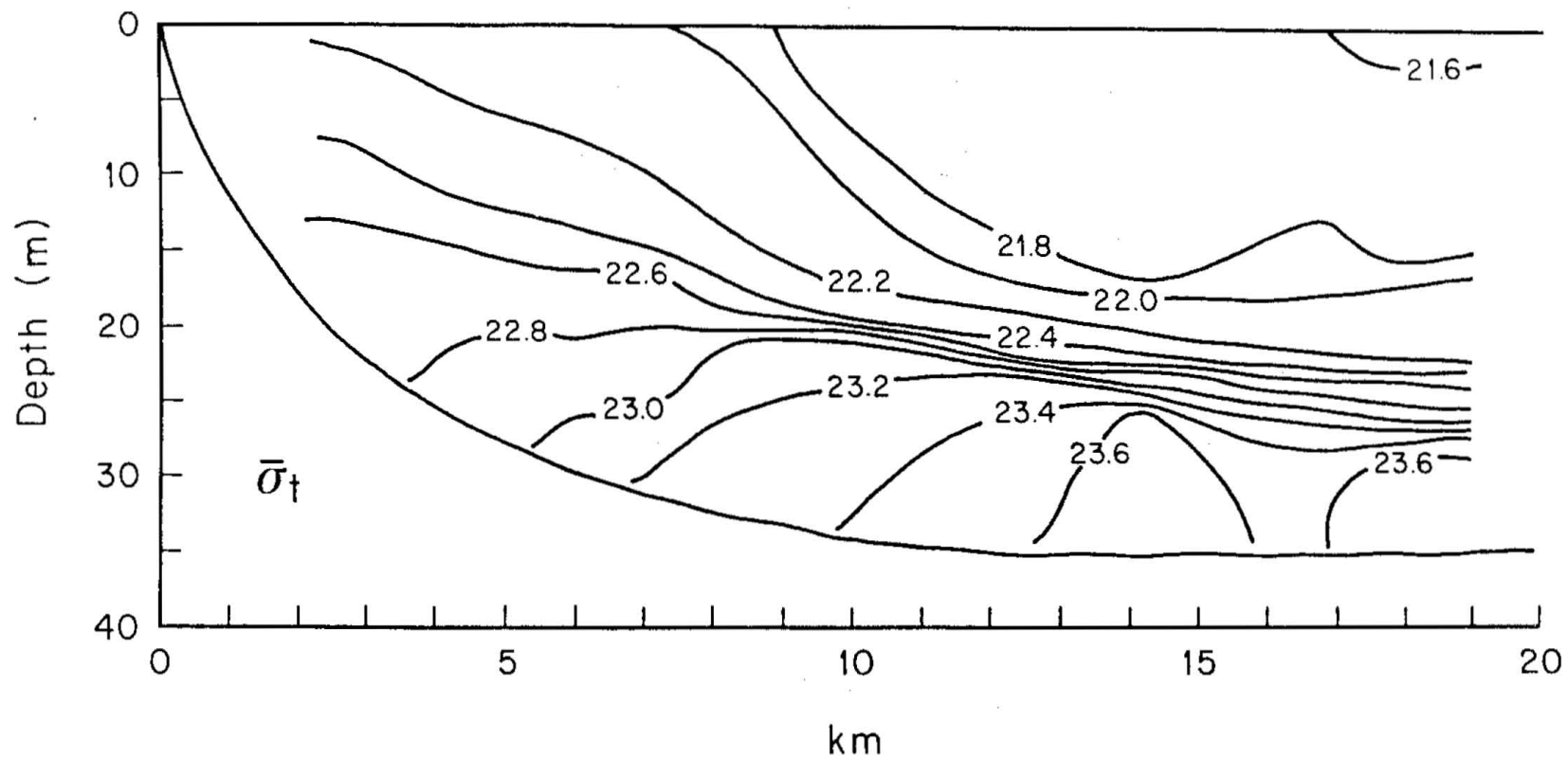
Figure 4.11 Typical daily density section.

1978 and May 1977 experiments. In calculating the correlations, defin-
itions $u' = u - \bar{u}$, $T' = T - \bar{T}$ and $S' = S - \bar{S}$ were used so that the primed, or
fluctuating components, are defined as the difference between the ins-
tantaneous value and the overall experimental mean. Using these defin-
itions the calculated fluctuation cross products represent on-offshore
transport due to motions on all time scales shorter than the experi-
mental duration (i.e., they include such diverse effects as short
period, tidal, and wind-driven variability).These products represent
fluxes and for this reason are ususally represented by a gradient
transport law involving an exchange coefficient and the mean scalar
gradient, in analogy to classical Fickian diffusion.

4.5.1 Calculation of horizontal exchange coefficients

The COBOLT data, which provide measurements of both the cross-
products and mean gradients, afford an opportunity to directly estimate
local horizontal exhange coefficients from the relation

$$K_T = - \overline{<u'T'>} / (\partial T / \partial x) \qquad (4.1)$$

where the over bar represents a time average over the experimental
period and the brackets represent a horizontal, or intermooring, aver-
age. Estimates of horizontal mean gradients were provided for each of
four vertical positions via linear regression. Table 4.1 lists the

TABLE 4.1

Horizontal Exchange Coefficients and Corresponding Fluxes

	May '77				Aug '78	
	$\langle u'T' \rangle$	K_T	$\langle u'S' \rangle$	K_S	$\langle u'T' \rangle$	K_T
Level 1	-1.4*	2.1×10^6	0.2	1.2×10^6	-0.7	0.8×10^6
Level 2	-0.4*	1.0×10^6	0.1	2.1×10^6	-0.8*	1.0×10^6
Level 3	-1.0*	3.6×10^6	-0.1*	0.7×10^6	2.3*	1.7×10^6
Level 4	0.1	1.6×10^5	0.0	4.5×10^4	1.6	2.8×10^5
Average		1.7×10^6		1.0×10^6		1.0×10^6

Asterisks denote correlation coefficients statisitically different from zero at the 0.80 significance level.

fluctuation products and calculated exchange coefficients. While the general consistency shown is taken as an indication of the success of the methodology, and support for the idea that meaningful exchange coefficients may be empirically defined for particular realizations, the general statistical significance of the quadratic quantities is not easily established. As pointed out by Flierl and McWilliams (1977), the magnitude of estimated errors for calculated second moments of eddy variability suggest that obtaining precise estimates of these quantities requires prohibitively lengthy records, and that they should be viewed only as order of magnitude or qualitative estimates. In table 4.1 asterisks mark those fluxes which could be demonstrated to be signif-icantly different from zero to at least the .80 confidence level (Bendat and Piersol, 1971).

4.5.2 Estimation of the vertical exchange coefficient

As was noted in the previous discussion of figure 4.2, the May 1977 experiment took place during a period of marked nearshore vernal warm-ing. This situation provides an opportunity to estimate a vertical heat exchange coefficient. If it is assumed, as seems reasonable, that significant heat gains by the water column were due to surface heating and subsequent downward diffusion, the rate of change of heat may be set equal to the flux through the surface. Further assuming that this heat flux may be expressed in terms of an exchange coefficient and mean

gradient leads to

$$\int \rho c_p \partial T / \partial t \, dV = K \int \partial^2 T / \partial z^2 \, dV \qquad (4.2)$$

where ρ is the water density, c_p its specific heat, T is temperature in degrees Celsius, and V is the control volume of the CBL defined as its cross sectional area out to buoy 4 multiplied by a unit thickness. Equation (4.2) may be rewritten as

$$\rho \, c_p \, \underline{h} \, \partial \underline{T} / \partial t = k \, \partial \underline{T} / \partial z \, \lfloor_0$$

where h is the water depth, and the underline notation denotes an average over the free surface of the control volume. Rearranging the above leads to

$$K_v = \frac{(\partial \underline{T} / \partial t)}{(\partial \underline{T} / \partial z)} \qquad cm^2/sec \qquad (4.3)$$

where $K_v = k / \rho \, c_p$. The mean near surface temperature gradient required in the above formulation was first calculated from thermistor data at 1 and 4 m below the surface. The gradient was then also estimated by comparison between once-daily surface bucket temperatures and coincident 1 m thermistor readings. While this second method drastically undersamples the variable temperature gradient, it has the advantage of utilizing only measurements from the top meter of water. These two methods lead to

$$K_v = (0.75 - 3.0) \quad cm^2/sec \quad (z=0).$$

The nature of this calculation is such that all vertical heat transport mechanisms have been lumped together in one parameterization. It is reasonable to suppose, however, that turbulent diffusion is the dominant influence in vertical transport within the near surface layer. Estimates of mean transport of heat (advective and diffusive) out through the seaward boundary indicate that the above values could be low by a factor of two.

4.6 A diffusive equilibrium density distribution

It is interesting to determine (using calculated exchange coeffic-ients) the diffusive equilibrium density distribution which would exist in a nearshore domain subject to no flux conditions at surface and solid boundaries, and a prescription of shelf stratification over the seaward boundary. This procedure represents a modelling of the long-term effects of mixing processes upon the CBL in the absence of other complicating factors such as heating (or cooling) and mean advective fluxes. By limiting attention to periods in which net surface heating is neglig-ible, the simplified model is not directly applicable to the May 1977 experiment which allowed estimation of K_v.

Consider a long straight coastline with linear bottom slope and surface and solid boundaries which are insulating with respect to both

salt and heat. It is convenient for this purpose to use polar coord-
inates where θ is measured counterclockwise from the horizontal. For
the particular nearshore morphometry of the study area, a sector of an
annulus has somewhat greater geometric correspondence to the coastal
domain than does a circular sector, and is thus chosen to facilitate
comparison with observation. Figure 4.12 shows the definition sketch of
the topography where α is the bottom slope, and ℓ the scale of the
nearshore region over which diffusion is postulated to be a dominant
influence. Neglecting mean advective effects, the steady density field
is given by

$$\frac{K_r}{K_\theta} \left(\frac{\partial^2 \rho}{\partial r^2} + \frac{1}{r} \frac{\partial \rho}{\partial r} \right) + \frac{1}{r^2} \frac{\partial^2 \rho}{\partial \theta^2} = 0 \qquad (4.4)$$

where K_r and K_θ are the radial and angular diffusivities respec-
tively. For the very small slopes occurring off natural barrier beaches
such as Long Island's south shore, K_r and K_θ are approximately
equal to the horizontal and vertical diffusivities.

The inner shelf stratification to which the CBL diffusive solution
must match at $r = r_1 + \ell = L$ may be represented by a Fourier cosine
expansion as

$$\rho(L,\theta) = \rho_r + \sum_1^\infty a_n \cos \left(\frac{n \pi}{\alpha} \theta \right) \qquad (4.5)$$
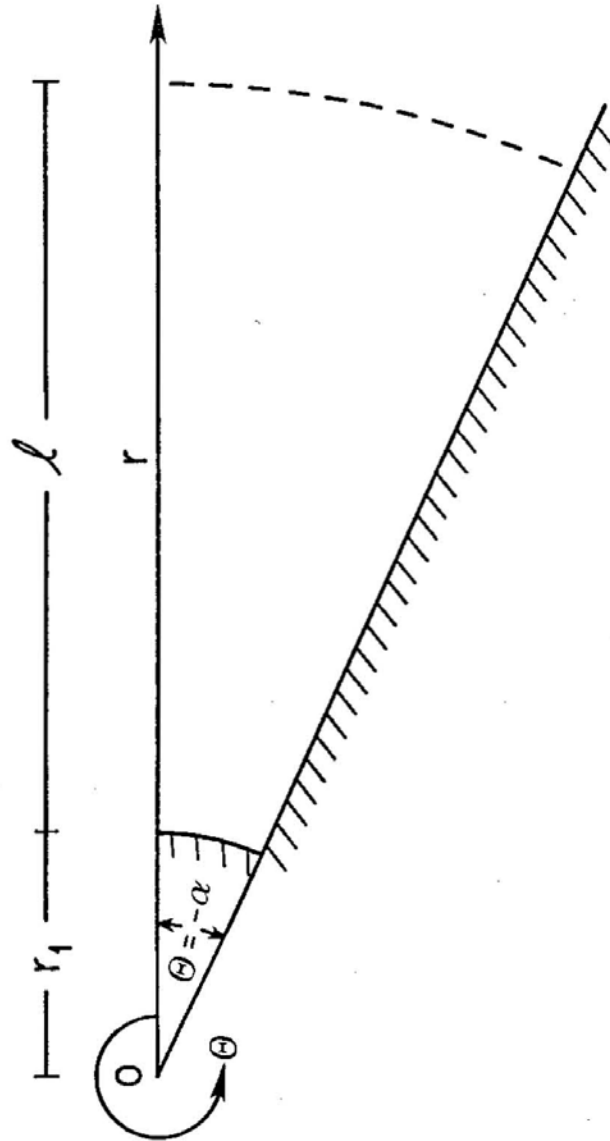
Figure 4.12 Definition sketch showing boundaries and coordinate system of diffusive model

where ρ_r is the mean density of the water column at $r = L$. The insulating boundary conditions are

$$\partial\rho/\partial r = 0 \qquad \text{at } r = r_1 \qquad\qquad (4.6)$$

and

$$\partial\rho/\partial\theta = 0 \qquad \text{at } \theta = 0, -\alpha. \qquad\qquad (4.7)$$

Assuming a separable solution of the form

$$\rho(r\theta) = F(r)G(\theta)$$

in equation (4.4) leads to

$$r^2 \frac{d^2F}{dr^2} + r \frac{dF}{dr} - \frac{\beta^2}{\gamma^2} F = 0 \qquad\qquad (4.8)$$

and

$$\frac{d^2G}{d\theta^2} + \beta^2 G = 0 \qquad\qquad (4.9)$$

where $\gamma^2 = K_r/K_\theta$ and β^2 is the separation constant. Equation (4.8) is of equidimensional form with solution

$$F(r) = \begin{cases} A_0 + B_0 \ln r & \beta = 0 \\ \\ A_n r^{\theta/\gamma} + B_n r^{-\theta/\gamma} & \beta \neq 0 \end{cases} \qquad\qquad (4.10)$$

while (4.9) has solution

$$
G(\theta) \;=\; \begin{cases} C_0 + D_0 \theta & \beta = 0 \\[2em] C_n \cos \beta\theta + D_n \cos \beta\theta & \beta \neq 0 \end{cases} \tag{4.11}
$$

The general solution for the density field is given by

$$
\rho(r,\theta) \;=\; A_0 + B_0 \ln r + (C_0 + D_0 \ln r)\,\theta
$$

$$
\tag{4.12}
$$

$$
+ \sum_{n=1}^{\infty} (A_n\, r^{\beta/\gamma} + B_n\, r^{-\beta/\gamma})\,(C_n \cos \beta\theta + D_n \sin \beta\theta)
$$

Using (4.7) yields

$$
C_0 = D_0 = D_n = 0 \quad \text{and} \quad \beta = n\pi/\alpha
$$

while (4.6) leads to

$$
B_0 = 0
$$

$$
B_n = A_n\, r_1^{2(n\pi/\alpha\gamma)}.
$$

Substituting the above expressions and using (4.5) allows evaluation of

$$
A_0 = \rho_r
$$

and

$$C_n A_n = a_n /[L^{(n\pi/\alpha\gamma)} + (r_1^2/L)^{(n\pi/\alpha\gamma)}]$$

where the a_n are the known Fourier coefficients of the interior

stratification. The final solution may now be expressed as

$$\rho(r,\theta) = \rho_r + \sum_{n=1}^{\infty} \frac{r^{\frac{n\pi}{\alpha\gamma}} + (r_1^2/r)^{\frac{n\pi}{\alpha\gamma}}}{L^{\frac{n\pi}{\alpha\gamma}} + (r_1^2/L)^{\frac{n\pi}{\alpha\gamma}}} \; a_n \; \cos \frac{n\pi}{\alpha} \theta \qquad (4.13)$$

It is readily verified via the ratio test that the infinite series in

(4.13) is convergent for any imposed stratfication whose first deriv-

ative with respect to θ is at least piecewise continuous.

The length scale (ℓ) of the postulated diffusion dominated zone is

estimated from figure (4.11) to be 13 km. This distance corresponds to

the transition between flat parallel density contours and the region

fanlike stratification reduction. The θ dependence of the density field

in the outer (non-diffusive) region may be adequately idealized as

$$\rho(L,\theta) = \rho_r - \lambda \cos \frac{\pi\theta}{\alpha}$$

corresponding to $a_0 = \rho_r$, $a_1 = -\lambda$ and $a_n = 0$ ($n = 2,3,\ldots$) in equation

(4.5). With this choice of Fourier coefficients (4.13) becomes

$$\rho(r,\theta) = \rho_r - \lambda \left(\frac{r^{\pi/\alpha\gamma} + (r_1^2/r)^{\pi/\alpha\gamma}}{L^{\pi/\alpha\gamma} + (r_1^2/L)^{\pi/\alpha\gamma}} \right) \cos \frac{\pi\theta}{\alpha} \qquad (4.14)$$

Sufficient similarity between model and observed geometric configurations is achieved by choosing $\alpha = 2 \times 10^{-3}$ and $r_1 = 6.5$ km. For the September 1974 data ρ_r and λ are given by 1.0222 and 1.001 gm/cm^3 respectively.

Figure 4.13 shows the sigma-t distribution resulting from the ratio $\gamma^2 = (K_r/K_\theta) = 10^6$ as suggested by the empirical diffusivity ratio estimated earlier. The qualitative agreement between this and figure 4.10 is quite good. What is somewhat more surprising is the degree of quantitative agreement between the observations and the diffusive fan. The positions at which the sigma-t contours intersect the boundary are predicted very accurately considering the crude idealizations involved in the model. This behavior is sensitively dependent upon the diffusivity ratio, and calculations using values an order of magnitude to either side of 10^6 show a lack of even qualitative agreement with observation. These results seem to suggest both that the empirically determined diffusivity ratio of 10^6 is realistic and that nearshore pycnocline fans are a signature of mixing.

It should be noted that the use of the polar coordinate system rather than solving the more difficult problem of a sloping boundary in a cartesian frame, results in the introduction of an artificial tilt to the computed density field.
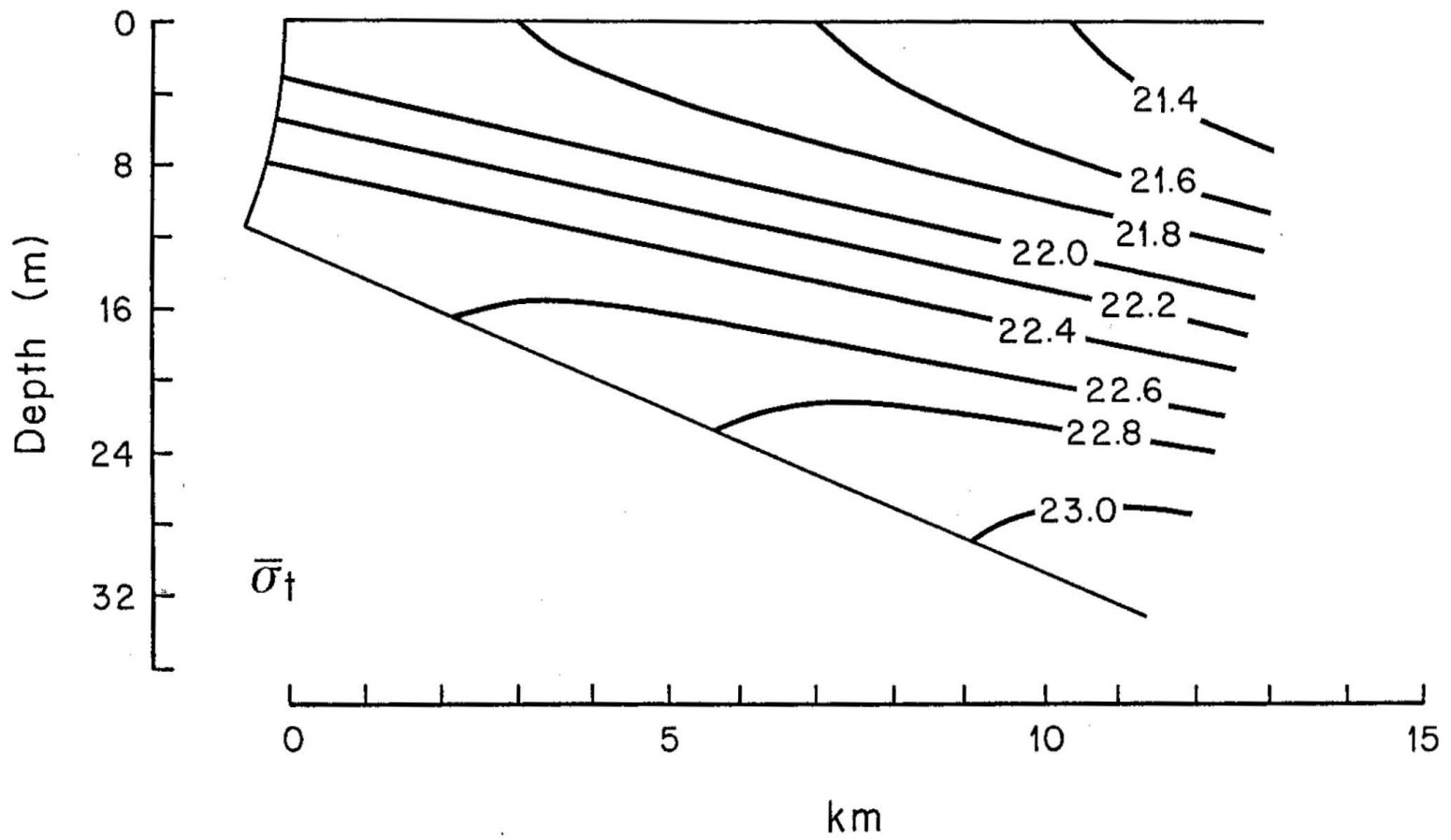
Figure 4.13   Computed equilibrium density distribution

CHAPTER V

OBSERVATIONS OF NEARSHORE CURRENTS AND SEA LEVEL SLOPE

5.1 Introduction

The importance of the along-isobath gradient of coastal sea surface elevation to the understanding of the dynamics of the New England Shelf was first indicated by the two-dimensional model of Stommel and Leetmaa (1972). In the absence of such a gradient, this model of wind-driven and thermohaline coastal circulation predicted a substantial alongshore velocity in the same direction as the longshore wind stress. Within the framework of linear boundary layer theory this may be viewed as a requirement to conserve mass via a bottom Ekman layer. The prediction is in direct contradiction to the observational evidence which shows a consistent mean longshore flow in opposition to the mean longshore wind stress. This conflict may be removed in the model by allowing an alongshore sea level gradient to exist. If sea level were to rise in the upcoast direction the associated shoreward geostrophic interior flow could balance not only wind driven and thermohaline surface Ekman layer transport, but also some offshore transport in a bottom Ekman layer arising from the observed downcoast longshore currents.

The observation of onshore flow in the middle water column, away from surface and bottom frictional layers, can be considered important indirect evidence of the existence of a longshore sea level gradient

which slopes upward toward the northeast. The data of Beardsley et al. (1976) and Luyten (1977) show such an onshore drift of a magnitude which implies the existence of a mean longshore pressure gradient of order 10^{-7} over the shelf and upper slope region. Closer to shore, in shallow water, the longshore pressure gradient cannot be expected to be in geostrophic balance. In this region one might expect to observe a greater tendency for longshore flow in the direction of the wind.

Another degree of freedom is added to such a model when the three dimensional nature of the shelf circulation is taken into account. In this situation the necessity of constraining the flow to have zero cross-shore transport at every position along the coast is removed. Regions of offshore transport may then be balanced by net onshore flow at other longshore positions. The associated variation in longshore flows could be driven by an alongcoast modulation of the pressure distribution.

The existence of a mean sea level rise from Cape Hatteras to Nova Scotia was believed to be established by direct measurement via geodetic levelling techniques as early as the 1920's (Avers, 1927). The consequences, with regard to shelf circulation of such an alongshore slope, seem to have been first discussed in Sverdrup, Johnson and Fleming (1942). The authors reasoned that the excess water must be piled up against the coast and not extend beyond the continental slope since no sign of compensation was noted in the hydrographic structure of waters offshore. As a direct consequence, the authors suggest that "a south current must flow over the shallow portion of the shelf where it flows

downhill and where the balance of forces is maintained by the effect of friction." The perceptiveness of these remarks is more fully appreciated when it is realized that they were made prior to the time that the general southwestward mean flow of the region was established (Bumpus, 1973). The ability of geodetic leveling techniques to accurately detect sea surface slopes of order 10^{-7} along the coast has recently come into question (cf. Sturges, 1977) and direct verification of such features may have to await new technological advances (e.g., satellite altimetry). In any case, as noted by Csanady (1979), although geodetic level surface may be in doubt, the southwestward mean flow along the coast certainly exists and so, by implication, should a longshore pressure gradient of this order.

Once the reality of the large scale longshore variation in sea level is accepted, it still remains to account for its physical origin. Three primary mechanisms have been frequently suggested as possible contributors (cf. Csanady, 1979). They are:

1) Set-up due to mean winds

2) Riverine input of fresh water

3) Influence of deep water circulation and associated western boundary currents

In his analysis, Csanady (1979) concluded that thermohaline influence due to fresh water influx seems to be capable of only minor contributions to the mean pressure field. He also concluded that wind driven

set up is likely to play a significant role only along particular sec-
tions of the coastline where the geometrical configuration is favorable.
By this process of elimination, the general circulation of the western
North Atlantic emerged as the designated originator of the mean long-
shore sea surface slope. This belief was also expressed by Beardsley
and Winant (1979) who suggested that the shelf circulation is a boundary
layer component of the large scale ocean circulation. The authors went
on to point out that steady solutions of a reasonably comprehensive
numerical model of the North Atlantic by Semtner and Mintz (1977), which
included simple shelf and slope topography, show a cyclonic gyre north
of. the Gulf Stream which imposes a realistic longshore flow field and
pressure gradient upon the shelf. It is interesting to note that
Sverdrup, Johnson and Fleming (1942) also predicted the existence of
such a gyre primarily on the basis of the geodetic evidence of an
alongcoast sea level slope.

Despite the growing consensus of opinion and the apparent consis-
tency of the evidence, it must be admitted that the primary physical
cause of the mean sea surface slope from Cape Hatteras to Nova Scotia
cannot be considered firmly established.

5.2 Variations in the longshore sea level gradient

Although absolute sea level differences are not at present observ-
able, variations in the longshore sea surface slope may be directly

measured. The principal driving mechanisms for these longshore fluctu-
ations may be expected to differ as a function of their characteristic
time scales. On short time scales of the order of a day or less, ele-
vation differences due to tidal fluctuations predominate. Figure 5.1,
which shows the variation of the surface elevation gradient calculated
from hourly elevations at Montauk N.Y. and Sandy Hook N.J., clearly dem-
onstrates that not only are the tides dominant over short time scales,
but in additon, the signal is so large that it effectively masks all
other frequencies present in the unfiltered records.

Low frequency longshore gradient fluctuations and their relation to
atmospheric forcing have been studied recently by Chase (1978), Wang
(1978), and Noble and Butman (1979). The results of these studies seem
to indicate that various sections of the coastline may respond differ-
ently to coastal winds. While all researchers found marginal coherence
between the longshore component of local winds and the Sandy Hook-to-
Nantucket pressure gradient, Noble and Butman concluded that, overall,
the pressure gradient along the east coast was incoherent with wind
forcing.

The present work investigates the wind stress-pressure gradient rel-
ationships during the various COBOLT experimental periods in 1976-1978.
Meteorological data were collected at either a shore tower at the Tiana
Beach site or at BNL some 35 km distant. The pressure gradient along
the Long Island coast was calculated from differences in hourly surface
elevation between NOAA, NOS tide stations at Montauk, Long Island and
Sandy Hook, New Jersey (figure 5.2). Atmospheric and steric pressure
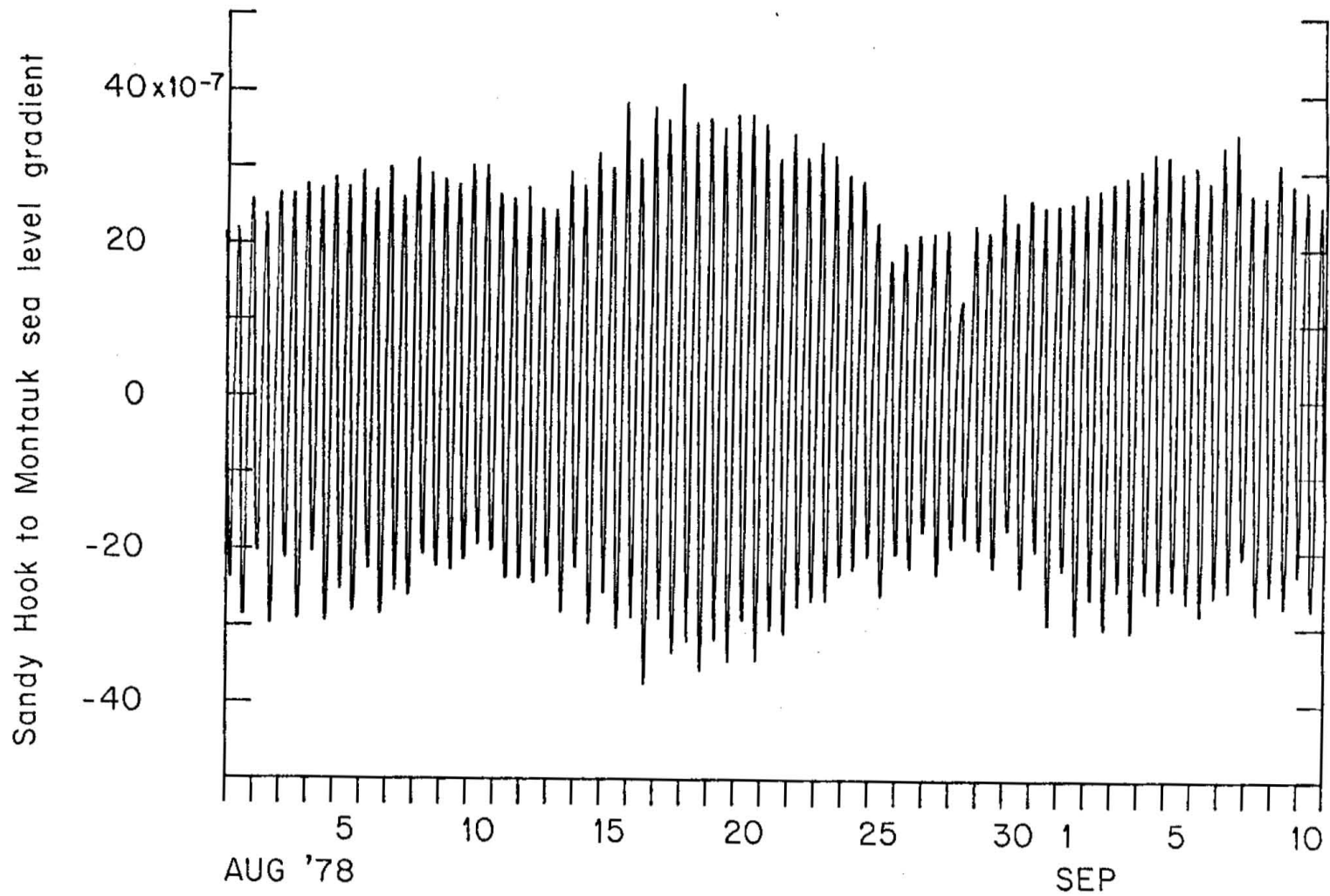
Figure 5.1 Sea level gradient between Sandy Hook, N.J. and Montauk, N.Y. during Aug '78 COBOLT deployment
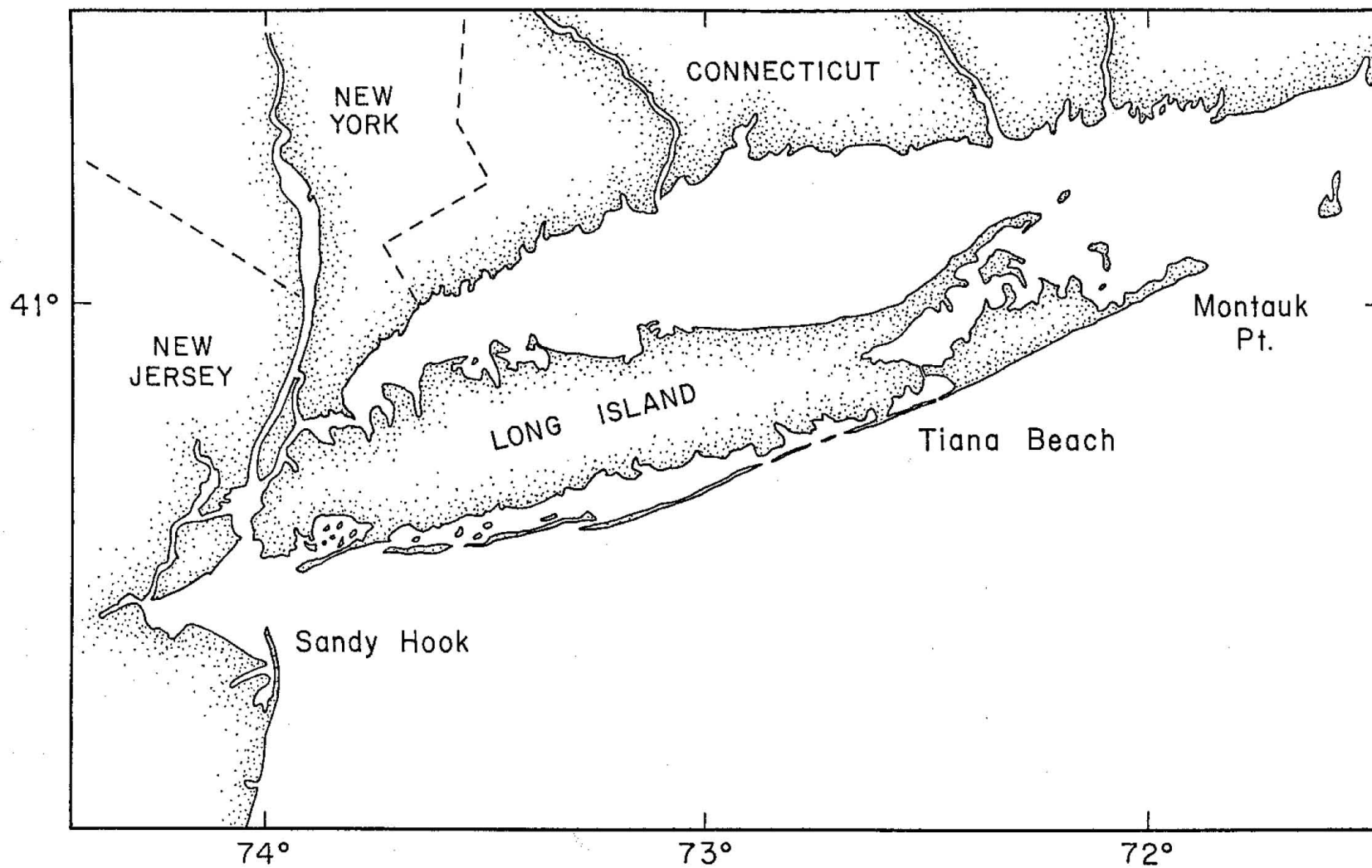
Figure 5.2   Map of study area

corrections were neglected on the basis of their insignificant contri-
bution in Chase's (1978) study. In an attempt to correct for the local
subsidence taking place at the Sandy Hook tide station (Hicks, 1978) and
thus to approximate more nearly a true zero, 2.25 cm was subtracted from
all Sandy Hook values in accordance with an estimate by Chase (1979)
based on regression techniques. All calculated pressure gradients were
low pass filtered with a Stallings P-3 filter (Hunt, 1977; McCullough,
1968) with a 26 hour cutoff, in order to remove the tides.

Figure 5.3 shows the low passed time series of the longshore compon-
ents of wind stress and the pressure gradient between Montauk and Sandy
Hook for the period of the August '78 COBOLT experiment. The degree of
visual correlation between the two records is quite striking and it is
apparent that the major portion of the subtidal longshore pressure grad-
ient fluctuations is related to wind-stress forcing. This relationship
is quantified by the high coherences in the 4-8 day band emergent from
cross spectral calculations. At the same time cross-shore winds and the
Montauk to Sandy Hook sea surface slope are not statistically coherent.
These results, however, do not seem to be uniformly valid during all
experimental periods. Table 5.1 lists coherence and phase relationships
along with spectral energy of the wind stress for the various experimen-
tal deployments. Starred coherence values are those statistically dif-
ferent from zero at the 95 percent confidence level. While no immutable
conclusions can be drawn from these calculations, they seem to show that
when longshore wind-stress values are comparable or greater than cross-
shore values, often only the longshore stress is coherent with the
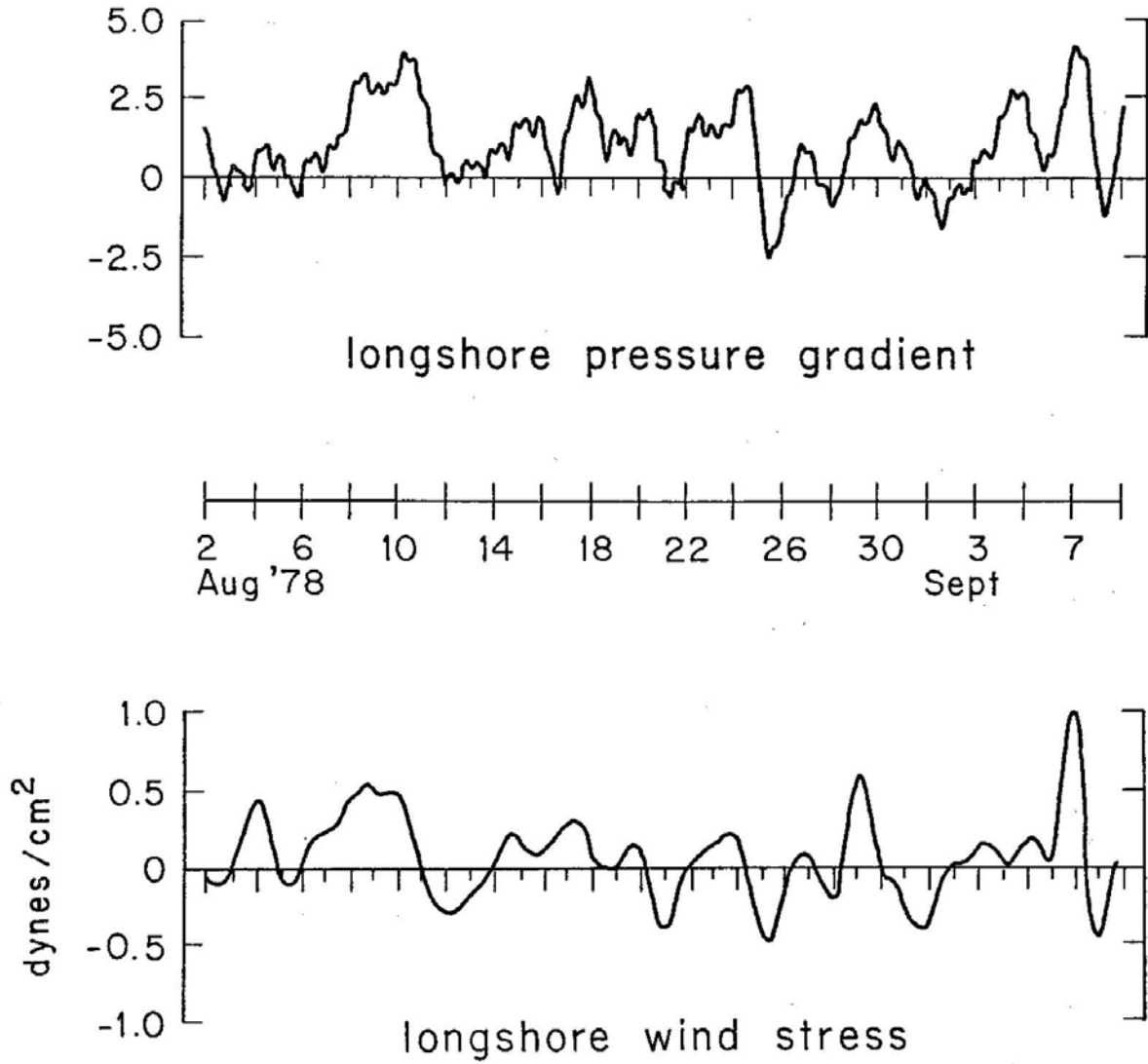
Figure 5.3 Aug '78 low pass filtered longshore components of pressure
gradient and wind stress

Table 5.1

Period (hrs.)	Longshore Energy	Coh.	Phase	Offshore Energy	Coh.	Phase
Aug '78						
200	3.5E-2	0.83*	40°	1.7E-2	0.36	-124°
100	1.5E-2	0.69*	62°	1.7E-2	0.36	-87°
67	8.0E-3	0.48	75°	1.2E-2	0.49	-39°
50	4.0E-3	0.53	55°	6.0E-3	0.57	-84°
Mar '78						
200	1.3E-1	0.87*	6°	7.0E-2	0.46	-78°
100	7.0E-2	0.74	7°	5.0E-2	0.87*	-60°
67	4.0E-2	0.36	-17°	4.0E-2	0.92*	-56°
50	1.0E-2	0.48	10°	3.0E-2	0.91*	-69°
May '77						
200	1.2E-1	0.62	8°	5.7E-1	0.75	-7°
100	7.8E-2	0.59	-14°	6.8E-1	0.96*	-29°
67	5.3E-2	0.71	20°	4.9E-1	0.87*	-34°
50	1.7E-2	0.58	-60°	2.6E-1	0.79	-43°
Oct-Nov '76						
200	1.8	0.73*	48°	1.0	0.44	-137°
100	1.3	0.66*	41°	1.3	0.37	-54°
67	6.0E-1	0.27	5°	1.0	0.59	-45°
50	6.0E-1	0.26	-23°	7.6E-1	0.54	-72°

Table 5.1 Low frequency wind stress component energy $[(dynes/cm^2)^2]$ and wind stress-pressure gradient coherence and phase calculations. Asterisks are indicative of coherences significant at the .95 level.

pressure gradient signal. On the other hand, if offshore stresses are substantially larger than those alongshore, the situation reverses as seen for example in the May'77 tabulations.

One interesting feature, reflected in the phase calculations in table 5.1, is that while coherent alongshore stresses lead the pressure gradient, as is also visually evident in figure 5.3, the opposite is true in the case of cross-shore winds. This relationship is not quite so surprising when it is realized that, unlike the alongshore wind, cross-shore stresses cannot directly set up sea level gradients along the coast. They can be effective only if their magnitude varies significantly in the alongshore direction. Csanady (1980) has shown that the dominant offshore wind event in the May'77 record was a travelling disturbance which affected Sandy Hook roughly half a day before Montauk. This situation resulted in the pressure gradient response leading the local Tiana Beach winds as the storm traveled toward the northeast. It seems plausible that such traveling storms are largely responsible for the phase relationship noted above.

In general one can conclude that the longshore wind stress is primarily responsible for the longshore pressure gradient fluctuations of 4-8 day period, and that cross-shore winds appear most effective in forcing variations of 2-3 day period. Since in the present studies both low pass filtered meteorological and sea level spectra are "red" in character, shore parallel winds are by far the more important source of variance in the pressure gradient observed along Long Island.

In light of the lack of compelling evidence of high coherence be-

tween wind forcing and the longshore pressure gradient for the east coast as a whole, the clear correlation observed off Long Island may suggest the importance of local effects. Previous investigations have noted a lack of uniformity of response along the coast, and as Csanady (1978) demontrates, one might well expect local effects due to changes in coastline orientation. The Long Island coastline seems a likely candidate for such effects due in part to the sharp angle it makes with the New Jersey shore. In addition, it seems quite likely that the presence of Long Island Sound, which is known to have a marked influence upon tides (Swanson, 1976) and upon the hydrography of the region (Ketchum and Keene, 1955), may also have a significant effect upon the wind-driven response of the nearshore pressure field.

Another factor which may contribute to the relatively high coherence found in this study is the frequency band considered. The lower the frequency considered, the more likely there is to be a deep ocean influence which is uncorrelated with local winds. Noble and Butman (1979) present coherences averged over a 600-120 hr band while the lowest period oscillation resolved in the present study is 200 hr.

A complementary, and perhaps intuitively more appealing, picture of the nature of the relation between winds and longshore sea level gradients is obtained by linear regression. Figures 5.4-5.7 display the linear trends of low passed scatter plots of longshore pressure gradient versus the cross-shore and alongshore components of wind stress. From these figures, and from table 5.2 which lists the regression coefficients, it is quite apparent that computed regression slopes are consis-

AUG '78
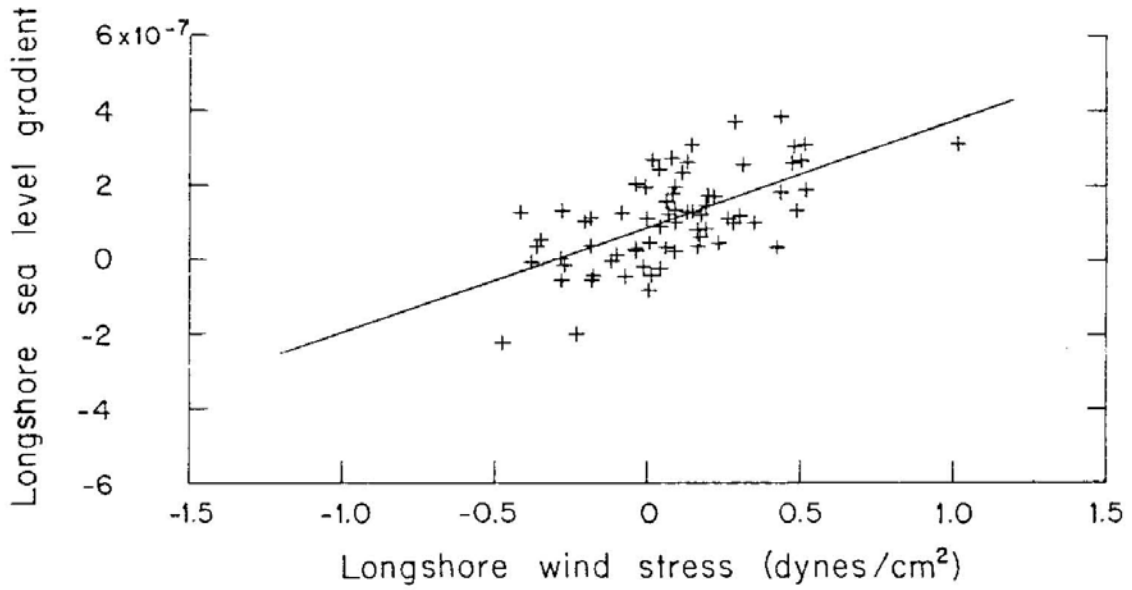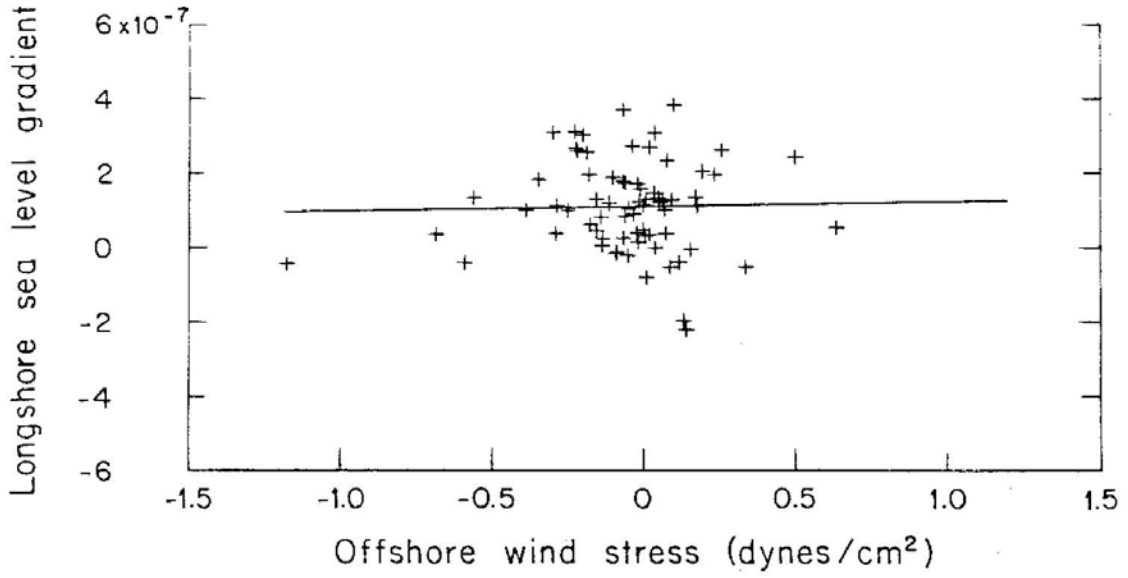
Figure 5.4 Aug '78 longshore sea level gradient versus wind stress.
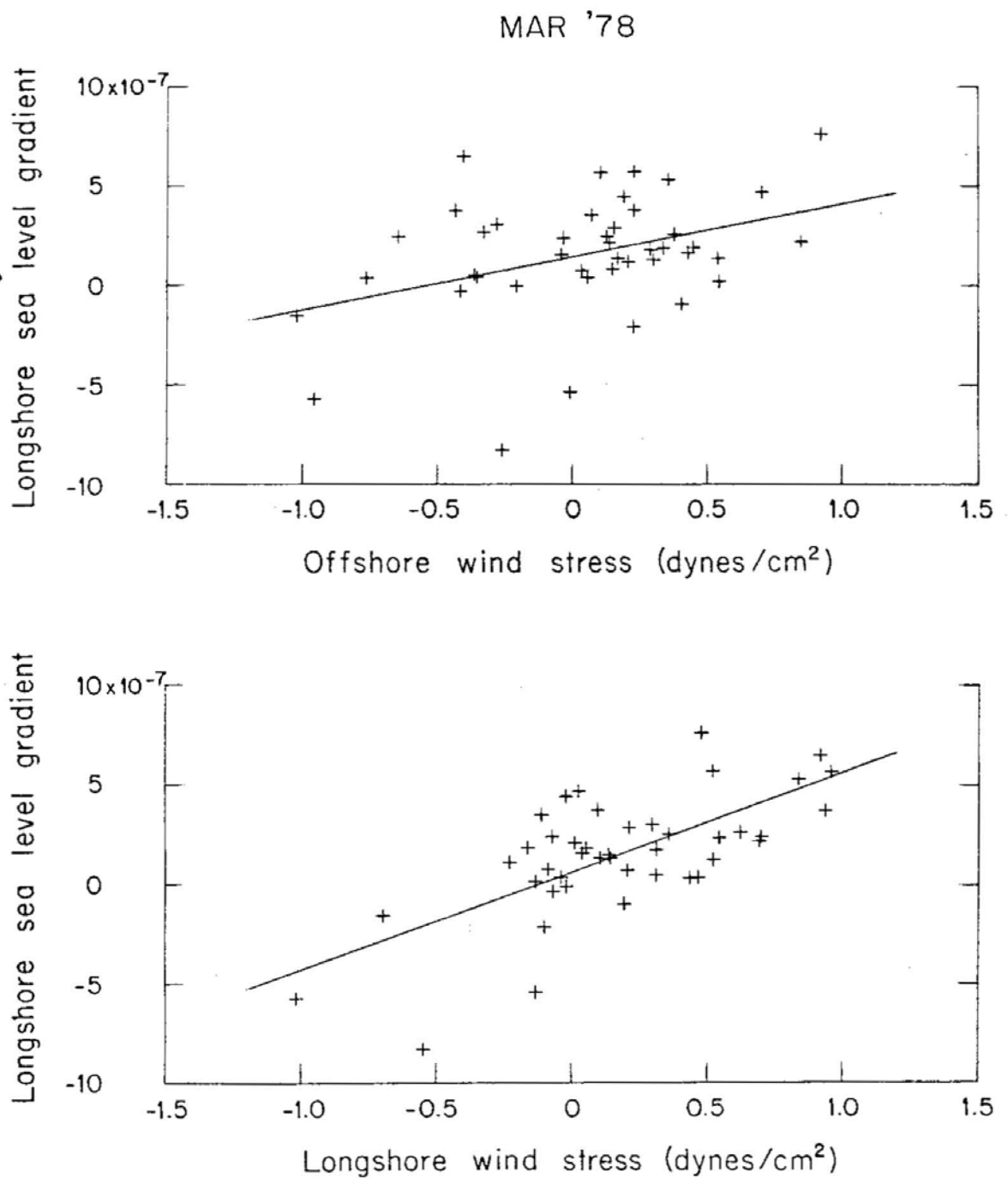
Figure 5.5 Mar '78 longshore sea level gradient versus wind stress.

MAY '77
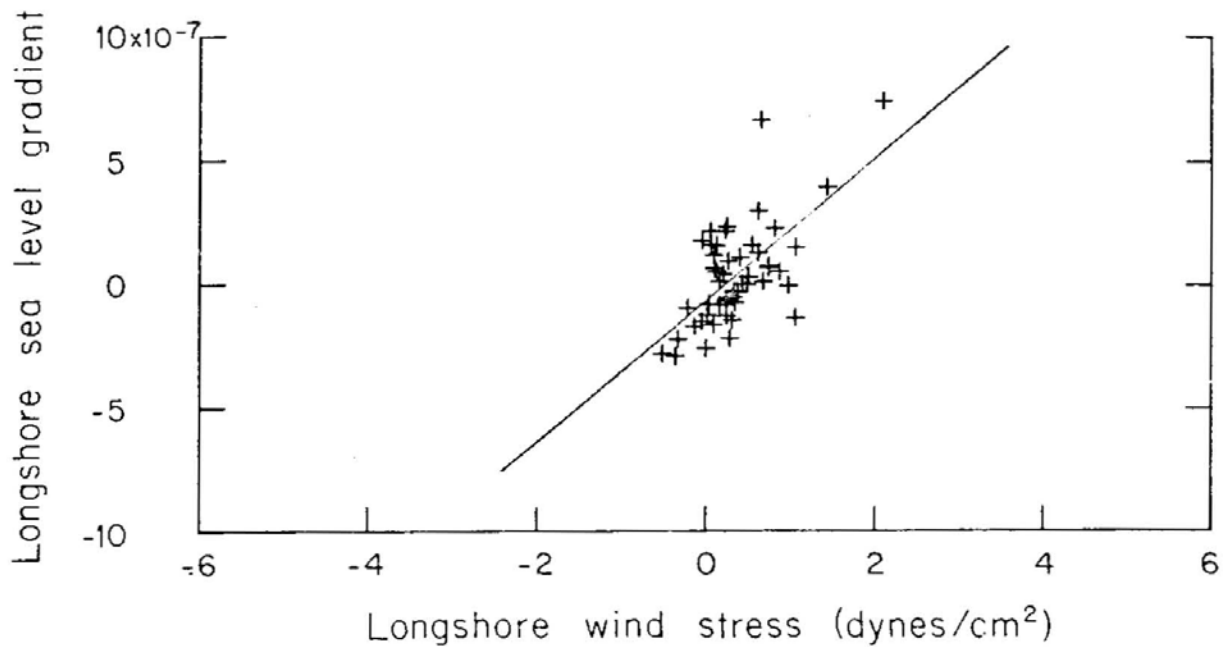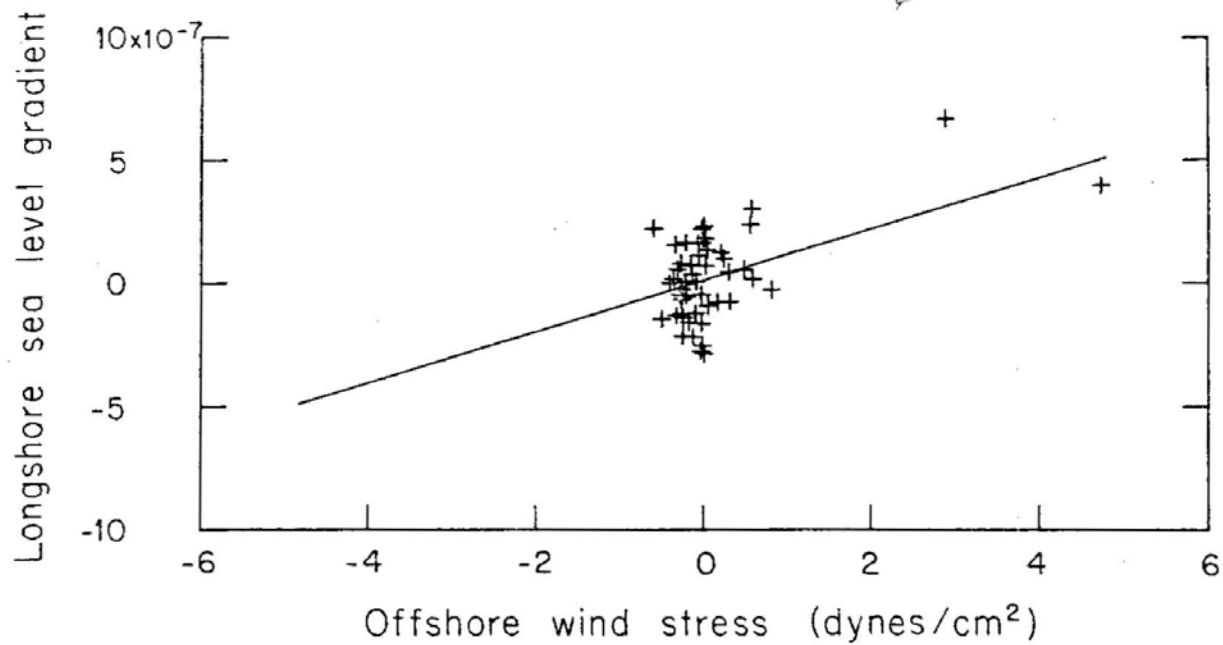
Figure 5.6 May '77 longshore sea level gradient versus wind stress.

OCT - NOV '76
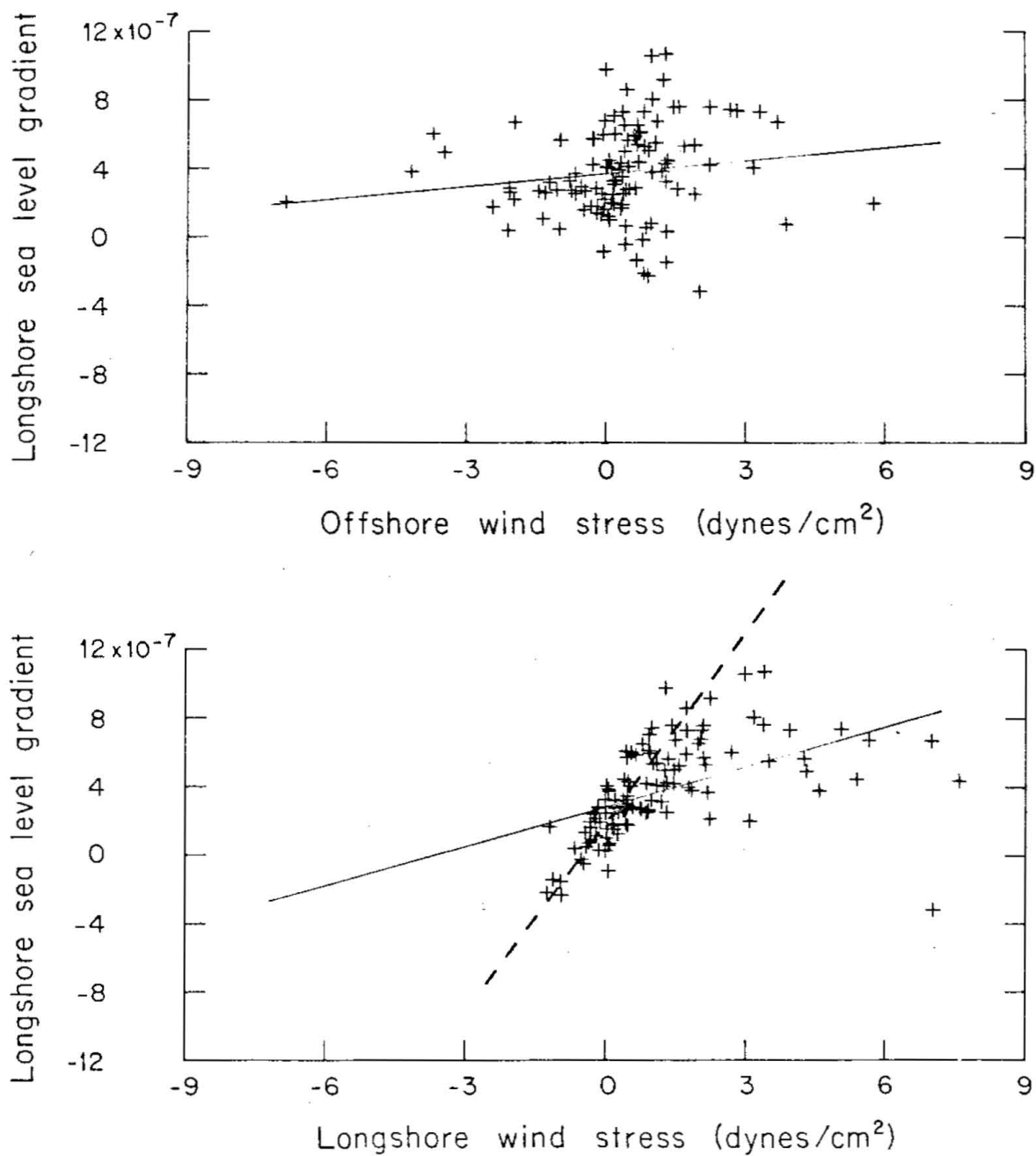
Figure 5.7 Oct-Nov '76 longshore sea level gradient versus wind stress.

Table 5.2

$$(\partial \zeta / \partial y) \times 10^7 = \alpha + \beta \, \tau_x$$
$$(\partial \zeta / \partial y) \times 10^7 = \delta + \gamma \, \tau_y$$

	α	β	δ	γ
Aug '78	1.11	0.13	0.88	2.83*
Mar '78	1.43	2.67*	0.67	4.96*
May '77	0.93	1.04	−0.68	2.86*
Oct-Nov '76	4.60	0.32	3.61	0.96*

* notation signifies slopes statisically different from zero at the 90 percent confidence level. β has units of inverse dynes/cm^2.

tently greater for alongshore wind than for cross-shore. In fact, only one of the cross-shore regression coefficients is statistically different from zero. This means that, in general, variation in cross-shore wind stress did not contribute significantly to variations in the longshore pressure gradients. In contrast, all longshore coefficients are at least marginally significant at the 90 percent confidence level, although deviation from the linear the linear trend calculated for October-November 1976 is considerable. In this case the corresponding scatter plot seems to indicate that a significant linear relationship does hold for the lower wind stress values but that for stresses greater than about 3 dynes the pressure gradient response levels off. This suggests that the response of sea level may be more complicated for extremely strong winds. An "adjusted" linear trend, excluding the extreme points, is shown in figure 5.7 by a dashed line, the slope of which is more consistent with other calculations. Averaging the results of these four experiments leads to the conclusion that, at least for stresses of roughly 3 dynes or less, a longshore wind-stress event induces longshore sea level gradient of approximately (3×10^{-7}/dyne) along Long Island.

While cross-shore wind-stress events were not generally effective in producing fluctuations in the longshore pressure gradient, they are evidently quite capable of doing so in isolated instances. As noted in the upper panel of figure 5.6 the regression slope is effectively determined by a few points at high offshore stress values. That this single event is not sufficient to establish a statistical relationship does not

cast doubt upon the notion that the pressure gradient and offshore wind stress during this episode were physically related as demonstrated in Csanady (1980).

5.2.1 Variation on monthly and seasonal time scales

Although the primary focus of the foregoing discussion of Long Island's nearshore pressure field has been on fluctuations or events of several days duration, experimental mean quantities reveal interesting patterns as well. Table 5.3 lists mean values of longshore pressure gradients and wind-stress components, together with average water levels and their standard deviations, at Montauk and Sandy Hook for various experimental deployments. These data seem to show evidence for both the influence of wind stress and for other, nonlocal effects.

There is a suggestion that the alongshore magnitude of the component of the wind stress and the longshore pressure gradient are positively correlated, although this pattern is to a large extent apparent mainly due to the occurrence of high winds and large gradient in October-November 1976. This is perhaps to be expected since if there are several contributors to the "mean" gradients the wind driven component should stand out under strong wind conditions. On the other hand, a comparison of experimental mean sea surface heights and their standard deviations gives clear evidence of the importance and perhaps dominance of nonlocal effects. Note that for all experimental periods the stan-

Table 5.3

	Aug '78	Mar '78	May '77	Oct-Nov '76
τ_x (dynes)	-0.62E-1	0.49E-1	0.27	0.30
τ_y (dynes)	0.71E-1	0.19	0.37	1.14
$(\partial\zeta/\partial y)\times10^7$	0.99	1.56	0.30	4.55
ζ_{mk} (m)	1.574	1.436	1.393	1.483
σ_{mk} (m)	7.20E-2	1.14E-1	2.87E-1	1.32E-1
ζ_{sh} (m)	1.555	1.406	1.388	1.395
σ_{sh} (m)	8.80E-2	1.38E-1	2.88E-1	1.82E-1

Table 5.3 - Experimental mean values of wind stress components and longshore pressure gradient together with means and standard deviations of subtidal sea surface elevations at Montauk Point and Sandy Hook.

dard deviation or fluctuation of the low frequency sea level at Sandy Hook is larger than that observed at Montauk Point. This observation is in agreement with the work of Wang (1978) who noted that Sandy Hook underwent the largest fluctuations in the middle Atlantic Bight during 1975. However, a comparison of mean sea levels shows that the changes in alongshore pressure gradient from experiment to experiment were due largely to changes in mean water level at Montauk. Ignoring the August '78 experiment momentarily, it is seen that while the mean water level at Sandy Hook remained fairly constant, that observed at Montauk ranged over nearly 10 cm. This would seem to indicate that the mechanism controlling the gradient fluctuations and mean are different. As the fluctuating signal was shown to be primarily wind related, one concludes that the "monthly" mean gradient is not.

Further evidence of the presence of outside influence is apparent from mean sea level records of August '78. During this period sea level was higher by some 15 cm at both coastal stations relative to previous experiments. It is noteworthy that August '78 was also a period of southwestward longshore flow (15-20 cm/sec) which was more than a factor of two greater than the currents previously observed. This situation is consistent with the idea that the coastal sea level rise was associated with a geostrophic flow along the coast. The origin of this striking sea level rise is not clear, except that it is certainly not related to local winds. There is some evidence that this event is a manifestation of a general seasonal cycle. In some comments by Sturges (1978) it is shown that from 1941-1959 sea level at Atlantic City in early autumn was

generally 10-15 cm higher than during the spring or winter seasons. A similar pattern of lesser amplitude was also pointed out for water levels at Boston. It seems likely that the variation of sea level and its longshore gradient, from one experiment to the next, is generally a function of large scale low frequency driving.

5.3 Current meter observations in the CBL

Perhaps the single most striking feature common to all current meter records from the COBOLT experiment, is the visual predominance of fluctuations of inertial-tidal frequency. These relatively short period and large amplitude (order 10 cm/sec) oscillations in some instances all but obscure the underlying long period and aperiodic content of the data. Figure 5.8, representing measurement of the alongshore component of velocity at four vertical positions 3 km from shore, displays several other features which are also quite characteristic of records gathered at this location during all seasons. In addition to the vigorous tidal motions, it is evident that the longshore currents have a substantial negative mean value despite the fact , as revealed in Table 5.3, that the mean longshore wind-stress value was positive during August '78. This situation is the general rule for data collected during the COBOLT program and indicates that the very low frequency currents are not locally wind-driven but are forced primarily by a nearshore pressure distribution which, as discussed above, probably varies on seasonal time scales.

BUOY 1
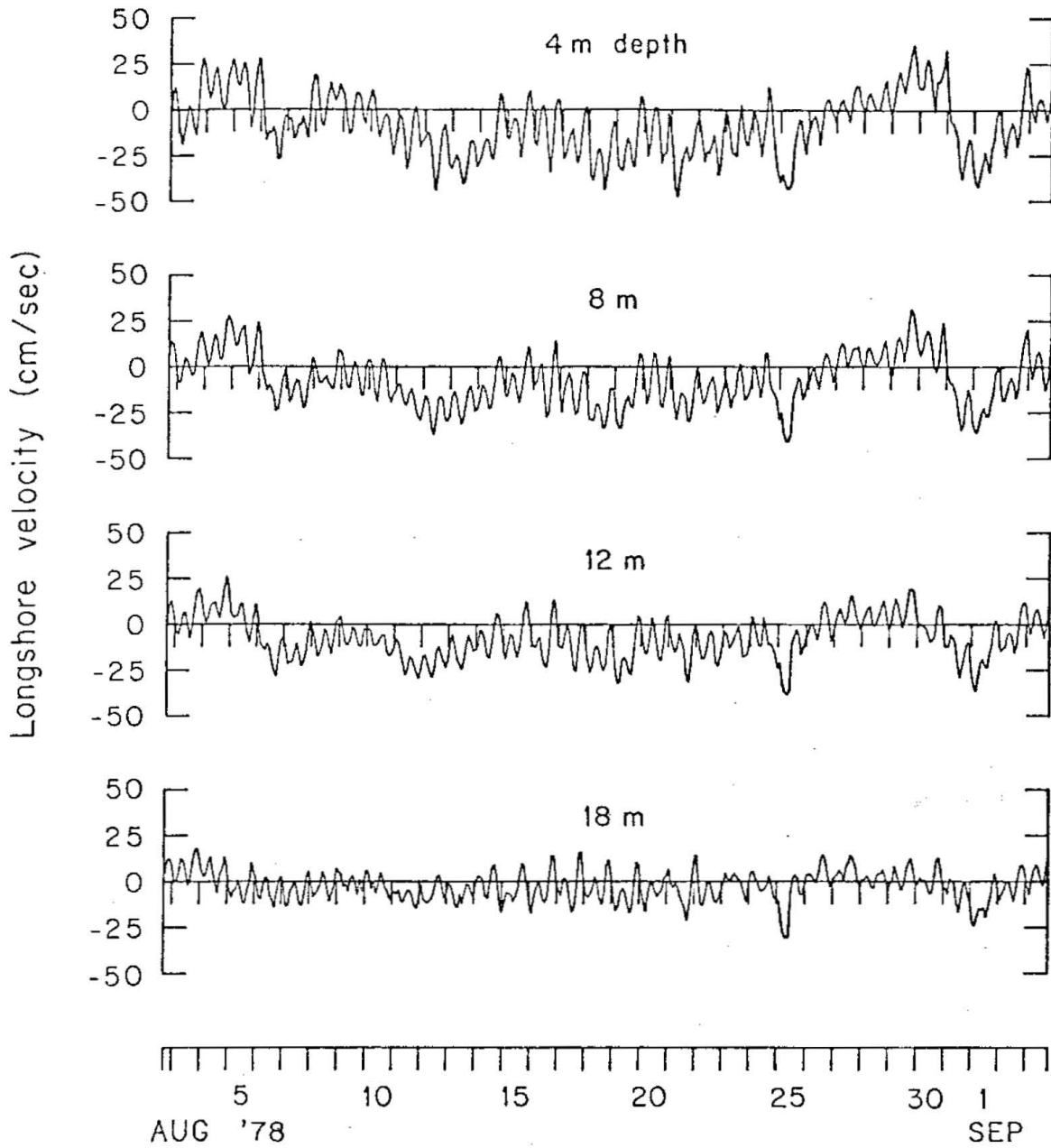
Figure 5.8 Aug '78 current meter records from mooring 1, 3 km from
shore

Another distinguishing characteristic of the nearshore flow behavior is the importance of large magnitude flow episodes which are interspersed throughout the current meter records. Two clear examples of such events occurred on August 25 and September 1. In these instances the accelerations were strong enough to produce currents which rose well above the ambient tidal "noise". The strong southwestward flows encompassed the entire water column, even penetrating to the deepest current meter which was located a scant 2.5 m above the bottom and well within the frictional bottom boundary layer.

Removing the tides via low pass filtering makes more clear the contribution of such events to the overall subtidal flow. Figure 5.9 shows the subtidal alongshore velocity signal at mooring number 4, 12 km from shore. With the short period fluctuations eliminated, several other episodes of first order become apparent. Additional southwestward flow events appear centered at August 13 and 21, as well as one only partially defined at the beginning of the record. In addition, a near surface northeastward event centered around August 8 is evident, as are substantial decelerations in the general negative flow on August 20th, 24th, and 31st. Comparison with either of figures 4.7 or 5.2 reveals that these fluctuations in alongshore velocity are clearly tied to meteorological events. In fact, the subtidal velocity signal is completely dominated by the wind forced component and is fundamentally episodic rather than periodic in nature.

In section 2.4, consideration of complex empirical orthogonal eigenmodes suggested that subtidal velocity fluctuations observed during the

BUOY 4 (filtered)

4 m depth

8 m

16 m

30 m

Longshore velocity (cm/sec)

5   10   15   20   25   30   1
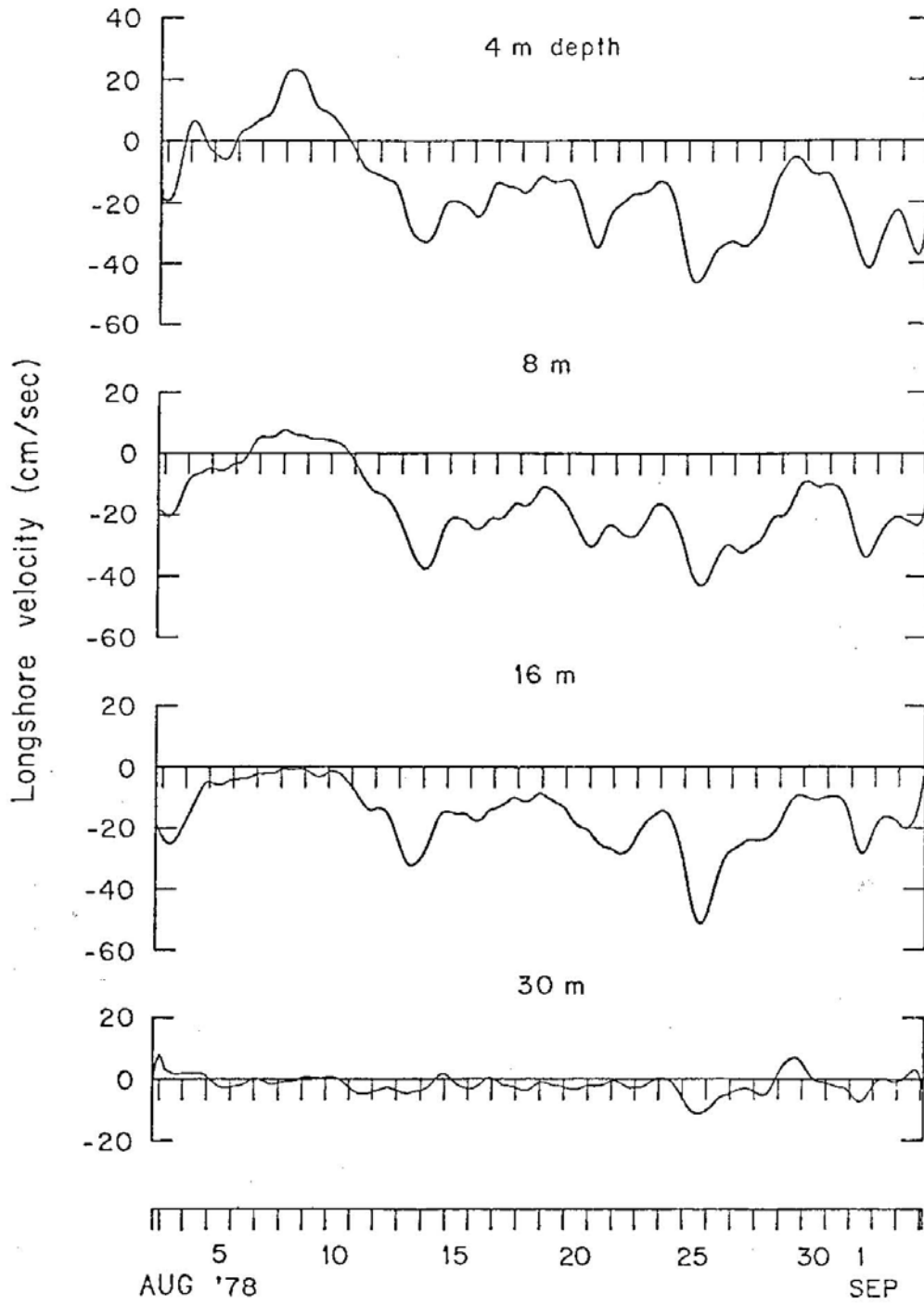
AUG '78   SEP

Figure 5.9   Aug '78 subtidal currents from mooring 4, 12 km from shore

COBOLT program were essentially barotropic in nature and that the sub-
stantial vertical shears observed were of frictional origin. Further
support for this notion comes from the fact that no qualitative differ-
ences in vertical shear were observed between highly stratified (August
'78, May '77) and nearly homogeneous (March '78) hydrographic condi-
tions. The fact that the presence of stratification does not appear to
be of fundamental importance in understanding the behavior of subtidal
currents allows substantial simplifications to be made with regard to
its analysis and interpretation. The current meter data may be verti-
cally averaged (resulting in the reduction of errors due to individual
current meters) without fear that the averaging process has altered or
concealed the basic nature of the signal. In addition, the dynamics of
the system may be investigated in terms of the vertically averaged
equations of motion: a procedure which formally removes the unmeasurable
vertical velocities from consideration.

5.3.1 Depth-averaged longshore currents

Figure 5.10 shows the low passed version of the alongshore component
of wind stress and vertically averaged subtidal longshore currents at
positions 3, 6, and 12 km from shore during the August '78 COBOLT exper-
iment. The vertical averages were calculated by weighting the output of
each current meter according to the proportion of the total water column
it represented, and using a trapazoidal integration procedure. Results
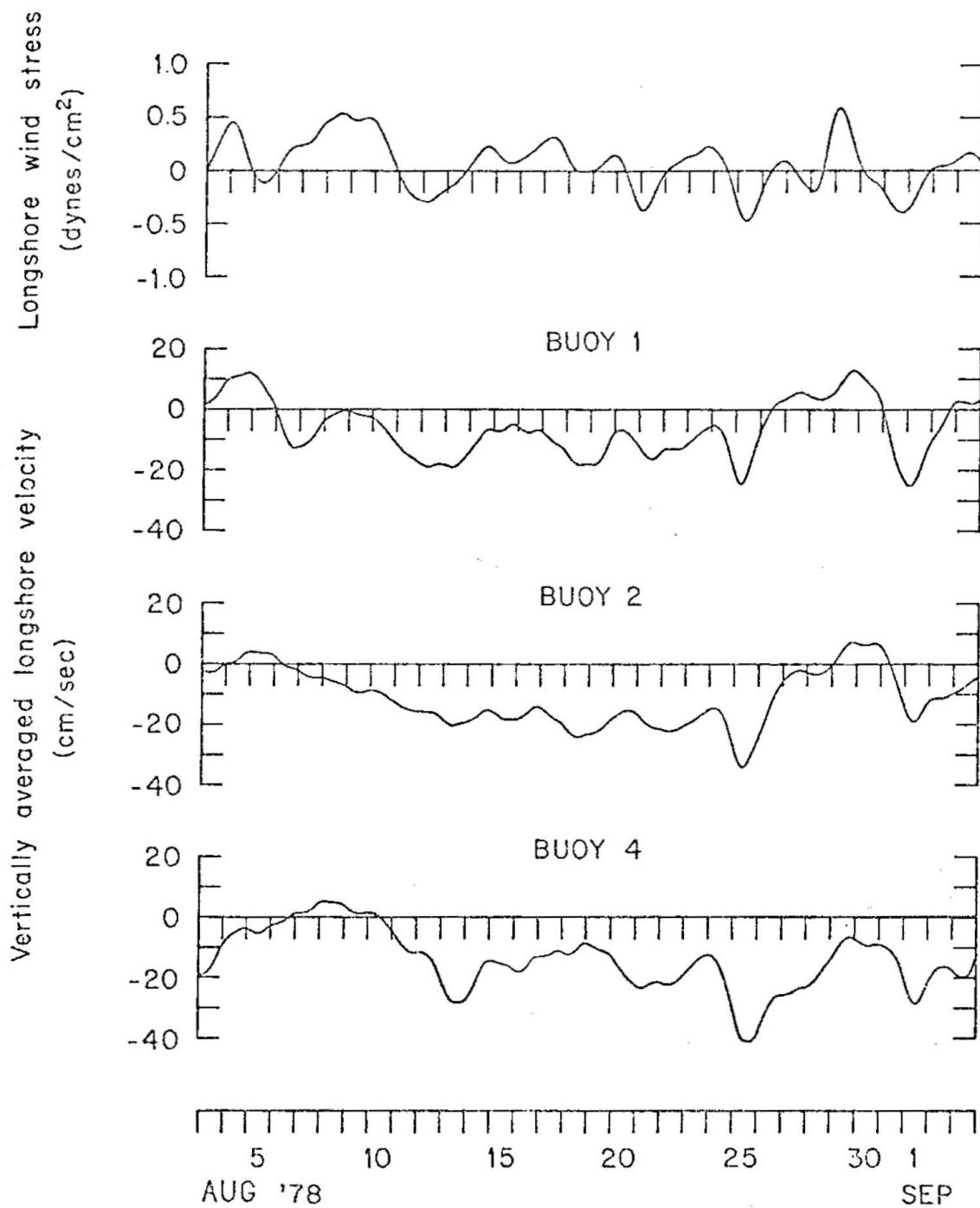
Figure 5.10 Longshore components of wind stress and depth averaged velocity

from the third mooring, 9 km from shore, are not presented here since the most heavily weighted sensor (at 16 m depth) malfunctioned.

Figure 5.10 demonstrates several interesting points. First the visual correlations between all four time series are high, especially in the latter half of the experiment when the wind-stress episodes tended to be of short duration. There can be little doubt that the deviations from the mean longshore current are wind related, just as there is little doubt that the mean flow itself is not. A closer examination of the longshore wind stress and velocity records reveals a suggestion of an asymmetry between the water column response to northeastward and southwestward forcing. This appearance seems to be primarily due to the presence of a substantial mean flow toward the southwest. In this situation even light southwestward winds are associated with strong longshore flow of the same direction while under the influence of northeastward (positive) wind-stress event, currents would be generally weaker and could be of either sign.

Beardsley and Butman (1974) noted a pronounced asymmetry in the response of the continental shelf to three major storms which occurred in March 1973. In this study large wind stresses (~ 3 dynes) acting in nearly opposite directions were observed to produce remarkably different currents. In the one instance of positive longshore wind stress (in our coordinate system) a very large opposing pressure gradient response was noted with little change in the momentum of the water column. The implication of these data was that the pressure gradient and wind forces maintained an approximate equilibrium throughout the event so that there

was little net force accelerating the water column. By contrast, during the two cases of negative wind stress, massive downshelf flow was observed, and the longshore pressure gradient between Nantucket Island and Sandy Hook was an order of magnitude smaller than noted during the positive stress episode. These variations were ascribed to differences in the storm tracks which in the first case resulted in a large longshore gradient in wind stress and precipitated a correspondingly large opposing pressure gradient (cf. Csanady, 1978).

Figures 5.3–5.7 do not show any tendency for there to be a weaker pressure gradient response to negative winds than for positive, although no negative alongshore wind-stress events of comparable magnitude to those observed by Beardsley and Butman occurred in the COBOLT data set. The conclusion drawn is that there is little compelling evidence for a truly asymmetric dynamic response of the CBL under the conditions of predominantly light winds measured during the COBOLT program.

One of the most interesting and dynamically revealing observations arising from the COBOLT experiment is the appearance of a dramatic spatial reversal in the shore-parallel velocity within the coastal boundary layer. Reference to the lower three panels of figure 5.10 shows a clear manifestation of this phenomenon during August 29–30. During this time the vertically averaged currents were flowing in the positive y direction at roughly 10 cm/sec at the two nearshore moorings, while at buoy 4 the flow was nearly –10 cm/sec. This reversal constitutes a mean low frequency shear of 20 cm/sec over just six kilometers. Another perspective of this event is provided by figure 5.11 which presents a daily

AUG 30, 1978
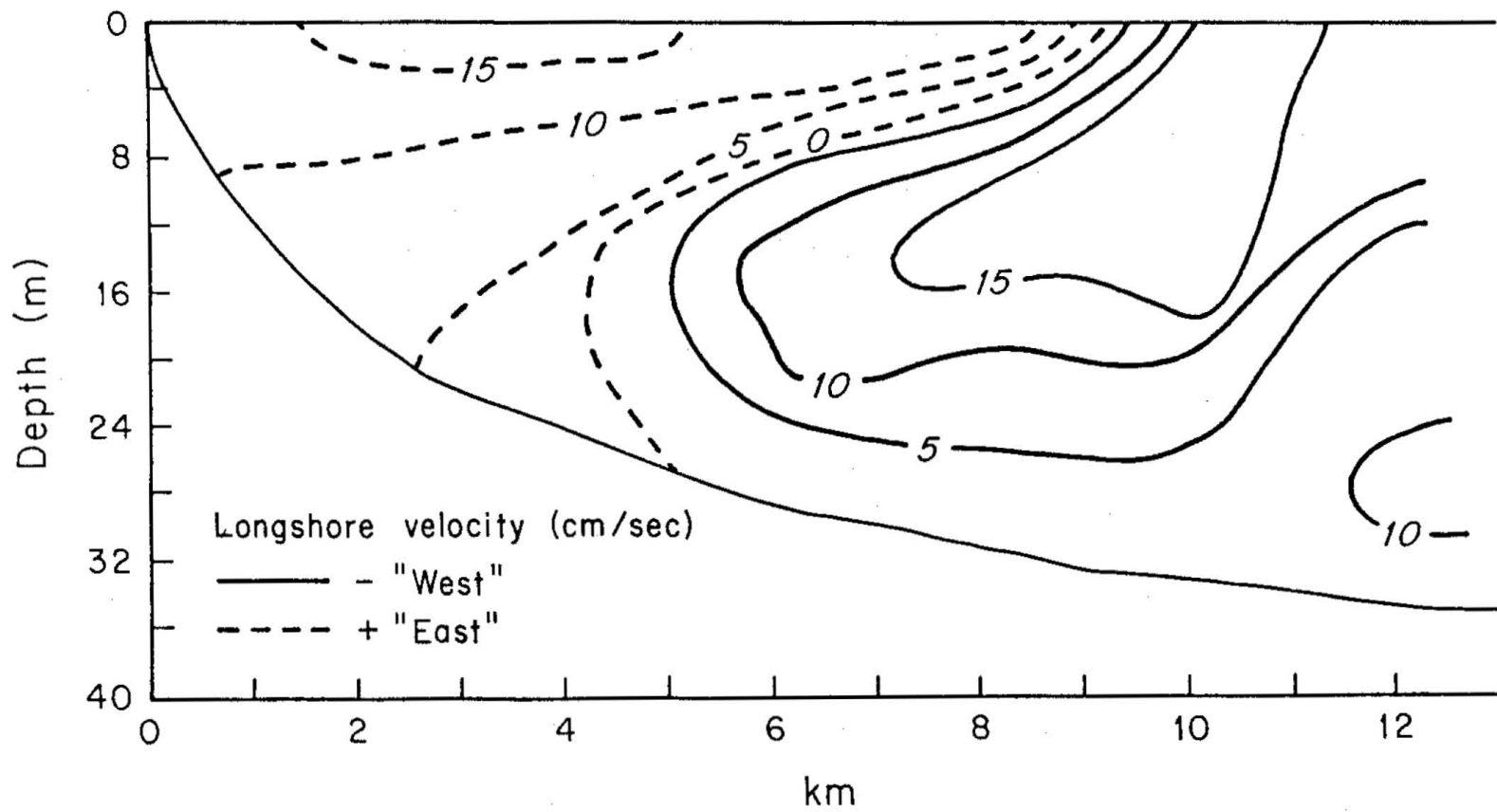
Figure 5.11 Current-meter transect across longshore velocity reversal.

transect from the COBOLT profiling program. Although this picture is influenced and aliased by tidal and higher frequency fluctuations, the overall pattern remains distinguishable. Reference to figure 5.10 seems to indicate the presence of another such event at the beginning of the experiment. Comparison with the wind-stress records shows that, very close to shore, currents flow with the wind while further from the coast, in deeper water, the flow is against the wind. This peculiar behavior has been observed during all COBOLT multi-mooring experiments and generally constitutes approximately 20 percent of the total record length. Figure 5.12 shows a particularly sharp and clear spatial picture of one of the flow reversals which were observed to occur during May 1977. It is noteworthy that these events are exclusively associated with northeastward wind-stress events.

The observation that flow is in the direction of the wind in shallow water but in the opposite direction in deeper environs suggests that this flow pattern is related to spatial variations in the relative magnitudes of the depth-averaged wind-stress and pressure gradient forces. The relative importance of these two forces is topographically controlled as evidenced by the 1/h dependence of the wind-stress forcing. As the water gets deeper a constant wind stress becomes less effective in accelerating the fluid column. Conversely, in very shallow water the nearshore wind stress would be highly effective as its momentum is distributed only over a thin layer. These simple considerations lead one to expect that in the presence of opposing wind stress and pressure gradient forces (the usual situation in the Middle Atlantic Bight)

MAY 23, 1977
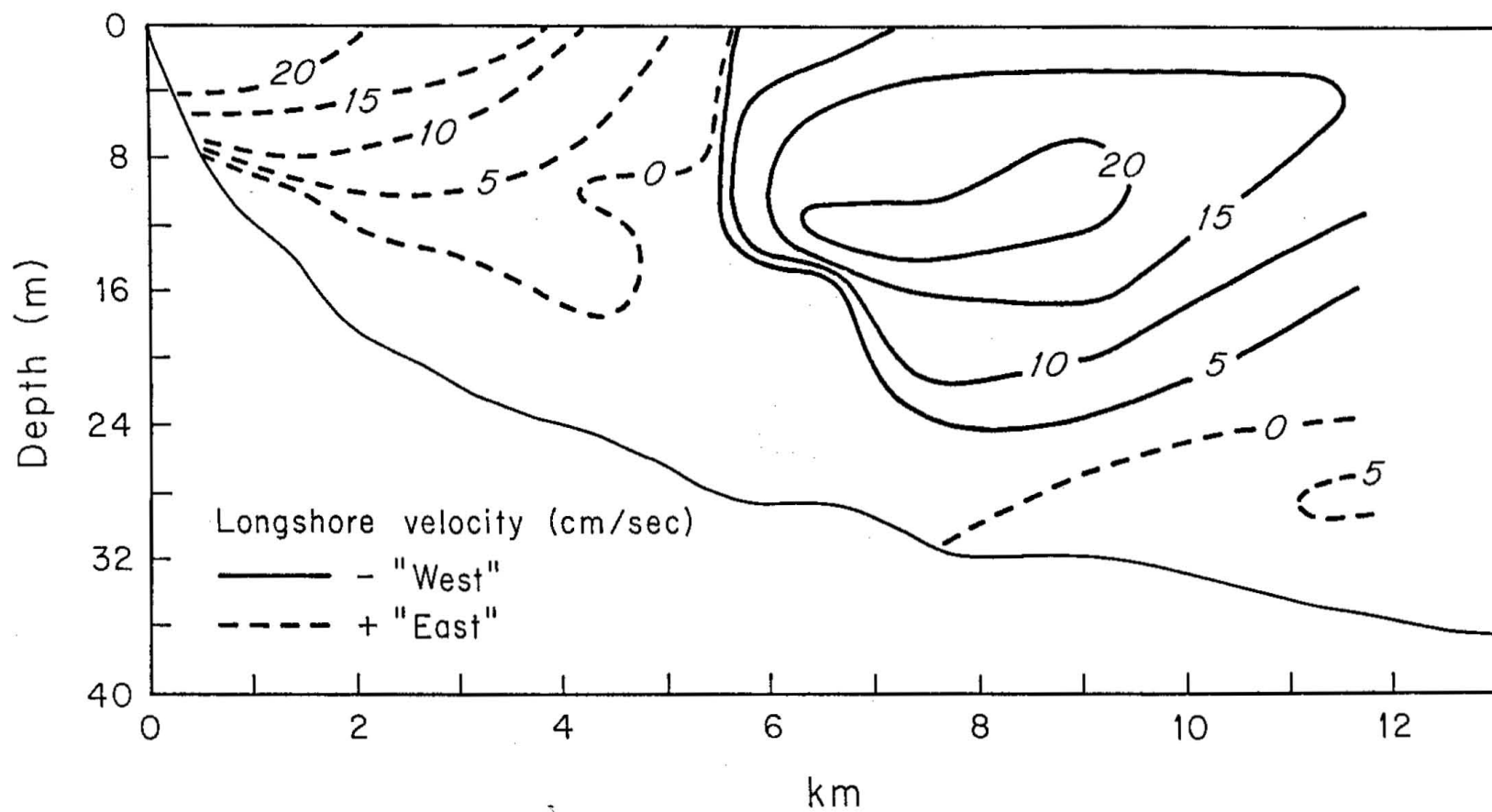
Figure 5.12   Current meter transect across longshore velocity reversal

longshore currents should flow with the wind near shore, pass through zero at some critical depth where there is a force balance, and then reverse farther seaward as the wind stress effects diminish and the pressure gradient predominates. A more detailed consideration of these effects, including the probable physical origin of the pressure fields and the expected locus of the current reversal along the Long Island's shore, is postponed until Chapter VI which discusses theoretical models of nearshore circulation. It is already evident from observations that the Long Island nearshore zone is a region of intense competition between the primary driving forces of the coastal boundary waters.

5.3.2 Depth-averaged cross-shore flow

The measurement of the cross-shore velocity component in the coastal environment is especially difficult. These difficulties arise, either directly or indirectly, as a result of the presence of the coastal boundary which acts as a barrier to the normal flow component. Because of this blocking of flow perpendicular to the coast, cross-shore velocities are generally smaller than longshore velocities. This situation places severe demands upon current meters which may be required to accurately measure flow components differing by as much as an order of magnitude.

A related problem, and one which is not easily resolved, is that of choosing the proper orientation of the coordinate system. All shorelines are curved and irregular to a greater or lesser degree, so that

choosing an alongshore direction to within a degree or so is purely a subjective exercise. In addition, the nearshore isobaths are rarely strictly parallel to the coastline (or to one another) suggesting that the most appropriate coordinate system may vary with distance from shore. In a region where longshore currents are more than an order of magnitude greater than their cross-shore counterparts, an orientation error of a few degrees gives an entirely spurious cross-shore signal. Therefore, before interpreting cross-shore velocity records it is necessary to demonstrate that they contain physically meaningful information.

For the purposes of the present study the onshore coordinate (-x) was chosen to be 22° west of true north (to the nearest degree) by inspection of NOAA chart 12300. In order to test the validity of this estimate, the mean rotary spectral ellipse orientations were calculated for the low frequency (200 hr) currrents at each level and mooring for the three full deployment COBOLT experiments. The major axis, except in the bottom frictional layer, may be considered to define a "dynamical" shoreline in the sense of minimizing low frequency cross-shore motions. The average value was found to be $2.5^{\circ} \pm 2.2^{\circ}$ (95 percent confidence level) clockwise of the graphically determined coastline. Since this small deviation was within the earlier stated (Chapter I) angular resolution of the data acquisition system, further adjustment was not deemed necessary.

Figure 5.13 displays vertically averaged offshore velocities for moorings 1, 2, and 4 during the August '78 experiment. Note that all moorings show a mean offshore flow (and thus transport) over the course
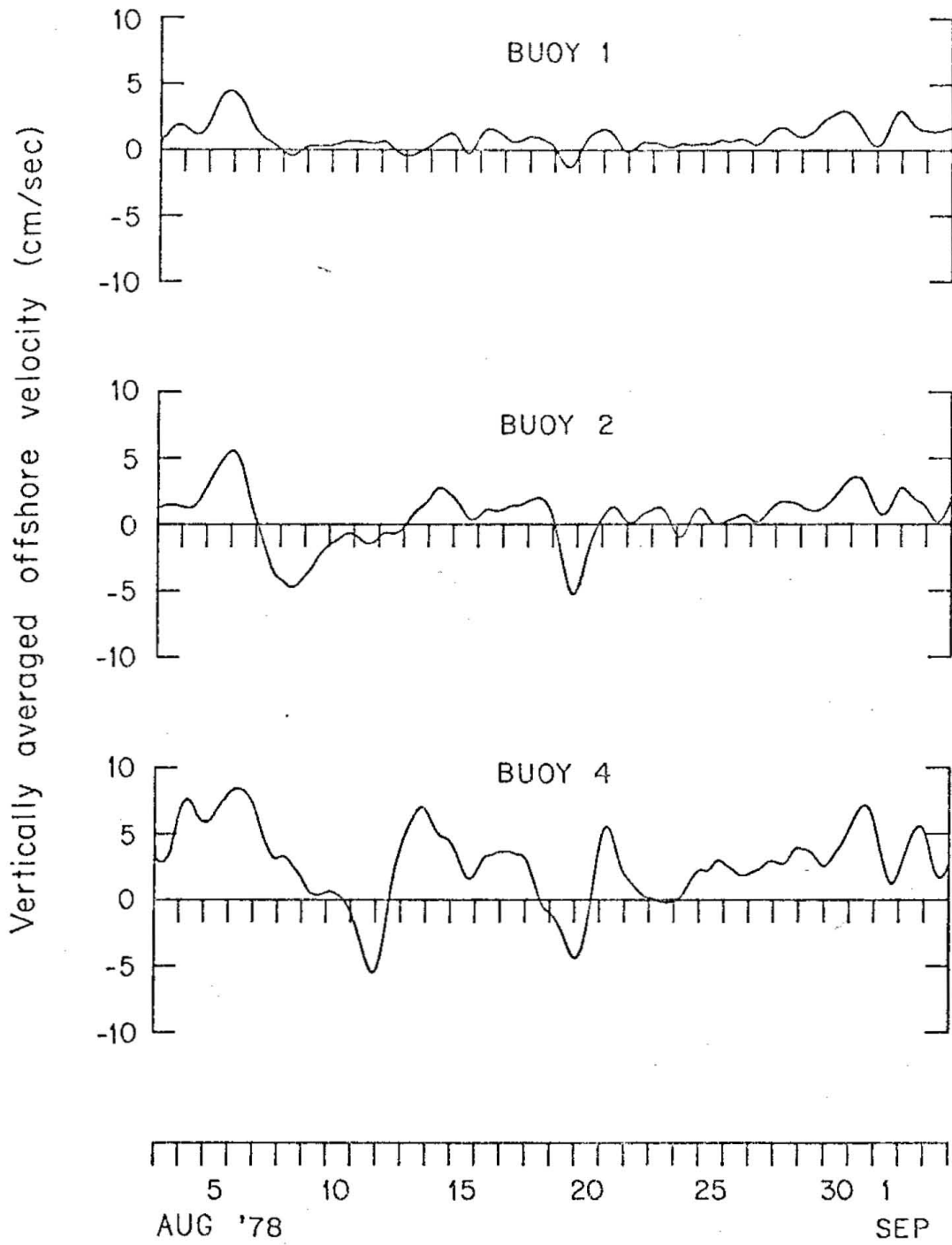
Figure 5.13   Depth averaged offshore velocities

of the experiment. These data suggest that a local two dimensional mass balance, in which surface inflow or outflow is balanced by a compensating return flow elsewhere in the water column, holds neither for particular episodes nor on average. Continuity requirements therefore demand that the coastal circulation be three dimensional in character, so that net offshore flow at one location may be balanced by onshore flow at some other longshore position.

The surprisingly large magnitude of the offshore flow, while to some extent perplexing, is actually strong evidence of its physical reality. As just discussed, a fictitious cross-shore flow could easily be due to uncertainty in the true longshore coordinate direction. However, the large mean value apparent at buoy four, if truly zero, would require an orientation error of nearly 15°. This value is well outside any possible uncertainties. Even more convincing is the evidence of large cross-shore flow events of several days duration. The largest of these, near the beginning of the experiment, would require a 45° rotation to be made shore parallel. In addition to these features being outside the bounds of experimental error, further evidence of their reality comes from their consistent observation. Table 5.4 lists time mean values of the alongshore and offshore velocity components for the entire COBOLT program. In order to avoid severe under-sampling of the water column, vertically averaged values are computed only for those moorings for which all current meters were functional. While these results do show evidence of experimental error, the fact that the cross-shore vertical averages are all directed offshore gives credence to the idea that this

Table 5.4

Mean Values (u,v)

May '77

Bouy number	1	2	3	4
level				
1	----------	(4.9,-4.1)	----------	(3.8,-11.4)
2	----------	(2.7,-5.0)	(0.1,-9.0)	(3.7,-10.0)
3	----------	(-1.3,-2.1)	(-1.7,-5.8)	(-2.6, -7.4)
4	----------	(-2.2,-1.2)	(-1.5,-2.2)	(0.1. -2.3)
depth average	----------	(0.8,-2.7)	----------	(0.2,-7.8)

Aug '78

	1	2	3	4
level				
1	(4.5,-8.0)	(2.8,-12.6)	(5.1,-13.2)	(8.4,-15.7)
2	(-2.8,-7.5)	(-0.2,-12.2)	(-1.9,-14.7)	(2.5,-17.3)
3	(0.4,-7.5)	(-0.9,-13.5)	----------	(-0.7,-16.5)
4	(0.2,-2.3)	(1.5, -4.1)	(-0.5, -3.2)	(1.7, -1.8)
depth average	(0.8,-6.4)	(0.6,-12.1)	----------	(2.3,-14.2)

	Mar '78		Sep '75	Oct-nov '76
	1	3	4	4
level				
1	(0.9,-6.6)	(1.4,-5.0)	(3.1, 14.7)	(3.6, -4.9)
2	(-2.8,-7.5)	(0.2,-5.8)	(2.9, 14.5)	----------
3	(0.4,-7.5)	----------	(1.6, 9.5)	(-1.3, -6.2)
4	(0.2,-2.3)	(-1.4,-2.3)	(-1.1, 4.9)	(-0.2, -3.1)
depth average	(0.6, 6.0)	----------	(1.7, 10.7)	----------

feature is characteristic of the study area.

The occurrence of sizeable offshore transports within a few kilometers of the coast suggests that the routine neglect of cross shore transport in simplifying the vertically averaged equations of motion must be viewed with some caution. The horizontal extent of the boundary condition's prohibition of such transport may apparently be quite limited. The persistence of mean offshore transport at the field site suggests that the circulation cell necessary to conserve mass is a stable feature of the region and that its longshore position may be determined in part by geographical factors. This point of view is consistent with the idea, earlier discussed in terms of pressure data, that the Long Island coast may be subject to influences directly due to its geography.

Although the spatial variations in depth-averaged offshore velocity cannot in general be accurately established in the COBOLT data, the difference between moorings 1 or 2 and 4 shown in figure 5.13 and table 5.4 is significant (see section 5.5.1). The seaward increase of the cross-shore flow component conforms to one's expectation for flow near a coastal boundary, and is analogous to the variation of inertial currents found in Chapter III. In order to satisfy continuity this offshore divergence must be balanced by an alongshore convergence. The alongshore velocity convergence in turn implies longshore variations of the nearshore pressure field. An interpretation of these spatial variations, in terms of a simple conceptual model, is described later in chapter VI.

5.4 <u>Evidence of mean flow against the pressure gradient</u>

Current meter data discussed so far have been primarily from the August '78 experiment. These data represent the most complete coverage in both space and time and are quite representative of the general features observed during other COBOLT deployments. As mentioned in Chapter I, the Brookhaven National Laboratory carried out a single mooring experiment in October-November 1976 at the Tiana Beach site. These data, reported by Scott et al. (1978), in certain respects represent an important exception to the general climatology reflected in other current meter observations collected at this location. Figure 5.14 has been redrawn from Scott et al. and presents daily averaged values of the longshore and offshore flow components at four levels roughly 12 km from shore. This experimental period was characterized by extremely high alongshore velocities which flowed predominantly toward the northeast. These rather spectacular longshore currents, which flowed opposite to the direction in which they are characteristically observed, were associated with equally spectacular wind stresses. Figure 5.15 shows the low passed wind stress records for the months of October and November. The mean alongshore wind stress during this period (see table 5.3) is roughly an order of magnitude higher than values observed during other experiments at this location and the long-term mean during this season (Saunders, 1977). The fact that the mean flow is in the direction of the wind implies that both the pressure gradient and the bottom stress oppose the wind stress 12 km from shore
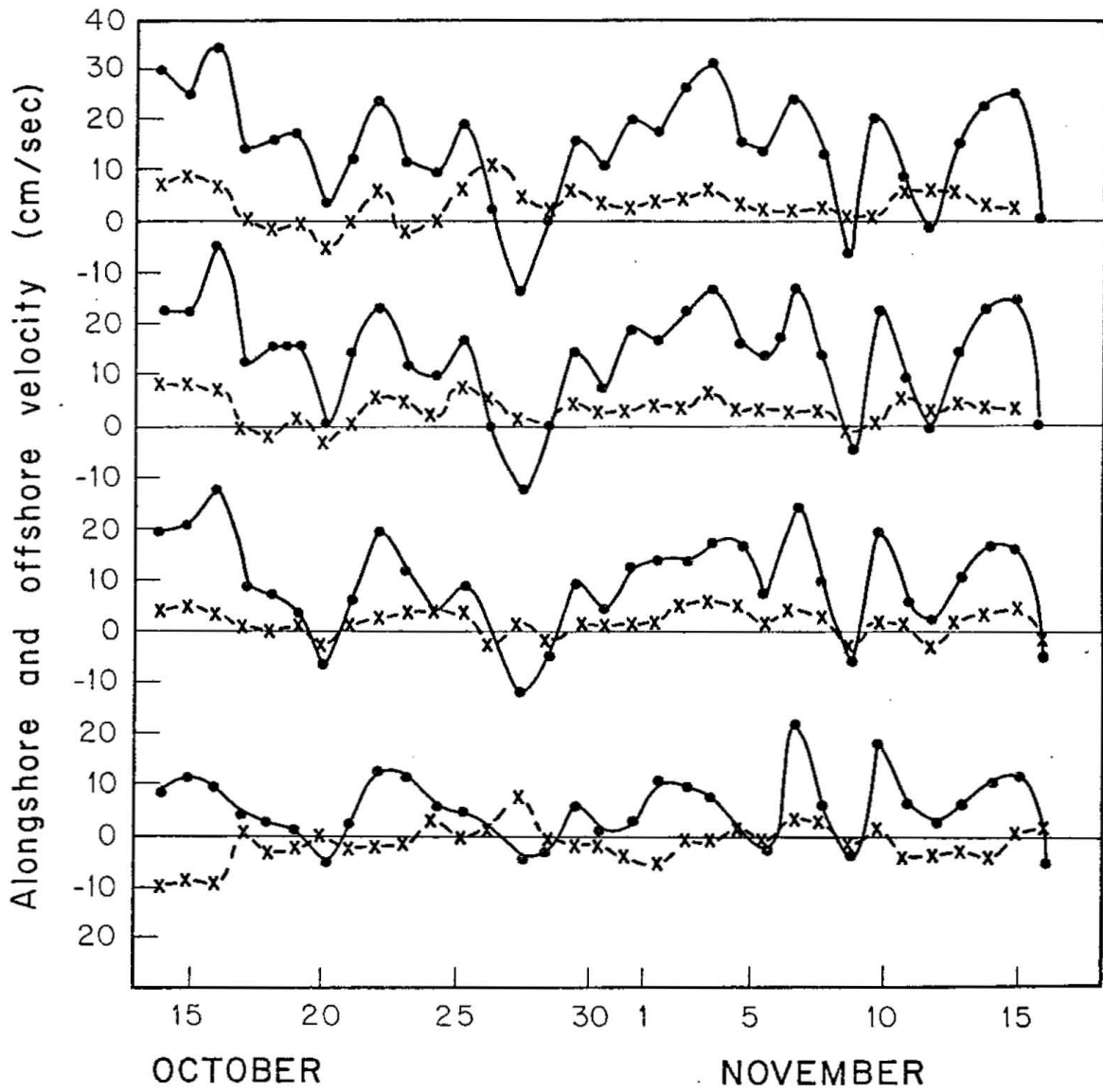
Figure 5.14   Daily averaged velocity components at 4, 8, 16 and 30 m
depths, 11 km from shore
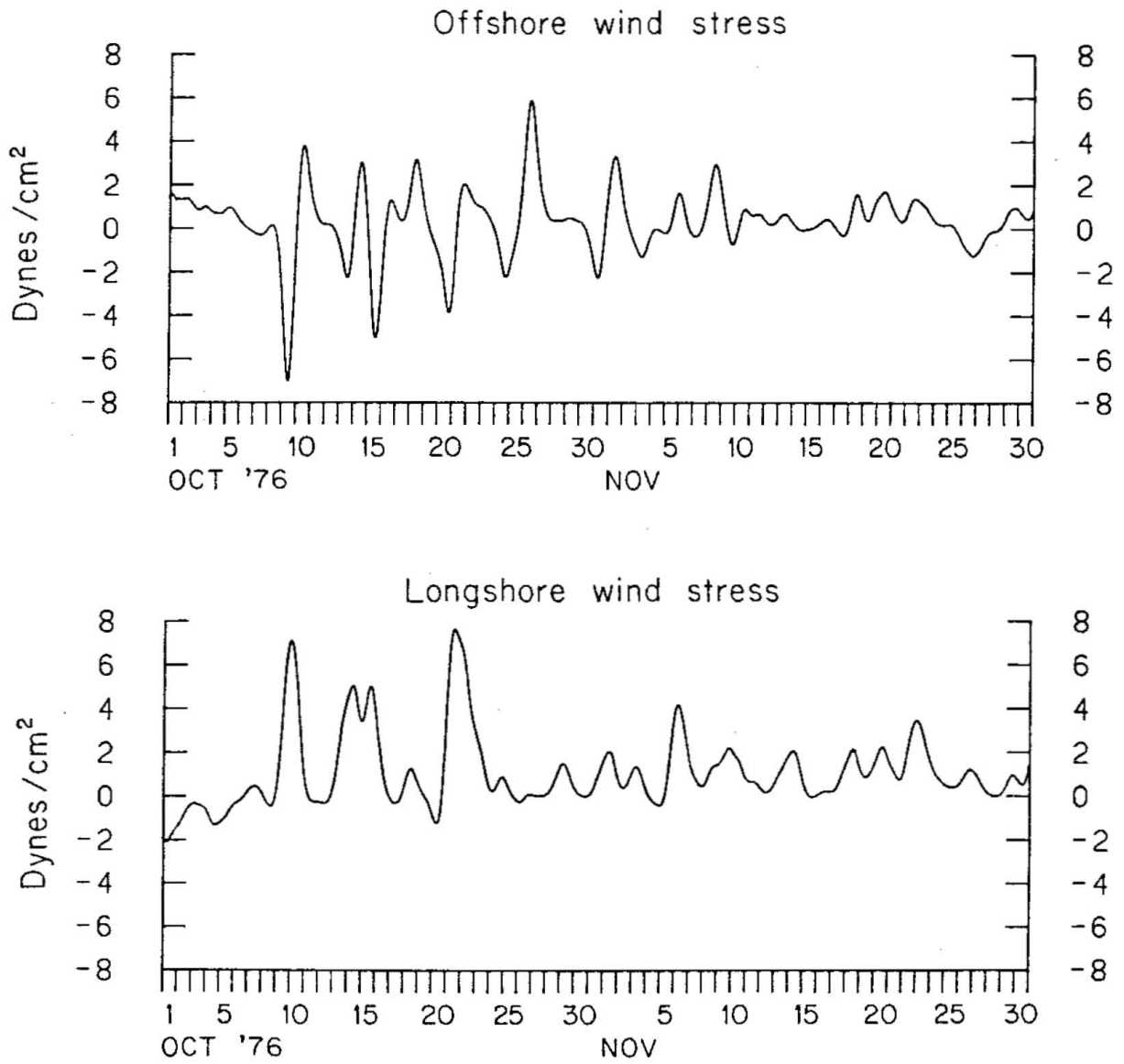
Figure 5.15   Oct-Nov '76 wind-stress records.

and presumably some distance farther offshore. This situation might
have been anticipated in view of figure 5.7 which relates the wind-
stress and pressure gradient forces during this period of high winds.
In the previous discussion of this figure it was noted that a linear
relationship seemed to exist between wind and pressure gradient only for
wind-stress values under 3 dynes. Higher wind-stress values did not
seem to induce a correspondingly higher opposing gradient. This
indicates that under the influence of higher winds, wind stress forces
were not balanced by the sea level response, thereby resulting in large
northeastward velocity and a large opposing bottom stress. Why this
should be so is unclear, but it is certainly a question of the
large-scale response of the shelf to wind stress.

5.5 Momentum balance calculations

One of the most useful methods of obtaining an understanding of the
dynamics of a particular oceanographic environment is the use of obser-
vations in the evaluation of terms in the fundamental equations of
motion. Not all terms in the Navier-Stokes equations can be treated in
this manner. All data sets have limitations with regard to the vari-
ables measured, as well as their accuracy and resolution, which may
preclude useful estimates of various dynamical quantities. Other terms
in the equations may be eliminated from consideration a priori by
scaling arguments which demonstrate their insignificant contribution to

the overall momentum balance. For example, the influence of molecular viscosity may be safely disregarded in consideration of flow features which possess intrinsic spatial scales of order 1 m or more.

From the fundamental equations of motion and continuity, with the use of hydrostatic, Boussinesq, and f-plane approximations, the following time and depth averaged momentum balances may be derived:

$$\frac{\partial \overline{u}}{\partial t} + \frac{1}{h} \left[\frac{\partial}{\partial x} \int_{-h}^{\zeta} <u>^2 dz + \frac{\partial}{\partial y} \int_{-h}^{\zeta} <u \times v> dz - f\overline{v} \right.$$

$$= - g\frac{\partial \zeta}{\partial x} - \frac{1}{h} \int_{-h}^{\zeta} \left[\frac{\partial <u'^2>}{\partial x} + \frac{\partial <v'u'>}{\partial y} \right] dz + \frac{\tau_w^x - \tau_b^x}{h}$$

$$(5.1)$$

$$\frac{\partial \overline{v}}{\partial t} + \frac{1}{h} \left[\frac{\partial}{\partial x} \int_{-h}^{\zeta} <u \times v> dz + \frac{\partial}{\partial y} \int_{-h}^{\zeta} <v>^2 dz + f\overline{u} \right.$$

$$= - g\frac{\partial \zeta}{\partial y} - \frac{1}{h} \int_{-h}^{\zeta} \left[\frac{\partial <u'v'>}{\partial x} + \frac{\partial <v'^2>}{\partial y} \right] dz + \frac{\tau_w^y - \tau_b^y}{h}$$

where $(\overline{u},\overline{v})$ are depth averaged velocities approximated by

$$(\overline{u},\overline{v}) = \frac{1}{h} \int_{-h}^{\zeta} <(u,v)> dz$$

is the sea surface elevation, g is the acceleration of gravity, f is the Coriolis parameter, the τ_w^i and τ_b^i are the components of wind

stress and bottom stress respectively, and the brackets represent the time average operator. The horizontal momentum flux terms have, for the moment, been retained.

5.5.1 Error analysis

Terms involving spatial gradients are a principal difficulty in balance type calculations. Experimental errors may completely mask the true variations across small separations. In Chapter I it was noted that there exists a ± 1 cm/sec uncertainty in each of the component directions due to instrument error. In addition, the coordinate system ambiguity already discussed, while having negligible effect upon long-shore measurements, could on average add an additional 0.5 cm/sec error to the offshore velocities. If the measured offshore velocities u consist of the true velocity u° plus an error ε, a calculated difference between two moorings would on average be

$$\Delta u = \Delta u^{\circ} + \varepsilon \tag{5.2}$$

Although the realized error is likely to be reduced by the vertical averaging process, using an upper bound of $\varepsilon \sim 1.5$ cm/sec, and referring to table (5.4), reveals that the offshore velocity differences between moorings 1 or 2 and 4 in August '78 are marginally significant and could thus provide a crude estimate of $\partial u/\partial x$. In all other cases the errors

are larger than the measured differences.

The situation is even more problematic in the case of quadratic quantities such as the nonlinear advection terms on the left hand side of equation (5.1). Proceeding as before we estimate

$$\Delta u^2 = \Delta u^{\circ 2} + 2\varepsilon (u_i + u_j) \qquad (5.3)$$

Using moorings 1 and 4 of August '78 shows that the error term is several times larger than the measurement so that reliable estimation of the nonlinear terms is not possible. Similar difficulties arise with respect to the horizontal gradients of Reynolds stress terms.

While the inability to directly evaluate the role of nonlinear terms is certainly disappointing, there are good indications that they are probably not of crucial importance. Allen and Kundu (1978) present the results of some approximate calculations which show that, off Oregon, nonlinear effects were small relative to local acceleration and Coriolis terms, although no estimation of errors was given. Flagg (1977) found similar results in his analysis of data from the New England shelf. A numerical model of nearshore currents by Bennett and Magnell (1979) also showed nonlinear effects to be unimportant, especially under high-flow conditions associated with longshore winds. Further support for the notion that nonlinear advection may be neglected with relative impunity comes from scaling considerations which show low frequency nonlinear terms to be insignificant in comparison with frictional forces in the shallow coastal environment. Indications are that the Reynolds stress

divergences may also be ruled out except possibly under conditions of light winds.

5.5.2 The linear time dependent dynamic balance

Dropping the horizontal momentum flux divergences equations (5.1) may be written

$$\frac{\partial u}{\partial t} - fv = -g\frac{\partial \zeta}{\partial x} + \frac{\tau_w^x - \tau_b^x}{h} \qquad (5.4a)$$

$$\frac{\partial v}{\partial t} + fu = -g\frac{\partial \zeta}{\partial y} + \frac{\tau_w^y - \tau_b^y}{h} \qquad (5.4b)$$

where the over-bar notation has been dropped. As greatly simplified as these equations are, several formidable obstacles to accurate dynamic balance calculations still exist. Chief among these weaknesses is the necessity of parameterizing wind and bottom stresses. The drag coefficients used in the traditional quadratic drag laws are uncertain and can easily vary by a factor of 2 depending upon the sea state and bottom topography. This means that any shallow water dynamic balance calculations must be treated largely as a qualitative exercise in which only general correlations and orders of magnitude may be demonstrated. In the following calculations a bottom drag coefficient of 5×10^{-3} was

taken as representative for this environment (private communication W. Grant), and once again the variable drag coefficient of Amorocho and Devries (1979) was used to calculate the wind stress.

Figure 5.16 shows the horizontal (across the mooring array) average of the terms in the cross-shore momentum balance with the important exception of the cross-shore sea surface gradient which was not measured. Since none of the other terms are comparable to the Coriolis force we must assume that the latter is balanced by the cross-shore pressure gradient. The overwhelming dominance of the Coriolis force associated with longshore flow is strong evidence of a nearly geostrophic cross-shore momentum balance. This finding is no surprise as there is ample evidence of cross-shore geostrophic balance in other coastal regions (e.g., Huyer et al. (1978), Winant (1980)).

The nature of the longshore momentum balance in coastal regions has been a bit harder to deduce and has received increasing attention in recent years. Scott and Csanady (1976) supposed a mean balance to exist between frictional effects and a constant longshore pressure gradient, and interpreted nearshore currents off Long Island in terms of this balance. Bennett and Magnell (1979), and Beardsley and Winant (1979) later concluded that a pressure gradient which responded to wind forcing was a much more attractive hypothesis. Systematic attempts at directly evaluating the mean dynamic balance of the eastern shelf of North America were made by Flagg (1977) and by Smith et al. (1978). Smith et al. showed that Reynolds stress divergences associated with tidal and wind forcing were negligible on the Scotian Shelf and found support for
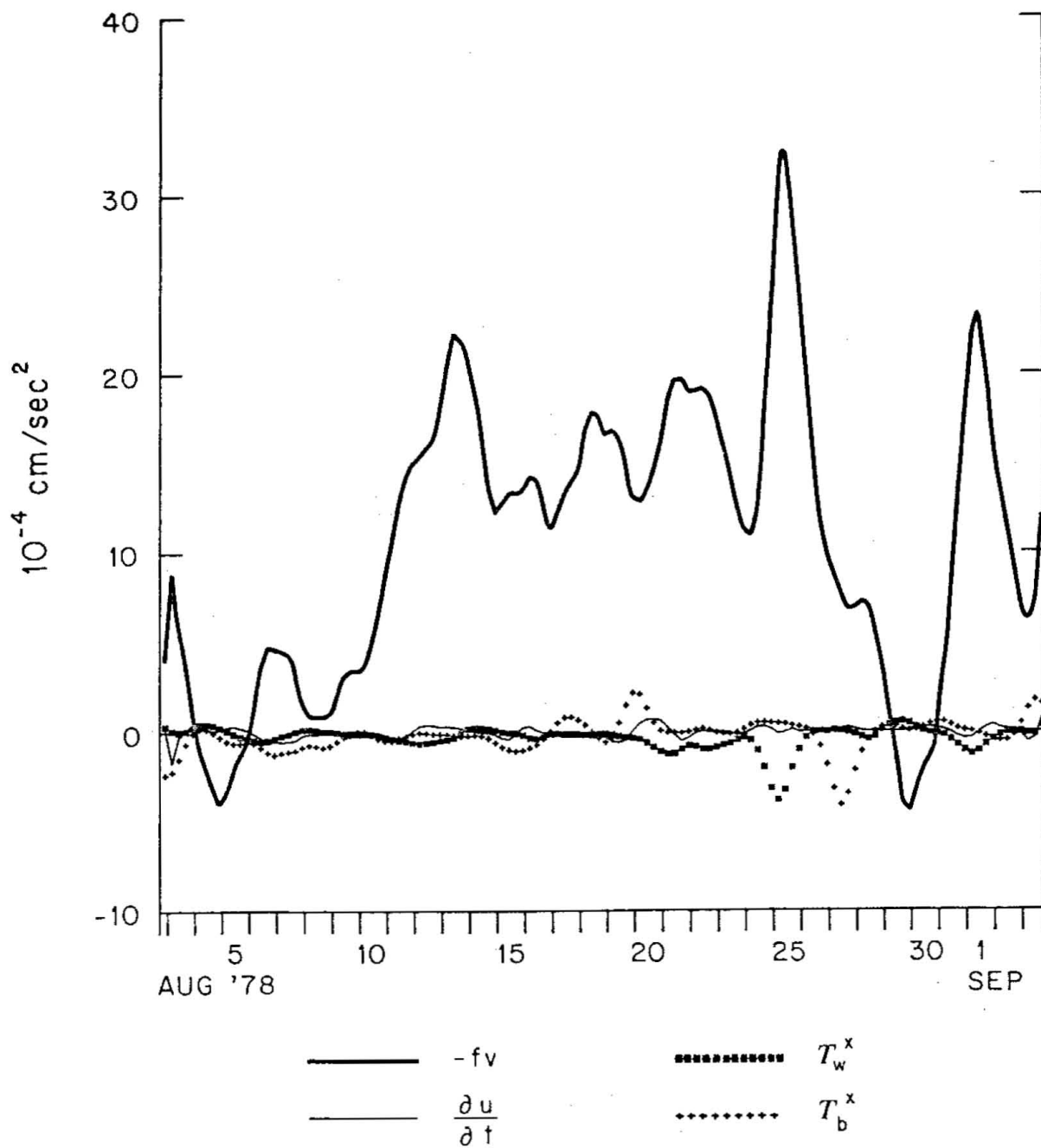
Figure 5.16 Comparison of terms in the cross-shore momentum balance.

the ideas of Scott and Csanady. Unfortunately neither the Coriolis force associated with the vertically averaged cross-shelf flow nor the longshore pressure gradient could be estimated. Flagg indicated that while momentum advection was negligible relative to Coriolis acceleration in the time dependent balance, it could be important in steady state. As mentioned earlier, Allen and Kundu (1976) performed dynamic balance calculations for an assumed inviscid interior off the coast of Oregon but as Csanady (1981) has recently pointed out these data actually show strong evidence of the importance of frictional effects. Brink et al. (1975), in a related study of the Peruvian coast concluded that bottom friction played an important role but did not include it in balance calculations.

In the present study estimates of all terms appearing in equation (5.4b) are calculated for Aug. '78 and their horizontal average is presented in figure 5.17. The top panel of the diagram represents the longshore pressure gradient force $(-g\ \partial\zeta/\partial y)$. As before y is positive toward the northeast so that a negative force represents highwater at Montauk relative to Sandy Hook. The true zero of the time series is unknown although as earlier mentioned, it has been estimated from Chase (1978). The second panel displays the depth averaged values of wind stress (solid line) and bottom stress (dashed line). There is a clear tendency for wind stress and bottom stress to oppose one another during negative windstress episodes. For positive winds the two stresses often act in concert as a consequence of the general negative longshore mean flow. It is also notable that the major wind stress and pressure
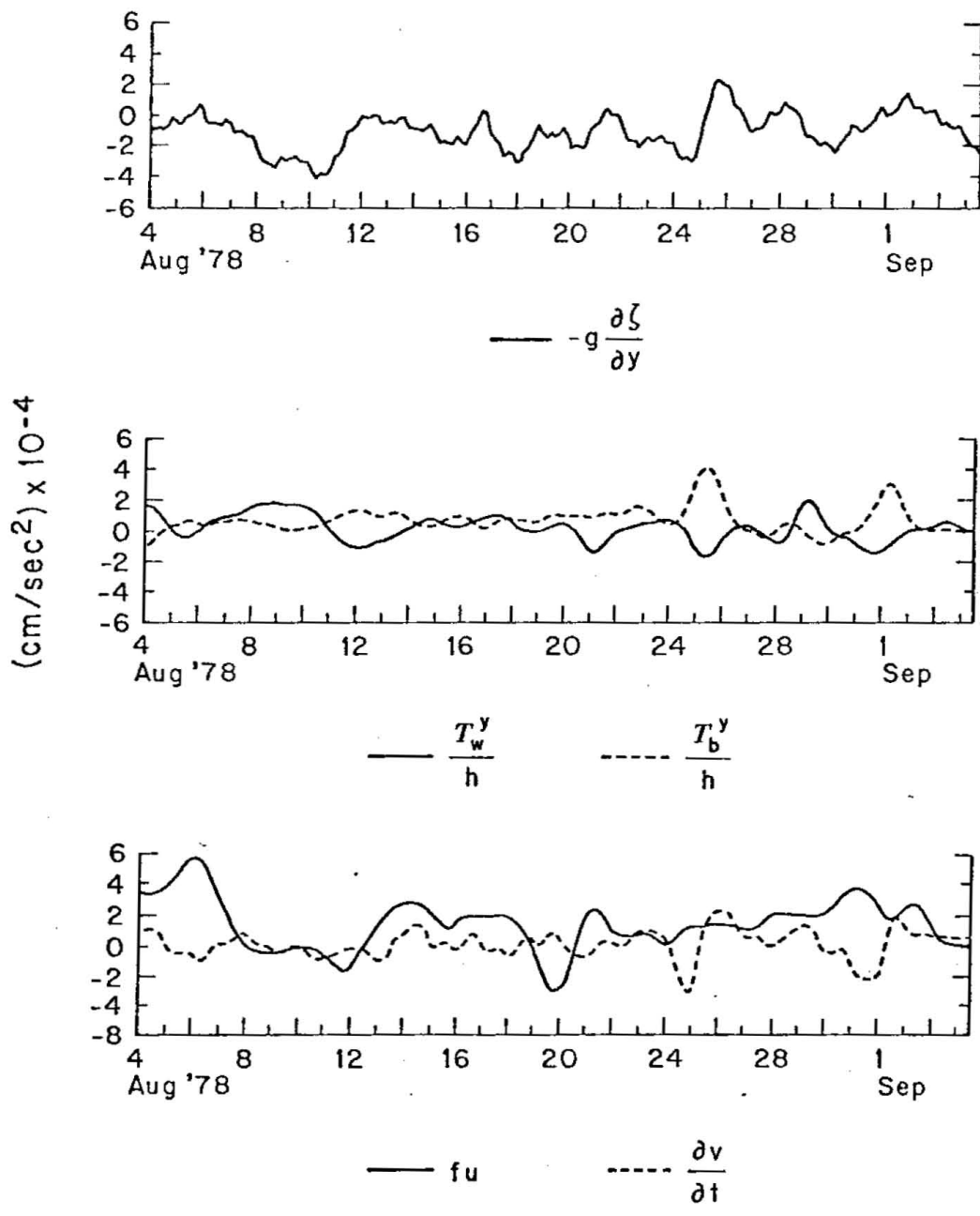
Figure 5.17 Comparison of terms in the alongshore momentum balance.

gradient events are negatively correlated and of comparable magnitude.

The bottom panel of figure 5.17 displays the lefthand side of equation (5.4b) with the solid line representing the Coriolis acceleration associated with cross-shore flow (fu) and the dashed line the local acceleration ($\partial v/\partial t$). Several interesting features are noted in this figure. First, although the cross-shore velocity is generally positively correlated with wind forcing, the large magnitude events at either end of the record (centered at August 6 and September 1) violate this pattern. While the September 1 event is largely balanced by the local acceleration term, perhaps indicating the presence of a shelf wave (Allen and Kundu, 1978), the Coriolis force associated with the August 6 event appears to be unbalanced by any of the other terms in the linear equation of motion. Although it was previously pointed out that this offshore flow is much too large to be ascribed to measurement error, it is nevertheless reassuring to have some independent verification. Figure 5.18 shows an offshore velocity cross section for August 7 as measured by a ducted impeller current meter with a directional vane which was lowered over the side of the R.V. COBOLT. The contours display a somewhat complex structure and the data are undoubtedly aliased to a certain extent, but the measurements do clearly reflect the anomalously high offshore flow in confirmation of the time series data.

Once the physical reality of this offshore flow is accepted, one must conclude that its associated Coriolis force is in fact balanced by other dynamical terms. As already discussed, any of the terms which have been neglected in equation (5.4b), and therefore not represented in

AUG 7, 1978
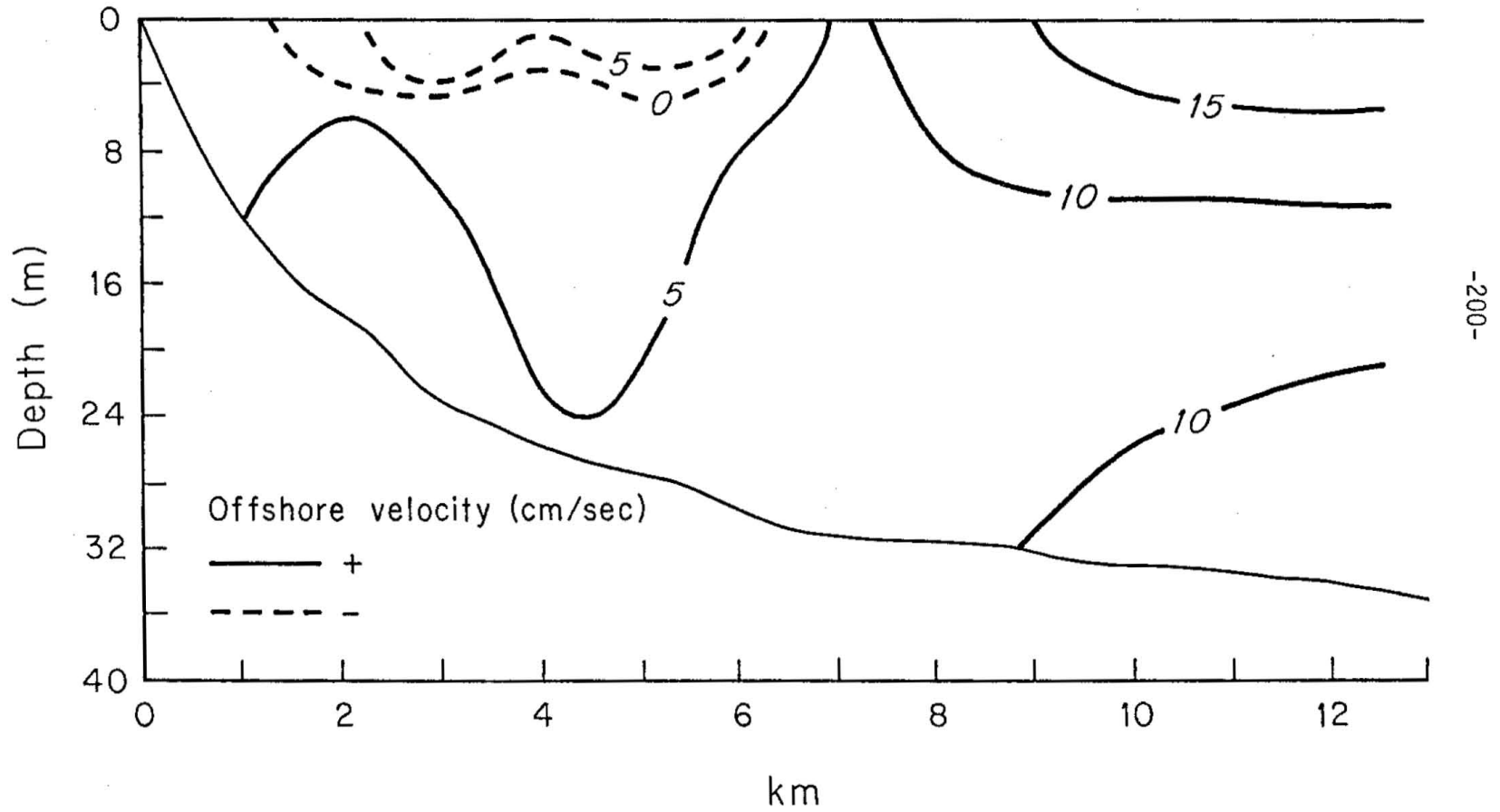
Figure 5.18 Aug 7, 1978 offshore velocity section.

figure 5.17, are unlikely to be capable of achieving the necessary magnitude. This dilemma may be resolved by the recognition that the pressure gradient measured between Sandy Hook and Montauk may not be an accurate estimator of the local gradient; especially in instances where the alongshore length scale is small relative to this separation. Referring back to figure 5.13 shows that during the episode under consideration the value of $\partial u/\partial x$ is massive ($\sim 3\times10^{-6}$ sec^{-1}). From continuity we expect $\partial v/\partial y$ to be of similar magnitude and may estimate the scale of longshore variation in v to be $\sim$ 30 km. This distance, which likely also scales the trapped pressure field, is nearly an order of magnitude smaller than the $\sim$ 200 km separation between the coastal sea level stations. It seems plausible that the Coriolis force in this episode is largely balanced by a local sea surface slope of roughly 1 cm over 30 km.

Further examination of figure 5.17 reveals that although on two occasions the local acceleration $\partial v/\partial t$ is comparable to the Coriolis acceleration, in general its relative contribution is insignificant. This suggests that for the major portion of the record, the dynamic balance may be considered approximately steady. One should remember at the same time, however, that the acceleration has an rms amplitude which is similar to that of bottom friction. The important difference between these two effects is that the local acceleration averages to zero over short (several day) periods whereas bottom friction maintains significant nonzero values over all time scales.

5.5.3 The steady dynamic balance

Table 5.5 shows the horizontal and time mean values of dynamical terms in the vertically averaged linear equations of motion, for the May '77 and Aug. '78 COBOLT observations. $\partial v/\partial t$ over such long periods is insignificant as just mentioned. These calculations support the widespread idea that the cross-shore momentum balance in coastal regions is primarily geostrophic. The relatively high mean offshore wind stress in May '77 is due largely to a single storm which occured on May 10 as was previously shown in figure (4.3). If this extraordinarily large event is. removed from consideration, the monthly mean value of τ_w^x would be 0.3 rather than 1.0. A similar treatment of the longshore velocity would reduce fv to 4.6 which is still an order of magnitude greater than the wind-stress forcing.

The results of the alongshore calculations are not as definitive. While the magnitudes of all terms estimated are within a factor of 3 or 4 of one another, indicating that all have non-negligible effects, there is also a sizeable force imbalance. This fact may or may not be a reflection of the importance of additional terms which have been neglected in the mean balance. As stated earlier, there are uncertainties on the order of 50 percent in the estimation of all these terms and the longshore equation does in fact balance within these error bounds. In addition, the mean values of the local alongshore sea surface slope may not be well represented by the Montauk to Sandy Hook averages.

While these calculations do not demonstrate the insignificance of

Table 5.5

Mean Momentum Balance
in units of 10^{-4} cm/sec^2

Cross-shore equation:

	$-fv$	$=$	$-g\partial\zeta/\partial x$	$+\ \tau_w^x/h$	$-\ \tau_b^x/h$
May '77	5.8		-----	1.0	0.1
Aug '78	10.8		------	-0.2	-0.1

Alongshore equation:

	fu	$=$	$-g\partial\zeta/\partial y$	$+\ \tau_w^y/h$	$-\ \tau_b^y/h$
May '77	0.5		-0.3	1.3	0.6
Aug '78	1.2		-1.0	0.3	0.8

neglected terms, they do at least demonstrate the significance of those included. In this spirit, the equations

$$fv = g \frac{\partial \zeta}{\partial x}$$

and

$$fu = - g \frac{\partial \zeta}{\partial y} + \frac{\tau_w^y - \tau_b^y}{h}$$

(5.5)

may be thought of as a set of dynamical terms which are necessary (and may be sufficient) to adequately model the observed steady flow structures within the CBL off Long Island. Because the time dependent balance calculations, as reflected in figures 5.16 and 5.17, demonstrated the relative unimportance of the local acceleration term for periods of several days, it is also suggested that the steady equations (5.5) are also appropriate for consideration of quasi-steady episodes of such duration.

5.6 A comparison of linear and quadratic bottom friction

The introduction of a linear bottom frictional drag law into equation (5.5b), in place of the quadratic form used in the calculation of the previous sections, would represent a substantial analytical simplification in the consideration of models of nearshore flow. As Csanady (1976) has pointed out, in flow regimes in which the fluctuations are much greater than the mean, substitution of a linear drag law may be

made with relative impunity. Because of this and other flow conditions, the coastal boundary layer is a region in which the assumption of linear bottom friction is particularly appropriate.

Use of a Reynolds decomposition allows the quadratic bottom drag to be written as

$$\tau_b^y = c_d vq = c_d (v'q' + v'<q> + <v>q' + <v><q>) \qquad (5.6)$$

where c_d is the drag coefficient, and $q = (u^2 + v^2)^{1/2}$. The filtered or time-averaged version of this expression reads

$$<\tau_b^y> = c_d(<v'q'> + <v><q>) \qquad (5.7)$$

which represents the appropriate frictional force acting on the slowly varying flow field. As Csanady points out, in a flow characterized by large fluctuations such that v' >> <v>, <q> is of order v' and very nearly independent of <v>. This situation allows the term <v><q> to be written as r<v> (where $r = c_d <q>$ and has units of velocity). The additional fact that the coastal boundary constrains energetic fluctuations to be strongly polarized in the longshore direction suggests that the second term in (5.7) (<v'q'>) will be small. Consider, for example, a sinusoidally fluctuating component

$$v' = A \sin(\omega t)$$

If $v' \gg u'$, the term $\langle v'q' \rangle$ may be approximated by

$$\langle A \sin(\omega t) (A^2 \sin^2(\omega T))^{1/2} \rangle$$

which is identically equal to zero. Therefore if v' is sufficiently greater than u' and $\langle v \rangle$ one expects quadratic and linear formulations to be equivalent and the bottom stress may be written

$$\langle \tau_b^y \rangle = r \langle v \rangle \tag{5.8}$$

. In order to test this hypothesis, the low passed time histories of quadratic and linear terms were compared during the May '77 and Aug. '78 experiments. The results of these correlations are listed in table 5.6 along with the ratio of the standard deviation of the alongshore flow (v_{sd}) to its mean, and the ratio v_{sd}/u_{sd}. The correlation coefficients calculated are all highly significant at the 99 percent confidence level, and are in fact near unity. The table also shows that values of $v_{sd}/\langle v \rangle$ and v_{sd}/u_{sd} of only 2 or 3 are apparently large enough to satisfy the conditions leading to equation (5.8).

The degree of correspondence between the two parameterizations is self evident in figure 5.19 which compares linear and quadratic stresses at 3 offshore positions during Aug. '78. A drag coefficient of 5×10^{-3} and an r value of 0.05 cm/sec were used in these comparisons. It seems clear that no features of importance are either missed or introduced by the linearized stress, and that the two formulations are equivalent in their effects.

Table 5.6

Linear-Quadratic Bottom Stress Correlation

	Bouy	correlation coefficient	v_{sd}/v	v_{sd}/u_{sd}
	2	0.97	6.39	1.92
May '77	3	0.95	3.96	2.00
	4	0.95	4.06	1.83
	1	0.92	3.47	1.54
Aug '78	2	0.93	1.96	1.54
	4	0.96	3.93	1.29

Table 5.6 - Comparison of bottom stresses calculated by linear and quadratic formulations.

BOTTOM STRESS
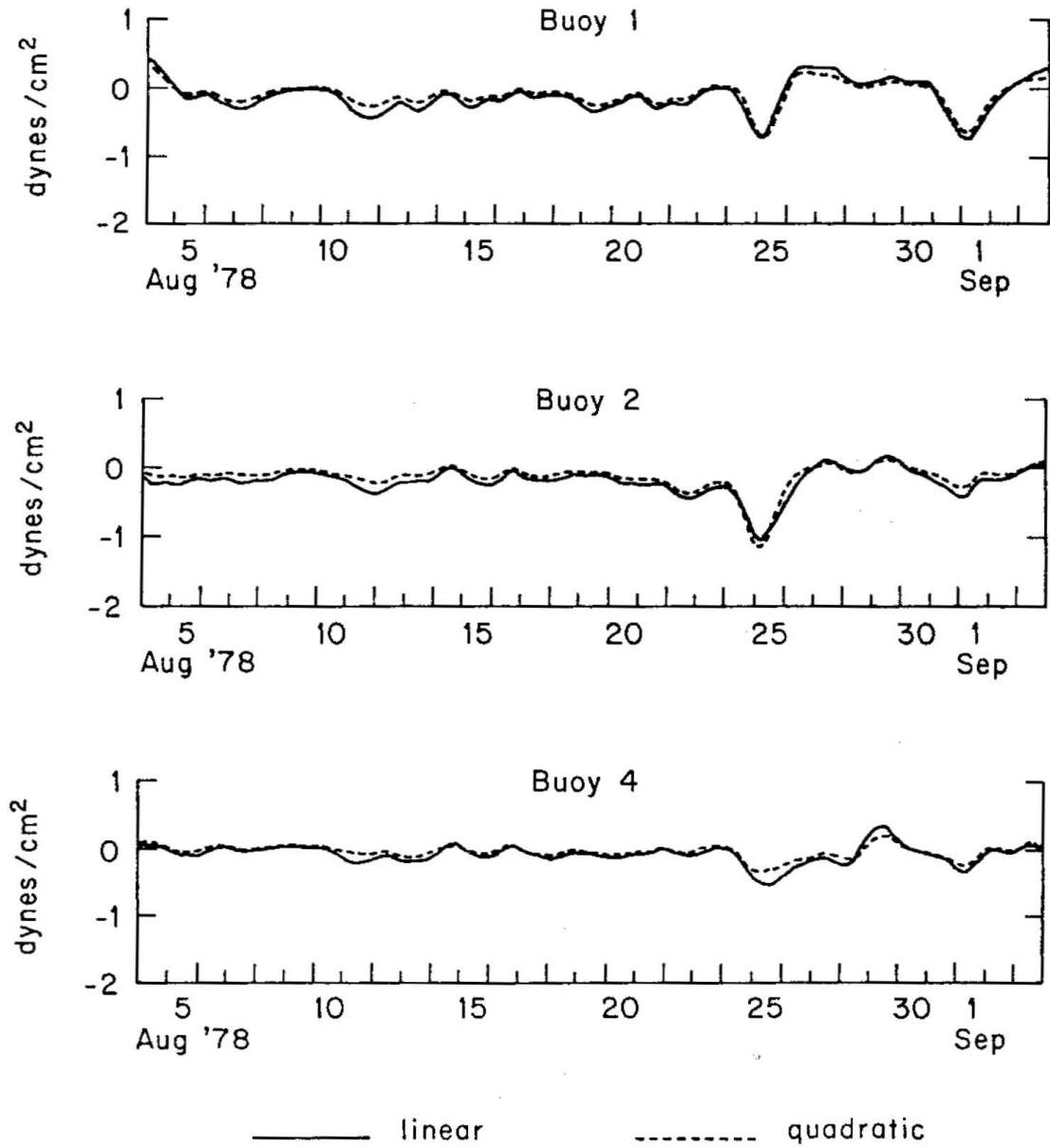
Figure 5.19   Aug '78 comparison of linear and quadratic bottom-stress
calculations.

5.7 Summary

Evidence has been presented which shows that variations in the along shore wind stress are primarily responsible for the energetic fluctuations of the 4-8 day period in the alongshore sea surface slope along Long Island. It is suggested that the presence of Long Island Sound may have a significant influence upon the local sea level response to winds.

Current meter records reveal that subtidal currents are essentially barotropic in nature and are strongly correlated with local wind stress forcing. The mean flow, on the other hand, generally flows toward the southwest in opposition to the mean wind field. This behavior is clear evidence that monthly mean flows in this region are not wind-driven.

Depth-averaged longshore currents frequently show a reversal with distance from shore: the nearshore column flowing with the wind and water further seaward against it. Depth-averaged offshore currents consistently displayed a net offshore transport in the study area. These features are consistent with the notion that shore-trapped pressure fields and nearshore circulation cells are characteristic of the region.

Momentum balance calculations clearly indicate that the cross-shore balance is very nearly geostrophic and suggest that the longshore balance may be reasonably represented by a steady linear equation of motion including surface and bottom stresses.

It has been demonstrated that linear and quadratic bottom stress formulations are essentially equivalent in the coastal boundary layer off Long Island.

Chapter VI

MODELS OF STEADY AND QUASI-STEADY FLOW WITHIN THE CBL

6.1 Introduction

The analysis of the previous chapters has allowed several general-
izations to be made with regard to the nature of the low frequency flow
field within Long Island's coastal boundary layer. These motions have
been observed to be predominantly barotropic in nature in that they are
highly coherent, and exhibit nearly constant phase throughout the water
column. This characteristic has permitted the substantial interpretive
and analytic simplification of vertically averaging both the observa-
tions and the equations of motion.

Current meter records from all experimental deployments indicate
that the region is strongly influenced by frictional forces. The close
correspondence between longshore wind stress and nearshore currents is
one of the chief characteristics of these data, and the large vertical
shear and conspicuous lack of evidence of free oscillations attest to
the importance of frictional dissipation. These findings have been
corroborated by dynamic balance calculations which, in addition, indi-
cate that, to within estimated errors, steady linear equations of motion
represent a reasonable approximation to the dynamics of the mean and
quasi-steady flow within the CBL.

Several key phenomena, such as the occurrence of longshore current reversals with distance from shore, and net offshore transport have been identified. These features are considered diagnostic of the CBL region and the present chapter attempts to relate these observations to models of nearshore equilibrium flow over bottom topography.

The conspicuous presence of net cross-shore transport and the associated failure of two dimensional mass balance ideas has mandated some consideration of, and allowance for, longshore variability in the flow field. This variability is envisioned such that mass may be conserved in the nearshore zone by coastal circulation cells which transport water from regions of excess (highs) to regions of shortage (lows). The formal inclusion of longshore dependence generally introduces substantial mathematical complication. However, if one neglects small scale longshore variability and retains only variations of the order of meteorological systems and major coastline features, it is still possible to assume that the alongshore length scale is much greater than the offshore scale and thereby salvage the vital simplifications afforded by the boundary layer approximation. This approach has been successfully used by Gill and Schumann (1974) and Csanady (1978) and will be employed here as well.

6.2 Nearshore parallel flow

As a first step toward understanding the steady flow conditions of the nearshore region it is useful to briefly consider the dynamical

consequences of the particularly simple momentum balance (without long-
shore variability) supposed by Scott and Csanady (1976). This balance
is based upon the assumption that the coastal boundary condition prohi-
biting net cross-shore transport is a powerful constraint as far seaward
as several tens of kilometers, and that the dynamical terms involving a
vertically averaged cross-shore velocity may therefore be neglected. As
we have previously noted this supposition is, somewhat surprisingly, not
always realistic even within the CBL. Nevertheless, it leads to some
interesting insight into nearshore flow conditions.

After the additional and very reasonable assumption that the off-
shore stress components may be neglected in comparison to the Coriolis
force due to the longshore current, the vertically averaged equations of
motion may be written as

$$fv = g \frac{\partial \zeta}{\partial x} \tag{6.1a}$$

$$\frac{(\tau_w - \tau_b)}{h(x)} = g \frac{\partial \zeta}{\partial y} \tag{6.1b}$$

where τ_w and τ_b are the longshore components of the surface and
bottom stresses respectively, $h(x)$ is the water depth, g the acceler-
ation of gravity, ζ the surface elevation, f the Coriolis parameter, and
v the depth averaged longshore current. The right handed coordinate
system used throughout this chapter is x positive offshore, y along-

shore, and z positive upward.

The assumption that u=0 under steady flow conditions has rather far-reaching consequences. It implies, through the vertically averaged steady continuity equation, that $\partial v/\partial y$ vanishes everywhere. This condition, in conjunction with eqs. 6.1, in turn requires that $\partial^2 \zeta/\partial x \partial y$ also vanish so that the alongshore pressure gradient is constant with distance from shore. In fact, equations (6.1) form a consistent set only if $\partial \zeta/\partial y$ is a function of neither x nor y.

If the bottom stress is parameterized linearly in terms of the longshore velocity as rv, eq. (6.1b) may be rewritten as

$$v = \frac{\tau_w}{r} - g \frac{h(x)}{r} \frac{\partial \zeta}{\partial y} \tag{6.2}$$

where r is a resistance coefficient with dimensions of velocity. In this scheme the alongshore current is seen to arise from a force imbalance between the wind stress and longshore pressure gradients. Close to shore, as $h(x) \to 0$, v must be in the direction of the wind and is approximately given by τ_w/r. If $\partial \zeta/\partial y$ and τ_w were to act in the same direction, the longshore velocity would increase seaward with the same functional dependence as the bottom topography. On the other hand, if the pressure gradient and wind stress were to oppose one another as is usually observed, the longshore velocity would decrease seaward, go through zero at the critical depth $h_c = \tau_w/(g \, \partial \zeta/\partial y)$ at which the two forces cancel, and then reverse direction seaward of that point. Clearly

the position of this longshore velocity reversal would vary as a func-
tion of the relative magnitudes of the wind stress and pressure gradient
forces. For fixed pressure gradient and vanishing winds, the region of
negative alongshore flow would begin right at the shoreline while under
the influence of vigorous wind stress episodes the turning point might
be expected to be located well offshore. This behavior is in excellent
qualitative agreement with observational evidence, as pointed out in the
previous chapter, and it appears possible that the foregoing dynamic
balance may approximately model one component of the observed flow near-
shore under conditions of high wind stress forcing. On the other hand,
in spite of the rather remarkable successes of the coastal constraint
flow model, it is overly restrictive in several important and related
respects. First among its inadequacies is the hypothesis itself: that
$u = 0$ throughout the coastal zone. As previously pointed out, this is
often decidedly not the case even within order 10 km of the shore. In
addition, contrary to the tenents of this model, there is direct evi-
dence of substantial alongcoast variation in the magnitude of the along-
shore pressure gradient (Noble and Butman, 1979) and indirect indication
that this is also true for both components of velocity.

6.3 The arrested topographic wave

As a first step in refining the coastal circulation model and bring-
ing its behavior more in line with obervations, the terms involving the

depth averaged cross-shore velocity may be retained, and the meteorolog-
ical forcing considered to be dependent upon the longshore coordinate.
These changes result in the set of equations

$$-fv = -g \frac{\partial \zeta}{\partial x}$$

$$fu = -g \frac{\partial \zeta}{\partial y} + \frac{\tau_w^{(y)}}{h(x)} - \frac{rv}{h(x)} \qquad (6.3)$$

$$\frac{\partial uh}{\partial x} + \frac{\partial vh}{\partial y} = 0$$

where once again cross-shore stresses have been neglected in comparison
with the Coriolis force due to longshore flow and h is a function of x
alone. The y dependence of the alongshore wind stress is considered to
arise not only from spatial differences in the wind field, but also due
to changes in coastline orientation. In this way major coastline
changes are taken into account insofar as they affect the longshore com-
ponent of the wind stress, while at the same time retaining the geome-
tric and analytic simplicity of an infinite straight coast.

The vorticity equation corresponding to (6.3) is given by

$$\frac{\partial}{\partial x} \left(\frac{\tau_w}{h(x)} - \frac{rv}{h(x)} \right) + \frac{fu}{h(x)} \frac{dh}{dx} = 0 \qquad (6.4)$$

The first term represents the curl of the column averaged net stress and
is balanced by a vortex stretching term due to across isobath flow.

This stretching term is sometimes called the topographic "beta" effect in Rossby wave problems. The vorticity dynamics indicated in (6.4) seem to be a topographic analogy of the Sverdrup relation which governs flow in the deep ocean's interior. Thus solutions to (6.3) may be thought of as a topographic Sverdrup flow. Alternatively, Csanady (1978) has termed it the "arrested topographic wave" after noting the mathematical similarity to Gill and Schumann's (1974) study of topographic wave generation by wind.

By eliminating u and v from the above set of equations, a single expression written in terms of the sea surface elevation is obtained of the form

$$\frac{\partial^2 \zeta}{\partial x^2} + \frac{f}{r} \frac{dh}{dx} \frac{\partial \zeta}{\partial y} = 0 \qquad (6.5)$$

In his illuminating discussion, Csanady (1978) (hereafter referred to as ATW) pointed out the heat conduction analogy to eq. (6.5) for the case of a linear bottom slope, and exploited this relationship in finding solutions for several interesting forcing functions. This analogy remains useful in developing some physical intuition with regard to the general diffusive nature of solutions to equation (6.5), however its mathematical advantage is lost when considering more complex forms of bottom topography.

Earlier discussions of equation (6.5) by Birchfield (1972) and Pedlosky (1974) arose from viscous boundary layer expansions in terms of

Ekman number, for closed basins with finite water depth at the coast.
These studies demonstrated that this barotropic flow component persists
in the presence of stratification and the additional complexities of
side wall frictional layers. These results point out the robustness of
ATW type flows and are considered, to a certain extent, an exoneration
of the simple approach used here. The derivations in ATW clearly showed
that application of this equation need not be limited to regions in
which the water depth is large in comparison with the Ekman depth, and
in fact avoided this artifice entirely, by allowing the linear bottom to
shoal to zero at the coast. What has not yet been made clear is the
effect that topographic differences of this type may have upon solu-
tions. Inspection of eq. (6.5) reveals the central role played by the
form of the depth changes in determining the offshore behavior of the
surface elevation. It seems likely that topographic details may have
significant effects, especially within the CBL where considerable depth
variation occurs.


6.3.1 The influence of nearshore topography

Before the detailed consideration of more realistic nearshore mor-
phometry, it seems appropriate to look at the case of the linear bottom
slope with a vertical wall at the coast. By allowing the water depth at
the shore to vary, a definite idea of the importance of the nearshore
configuration may be obtained while at the same time reviewing the

arrested topographic wave solution.

Figure 6.1 is the definition sketch of the model topography where h_o is the water depth at the coast and s is the slope of the bottom boundary. The shoreline boundary condition of no normal transport may be written as

$$-g\frac{\partial \zeta}{\partial y} + \frac{\tau w}{h_o} - \frac{g}{f}\frac{r}{h_o}\frac{\partial \zeta}{\partial x} = 0 \qquad at \quad x = 0 \qquad (6.6)$$

where equations (6.3) have been used. Choosing a seaward boundary cond-ition requires some decision as to the role that conditions in deeper water have in influencing nearshore flow. Because of this situation it is convenient to treat the CBL and the continental shelf as a unit and apply boundary conditions far from shore where more clear choices can be made. By demanding that $\zeta \to 0$ as $x \to \infty$ one assumes the deep ocean to be "inactive". Physically this problem corresponds to consideration solely of the effects of the wind stress acting over topography with no "out-side" interference. The alternative, setting (x,y) equal to some pre-scribed function at the shelf break, corresponds to making some assump-tions about the mean state of an "interactive" deep ocean interior which impresses a pressure field upon the coastal zone. Since it is not clear what pressure field would be appropriate, and in view of observational evidence which shows that the major coastal pressure signal is corre-lated with wind stress events, possible deep water influence will not be considered here, and it is assumed that the surface elevation field van-ishes far from shore.
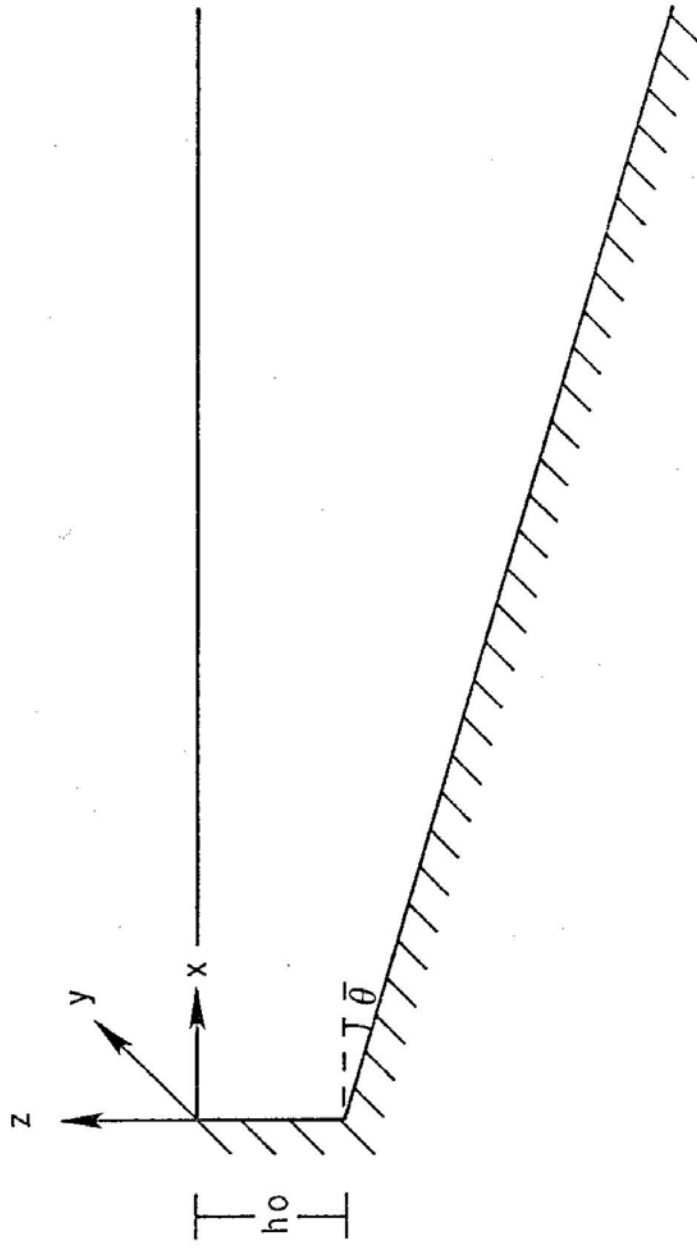
$$s = \tan \theta$$

Figure 6.1   Definition sketch showing model topography and coordinates

In order to investigate the effect of alongshore variability in wind stress forcing, Csanady employed both sinusoidal and "top hat" wind functions in ATW. The analytical convenience afforded by use of the sinusoidal form is substantial, and the differences between the two idealizations are not fundamental. As noted by Winant (1978) in some clarifying comments on ATW, the "top hat" and sinusoidal winds are directly analogous and lead to the same scales of motion. In addition, it is clear that any reasonable wind may be represented by a Fourier series. One could therefore represent the results for a complicated wind-stress distribution by linear superposition of the solutions for individual Fourier components. For convenience only a single, dominant Fourier component is included here and the alongshore wind stress is represented by $\tau_w^y = F_0 e^{iky}$ where k denotes the alongcoast wave number of the wind stress distribution. Consideration of the suitability of this idealization, and the probable physical origin of such variation, is deferred until the following section.

Assuming that the sea surface elevation field also displays this type of alongshore variation, and substituting the expression

$$\zeta \sim e^{iky} Z(x)$$

into eq. (6.5) leads directly to

$$\frac{d^2 Z}{dx^2} + \frac{ikf}{r} \frac{dh}{dx} Z = 0 \tag{6.7}$$

Substitution of $h = sx$ into this equation yields the solution

$$Z_1 = A e^{-(1-i)x/L} + B e^{(1-i)x/L} \qquad (6.8)$$

where

$$L = (2r/fks)^{1/2} \qquad (6.9)$$

and is the e-folding length scale. Use of the asymptotic condition that vanishes far from shore determines that $B = 0$. Equation (6.6) then leads to

$$A = -\frac{F_0 fL}{rg} \left[\frac{1 + i(1+\alpha)}{1 + (1+\alpha)^2}\right] \qquad (6.10)$$

where

$$\alpha = (h_0 kfL)/r = h_0 (2kf/rs)^{1/2} \qquad (6.11)$$

is given by the real part of the expression $A e^{-x/L} e^{i(ky+x/L)}$. The complex constant A not only determines the magnitude of the coastal response, but also controls the phase relationship between the wind stress and surface elevation fields.

In the case of zero water depth at the coast ($h_0 = 0$), $\alpha = 0$ and A has real and imaginary parts of equal magnitude. The real solution then

takes the form

$$\zeta = \frac{F_o fL}{2rg} e^{-x/L} \sin (ky + x/L - \pi/4)$$

$$v = \frac{F_o}{2r} e^{-x/L} \cos (ky + x/L) \qquad\qquad (6.12)$$

$$u = F_o \frac{\cos ky}{hf} - \frac{F_o}{2hf} e^{-x/L} \cos (ky + x/L)$$

$$- \frac{F_o Lk}{2r} e^{-x/L} \cos (ky + x/L - \pi/4)$$

This is Csanady's result, and at the shoreline the pressure gradient force and wind stress oppose one another over 3/4 of the coast. Far from shore we have, as expected, Ekman drift with the offshore velocity in phase with the wind stress.

In order to see how these relationships may change, consider the case in which h_o is large so that $\alpha \gg 1$. In this case A is nearly pure imaginary and approximately given by

$$A \approx - \frac{F_o fL}{rg} \frac{i}{\alpha}$$

The magnitude of the pressure signal is reduced to $\sqrt{2}/\alpha$ of its value in the previous example, and the longshore components of the wind stress

and pressure gradient at the shore would be out of phase over the entire coastline. Thus Csanady's results seem to be a limiting case of least opposition between wind and pressure gradient forcing, and maximum response over a linear bottom slope.

The question then arises as to whether significant alteration of solutions occurs as a result of the introduction of a vertical coast of modest (say 10 m) dimensions as is common practice in coastal modeling for analytical convenience. It must be remembered that such a topography may be preferable to the simple linear beach in some regions. In order to quantify these effects we simply calculate A with some knowledge of the parametric values of the problem.

Bottom resistance coefficients have been estimated by regression techniques for the Mid-Atlantic Bight region by Scott and Csanady (1976), Winant and Beardsley (1979), and Bennett and Magnell (1979). These studies all suggest values close to 0.1 cm/sec as appropriate for nearshore shallow water environments. Tidal analyses undertaken by May (1979) led to confirmation of this number via a somewhat different approach. Using current measurements from the COBOLT experiment, the vertical structure of tidal currents was compared to the predictions of a turbulent wall layer model. May concluded that $r = (0.09-0.14)$ cm/sec in excellent agreement with previous estimates. Calculations by Bowden (1962), Groen and Groves (1962), Forrestal et. al. (1977) and Winant and Beardsley (1979) imply that this value may be applicable to many regions of shallow (<50 m) depth.

In all of the above investigations, the calculated resistance

coefficient was that appropriate for the bottom velocity, while in the model, friction is parameterized in terms of the depth averaged velocity. A more appropriate value to be used in this case would be an effective coefficient defined as $r_e = (V_b/\langle V \rangle) r$, where V_b is the time averaged bottom velocity, and $\langle V \rangle$ is the time and depth averaged value. The ratio $V_b/\langle V \rangle$ was determined for all moorings in the COBOLT experiments and exhibited a surprisingly limited range of values (0.36 ± 0.07). In view of these results an average (to one significant figure) effective resistance coefficient of 0.04 cm/sec was used in model calculations.

If one assumes that in a steady state the primary source of longshore wind stress variation in the COBOLT study area results from the orientation of the finite coastline of Long Island, a reasonable choice of wavelength is 400 km or $k = 1.6 \times 10^{-7}$ cm. With $f = 10^{-4}$ sec^{-1}, $s = 10^{-3}$ and $h_o = 10^3$ cm, eqs. (6.10 and 6.11) give

$$A = -(F_o fL/5rg) (1 + i(1.9))$$

These solutions are seen to be fairly strongly affected by the details of the topography. The introduction of the vertical coast reduces the amplitude of the coastal response by roughly half and changes the force opposition along coast from 75 percent to 85 percent. These changes, resulting from such minor topographic variation, suggest that it behooves one to consider nearshore topography carefully and that different geographical regions might display quite different responses.

6.4 Wind stress variation in shoreline coordinates

The parabolic nature of equation (6.5) attests to the fact that there is a definite upstream-downstream aspect to the relationship between forcing, which enters the equation through the shoreline boundary condition, and response. In terms of the heat conduction analogy, the temperature (sea level) distribution at any particular time (longshore position) is a function of its past history (upstream) just as it in turn influences the future (downstream) distribution. Physically the downstream direction coincides with the direction of propagation of free topographic waves so that conditions at any position alongshore would be determined by variations of the wind stress forcing upcoast (alongshore with land to the left) of that location.

Because of the presence of the Long Island Sound, the study region might be expected to be characterized by extreme alongcoast divergences of wind-driven nearshore velocities. Figure 6.2 shows a schematic diagram of the Long Island vicinity. The right handed coastal coordinate system is defined such that the x direction is always offshore, and y points alongshore with the land on the left. As demonstrated in this figure, a wind stress which is uniform in geographic coordinates will undergo several reversals in this coordinate system due to the convoluted coastal configuration. That is to say, a wind stress oriented along the axis of Long Island, acts with the coast on its left along Connecticut and Long Island's Atlantic shore, while along Long Island's north shore the wind blows with the land to the right. The flow pattern
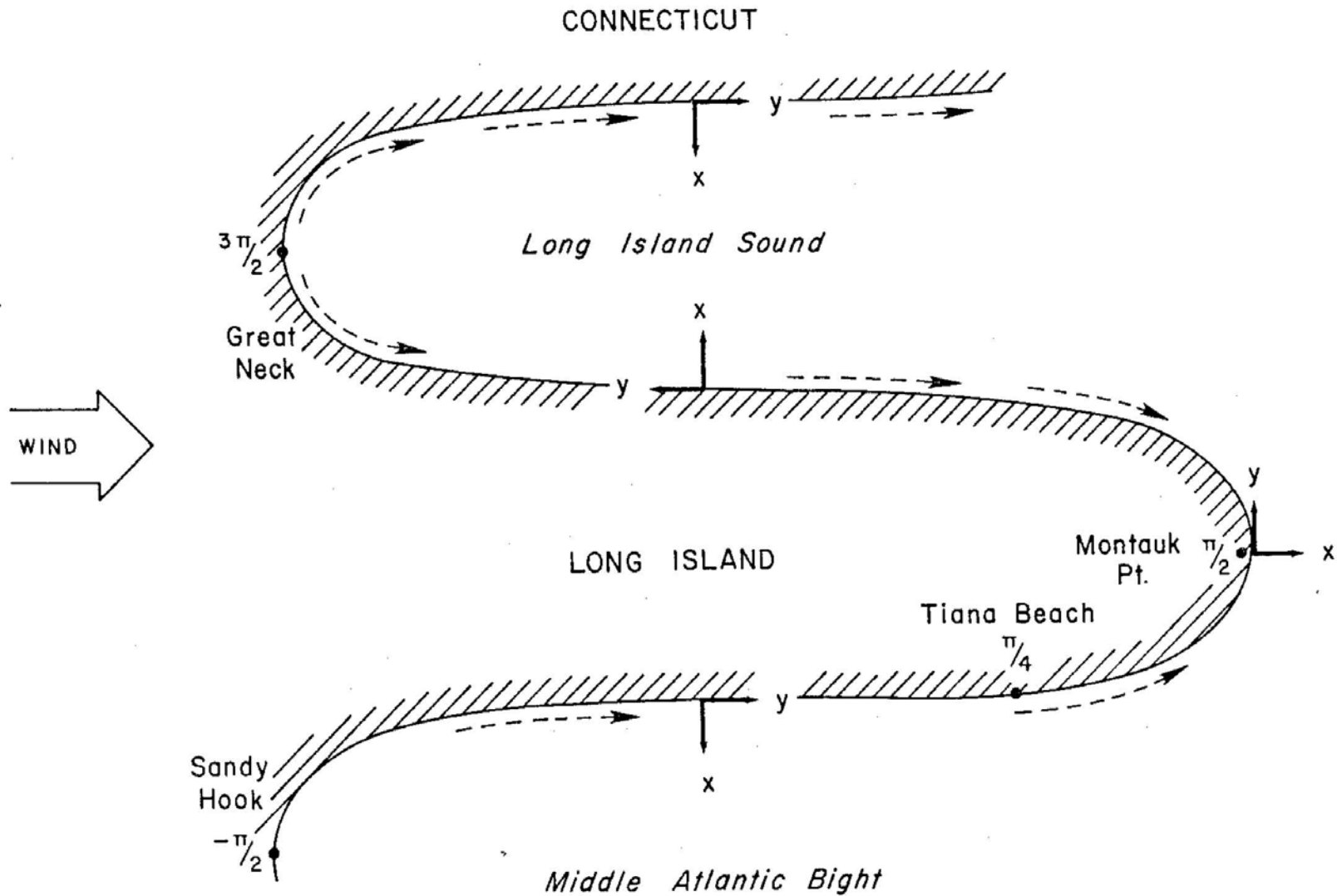
Figure 6.2 Schematic conceptualization of the effects of a meandering coastline.

of the coastal currents, which must flow in the direction of the wind in
shallow water, would lead to a nearshore divergence of the flow near
Great Neck and a convergence in the vicinity of Montauk Point. This
pattern of flow convergence and divergence could be a prime contributor
to that component of the Montauk to Sandy Hook pressure gradient which
is found to be correlated with alongshore winds.

The question arises as to whether coastline features of the scale of
Long Island Sound warrant reorientation of the coordinate system as
suggested above, or whether they more nearly represent neglectable per-
turbations of an essentially straight coast. Clearly the answer depends
upon the scale of the motions being considered. If one's primary inter-
est is in shelf-wide motions of low frequency, the approximation of a
long straight coast can likely be made with relative impunity. On the
other hand, if the offshore scales of shore trapped solutions, such as
the arrested topographic wave, turn out be comparable to or less than
the width of the sound, the effects of the meandering shoreline would be
of primary importance. In the following development the decay scale of
solutions is assumed, subject to later verification, to be sufficiently
small in comparison with the cross-sound length scale to warrant its
consideration as a major coastline reorientation.

Further consideration of figure 6.2 shows that the modelling of
alongshore variations in wind stress as a sinusoidal function of
alongshore position (leading to equation 6.6) is a particularly useful
idealization in view of the generally sinuous configuration of this
section of the coast. Although a more precise representation could be

achieved by Fourier series expansion, the single fundamental component
is capable of adequately representing the physically important reversals
in the wind stress-coastline relationship. The numerical values of the
nondimensional longshore coordinate ky were fixed by the assumption
that $\tau \sim \cos(ky)$, and values have been noted on the figure for the field
site and other geographical points of interest.

6.5 The matched exponential bottom profile

Equation (6.6) may be solved for several simple analytical forms of
bottom topography. One formulation which is particularly flexible and
is capable of realistically modelling a wide variety of coastal
configurations, is the "matched exponential" bottom profile. This
general analytical topography, shown schematically in figure 6.3 is
given in an inner region by

$$h(x) = h_0(1-e^{-\alpha x})$$ Region I

and matched at x_L to the outer region expression (6.13)

$$h(x^*) = h_c e^{\gamma x^*}$$ Region II

where $x^* = x-x_L$, $h_c = h_0(1-e^{-\alpha x_L})$, and α, γ, and h_0 are all positive
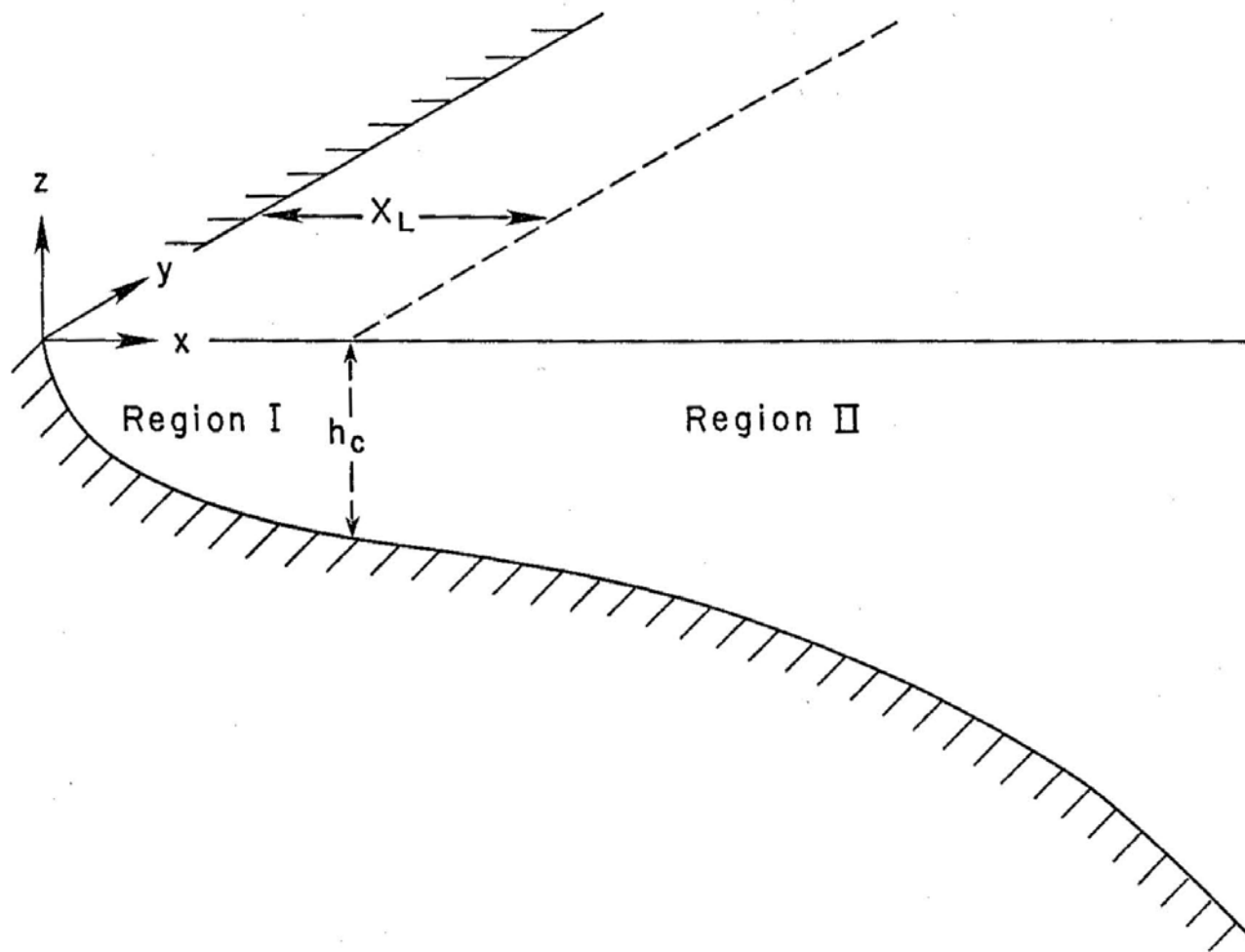constants which may be chosen in order to achieve a realistic topo-

Figure 6.3   Schematic diagram of "matched exponential" bottom topography

graphic representation. By varying these parameters any bottom profile, from the broad shallow "east coast" type shelf to steep narrow "west coast" configurations, may be produced. The matching point x_L may be chosen such that the bottom slope is perfectly smooth, by the relation $x_L = -1/\alpha \ln(\gamma/\alpha)$, or it can be picked to be any convenient point where $e^{-\alpha X}$ is reasonably flat.

Use of relations (6.13) in eq. (6.5) leads to

$$\frac{d^2 Z}{dx^2} + i \, \Omega \, e^{-\alpha X} \, Z = 0 \qquad \text{Region I}$$

and   (6.14)

$$\frac{d^2 Z}{dx*^2} + i \, \Gamma \, e^{\gamma X^*} \, Z = 0 \qquad \text{Region II}$$

where

$$\Omega = \frac{kfh_o\alpha}{r} \qquad \text{and} \qquad \Gamma = \frac{kfh_c\gamma}{r}$$

These equations can be rewritten in more standard form through the change of variable transformations

$$\xi = e^{-\alpha X} \quad ; \quad Z(x) = Y(\xi) \qquad \text{I}$$

and   (6.15)

$$\xi^* = e^{\gamma x^*} \quad ; \quad Z(x^*) = Y(\xi^*) \qquad \text{II}$$

resulting in

$$\alpha^2 \xi \frac{d^2Y}{d\xi^2} + \alpha^2 \frac{dY}{d\xi} + i\Omega Y = 0 \qquad\qquad \text{I}$$

$$(6.16)$$

$$\gamma^2 \xi^* \frac{d^2Y}{d\xi^{*2}} + \gamma^2 \frac{dY}{d\xi^*} + i\Gamma Y = 0 \qquad\qquad \text{II}$$

The solutions of eqs. (6.16) are found to be

$$Z_I = A_1 J_0\left(\frac{2}{\alpha}\sqrt{i\Omega}\ e^{-\alpha/2\ x}\right) + B_1 H_0^1\left(\frac{2}{\alpha}\sqrt{i\Omega}\ e^{-\alpha/2\ x}\right)$$

and $\qquad\qquad\qquad\qquad\qquad\qquad\qquad\qquad\qquad\qquad (6.17)$

$$Z_{II} = A_2 J_0\left(\frac{2}{\gamma}\sqrt{i\Gamma}\ e^{\gamma/2\ x^*}\right) + B_2 H_0^1\left(\frac{2}{\gamma}\sqrt{i\Gamma}\ e^{\gamma/2\ x^*}\right)$$

where J_0 is the zero order Bessel function of the first kind, H_0^1 is the zero order Hankel function of the first kind, the A_i and B_i are complex constants, and the subscript on Z refers to regions I and II. These expressions may be written in terms of the somewhat more familiar Kelvin functions (cf. Jahnke, Emde and Losch, 1960) as

$$Z_I = A_1\left[\text{ber}(f(x)) - i\ \text{bei}(f(x))\right] - \frac{2B_1}{\pi}\left[\text{kei}(f(x)) + i\ \text{ker}(f(x))\right]$$

and $\qquad\qquad\qquad\qquad\qquad\qquad\qquad\qquad\qquad\qquad (6.18)$

$$Z_{II} = A_2\left[\text{ber}(g(x^*)) - i\ \text{bei}(g(x^*))\right] - \frac{2B_2}{\pi}\left[\text{kei}(g(x^*)) + i\ \text{ker}(g(x^*))\right]$$

where

$$f(x) = \frac{2\sqrt{\Omega}\, e^{-\alpha x/2}}{\alpha} \qquad \text{and} \qquad g(x^*) = \frac{2\sqrt{\Gamma}\, e^{\gamma x^*/2}}{\gamma}$$

Since both ber and bei diverge for large arguments, the asymptotic boundary condition that ζ vanish far from shore determines that $A_2=0$. The remaining complex constants may be determined via the shoreline boundary condition

$$\frac{d\, Z_I}{dx} = \frac{f\, \tau_w}{rg} \qquad \text{at} \quad x = 0$$

and from the matching conditions

$$Z_I\, (x_L) = Z_{II}\, (x^*=0)$$

and

$$\frac{d\, Z_I(x_L)}{dx} \qquad \frac{d\, Z_{II}(x^*=0)}{dx^*}$$

which amount to requirements that the surface elevation and longshore velocity be smooth functions.

The full solution for the surface elevation is given by the real part of $e^{iky}\, Z(x)$. Once ζ is known, solutions for u and v may be derived from the governing equations (6.3). After some algebraic manipulation, solutions for regions I and II may then be expressed as

$$\zeta_I = \cos ky \; [a_1 \; ber(f(x)) + a_2 \; bei(f(x))] + \sin ky \; [a_1 \; bei(f(x)$$

$$- a_2 \; ber(f(x))] + \frac{2}{\pi} \; [\cos ky \; [b_2 \; ker(f(x)) - b_1 \; kei(f(x))]$$

$$+ \sin ky \; [b_1 \; ker(f(x)) + b_2 \; kei(f(x))]] \tag{6.19a}$$

$$v_I = - \frac{g}{f} \sqrt{\overline{\Omega}} \; e^{-\alpha x/2} \left\{ \cos ky \; [a_1 \; ber'(f(x)) + a_2 \; bei'(f(x))] \right.$$

$$+ \sin ky \; [a_1 \; bei'(f(x)) - a_2 \; ber'(f(x))] + \frac{2}{\pi} \; [\cos ky \; [b_2 \; ker'(f(x))$$

$$\left. - b_1 \; kei'(f(x))] + \sin ky \; [b_1 \; ker'(f(x)) + b_2 \; kei'(f(x))]] \right\} \tag{6.19b}$$

$$u_I = \frac{kg}{f} \left\{ \sin ky \; [a_1 \; ber(f(x)) + a_2 \; bei(f(x))] + \cos ky \; [a_2 \; ber(f(x)) \right.$$

$$- a_1 \; bei(f(x))] + \frac{2}{\pi} \; [\sin ky \; [b_2 \; ker(f(x)) - b_1 \; kei(f(x))]$$

$$- \cos ky \; [b_1 \; ker(f(x)) + b_2 \; kei(f(x))]] \right\} + \frac{1}{fh_o(1-e^{-\alpha x})} \left\{ \tau_o \; \cos ky \right.$$

$$+ \frac{rg}{f} \sqrt{\overline{\Omega}} \; e^{-\alpha x/2} \; [\cos ky \; [a_1 \; ber'(f(x)) + a_2 \; bei'(f(x))]$$

$$- \frac{2}{\pi} \; [\cos ky \; [b_1 \; kei'(f(x)) - b_2 \; ker'(f(x))]$$

$$\left. - \sin ky \; [b_1 \; ker'(f(x)) + b_2 \; kei'(f(x))]]] \right\} \tag{6.19c}$$

$$\zeta_{II} = \frac{2}{\pi} \; [\cos ky \; [c_2 \; ker(g(x^*)) - c_1 \; kei(g(x^*))]$$

$$+ \sin ky \; [c_1 \; ker(g(x^*)) + c_2 \; kei(g(x^*))]] \tag{6.20a}$$

$$v_{II} = \frac{2g}{f_\pi} \sqrt{T} \, e^{\gamma x^*/2} \, [\cos ky \, [c_2 \, ker'(g(x^*)) - c_1 \, kei'(g(x^*))]$$

$$+ \sin ky \, [c_1 \, ker'(g(x^*)) + c_2 \, kei'(g(x^*))]] \tag{6.20b}$$

$$u_{II} = \frac{2kg}{f_\pi} \, [\sin ky \, [c_2 \, ker(g(x^*)) - c_1 \, kei(g(x^*))]$$

$$- \cos ky \, [c_1 \, ker(g(x^*)) + c_2 \, kei(g(x^*))]] + \frac{1}{fh_c e^{\gamma x^*}} \left\{ \tau_o \cos ky \right.$$

$$-\frac{2rg}{f_\pi} \sqrt{T} \, e^{\alpha x^*/2} \, [\cos ky \, [c_2 \, ker'(g(x^*)) - c_1 \, kei'(g(x^*))]$$

$$\left. + \sin ky \, [c_1 \, ker'(g(x^*)) + c_2 \, kei'(g(x^*))]]] \right\} \tag{6.20c}$$

where $a_1 + ia_2 = A_1$, $b_1 + ib_2 = B_2$, and $c_1 + ic_2 = B_2$, as determined from the boundary and matching conditions, and the primed notation denotes differentiation with respect to x. Polynomial approximations to the Kelvin functions and their derivatives, found in Abramowitz and Stegun (1964), were used in calculating numerical values of solutions (6.19a, b,c) and (6.20a,b,c).

6.5.1 The character of matched exponential model solutions

Because the arrested topographic wave features shore trapped fields, it is expected that the linear bottom slope model can give an adequate

representation of solutions in region II, and thus its general charac-
teristics, so long as the solution decays shoreward of the shelf break
region. In the CBL, however, where considerable deviations from any
overall linear bottom slope occur, a more realistic treatment of topo-
graphy leads to interesting and important changes in the nearshore flow
pattern. Figure 6.4 shows the degree of correspondence between analytic
and observed nearshore bottom profiles. This fit was achieved by
choosing h_o = 35 m and α = 0.25 km^{-1} in the first of equations
(6.13). Choosing γ = 0.016 km^{-1} for region II and matching at 10 km
from shore yields the overall CBL-shelf profile shown in figure 6.5.
This configuration is very representative of the coastal zone of the
Middle Atlantic Bight, although as a practical matter it turns out that
a linear bottom slope could have been used in the outer region without
notable effect upon the final results.

Figure 6.6 gives a qualitative view of the three dimensional
variations of the coastally trapped surface elevation field resulting
from a 1 dyne cosinusoidal longshore wind acting over the previously
shown matched exponential topography. For ease of visualization the
alonghore coordinate Ky extends over 4π. The offshore extent of the
plot is 80 km and the amplitude of the signal at the shore is roughly
2.5 cm.

A comparison of the alongcoast behavior of pressure gradient and
wind-stress forcing is displayed in figure 6.7. It is seen that the two
forces oppose one another over 85-90 percent of the shoreline. The wind
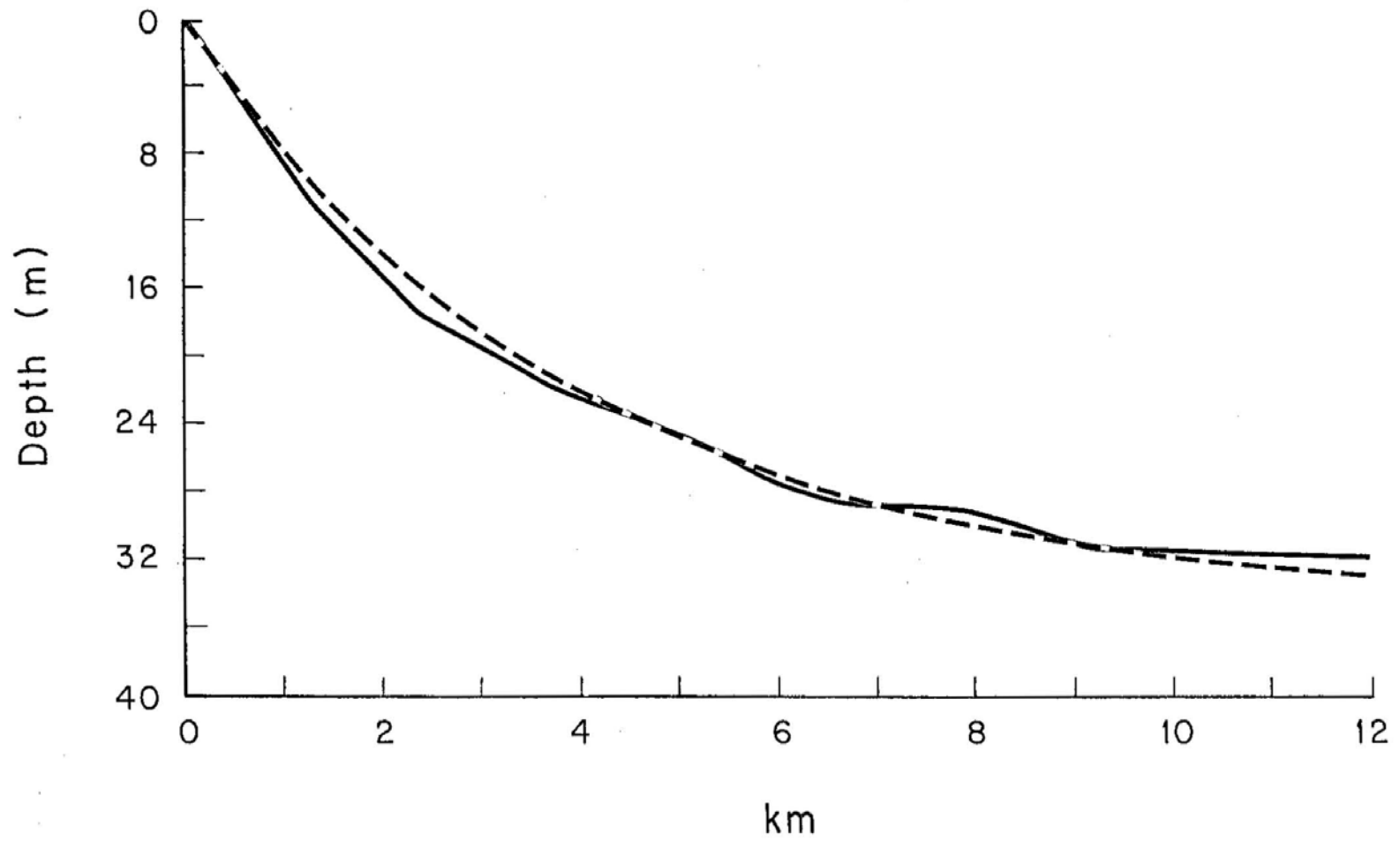stress-pressure gradient opposition is a characteristic signature of ATW

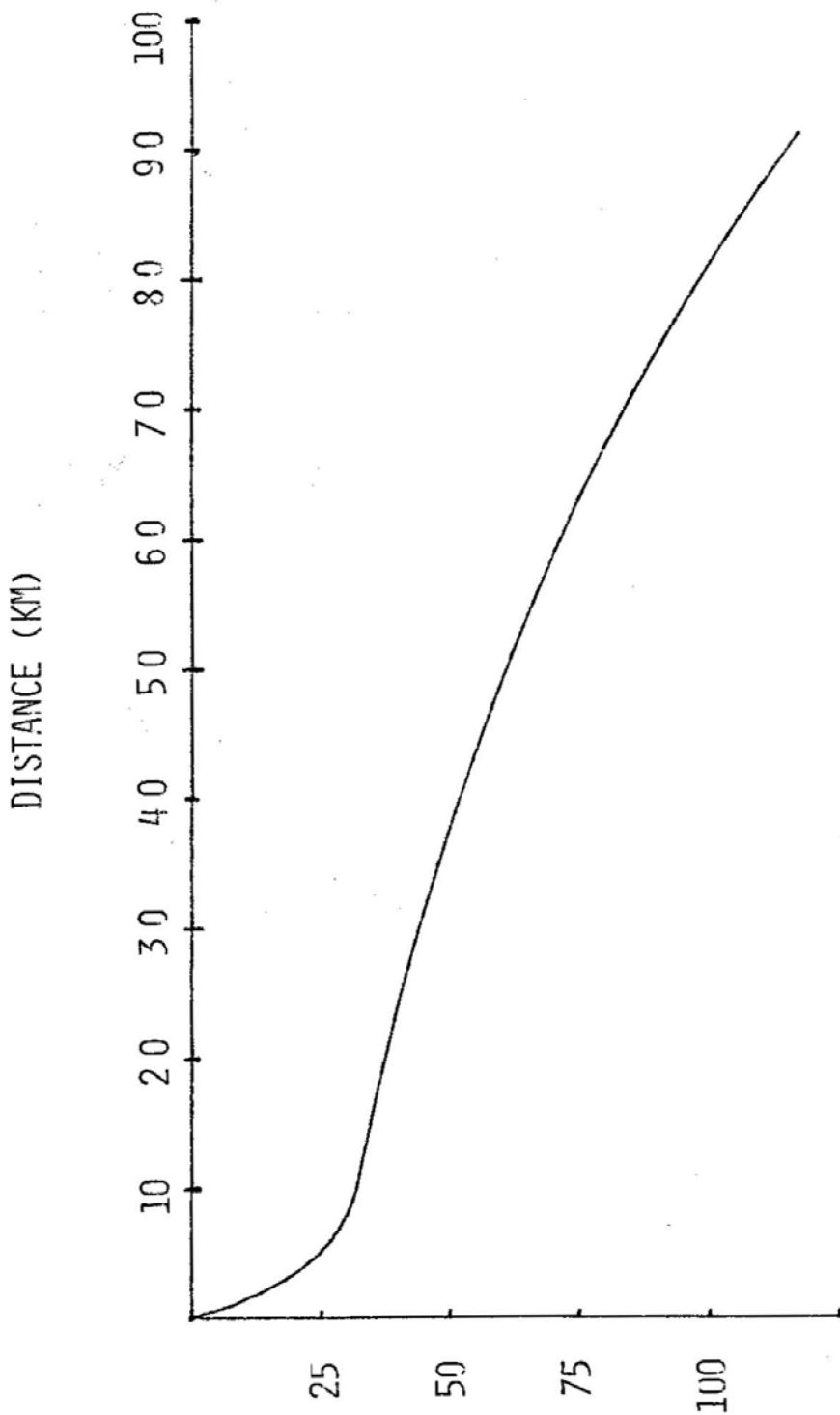Figure 6.4   Comparison of observed (solid) and analytical (dashed) bottom profiles

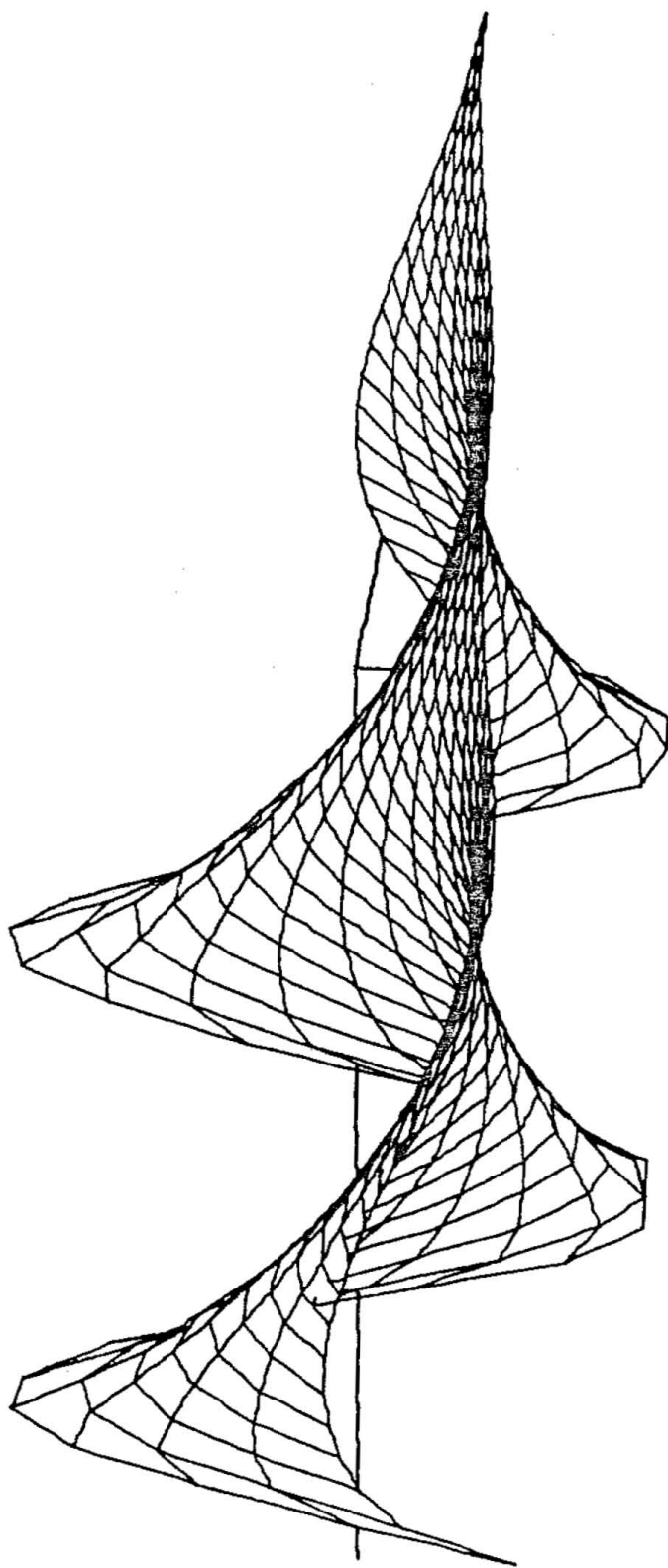Figure 6.5 Analytical CBL-Shelf profile

Figure 6.6 Three-dimensional view of the surface elevation field.

solutions. This situation leads to longshore current behavior similar to that earlier discussed in connection with the coastal constraint flow model. That is, in shallow water longshore currents flow with the wind while further from shore, in deeper environs, the reverse is true. In the present development, the competition between wind and pressure grad-ient forcing exhibits a longshore dependence, and arises naturally from a divergence in the alongcoast wind field rather than being prescribed by assumption as in the coastal constraint model.

The regions of similarity and difference between the linear slope and matched exponential models are perhaps best illustrated in figure 6.8 which depicts the nondimensional variation of longshore velocity with distance from shore. The matched exponential profile solutions overlay those of the linear case which have been redrawn from (ATW). In plotting the matched exponential solutions versus the nondimensional variable x/L the e-folding length scale defined by equation (6.9) has been used. In this way the model results are directly compared to the corresponding linear bottom slope solutions. For the region offshore of Long Island, L is roughly 22 km. While the details would vary somewhat for various choices of the topographic parameters controlling the near-shore bottom profile, it is clear that the main effect of the rapidly changing water depth in the CBL is to substantially increase the near-shore decay of the solution. In this manner the region of strong flow in the direction of the wind is confined to a narrow band and the flow reversal occurs nearer the shore. Farther from shore the two solutions are nearly coincident, showing that for the alongshore scale associated
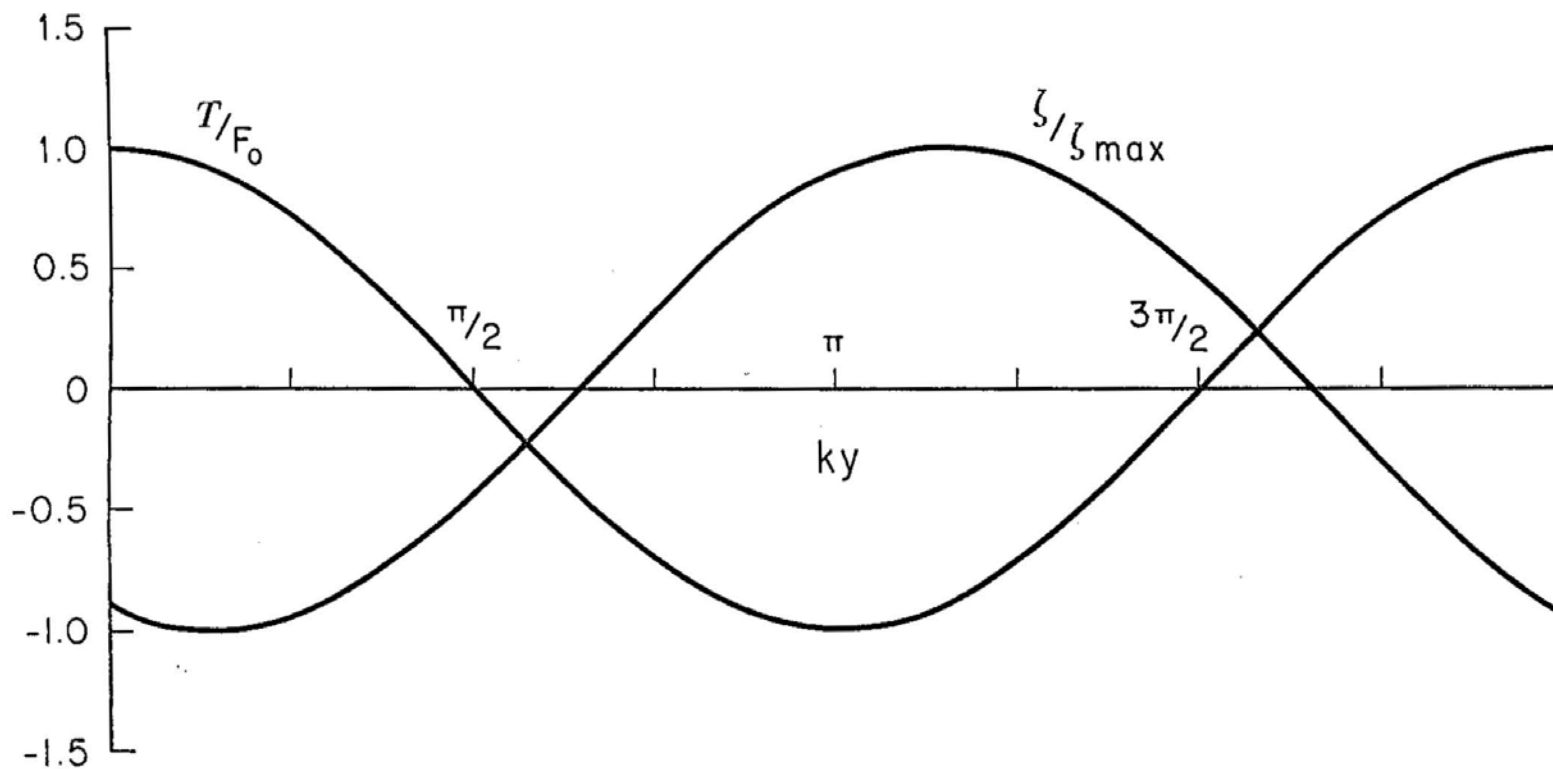
Figure 6.7   Normalized variation of wind-stress and pressure gradient forcing along the coast
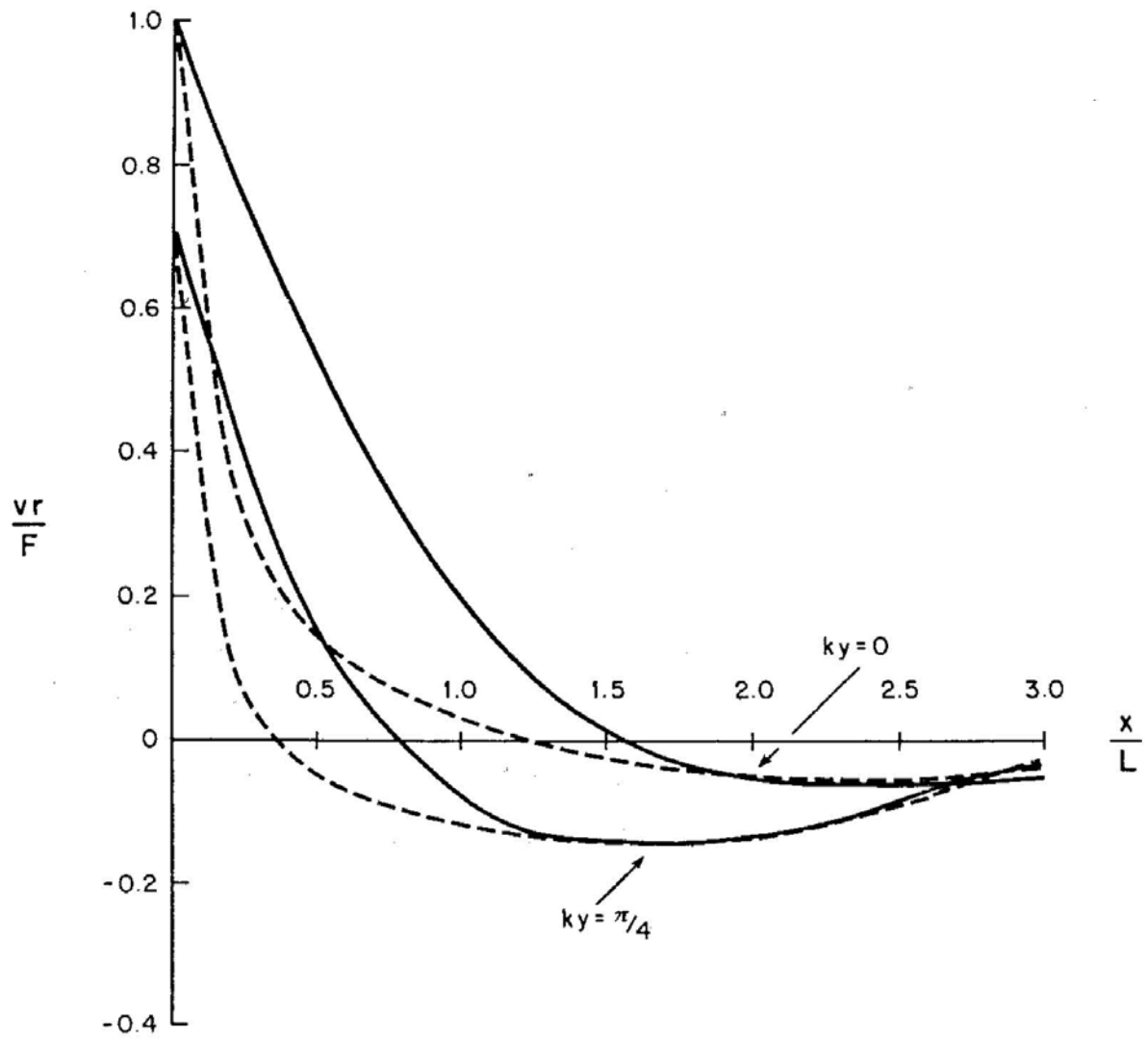
Figure 6.8 Comparison of nondimensional cross-shore variations
of longshore velocity solutions for linear (solid)
and "matched exponential" (dashed) bottom topography.

with Long Island's geometry, the solutions are trapped well shoreward of the shelf break and the plane shelf model represents a useful idealization in this outer region. Figure 6.8 suggests that for realistic topography, the nearshore decay scale of longshore currents associated with a 400 km wavelength arrested topographic wave, is roughly 10 km. This component of the regional wind driven response is thus very strongly trapped nearshore.

6.5.2 Comparison with observation

Figure 6.9 shows dimensional plots, at position $ky = \pi/4$, of the surface elevation and longshore velocity as a function of offshore position. Since a cosine representation of the wind field has been used the apex of the Mid Atlantic Bight corresponds to $ky = -\pi/2$, and $ky = \pi/4$ is roughly the position of the Tiana Beach field site. Note that the longshore flow reversal occurs within the CBL in excellent agreement with observations. The magnitude of the negative flow, however, is substantially less than is generally observed. This is likely to be due to the choice of seaward boundary conditions which neglects the shelf wide southwestward mean drift which has been observed to exist in the Mid-Atlantic Bight region. If such a flow component were superimposed upon the wind driven solution, in strengthening the negative flow component it would also move the point of flow reversal somewhat further landward. The matched exponential solution (including all significant
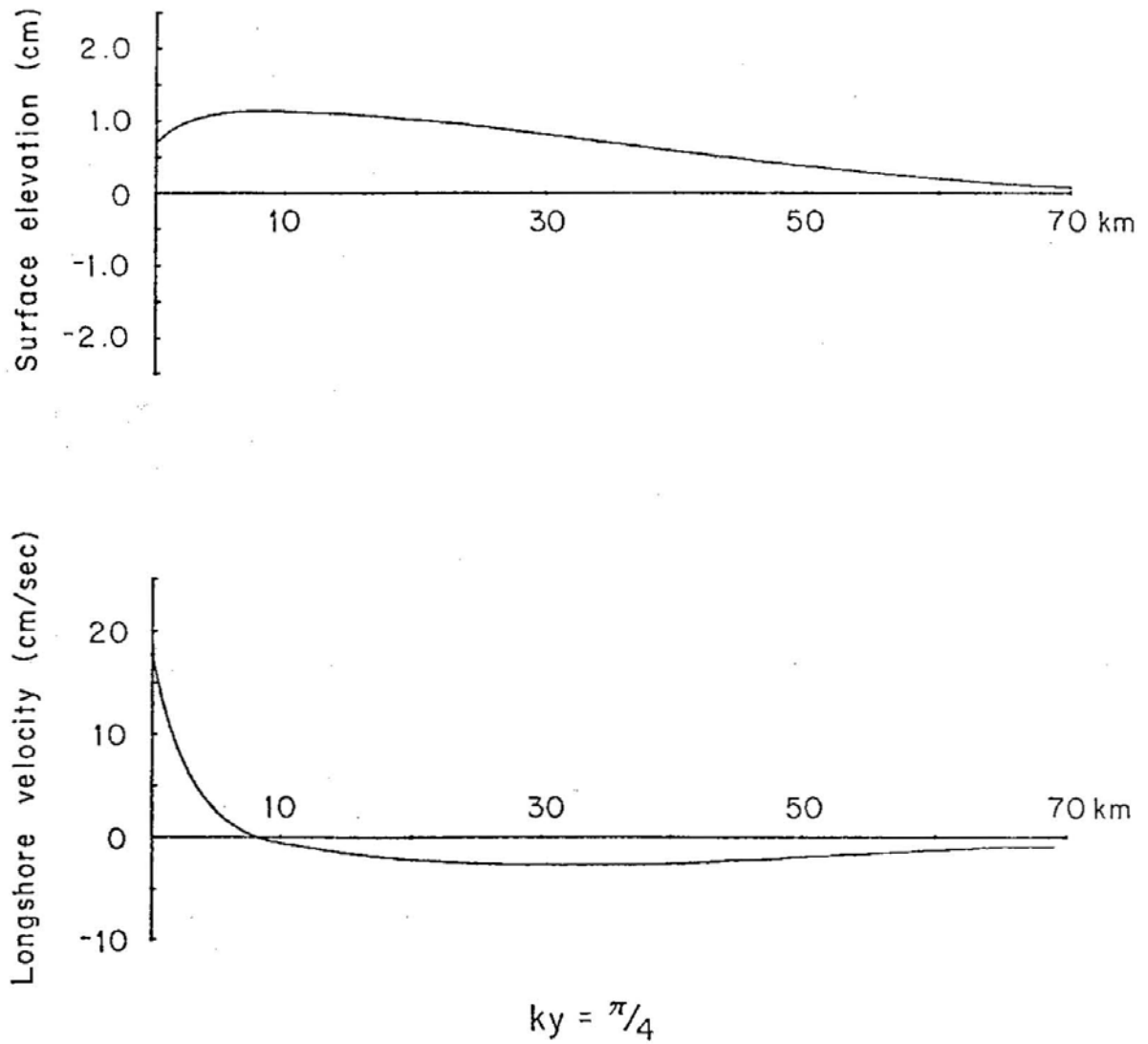
Figure 6.9   Surface elevation and longshore current at "Tiana Beach",
in response to a +1 dyne wind

wind components) thus gives the maximum seaward extent of the region of downwind flow.

The disparity in magnitude between downwind and upwind flow components associated with the model solutions, in conjunction with the southwestward mean flow, offers a plausible explanation for the fact that flow reversals were observed exclusively in response to northeastward wind stress episodes. During a southwestward wind stress impulse the relatively weak region of upwind currents would be superimposed upon, and overwhelmed by, the much larger negative regional mean flow. In this situation the longshore currents would be everywhere in the direction of the wind. In the opposite case of a northeastward stress, the mean flow would strengthen the upwind component, leading to an exaggerated and dramatic nearshore reversal.

Figure 6.10 shows the model predictions of offshore transport and corresponding vertically averaged velocity for $ky = \pi/4$. These results are in good qualitative agreement with the COBOLT observations which showed net offshore transport to be characteristic of the region, and in one experiment detected an offshore divergence of such flow. The model transport increases rapidly over the inner 30 km and thereafter asymptotes to Ekman transport values (which it initially over shoots) further from shore. In the lower panel of figure 6.10 the vertically averaged velocity is observed to peak near 30 km. The predicted value of $\partial u/\partial x$ over the CBL and the values of u themselves are in fair agreement with the observations of August 1978. Both the model and the data indicate that, for typical wind stress conditions at this location, averaged
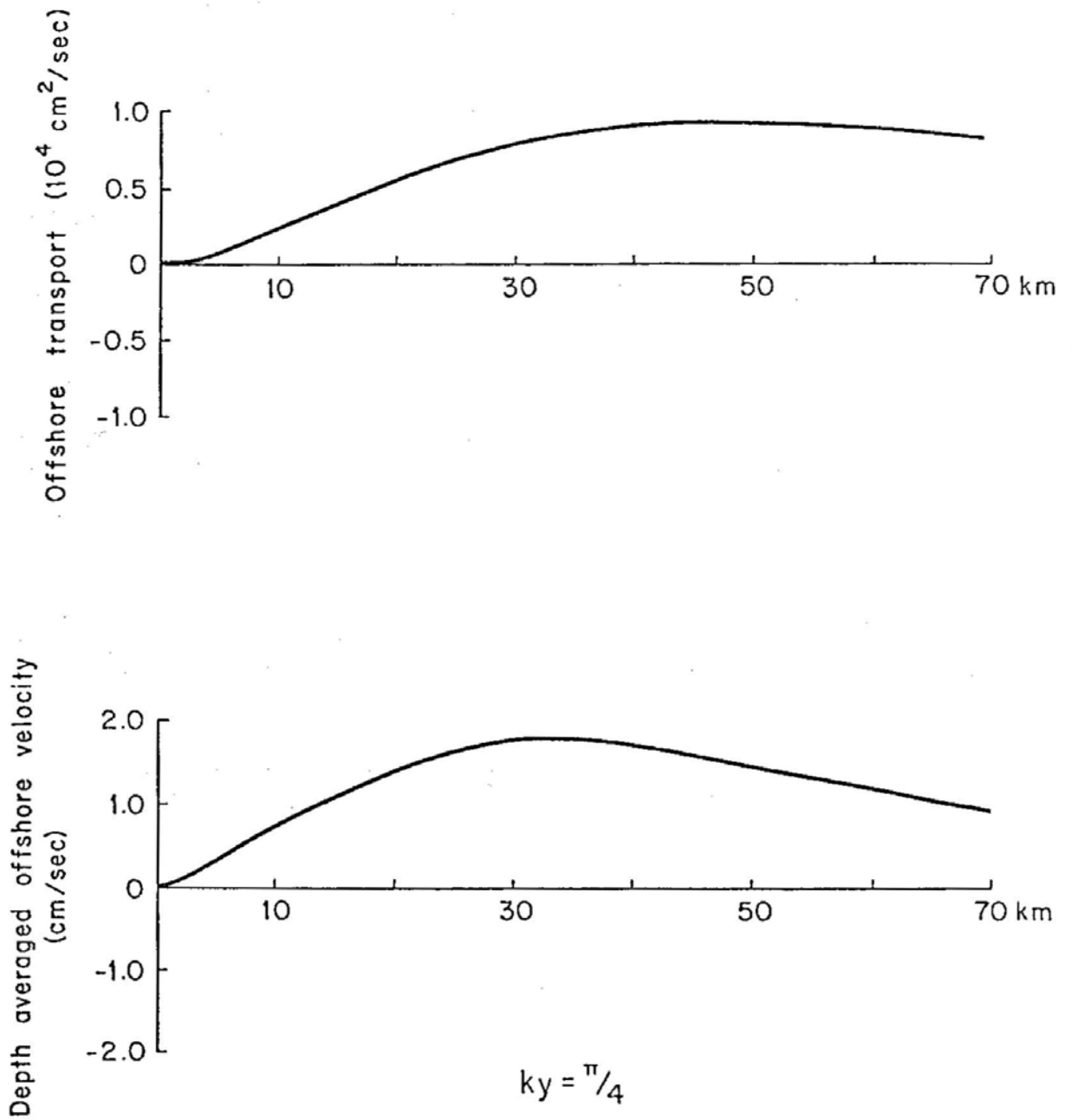
Figure 6.10 Offshore transport and depth averaged offshore velocity at "Tiana Beach", in response to a +1 dyne wind

offshore velocites on the order of 1 cm/sec are characteristic within 10 km of the coast.

Figure 6.11 shows the overall pattern of transport streamlines as a function of longshore position (ky) and offshore distance. The general mass balance is a strong function of the alongshore coordinate, and the net offshore transport in the vicinity of the field site is supplied by onshore transport at other locations via a longshore convergence of "feeder" currents. Since these are transport streamlines defined by $vh = -\partial\psi/\partial x$ and $uh = \partial\psi/\partial y$, the slightly closer spacing apparent near-shore corresponds to a large increase in the longshore velocity in this rapidly shoaling envirionment. A closer look at the details of the nearshore circulation pattern suggests that the Tiana Beach field site was a particularly fortuitous choice. The region in which the longshore current reversal occurs within the CBL, and could therefore be observed by the COBOLT experimental array, is roughly limited to the stretch of shoreline between Montauk Point and Tiana Beach. Had the moorings been set 25 km or so farther west, this strikingly diagnostic feature would likely have been missed entirely.

One problem in attempting to get quanitative information from applications of the foregoing models is that the effective resistance coefficient which may be appropriate within the CBL, may not be nearly as realistic farther from shore. As pointed out previously, the linear friction law used involves the vertically averaged longshore velocity rather than its near bottom value. The characteristic $V_b/<V>$ ratio (0.4 in the CBL) would be substantially lower in deeper water, so that a
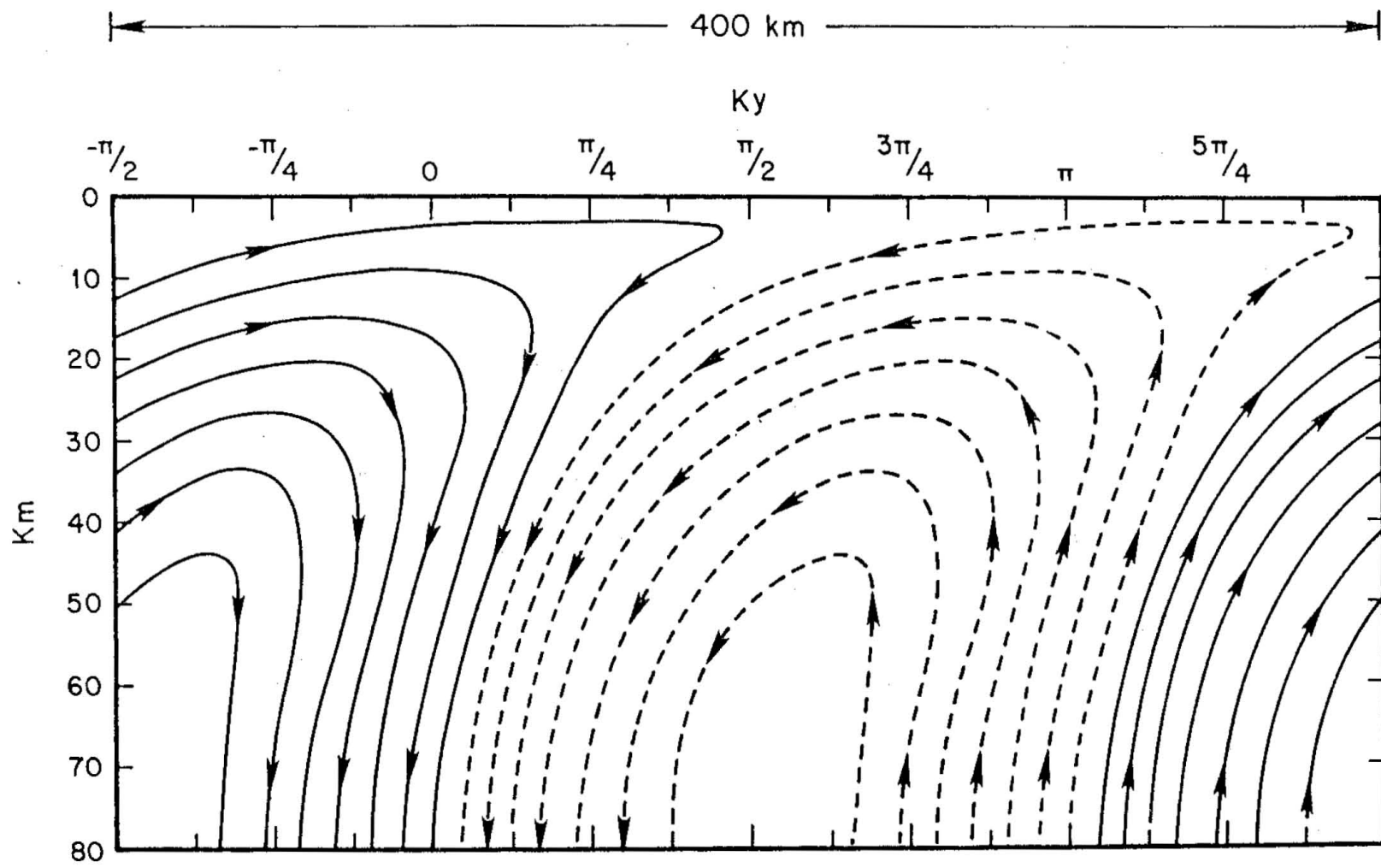
Figure 6.11 Streamline pattern showing circulation cells and longshore current reversals.

smaller r_e value would be more appropriate. The same argument
applies to other geographical locations which might have a deeper
nearshore zone. The physical effects of these differences would be to
narrow the trapping width of the solutions so that the scales shown
previously represent upper bounds.

6.6 Summary

It has been demonstrated that the details of nearshore bottom
topography have significant effects upon the offshore and alongshore
behavior of arrested topographic wave solutions. In particular, the
matched exponential model, which very accurately reflects observed
nearshore topography, is quite successful in reproducing several
striking characteristics of the experimentally observed circulation .
pattern. This model predicts both alongshore current reversals across
the coastal boundary layer and a divergent net offshore transport for
the longshore position corresponding to the COBOLT field site. The
cross-shore decay scales of these solutions are consistent with the
hypothesis that an arrested topographic wave is an expected response to
coastal winds in the presence of Long Island Sound. The analytic sol-
utions display a large degree of longshore variability and indicate that
the spatial reversals of longshore currents within the CBL are likely to
be limited to the eastern portion of the island. An experiment includ-
ing measurements at several longshore positions, preferably on both

sides of the island, would allow conclusive evaluation of this model of
the nearshore currents in the coastal boundary layer around Long Island.

APPENDIX: <u>Response to longshore forcing</u>

For the case of longshore wind, equations (3.13) yield

$$F_1 = \frac{F_o f c_1}{2h_1} \frac{1-e^{-\alpha P}}{p^3 \frac{}{P^2+f^2}}$$

$$F_2 = \frac{-F_o f c_2}{2h_1} \frac{1-e^{-\alpha P}}{p^3 \frac{}{P^2+f^2}}$$

(A.1)

and equations (3.12) become

$$U_1 = \frac{1}{k^2} \frac{\partial \Phi_1}{\partial x} + \frac{fF_o(1-e^{-\alpha P})}{h_1 P(P^2+f^2)}$$

$$V_1 = -\frac{fU_1}{P} + \frac{F_o(1-e^{-\alpha P})}{P^2 h_1}$$

(A.2)

$$U_2 = \frac{1}{k^2} \frac{\partial \Phi_2}{\partial x}$$

$$V_2 = -\frac{fU_2}{P}$$

These relations, in conjunction with equations (3.10), lead directly to the following expressions for the transformed velocities:

$$U_1 = \frac{-F_o f}{2h_1}\left(\frac{(1-e^{-\alpha P})e^{-\sqrt{P^2+f^2}\ x/c_1}}{P(P^2+f^2)} + \frac{(1-e^{-\alpha P})e^{-\sqrt{P^2+f^2}\ x/c_2}}{P(P^2+f^2)}\right) + \frac{F_o f}{h_1}\left(\frac{1-e^{-\alpha P}}{P(P^2+f^2)}\right)$$

$$V_1 = \frac{F_o f^2}{2h_1}\left(\frac{(1-e^{-\alpha P})e^{-\sqrt{P^2+f^2}\ x/c_1}}{P^2(P^2+f^2)} + \frac{(1-e^{-\alpha P})e^{-\sqrt{P^2+f^2}\ x/c_2}}{P^2(P^2+f^2)}\right)$$

$$- \frac{f^2 F_o}{h_1}\frac{(1-e^{-\alpha P})}{P^2(P^2+f^2)} + \frac{F_o}{h_1}\frac{(1-e^{-\alpha P})}{P^2}$$

$$(A.3)$$

$$U_2 = \frac{-F_o f}{2h_1}\left(\frac{(1-e^{-\alpha P})e^{-\sqrt{P^2+f^2}\ x/c_1}}{P(P^2+f^2)} - \frac{(1-e^{-\alpha P})e^{-\sqrt{P^2+f^2}\ x/c_2}}{P(P^2+f^2)}\right)$$

$$V_2 = \frac{F_o f^2}{2h_1}\left(\frac{(1-e^{-\alpha P})e^{-\sqrt{P^2+f^2}\ x/c_1}}{P^2(P^2+f^2)} - \frac{(1-e^{-\alpha P})e^{-\sqrt{P^2+f^2}\ x/c_2}}{P^2(P^2+f^2)}\right)$$

The differences between these transformed solutions and those of the offshore case are a multiplicative factor of $1/P$ and an additional term in the expression for the transformed upper-layer alongshore velocity (V_1). The effects of these changes may be simply investigated through

the elementary application of complex analysis techniques. The functions $U_i(P)$, and $V_i(P)$ have their singularities at points $P=0, \pm$ if. The only possible non-wavelike contribution arises from the singular point at $P=0$ which is a simple pole in expressions for $U_i(P)$, and a second order pole in $V_i(P)$. This fact allows the calculation of this "steady" contribution through use of the residue theorem which states that the inverse Laplace transform of a function $g(P)$ equals the sum of the residues of e^{Pt} $g(P)$ at the poles of $g(P)$. The residue for a pole of order n is given by

$$\text{Res}(a) = \lim_{P \to a} \frac{1}{(n-1)!} \frac{d^{n-1}}{dP^{n-1}} [(P-a)^n e^{Pt} g(P)] \qquad (A.4)$$

where $d^{(n-1)}/dP^{(n-1)}$ represents the $(n-1)$th derivative with respect to the transform variable P. The solution for the cross-shore velocity under longshore forcing is exactly the same as that of longshore velocity under cross-shore forcing. From previous discussions it is therefore clear that during the wind stress episode, the U_i's will have a nonzero mean value. Looking first at the residues for U_1, it is found that

$$U_1 \ \text{Res}(0) = \frac{-F_o f}{2h_1} [\ e^{-fx/c_1} (1-\mu(t-\alpha')) + e^{-fx/c_2}(1-\mu(t-\alpha))] \qquad (A.5)$$

with an analogous result for U_2. These zero residues reflect the fact that (as expected) no steady component to the offshore velocity arises in response to a longshore wind of limited duration, and the solution for $t>\alpha$ is a phase shifted version of that for an offshore wind.

The residue at the second order pole P=0 for the upper layer longshore velocity is found by

$$\frac{F_o f^2}{2h} \left[\frac{t\,e^{-fx/c_1}}{f^2} - \frac{(t-\alpha)\,e^{-fx/c_1}}{f^2} \mu(t-\alpha) \right.$$

$$\left. + \frac{t\,e^{-fx/c_2}}{f^2} - \frac{(t-\alpha)\,e^{-fx/c_2}}{f^2} \mu(t-\alpha) \right]$$

to be

$$V_1\ Res(0) = \frac{F_o \alpha}{2h_1} (\,e^{-fx/c_1} + e^{-fx/c_2}\,) \qquad\qquad (A.6)$$

$$t > \alpha$$

Following the same procedure for the lower layer one gets

$$V_2\ Res(0) = \frac{F_o \alpha}{2h_1} (\,e^{-fx/c_1} - e^{-fx/c_2}\,) \qquad\qquad (A.7)$$

$$t > \alpha$$

These results show that a non-wavelike component grows linearly in time during the wind impulse and remains constant thereafter. Thus, a steady shore trapped longshore velocity component arises in response to longshore wind forcing. This steady contribution does not occur under cross-shore forcing and represents the fundamental difference between the two regimes.

References

Abramowitz, M., and I. Stegun (eds.), 1964. Handbook of Mathematical Functions. U.S. Dept. of Commerce, Applied Mathematics Series-55, 1046 pp.

Allen, J. S., and P. K. Kundu, 1978. On the momentum, vorticity and mass balance off the Oregon coast. J. Phys. Oceanogr., 8, 13-27.

Allen, J. S., 1980. Models of wind-driven currents on the continental shelf. Ann. Rev. Fluid Mech., 12, 389-433.

Amorocho, J., and J. J. Devries, 1980. A new evaluation of the wind stress coefficient over water surfaces. J. Geophys. Res., 85, 433-442.

Avers, H. G., 1927. A study of the variations of mean sea-level from a level surface. Amer. Geophys. Un., Trans., Nat. Res. Council Bull. No. 61, Washington, D.C., 56-58.

Beardsley, R. C., and B. Butman, 1974. Circulation on the New England continental shelf: response to strong winter storms. Geophys. Res. Lett., 1, 181-184.

Beardsley, R. C., W. Boicourt, and D. Hansen, 1976. Physical oceanography of the Middle Atlantic Bight. Limnol. Oceanogr., Spec. Symp. 2, 20-34.

Beardsley, R. C. W. Boicourt, L. C. Huff, and J. Scott, 1977. CMICE 76: A current meter intercomparison experiment conducted off Long Island in February-March, 1976. W.H.O.I. Ref. No. 77-62, Woods Hole Oceanographic Institution, Woods Hole, Massachusetts, 123 pp.

Beardsley, R. C., and C. D. Winant, 1979. On the mean circulation in the Mid-Atlantic Bight. J. Phys. Oceanogr., 9, 612-619.

Bendat, J. S., and A. G. Piersol, 1971. Random Data: Analysis and Measurement. Wiley-Interscience, New York, 407 pp.

Bennett, J. R., and B. A. Magnell, 1979. A dynamical analysis of currents near the New Jersey coast. J. Geophys. Res., 84, 1165-1175.

Birchfield, G. E., 1973. An Ekman model of coastal currents in a lake or shallow sea. J. Phys. Oceanogr., 3, 419-428.

Blanton, J. D., 1974. Some characteristics of nearshore curents along the north shore of Lake Ontario. J. Phys. Oceanogr., 4, 415-424.

Bowden, K. F., 1962. Turbulence. In The Sea, Vol. 1, M. N. Hill, ed., Interscience Publishers, New York, 812-817.

Brink, K. H., J. S. Allen, and R. L. Smith, 1978. A study of low-frequency fluctuations near the Peru coast. J. Phys. Oceanogr., 8, 1125-1141.

Bumpus, D. F., 1973. A description of the circulation on the continental shelf of the east coast of the United States. In Prog. Oceanogr., Vol. 6, Pergamon Press, New York, 111-159.

Chase, R. R. P., 1979. The coastal longshore pressure gradient: temporal variations and driving mechanisms. J. Geophys. Res., 84, 4898-4914.

Crepon, M., 1969. Hydrodynamique marine en regime impulsionnel. Cah. Oceanogr., 21, 863-877.

Csanady, G. T., 1972a. The coastal boundary layer in Lake Ontario. Part I: The spring regime. J. Phys. Oceanogr., 2, 41-53.

Csanady, G. T., 1972b. The coastal boundary layer in Lake Ontario. Part II: The summer-fall regime. J. Phys. Oceanogr., 2, 168-176.

Csanady, G. T., 1976. Mean circulation in shallow seas. J. Geophys. Res., 81, 5389-5399.

Csanady, G. T., 1977a. The coastal jet conceptual model in the dynamics of shallow seas. In, The Sea, vol 6, eds. E. D. Goldberg, I. N. McCave, J. J. O'Brien, and J. H. Steele, 117-144. John Wiley, New York.

Csanady, G. T., 1977b. The coastal boundary layer. In Geophysics and Environment, C. Officer, ed., National Academy of Sciences, U.S.A., 57-68.

Csanady, G. T., 1977c. Intermittent "full" upwelling in Lake Ontario. J. Geophys. Res., 82, 397-419.

Csanady, G. T., 1978. The arrested topographic wave. J. Phys. Oceanogr., 8, 47-62.

Csanady, G. T., 1979. The pressure field along in western margin of the North Atlantic. J. Geophys. Res., 84, 4915-4914.

Csanady, G. T., 1981. Longshore pressure gradients caused by offshore wind. J. Geophys. Res., 85, 1176-1184.

Csanady, G. T., 1981. Circulation in the coastal ocean. Adv. in Geophys., 23, B. Saltzman, ed., Academic Press, in press.

Cushing, V., 1976. Electromagnetic water current meter. MTS and IEEE Oceans 76 Conf. Proc., 25C, 1-7.

Dimmler, D. G., D. Huszagh, S. Rankowitz, and J. Scott, 1976. A controllable real-time collection system for coastal oceanography. Ocean 76 Conf. Proc., 14E-1, 1-13.

EGaG, Environmental Consultants., 1975. Summary of oceanographic observations in New Jersey coastal waters near 39 28' N latitude and 74 15' W longitude during the period May, 1973 through May, 1974. A Report to the Public Service Electric and Gas Co., Newark, New Jersey.

Flagg, C. N., 1977. The kinematics and dynamics of the New England continental shelf and shelf/slope front. Ph.D. thesis, MIT/WHOI Joint Program, 217 pp.

Flagg, C. N., J. A. Vermersch and R. C. Beardsley, 1976. M.I.T. New England Shelf Dynamics Experiment (March, 1974) Data Report, Part II: the moored array. GFD Lab Report 76-1, Dept. of Meteorol., Massachusetts Institute of Technology.

Flierl, G. R., and J. C. McWilliams, 1977. On the sampling requirements for measuring moments of eddy variability. J. Mar. Res., 4, 797-821.

Forristal, G. Z., R. C. Hamilton, and V. J. Cardone, 1977. Continental shelf currents in tropical storm Delia: Observations and theory. J. Phys. Oceanogr., 7, 532-546.

Gill, A. E., and E. H. Schumann, 1974. The generation of long shelf waves by the wind. J. Phys. Oceanogr., 4, 83-91.

Gonella, J., 1971. A local study of inertial oscillations in the upper waters of the ocean. Deep-Sea Res., 18, 775-788.

Gonella, J., 1972. A rotary-component method for analyzing meteorological and oceanographic vector time series. Deep-Sea Res., 19, 833-846.

Groen, P., and G. W. Groves, 1962. Surges. In The Sea, Vol. 1, M. N. Hill, ed., Interscience Publishers, New York, 611-646.

Halpern, D., 1974. Observations of the deepening of the wind mixed layer in the Northeast Pacific Ocean. J. Phys. Oceanogr., 4, 454-466.

Hayes, S., and D. Halpern, 1976. Observations of internal waves and coastal upwelling off the Oregon coast. J. Mar. Res., 34, 247-267.

Hicks, S., 1978. An average geopotential sea level series for the United States. J. Geophys. Res., 83, 1377-1379.

Hogg, N. G., and W. J. Schmitz, 1981. A dynamical interpretation of low frequency motions near very rough topography -- the Charlie Gibbs Fracture Zone. J. Mar. Res., 38, 215-248.

Hopkins, T. S., J. Lofstrand, and E. G. Divis, 1979. Oceanographic data from moored instrumentation: August 1978. Data report, Oceanographic Sciences Division, Brookhaven National Laboratory (unpublished manuscript).

Hunt, M., 1977. A program for spectral analysis of time series. W.H.O.I. Technical Report 2-77, 188 pp.

Huyer, A., R. L. Smith, and E. S. C. Sobey, 1978. Seasonal differences in low-frequency current fluctuations over the Oregon continental shelf. J. Geophys. Res., 83, 5177-5189.

Jahnke, E., F. Emde, and F. Losch, 1961. Tables of Higher Functions. McGraw-Hill, New York.

Ketchum, B., and N. Corwin, 1964. The persistence of "winter" water on the continental shelf south of Long Island, New York. Limnol. Oceanogr., 9, 467-475.

Ketchum, B. H., and D. J. Keen, 1955. The accumulation of river water over the continental shelf between Cape Cod and Chesapeake Bay. Papers in Marine Biology and Oceanography, Deep-Sea Res., Suppl. to Vol. 3, 346-357.

Koopmans, L. H., 1974. The Spectral Analysis of Time Series. Academic Press, New York, 366pp.

Krauss, W., 1976a. On currents, internal and inertial waves in a stratified ocean due to variable winds. Part 1., Deut. Hydro. Zeit., 29, 87-96.

Krauss, W., 1976b. On currents, internal and inertial waves in a stratified ocean due to variable winds. Part 2., Deut. Hydro. Zeit., 29, 121-135.

Kundu, P. K., 1976. An analysis of inertial oscillations observed near Oregon coast. J. Phys. Oceanogr., 6, 879-893.

Kundu, P. K., and J. S. Allen, 1975. Some three-dimensional characteristics of low-frequency current fluctuations near the Oregon coast. J. Phys. Oceanogr., 6, 181-199.

Lowe, R. L., D. L. Inman, and B. M. Brush, 1972. Simultaneous data system for instrumenting the shelf. 13th Conf. on Coastal Eng., Vancouver, B. C.

Luyten, J. R., 1977. Scales of motions in the deep Gulf Stream and across the continental rise. J. Mar. Res., 35, 49-74.

Malone, F., 1968. An analysis of current measurements in Lake Michigan. J. Geophys, Res., 73, 7065-7081.

May, P. W., 1979. Analysis and interpretation of tidal currents in the coastal boundary layer. Sc.D. thesis, MIT/WHOI Joint Program, 197 pp.

Mayer, D. A., D. V. Hansen, and D. A. Ortman, 1979. Long term current and temperature observations on the Middle Atlantic Shelf. J. Geophys. Res., 84, 1772-1792.

Mayer, D. A., H. O. Mofjeld, and K. D. Leaman, 1980. Near-inertial internal waves observed on the outer shelf in the Middle Atlantic Bight in the wake of hurricane Belle. J. Phys. Oceanogr. (in press)

McCullough, J. R., 1968. Oceanographic applications of digital filters. W.H.O.I. Ref. No. 68-78, 31 pp.

Mysak, L. A., 1980. Topographically trapped waves. Ann. Rev. Fluid Mech., 12, 45-76.

Noble, M., and B. Butman, 1979. Low-frequency wind-induced sea level oscillations along the east coast of North America. J. Geophys. Res., 84, 3227-3236.

Nuttall, A. H., 1971. Spectral estimation by means of overlapped fast Fourier transform processing of windowed data. Naval Underwater Systems Center, Report No. 4169.

Pedlosky, J., 1974. Longshore currents, upwelling and bottom topography. J. Phys. Oceanogr., 4, 214-226.

Perkins, H. T., 1970. Inertial oscillations in the Mediterranean. Ph.D. thesis, MIT/WHOI Joint Program, 155 pp.

Pollard, R. T., 1970. On the generation by winds of inertial waves in the ocean. Deep-Sea Res., 17, 795-812.

Pollard, R. T., P. B. Rhines, and R.O.R.Y. Thompson, 1973. The deepening of the wind-mixed layer. Geophys. Fluid Dyn., 3, 381-404.

Pollard, R. T., and R. C. Millard, Jr., 1970. Comparison between observed and simulated wind-generated inertial oscillations. Deep-Sea Res., 17, 813-821.

Powell, M. D., and S. SethuRaman, 1979. Sea surface temperatures near a bay inlet zone. J. Geophys. Res., 84, 7012-7016.

Ruddick, B. R., 1977. Observations of interaction between the internal wavefield and low frequency flows in the North Atlantic. Ph.D. thesis, MIT/WHOI Joint Program, 330 pp.

Saunders, P. M., 1977. Wind stress on the ocean over the eastern continental shelf of North America. J. Phys. Oceanogr., 7, 555-566.

Scott, J. T., and G. T. Csanady, 1976. Nearshore currents off Long Island. J. Geophys. Res., 81, 5401-5409.

Scott, J., T. Hopkins, R. Pillsbury, and E. Divis, 1978. Velocity and temperature off Shinnecock, Long Island in October-November, 1976. Oceanographic Sciences Division, Brookhaven National Laboratory (unpublished manuscript).

Semtner, A. J., and Y. Mintz, 1977. Numerical simulation of the Gulf Stream and mid-ocean eddies. J. Geophys. Res., 7, 208-230.

SethuRaman, S., and G. S. Raynor, 1975. Surface drag coefficient dependence on the aerodynamic roughness of the sea. J. Geophys. Res., 80, 4983-4988.

Smith, N. P., 1972. Temporal variations of nearshore inertial motion in Lake Superior. Proc. 15th Conf. Great Lakes Res., Ann Arbor, Intern. Assoc. Great Lakes Res., 673-679.

Smith, P., B. Petrie, and C. Mann, 1978. Circulation, variability and dynamics of the Scotian Shelf and Slope. J. Fish. Res. Board Can., 35, 1067-1083.

Stommel, H., and A. Leetmaa, 1972. Circulation on the continental shelf. Proc. Nat. Acad. Sci., U.S., 69, 3380-3384.

Sturges, W., 1977. Comment on "Nearshore currents off Long Island" by J. T. Scott and G. T. Csanady. J. Geophys. Res., 82, 1451-1452.

Sverdrup, H., M. Johnson, and R. Fleming, 1942. The Oceans. Prentice-Hall, Inc., Englewood Cliffs, N. J., 1087 pp.

Swanson, R., 1976. Tides. MESA New York Bight atlas monography 4, New York Sea Grant Inst., Albany, N.Y., 34 pp.

Verber, J. L., 1966. Inertial currents in the Great Lakes. Proc. 9th Conf. Great Lakes Res., Great Lakes Res. Div. Publ. No. 15, University of Michigan, 375-379.

Wallace, J. M., 1971. Spectral studies of tropospheric wave disturbances in the tropical western Pacific. Rev. Geophys., 9, 557-612.

Wallace, J. M., and R. E. Dickinson, 1972. Empirical orthogonal representation of time series in the frequency domain. Part I: theoretical considerations. J. Appl. Meteorol., 11, 887-892.

Wang, D. P., 1979. Low frequency sea level variability in the Middle-Atlantic Bight. J. Mar. Res., 37, 683-697.

Webster, F., 1968. Observations of inertial-period motions in the deep sea. Rev. Geophys., 6, 473-490.

Winant, C. D., 1979. Comments on "The arrested topographic wave". J. Phys. Oceanogr., 9, 1042-1043.

Winant, C. D., 1980. Coastal circulation and wind-induced currents. Ann. Rev. Fluid Mech., 12, 271-301.

Winant, C. D., and R. C. Beardsley, 1979. A comparison of some shallow wind-driven currents. J. Phys. Oceanogr., 9, 218-220.

BIOGRAPHICAL NOTE

Neal Robert Pettigrew was born in Newark, New Jersey in 1951. He grew up along the shores of Lake Hopatcong and in the rural township of Andover. After graduating from high school in 1968, the author entered Dartmouth College where he was a member of the fencing team and the Dartmouth Outing Club. In the summer of his junior year Neal married his high school sweetheart, the former Miss Patricia Maier. He was elected to the Phi Beta Kappa Society, and was graduated magna cum laude in physics in 1972.

After spending a year as a laboratory technician at the New York Ocean Science Laboratory in Montauk, New York, the author studied beach and nearshore processes at the Coastal Studies Institute of the Louisiana State University, and received an M.S. degree in 1975. That same year he was admitted to the M.I.T./W.H.O.I. Joint Program in Oceanography.

In December, 1978 his daughter Sarah Morrow Pettigrew was born in North Falmouth, Massachusetts.

Publications:

Sonu, C.J., N.R. Pettigrew, and R.G. Fredericks, 1974. Measurement of swash profile and orbital motion on the beach. Proc. Int. Symp. on Ocean Wave Measurement and Anal., 621-638.

Suhayda, J.N., and N.R. Pettigrew, 1977. Observations of wave height and wave celerity in the surf zone. J. Geophys. Res., 82, 1419-1424.